4

Results and Discussion

The results obtained in the research work entitled "Development of Bioactive Drug Formulations Using Eco-friendly Metallic Nanoparticles for Sustained Drug Release Systems and Selected *In vitro* Biomedical Applications" are discussed and presented in following pages.

Phase-I Ionic liquid-based Solvent Extraction of Organo Sulphur compounds

4.1 Extraction of Garlic

Garlic extracts were obtained using two different solvents: methanol (GM) and ionic liquid-based (GI) medium, as described in section 3.3. The percentage yield of the extracts was found to be 33.4% for GM and 36.2% for GI. These results indicated that ionic liquid (IL) assisted extraction resulted in a higher extraction yield compared to conventional methanol extraction, which indicates that ILs significantly enhance the extraction efficiency of secondary metabolites from garlic.

The higher extraction yield observed in IL-based method is associated to the strong molecular interactions among the imidazolium-based IL and garlic phytochemicals. The interactions include are hydrogen bonding, electrostatic interactions, and other intermolecular forces, which collectively enhance the solubilisation and mass transfer of bioactive compounds from plant matrices **(Ventura *et al.*, 2012)**. IL-assisted extraction using [BMIM]Cl was previously shown to yield slightly higher amount of Rutin (18-24 g/100 g) from *Sophora japonica* compared to conventional methanol extraction (18-22 g/100 g), as reported by **Huang and Xie, 2010**. The ionic liquid (BMIMCl) is widely recognised as greener alternative to conventional organic solvents due to negligible vapor pressure, and high thermal stability, although it may exhibit moderate cytotoxicity and aquatic toxicity at higher concentrations **(Pham *et al.*, 2009; Zhang *et al.*, 2017)**. In this study, BMIMCl was utilised at a low concentration (0.05 M) for extraction purpose without any direct biological exposure. Finally, both extracts (GM and GI) were diluted with methanol to a final concentration of 5 mg/mL, and processed for chromatographic analysis.

4.1.1 Characterisation of Garlic Extract

Due to the high cost of commercially available standard Allicin (Rs. 4,00,317 per 10 g at Sigma-Aldrich), we utilised column chromatographic technique to isolate the compound from garlic extract. The isolated compound was subsequently analysed using FTIR spectroscopy, and its characteristic fingerprint region was compared with reported spectra of Allicin for identification.

4.1.2 Preparative Thin Layer Chromatographic (TLC) Analysis of Garlic Extract

Figure 5 presents the developed TLC chromatograms of GM and GI visualised under short UV (254 nm), and iodine vapour exposure. No distinct spots were observed under long UV 365 nm, for either extract, indicating that the major compounds present were not long UV active at this wavelength. However, three distinct bands were detected under iodine vapour, suggesting the presence of bioactive compounds in both extracts. The corresponding Rf values of GM and GI are given in **Table 7**. Among the observed bands, the spot with a Rf value 0.64, which are the most prominent and consistent across both extracts. This spot may be attributed to Allicin, based on its reported chromatographic behaviour in previous studies **(Albrecht *et al.*, 2017; Nair and Alka, 2017)**.

Allicin absorbs at UV 254 nm, due to lone pair (n→π* transition or S=O). However, it is not visible under UV 365 nm, due to absence of extended π -electron conjugation system, which is essential for fluorescence. Therefore, instead of fluorescing Allicin exhibits photo instability and rapidly degrading under UV exposure **(Parkin *et al.*, 2005; Dana *et al.*, 2023).** In contrast, iodine vapour staining enhanced clear visualisation of compound, which is due to the presence of allyl and thiosulfinate groups, which readily interact with iodine, forming distinct coloured complex.

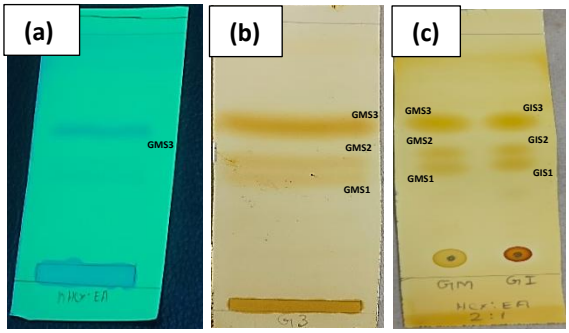

Figure 5. TLC chromatogram of garlic extracts (a) GM under 254 nm; (b) GM under iodine vapour; (C) GM and GI under iodine vapour

Table 7. Rf values and Visibility of TLC spots in Garlic Extracts

Sample code	Spots	Rf	Visible spots under short UV/ Iodine
GM	GMS1	0.41	Iodine
	GMS2	0.47	Iodine
	GMS3 (dark)	0.64	Iodine and short UV
GI	GIS1	0.41	Iodine
	GIS2	0.47	Iodine
	GIS3 (dark)	0.64	Iodine

In the GM chromatogram under 254 nm **(Figure 5a)**, spot (GMS3) appears as a distinct green band, indicative of partial UV absorption. Upon exposure to iodine vapour **(Figure 5c)**, all three spots (GMS1-GMS3 and GIS1-GIS3) were clearly visible, Where GMS3 and GIS3 appearing significantly darker, suggesting higher stronger iodine reactivity of compound.

The GI extract, visualised similarly **(Figure 5c)**, as comparable band patterns to GM, confirming the phytochemical extracted using IL based solvent is similar with the conventional methanol extraction. Hence, no additional bands correspond to IL were detected under either both UV or iodine vapour visualisation, confirming that IL component does not interfere with TLC based detection of garlic metabolites.

4.1.3 Column Chromatographic Separation of Garlic Extract

Following the TLC analysis, the column chromatographic separation of garlic methanol extract was carried out using a silica gel column, with hexane as packing solvent. The elution was performed using hexane and hexane-ethyl acetate mixtures of progressively increasing polarity, as described in section 3.3.3, to separate the bioactive constituent. A total of 93 fractions were collected, among them the fraction 16 to 20 were eluted with hexane-ethyl acetate proportion of 50:50 (v/v), exhibited similar single spots on TLC under iodine vapour visualisation **(Figure 6a)**. These spots showed Rf values in the range of 0.64 to 0.67, and the eluate appeared pale yellow in colour. Based on the Rf values and visual profile, these fractions (16 to 20) were combined, concentrated and recrystallised **(Figure 6b)**, which were labelled as GS (Garlic standard). The purified GS were refrigerated at 3˚C for further analysis. Meanwhile, all the other fractions displayed multiple spots under iodine vapour, indicating the presence of mixed compounds, which were excluded from further analysis. Due to high commercial cost of standard Allicin, the purified GS compound, isolated from garlic methanolic extract, was used as reference standard (GS) for subsequent analysis.

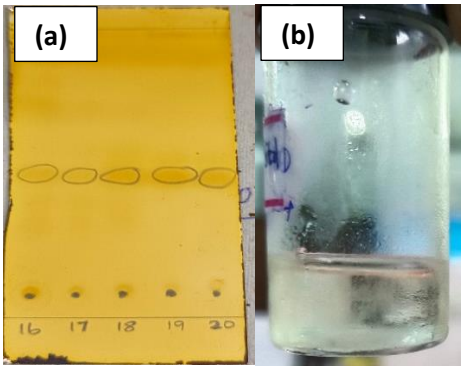

Figure 6. TLC chromatograph of garlic extract fractions obtained from Column chromatographic separation (a) Eluted fractions 16 to 20 showing single band on silica gel TLC plate under iodine vapour; (b) Purified fraction containing isolation of major compound (GS)

4.1.4 FTIR analysis of Garlic Extract

FTIR analysis was carried out to identify and characterise the functional groups present in the samples derived from garlic: GS (from column fraction), GM (methanolic extract), and GI (ionic liquid extract), by identifying the functional groups of Allicin and other sulphur compounds.

The FTIR spectrum of the GS fraction **(Figure 7)**, exhibited several characteristic peaks. The distinct peak observed at 529.371 cm^{-1}, and 451.406 cm^{-1} were assigned to C-S stretching vibrations, confirming the presence of sulphur containing bonds. The band observed at 1029.714 cm^{-1} is assigned to S=O stretching vibrations (sulfoxide group), indicates the presence of Allicin like compound. The additional peaks at 1136.492 cm^{-1} and 1222.426 cm^{-1} corresponds to C-O-C asymmetric stretching and C-N stretching, which are from carbohydrate and amino acid derived components of garlic. The band at 1359.885 cm^{-1} is attributed to C-H bending of aliphatic allyl groups, whereas the band near 1654.383 cm^{-1} represents C=C stretching of allyl group. The peak at 1703.669 cm^{-1} corresponds to C=O stretching, which maybe from the solvent residue, while the broad band at 3413.447 cm^{-1} represents the characteristics of O-H stretching vibrations of solvent. The earlier report shows that peak at 1020 to 1070 cm^{-1} represents to S=O asymmetric stretching, which is a marker of Allicin (Diallyl thiosulphinate) as reported by **Lawson *et al.*, 1991; Iberl *et al.*, 1990; Divya *et al.*, 2017**, these reports supports the presence of sulfoxide groups in the fractionated compound.

Similarly, the FTIR spectrum of GM extract **(Figure 8)**, exhibited the characteristic peak at 416.273 cm^{-1} corresponds to C-S stretching vibrations, and the strong band at 1024.182 cm^{-1} attributed to S=O stretching vibrations of Allicin from garlic. The peak at 1635.916 cm^{-1} corresponds to C=C stretching of allyl group, while the broad peak at 3264.305 cm^{-1} corresponds to O-H stretching vibrations of solvent residue.

FTIR spectrum of GI extract **(Figure 9)** exhibits the characteristic peak at 410.258 cm^{-1} corresponds to C-S stretching, confirms the sulphur linkage similar to GM and GS. The peaks at 1020.359 cm^{-1} attributed to S=O stretching of sulfoxide group, while the additional peaks at 1126.684 cm^{-1} and 1165.565 cm^{-1} represents C-N and C-O-C stretching vibrations of amino acid and carbohydrate residues. The prominent peak at 1572.929 cm^{-1} and 1629.161 cm^{-1} corresponds to C=C stretching vibrations. The broad peak corresponds to 3317.516 cm^{-1} represents hydroxyl (-OH) groups of residual solvent. The peak at 2959.904 cm^{-1}, 2876.118 cm^{-1}, and 2934.678 cm^{-1} represents C-H stretching of aliphatic groups.

Therefore, from the FTIR spectral analysis, it may be concluded the presence of distinct functional groups corresponding to S=O, C=C, and C-S in the GS fraction, are characteristic of Allicin and other organosulphur compounds. The presence of strong sulfoxide (S=O) stretching around 1030 to 1070 cm^{-1}, confirms the presence of Allicin group in garlic. The GM and GI spectra showed similar peaks, indicating the presence of Allicin. Further, HPTLC was performed on GS fraction along with crude extracts (GM and GI) to quantify the desired compound.

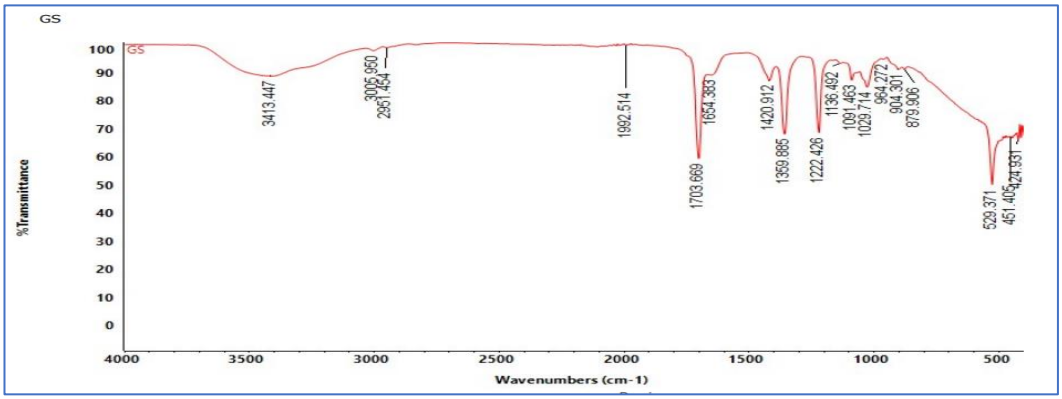

Figure 7. FTIR spectrum of GS fraction from column chromatography

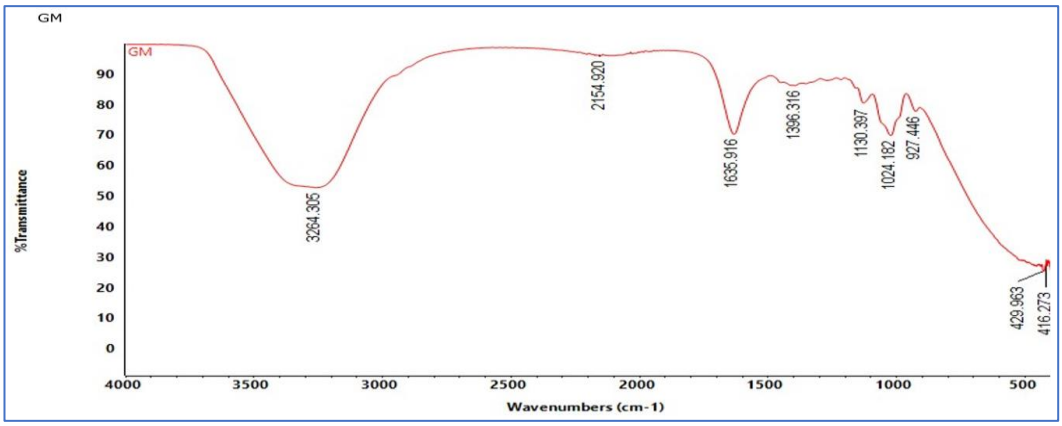

Figure 8. FTIR spectrum of methanolic garlic extract (GM)

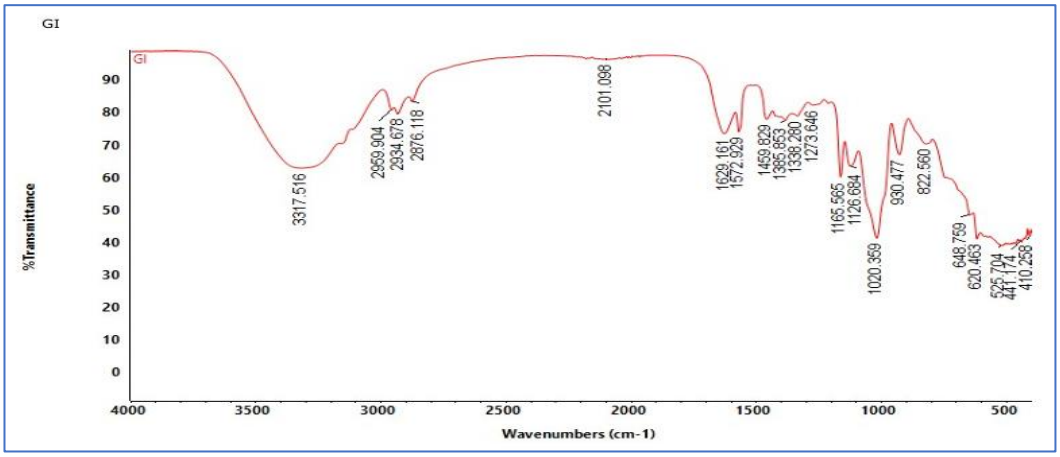

Figure 9. FTIR spectrum of ionic liquid-based garlic extract (GI)

4.1.5 Quantitation of Organosulphur Compounds by HPTLC Analysis

HPTLC analysis of garlic extracts such as GS (compound from column fraction), GI (ionic liquid extract), and GM (methanolic extract) was optimised using hexane: ethyl acetate (2:1) as the mobile phase. The solvent system was selected based on the preliminary TLC results. The HPTLC fingerprint profiles of GS, GI, and GM exhibited Rf values of 0.62 (GSS1), 0.68 (GIS3), and 0.66 (GMS3), respectively, which maybe corresponds to Allicin.

Several authors have reported similar Rf values for Allicin extracted using different solvent-based extracts such as aqueous extract (Rf 0.60 in hexane/ethyl acetate), hydroethanolic extract (Rf 0.68), buffer-based extract (Rf 0.34), and chemically synthesised Allicin (*via* reaction of Diallyl disulphide with formic acid and H_2O_2), depending on the solvent polarity **(Lawson, Wood *et al.*, 1991; Nair and Alka, 2017; Bosca and Mot, 2023; Albrecht *et al.*, 2017)**.

Figure 10 shows the HPTLC chromatograms of GS, GI and GM visualised under white light, UV 254 nm, UV 366 nm and iodine vapour. At UV 254 nm, all samples possess dark green bands, indicating the presence of UV-absorbing compounds. In particular, only the GS fraction displayed blue fluorescent zones under UV 366 nm, which were absent in both GM and GI, suggesting the presence of enriched compounds in the purified fraction. The Rf values of the GS fraction ranged from 0.08 to 0.97, indicating the diverse profile of separated compounds. A green band (GSS1) at Rf 0.62 was observed in GS under short UV 254, which may correspond to the presence of low concentration of Allicin (Diallyl thiosulphinate), consistent with the previously reported values in the literature.

In addition, a prominent dark green band (GSS2) at Rf 0.91 and a light green band (GSS3) at Rf 0.97 were also observed **(Figure 10b)**. The high Rf values in the range of 0.91 to 0.97, indicates the presence of non-polar compounds, like sulphur containing degradation products of Allicin such as Diallyl disulphide, Diallyl trisulphides, and Vinyl dithiins. These compounds are eluted in non-polar to mid-polar solvent systems such as hexane: ethyl acetate, due to lipophilicity and low polarity **(Freeman and Kodera,1995; Iberl *et al.*, 1989)**.

The appearance of blue fluorescent zones under UV 366 nm in the GS chromatogram strongly indicates the presence of conjugated double bonds and lipophilic sulphur compounds such as Allicin or Ajoene, which exhibits fluorescence due to π-electron system **(Figure 10c)**.

Similarly, the Rf values for GM and GI was ranged from 0.08 to 0.98. A dark green band at Rf 0.66 (GMS3) in GM and Rf 0.68 (GIS3) in GI, observed under UV 254 nm and iodine staining **(Figure 10b and d)**, corresponds to Allicin band in GS reference.

For quantification, densitometric scanning of the developed HPTLC plate was performed. The resulting densitograms of GI and GM **(Figure 11)** revealed that the third major peak (Rf 0.66 for GMS3 and Rf 0.68 for GIS3) showed peak areas of 22.49% and 24.89%, respectively, which are likely corresponding to Allicin, based on comparison with the GS calibration standard.

Using the GS calibration data, the Allicin concentration was found to be 1.355 mg/mL for GM and 3.446 mg/mL for GI. These results indicated that the ionic liquid-based garlic extract (GI) yielded approximately 86% Allicin, compared to 34% in the methanolic extract (GM). The enhanced Allicin yield in the GI extract can be attributed to the unique physicochemical properties of ILs, including their ability to form hydrogen bonding, electrostatic interactions, π–π stacking, as well as their high polarity. These characteristics helps to improve solubilisation and extraction efficiency of bioactive compound compared to conventional organic solvents.

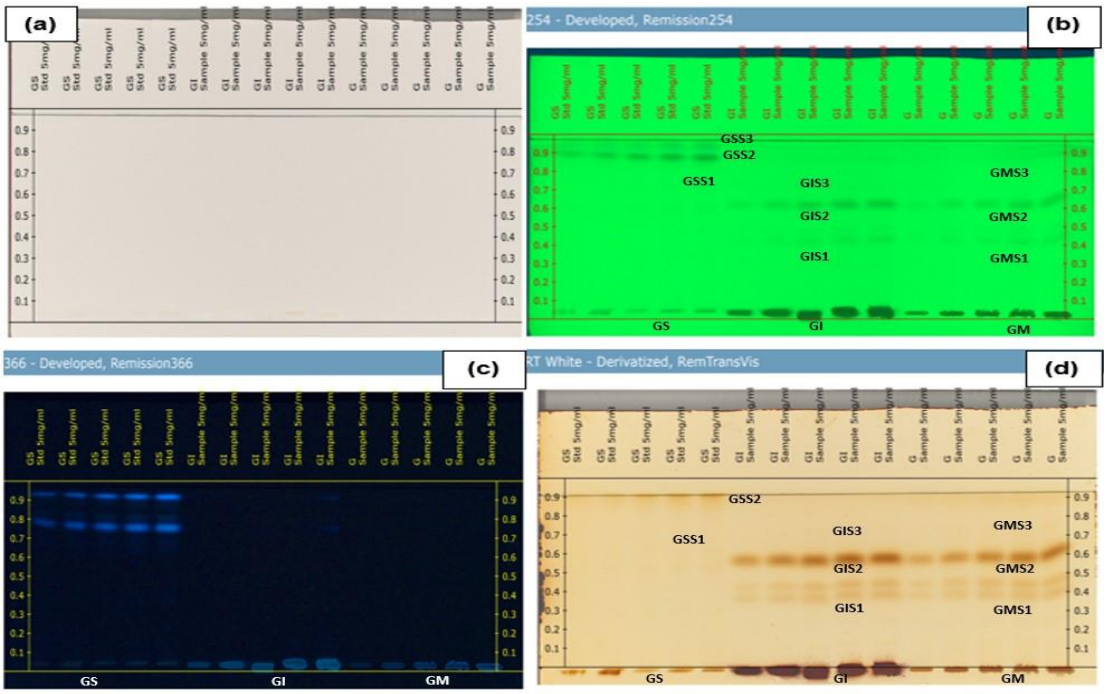

Figure 10. HPTLC chromatographs of GS, GI and GM were visualised under white light (a); UV 254 (b); UV 366 nm (c); and Iodine vapour (d).

Similar reports on the extraction of Rutin from *Asparagus officinalis* using 1-ethyl-3-methyl imidazolium bromide yielded 25.7 mg/g with a purity of 70.9%, compared to methanolic extract yielding 67.7% **(Chitrakar *et al.*, 2022)**. Similarly, the use of ILs such as [BMIM]Br and [BMIM]Cl in the extraction of polyphenolics from *Peperomia pellucida* exhibited maximum yield of Gallic acid (18.28 µg/g) under optimised conditions **(Ahmad *et al.*, 2017)**. A

comprehensive review on ionic liquid-based extraction techniques, highlighting their application in isolating plant-derived bioactive compounds, sustainability, toxicity, recovery, and computational optimisation is published **(Rajalakshmi *et al.*, 2025)**.

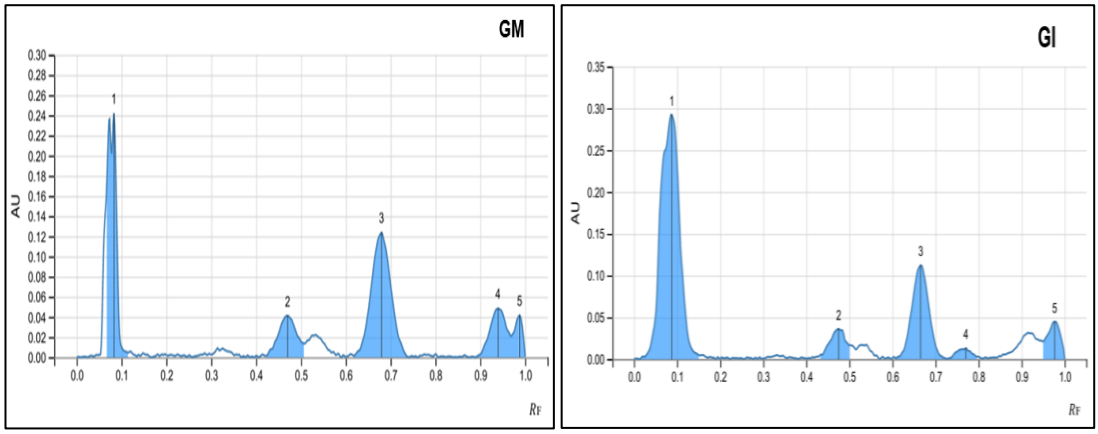

Figure 11. Densitograms of GM and GI

This study is the first to report the use of [BMIM]Cl based IL-based extraction for isolating bioactive compounds from garlic, specifically focusing on Allicin. *Based on our experimental findings, the fractionated compound obtained from column chromatography was used as a reference standard for evaluating the presence of Allicin in both methanolic (GM) and IL-based (GI) garlic extracts. The combined results from Thin layer chromatography (TLC), HPTLC and FTIR spectroscopy confirmed the presence of Allicin in both GI and GM extracts. These results suggesting that the IL-based extraction of garlic, enhanced the extraction efficiency of particular compound compared to conventional organic solvent. However, the study has certain limitations includes the recovery of ILs from garlic extract, stability and toxicity of Allicin were to be evaluated, as we focused solely on yield.*

Phase-II Sustained Release Floating Tablets and Microspheres for Drug Release Applications

Based on the instability and poor bioavailability of Allicin, we have attempted to develop garlic extract-based formulations for sustained release DDS, owing to their enhanced potential pharmacological activity. Sustained release floating tablets were formulated by varying their compositions and standardised using over the counter medication, ciprofloxacin hydrochloride. Similarly, microspheres containing bioactive Allicin-rich garlic extracts were prepared to facilitate prolonged drug release profiles.

4.2 Floating Tablet

Floating tablets are type of gastroretentive DDS, designed to prolong the gastric resistance time of drugs. These tablets remain buoyant in gastric fluids without affecting the natural gastric emptying rate. Once the tablet is ingested, the low-density tablet floats on the gastric fluid and gradually releases the drug at a controlled rate. The controlled or sustained drug release can be achieved through the use of polymer excipients and gas-generating agents incorporated into the formulations **(Mathur *et al.*, 2010)**.

4.2.1 Preparation and Standardisation of Floating Tablet

Preliminary trials were conducted to evaluate the floating ability of the formulated tablets as mentioned in **Table 8**. The compositions of the excipients were varied to study the impact on the tablet buoyancy. It was observed that increasing the quantity of binder-PVP, while keeping the other excipients constant, resulted in an increased total floating time (TFT) of 7 h (as seen in formulation F8C5c). The other formulations produced sink conditions and were therefore excluded from the study. Due to the increased floating time observed in the F8C5c formulation, the varying quantities of active hydrophobic polymers such as beeswax, filler agent as lactose, and the binder polymer PVP, significantly enhanced the floating performance. All other excipients such as cellulose acetate (coating agent), sodium bicarbonate (effervescent gas generating agent), stearic acid (binder and hydrophobic polymer), lubricant, and the active drug ciprofloxacin hydrochloride (CIP HCl) were kept as constant throughout the trials, as shown in **Table 9.** The optimised formulation, 18RF exhibited the highest TFT of 120 h.

In addition, fresh garlic juice (85 mg to 120 mg) were incorporated into the optimised formulation to evaluate its influence on the performance of the dosage form **(Table 10)**. Variations in the quantity of garlic juice produced noticeable impact on the matrix properties, particularly the floating behaviour. Increasing the concentration of fresh garlic juice up to 120 mg resulted in a longer total floating time (TFT). In trial 1 (18RFG), the formulation containing beeswax (35 mg), lactose (50 mg), PVP (35 mg), sodium bicarbonate (50 mg) and cellulose acetate (52 mg) exhibited a TFT of 30 min. Although sodium bicarbonate provided sufficient gas for floatation, the lower content of hydrophobic matrix such as beeswax and CA limited prolonged buoyancy. In trial 2 (18RFG2), the concentration of beeswax, PVP, CA, and sodium bicarbonate were doubled. However, the tablet was dispersed within 5 min, likely due to imbalance in the matrix caused by the high soluble components such as PVP and lactose.

In trail 3 (18RFG3), the increasing the amount of CA (104 mg) and PVP (70 mg), while reducing sodium bicarbonate to 20 mg allowed garlic juice loaded tablet to remain float for 2 h.

The CA and PVP polymer matrix effectively controlling the buoyancy. Trial 4 (18RFG4) was further optimised using CA (150 mg) and stearic acid (50 mg), while sodium bicarbonate was reduced to 5 mg. This formulation achieved an increased TFT of 3 h. These findings suggested that increasing hydrophobic polymers such as CA and stearic acid, combined with moderate effervescence, results in improved gastroretentive performance of the FTs.

Table 8. Results of Preliminary Formulations Trials for Ciprofloxacin Floating Tablets

Ciprofloxacin (CIP) at 70 mg, BW – 3 mg, and SA-5 mg were kept constant in all formulations. Additional excipients-lactose, PVP, sodium bicarbonate, CA and gelatin -were varied as mentioned in Table 1.

Sample code	Sink/ Float	TFT	Sample code	Sink/ Float	TFT
F1C	Sink	0	F8C2	Sink	0
F2C	Sink	0	F8C3	Sink	0
F3C	Sink	0	F8C4	Sink	0
F4C	Sink	0	F8C5	Float	10 s
F5C	Sink	0	F8C6	Sink	0
F6C	Sink	0	F8C7	Sink	0
F7C	Sink	0	F8C8	Sink	0
F8C	Float	15 s	F8C5a	Float	14 min
F9C	Sink	0	F8C5b	Float	14 min
F8C1	Sink	0	**F8C5c**	**Float**	**7h**

Table 9. Results of Formulated Composition of Ciprofloxacin hydrochloride Floating Tablet

Drug ciprofloxacin (Drug CIP) - 70 mg, Stearic acid (SA) – 5 mg, $NaHCO_3$ – 60 mg, and Cellulose acetate (CA) -52 mg were kept constant in all formulations. Additional excipients-BW, lactose, and PVP were varied as mentioned in Table 2. All the formulations (F8C5c to 19RF) were stayed floated in 0.1 N HCl

Sample code	FLT (s)	TFT (h)	Sample code	FLT (s)	TFT (h)
F8C5c	0	7	11RF	10	7
1RF	0	9	12RF	0	9
3RF	2	9	13RF	8	24
5RF	4	9	14RF	3	9
6RF	2	7	15RF	300	9
7RF	0	7	16RF	12	24
8RF	0	9	17RF	5	5
9RF	8	9	**18RF**	**6**	**120**
10RF	0	7	19RF	10	24

Table 10. Results of Formulated Composition of Fresh Garlic Juice Incorporated Tablets and their Total Floating Time

Sample code	TFT outcome
18RFG1	30 min
18RFG2	Dispersed <5 min
18RFG3	2 h
18RFG4	3 h

4.2.3 Characterisation Properties of Floating Tablets

4.2.3.1 Flow Properties of Floating tablets

The characteristic flow properties of the pre-compressed formulated tablet powders indicated good flow properties. The bulk and tapped densities of the formulated samples showed Carr's compressibility index values ranging from 13 to 20%, confirming good compressibility and flow. The Hausner's ratio for the eighteen formulations was ≤ 1.25%, further supporting the good flow properties of the physical mixture. The pH of the tablet dispersions in aqueous solution was basic, ranging from 7.98 to 8.92. All eighteen formulations also exhibited excellent angle of repose, ranging between 26.5˚ to 29.5˚.

Table 11. Evaluation of Pre-compression Parameters of Ciprofloxacin Floating Tablet Powders

Sample Code	Bulk density (mg/mL)	Tapped density (mg/mL)	Hausner's ratio	Carr's index (%)	Angle of Repose (˚)	pH
F8C5c	260.0	325.0	1.25	20	27.47	8.28
1RF	192.3	227.3	1.18	15	29.68	8.50
3RF	222.5	267.0	1.20	17	27.47	8.55
5RF	206.4	252.2	1.22	18	28.36	8.53
6RF	200.0	244.4	1.22	18	27.47	8.42
7RF	197.5	237.0	1.20	17	27.90	8.23
8RF	182.3	210.4	1.15	13	27.90	8.39
9RF	209.1	255.6	1.22	18	27.47	8.29
10RF	195.0	230.5	1.18	15	27.90	8.38
11RF	233.5	291.9	1.25	20	27.90	8.53
12RF	221.4	270.6	1.22	18	26.50	7.98
13RF	233.6	285.6	1.22	18	27.47	8.58
14RF	213.5	266.9	1.25	20	28.36	8.63
15RF	216.7	260.0	1.20	17	27.92	8.63
16RF	214.7	247.7	1.15	13	26.50	8.61
17RF	260.9	318.9	1.22	18	27.47	8.92
18RF	204.7	236.2	1.15	13	26.50	8.33
19RF	230.0	268.3	1.17	14	26.56	8.46

The solubility testing revealed that formulations 14RF, 17RF, 18RF, and 19RF were sparingly soluble in aqueous alcohol, while remaining formulations were sparingly soluble in dil. HCl (0.1 N). Also, the pH of the FTs dispersed in dil. HCl remained basic. **Table 11** represents the evaluation of the pre-compression parameters of the tablet powders.

The post-compression evaluation of the eighteen formulated tablets showed that all tablets were white and spherical in shape. The thickness of the tablets ranged from 0.12 to 0.23 cm, and the hardness ranged from 80.7 to 466.42 N, indicating sufficient mechanical strength to withstand the compression forces. The percentage friability of all formulations was less than 1%, ensuring good mechanical stability. Also, the weight variation of the tablets remained within the acceptable limit of the average weight. **Table 12** represents the post-compression evaluation parameters of the formulated FTs.

Table 12. Evaluation of Post-Compressed Ciprofloxacin Floating Tablets

Sample Code	Diameter (cm)	Thickness (cm)	Hardness (N)	Friability (%)	Weight variation (mg)
F8C5c	1.2	0.18	92.28	0.49	260.0 ±0.01
1RF	1.2	0.18	107.96	0.34	250.0 ±0.12
3RF	1.2	0.17	86.85	0.36	267.0±0.03
5RF	1.2	0.15	80.77	0.51	227.0 ±0.03
6RF	1.2	0.14	234.31	0.15	220.0 ±0.05
7RF	1.2	0.15	203.55	0.81	237.0 ±0.10
8RF	1.2	0.18	210.28	0.30	273.5 ±0.06
9RF	1.2	0.12	150.62	1.26	230.0 ±0.09
10RF	1.2	0.14	97.30	1.21	253.5 ±0.09
11RF	1.2	0.14	149.16	0.23	233.5 ±0.15
12RF	1.2	0.13	133.48	0.97	243.5 ±0.07
13RF	1.2	0.16	113.27	1.04	257.0 ±0.11
14RF	1.2	0.14	84.30	1.27	213.5 ±0.03
15RF	1.2	0.18	96.45	0.46	260.0 ±0.09
16RF	1.2	0.19	104.29	0.56	322.0 ±0.03
17RF	1.2	0.18	204.13	1.05	287.0 ±0.07
18RF	1.2	0.21	100.92	0.69	307.0 ±0.02
19RF	1.2	0.23	466.42	0.41	322.0 ±0.02

4.2.3.2 Buoyancy Study

The observed floating lag time (FLT) ranged from 0 s to 5 min, and TFT ranged from 5 to 120 h. The maximum floating time of 120 h was achieved with the 18RF formulation. This formulation, containing drug (70 mg), beeswax (35 mg), lactose (50 mg), PVP (35 mg), sodium bicarbonate (60 mg), cellulose acetate (52 mg) and stearic acid (5 mg) was evaluated for drug-polymer interaction using spectral analysis, such as FTIR, XRD and DSC-TGA.

4.2.4 Characterisation of Floating tablet

The FTIR spectra were recorded for both CIP HCl and the prepared 18RF floating tablet to assess potential interactions between the drug and excipients (**Figure 12 and 13)**. The characteristic peaks of CIP HCl were observed at 1265 and 1705 cm^{-1}, corresponding to C-F and C=O stretching within the COOH group. Similarly, these peaks were also present in the 18RF formulation, indicating no significant interactions between the drug and polymer excipients. The peaks at 2461 to 2684 cm^{-1} corresponds to NH_4^+ stretching vibrations and C=O stretching, while the peak at 1620 cm^{-1} confirmed the presence of a carbonyl group in the drug molecule. Overall, all characteristic absorption peaks of CIP HCl were retained in the 18RF formulation, confirming compatibility between the drug and excipients.

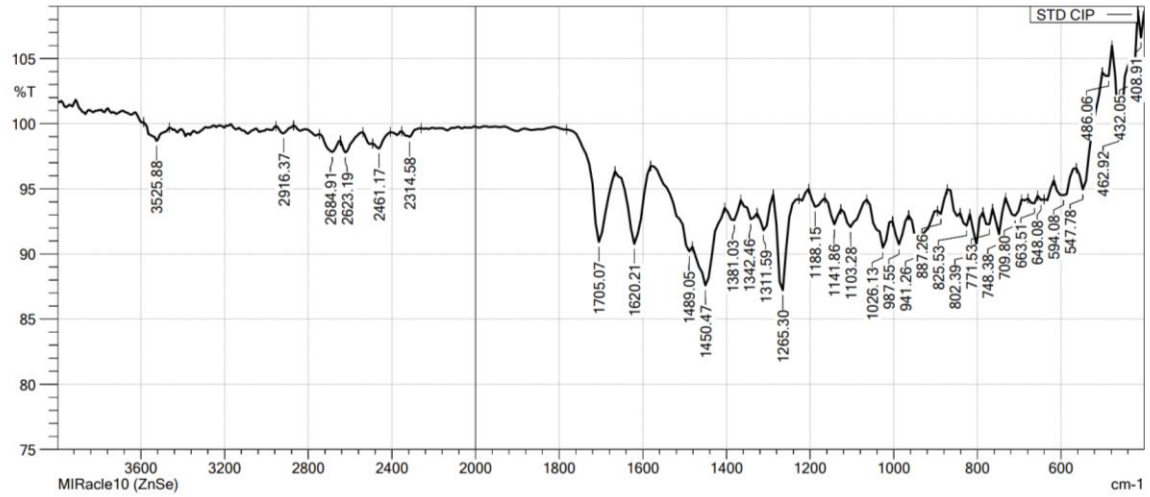

Figure 12. FTIR spectrum of CIP HCl

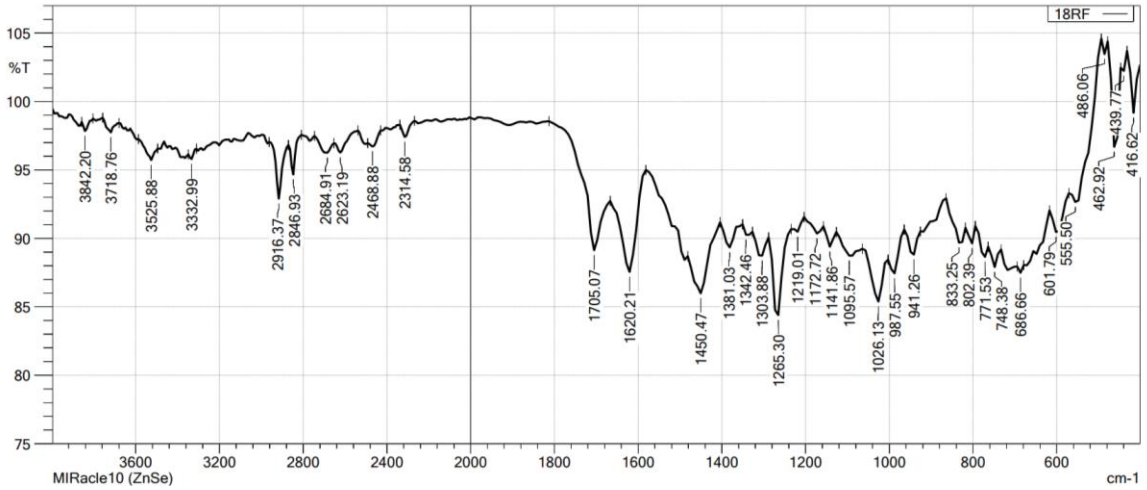

Figure 13. FTIR spectrum of 18RF containing drug + excipients

In addition, powder XRD analysis was recorded for both the pure drug and the physical mixture of the drug with polymer excipients in 18RF formulation (**Figure 14a** and **14b)**. The

XRD pattern of the CIP HCl and the 18RF sample confirmed their crystalline nature. TGA-DSC analysis was performed at a heating range of 30 - 900˚C with a scan rate of 10˚C/min under an inert (N_2) atmosphere. The TGA thermogram represents the percentage weight loss, while the DSC thermogram shows the heat flow (mW, endothermic) as a function of temperature (˚C). For CIP HCl, the TGA thermogram showed weight loss between 250 and 450˚C, which corresponds to the melting point observed in DSC thermogram at 280 to 290˚C **(Jacinto *et al.*, 2022)**. Previously reported DSC thermogram for CIP HCl showed endothermic peak at 158˚C and 335.8˚C **(Kulkarni *et al.*, 2008)**.

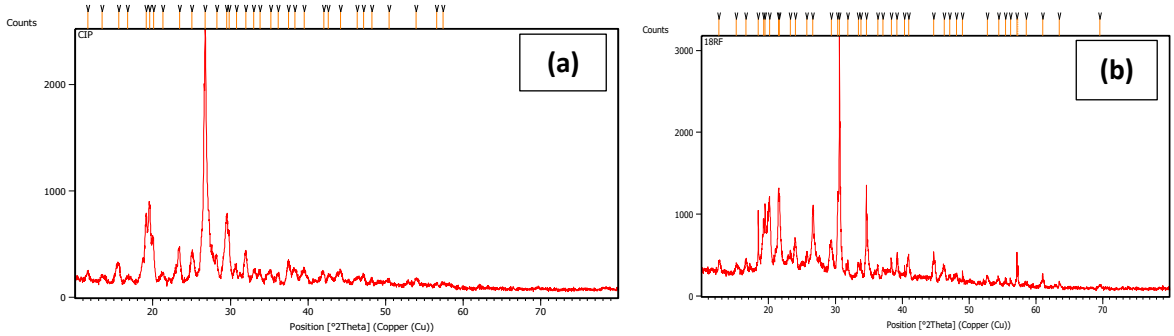

Figure 14. XRD pattern of (a) CIP HCl, (b) 18RF containing drug + excipients

Similarly, the TGA-DSC thermogram of the formulated 18RF tablet showed a percentage weight loss between 150 and 450˚C, with two distinct endothermic transitions. The first endothermic peak at 200˚C was due to the dehydration process, followed by a second endothermic peak at 410˚C. The presence of these endothermic peaks in the drug-excipient formulation indicates that there is no interaction between the polymer and the drug **(Figure 15).** Overall, the combined results from FTIR, XRD and TGA -DSC analysis confirming the absence of chemical interactions between CIP HCl and the polymer excipients.

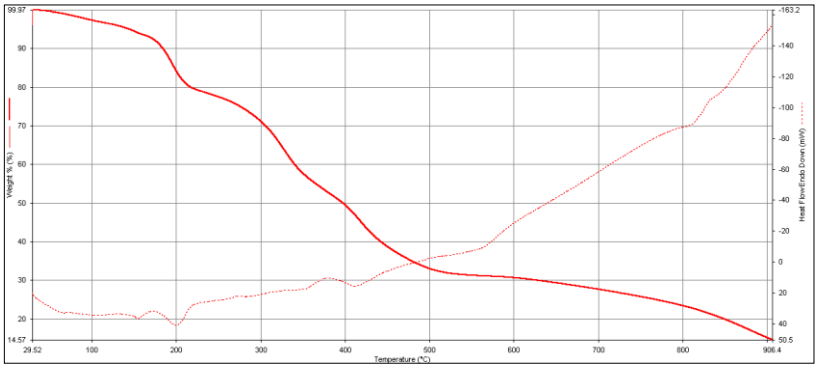

Figure 15. TGA-DSC of 18RF containing drug + excipients

4.2.5 *In vitro* Dissolution Study

The calibration curve for the standard CIP HCl (0.1 mg/mL) was prepared using concentration ranging from 10 µg/mL to 90 µg/mL and measured at λ_{max} 276 nm. The results indicated that the absorbance increased proportionally with the concentration of CIP HCl. The calibration curve, plotted with concentration (µg/mL) on the x-axis and absorbance on the y-axis showed a strong linear relationship with a regression (r^2) coefficient of 0.9983 (**Figure 16)**.

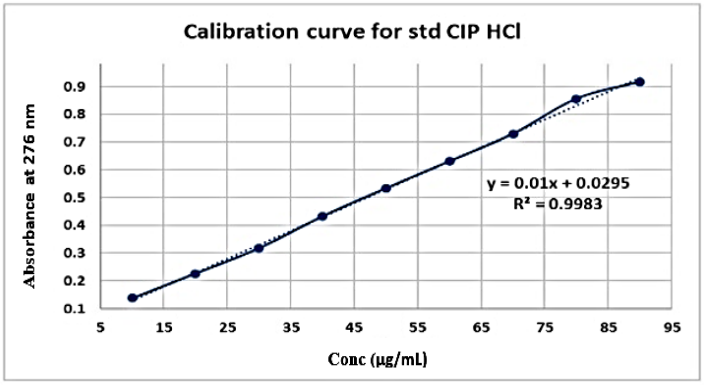

Figure 16. Calibration curve of CIP HCl

The formulations of the floating tablets (FTs) containing CIP HCl as the model drug were prepared in various compositions. The drug release study was performed in a simulated gastric medium (0.1 N dil.HCl). At predetermined time intervals, the required volume of dissolution medium was withdrawn, diluted, and analysed for absorbance using UV BioSpec at 276 nm. Based on the *in vitro* dissolution profile, formulation 18RF provides a better option for improved sustained release and enhanced bioavailability, maintaining drug release for approximately 120 h **(Figure 17)**.

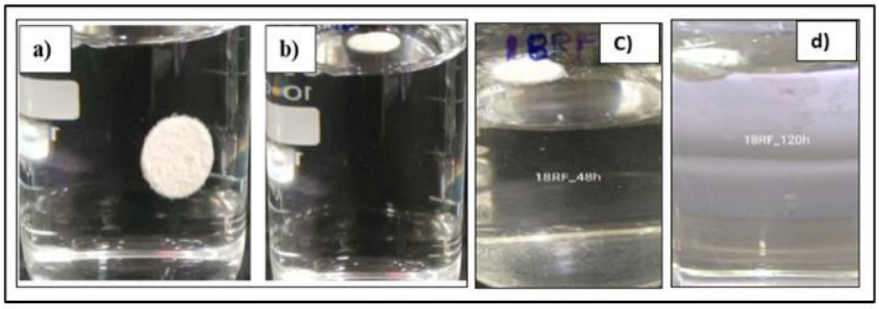

Figure 17. Photograph of floating tablet 18RF during *in vitro* floating study (a) Initial stage of tablet at 0 s; (b) Floating lag time of tablet at 6 s; (c) Tablet floating at 48h; (d) Tablet floating at 120h

In this study, all eighteen FTs formulations were prepared using fixed amount of drug CIP HCl, cellulose acetate, the gas-generating agent sodium bicarbonate, and stearic acid.

Among these, formulation 18RF containing the above-mentioned constant excipients with varying amounts of beeswax (35 mg), lactose (50 mg) and PVP (35 mg) exhibited the longest floating duration, remained buoyant for up to 120 h. The increased floating time can be attributed to the increased levels of the hydrophobic polymer (beeswax), the filler (lactose) and the binder (PVP). Other formulations showed comparatively shorter floating time: 17RF floated for 5h, whereas F8C5c, 6RF, 7RF, 10RF and 11RF remained afloat for 7 h. Formulations 1RF, 3RF, 5RF, 8RF, 9RF, 12RF, 14RF and 15RF floated for 9 h, while 13RF, 16RF and 19RF sustained buoyancy for about 24 h. Notably, formulation 17RF contained lactose (50 mg) and PVP (50 mg) but absence of beeswax, which contributes to its reduced floating performance in simulating gastric fluid. Therefore, the presence of hydrophobic retardant polymer beeswax, along with an optimal amount of PVP, plays a major role in enhancing buoyancy and improving the bioavailability of the developed CIP HCl floating tablets. The percentage drug release profiles for all formulations are represented in **Table 13a and 13b.**

Similar studies have reported the development of swellable and floating CIP formulations prepared using sangelose loaded HPMC, which exhibited biphasic drug release, a floating lag time of less than 4 s and a total floating duration of 24 h. In this formulation, 72.36% drug was released within 2 h, with sustained release extended up to 12 h **(Liang *et al.*, 2023)**. Floating ofloxacin tablets have also been formulated using HPMC K100M (release retardant), povidone (swelling agent), and a combination of citric acid and sodium bicarbonate *via*. the wet granulation method. The formulation exhibited a total floating time of around 16 h **(Shakya *et al.*, 2013)**.

More recently, prolonged release CIP FTs were prepared using HPMC (K15 and K4 grades), PVP-30, sodium bicarbonate, and citric acid. These tablets prolonged drug release for more than 12 h and followed first order kinetics model with a regression coefficient of 0.98 **(Rathore *et al.*, 2025)**. Similarly, 3D-printed PVA based FTs containing allopurinol exhibited extended release beyond 12 h and followed zero order kinetics, considered as potential for controlled delivery within the upper gastro intestinal tract **(Uboldi *et al.*, 2025)**.

In addition, bio adhesive metronidazole FTs formulated using guar gum, HPMC K4M, carbopol, microcrystalline cellulose, talc, magnesium stearate, and sodium bicarbonate *via* direct compression method exhibited a total floating time of more than 12 h and followed drug release fitting a zero order kinetic model **(Naseem *et al.*, 2022)**. These findings emphasise the need of innovation in FTs preparation and gastro retentive DDS to achieve improved therapeutic performance **(Mishra *et al.*, 2025; Bhuyar *et al.*,2024).**

Table 13a. Percentage Amount of Drug Released from Floating Tablet Formulations from F8C5c to 10RF

Time (h)	Drug release from floating tablets (%)								
	F8C5c	1RF	3RF	5RF	6RF	7RF	8RF	9RF	10RF
0	0	0	0	0	0	0	0	0	0
0.5	6.40	7.52	1.13	1.33	0.86	4.41	7.07	31.03	11.58
1	12.70	14.55	8.56	4.99	4.24	6.44	13.04	36.97	19.11
3	29.17	36.98	21.67	13.56	37.41	28.75	36.60	46.11	4.58
5	47.10	65.76	40.81	21.36	57.95	38.10	54.82	64.97	61.61
7	67.14	76.43	60.65	43.68	69.55	60.85	78.65	75.94	69.38
9	*	91.05	78.15	60.10	*	*	86.85	*	*

Note: * indicates floating tablet completely dispersed at particular time (h)

Table 13b. Percentage Amount of Drug Released from Floating Tablet Formulations from 11RF to 19RF

Time (h)	Drug release from floating tablets (%)								
	11RF	12RF	13RF	14RF	15RF	16RF	17RF	18RF	19RF
0	0	0	0	0	0	0	0	0	0
0.5	1.63	2.33	2.0	0.6	1.49	0.17	3.72	1.15	1.03
1	8.15	9.64	6.61	3.56	5.58	4.66	6.38	2.87	1.62
3	26.13	11.41	13.35	12.01	25.97	20.88	45.30	13.81	13.07
5	39.64	26.80	21.47	42.75	42.54	32.02	70.92	23.59	32.60
7	58.55	55.03	44.71	49.89	56.89	44.82	*	41.36	47.97
9	*	63.96	58.75	66.10	67.53	59.39	*	64.41	77.35
24	*	*	79.57	*	*	69.46	*	76.65	96.45
48	*	*	*	*	*	*	*	95.40	*
72	*	*	*	*	*	*	*	98.60	*
120	*	*	*	*	*	*	*	99.47	*

Note: * indicates floating tablet completely dispersed at particular time (h)

4.2.6 Stability of Floating Tablets

The stability study of the 18RF formulation was conducted by storing the tablets at temperature between 25˚C and 32˚C for period of 1, 3 and 6 months. At the end of each month, the tablets were assessed for visual colour change, pH, hardness, weight variation, floating lag time, total floating time and *in vitro* drug release. Throughout the study, no noticeable change in colour was observed, and the pH remained basic. A gradual decrease in tablet weight was recorded over 1, 3- and 6-month periods. The reduction in weight, along with decreased hardness values is likely due to moisture loss and subsequent physical and structural changes in the excipients under the storage conditions. The hardness values decreased from 76.34 N at 1 month, to 66.64 N at 3 months, and further to 55.04 N, at 6 months. Hydrophilic polymers such as PVP can absorb moisture, which weakens intermolecular binding forces and softens the matrix formulation, thereby reducing hardness and disrupts tablet compactness.

Similar findings have been reported, with tablet hardness decreasing from 7.2 -8.17 kg to 4 -8 kg after twelve months when stored in controlled conditions within high-density polyethylene bottles containing silica gel **(Rencber *et al.*, 2018)**. Despite these physical changes, the tablets buoyancy and drug release profile were not affected. The floating lag time remained between 6 and 8 s, and the total floating time was around 120 h. *In vitro* drug release at 120 h was recorded as 96.6% (1 month), 97.24% (3 months) and 97.8% (6 months) **(Figure 18)**. Overall, the stability studies indicated that minor physical changes occurred during storage, the FTs formulation suggests the acceptable performance. For enhanced long term stability, improvements in compression force and possible adjustments in packaging materials may be required.

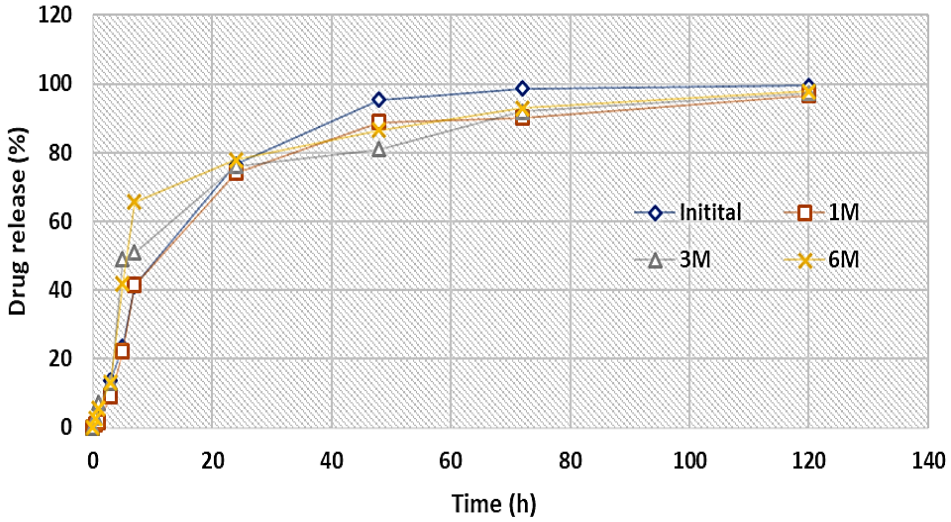

Figure 18. Drug release of 18RF floating tablet during initial, 1-month, 3-month and 6-month of stability studies.

4.2.7 Drug Release Kinetics

The *in vitro* drug release profiles of the eighteen formulated FTs were fitted to various kinetic mathematical models, and corresponding regression coefficient values (r^2) are presented in **Table 14**. The model exhibiting the highest r^2 value for each formulation considered the best fit, indicating the predominant drug release mechanisms. The zero order model represents a constant drug release rate within the therapeutic window and was plotted as time (h) versus cumulative percentage drug released **(Laracuente *et al.*, 2020)**. The first order model correlates drug release with the concentration remaining and is represented by a plot of log cumulative percentage drug release remaining versus time. The Higuchi model describes the drug release dissolution/ diffusion through a matrix, where the cumulative percentage drug release is plotted

against the square root of time. In order to understand diffusion mechanism, the release exponent "n value" from Korsmeyer-Peppas model was evaluated, which provides the type of release mechanisms within the polymer matrix **(Gouda and Baishya, 2017)**.

Based on curve fitting analysis, the formulations F8C5c, 1RF, 3RF, 7RF, 8RF, 11RF, 12RF, 14RF and 17RF showed the highest correlation with the zero order model. The other formulations, such as 5RF, 6RF, 9RF, 10RF, 13RF, 15RF, 18RF and 19RF best fitted the first order model, while 16RF followed the Higuchi model. Overall, the formulated FTs showed strong linearity across zero order, first order and Higuchi release kinetics. The evaluation of release exponent (n) using the Korsmeyer-Peppas model indicated that formulations F8C5c, 1RF, 8RF, 9RF and 10RF followed non-Fickian (anomalous) diffusion mechanism, suggesting combination of diffusion and polymer relaxation. The other formulations (3RF, 5RF, 6RF, 7RF, 11RF, 12RF, 13RF, 14RF, 15RF, 16RF, 17RF, 18RF and 19RF) exhibited super case II transport, indicating a release mechanism by polymer swelling and erosion.

Table 14. *In vitro* Drug Release Kinetics of Formulated Ciprofloxacin Floating Tablets

Sample code	MODEL NAME (r^2)					
	Zero order	First order	Higuchi	Korsmeyer-peppas		Hixson-Crowell
				r^2	n	
F8C5c	0.9979	0.9748	0.9377	0.6131	0.8526	0.9878
1RF	0.9797	0.9655	0.9623	0.6631	0.8673	0.9914
3RF	0.9965	0.9481	0.9082	0.8783	1.1670	0.9732
5RF	0.9037	0.9861	0.9810	0.9066	1.4788	0.9746
6RF	0.9731	0.9917	0.9140	0.9177	1.2081	0.9890
7RF	0.9875	0.9636	0.9120	0.7276	1.0212	0.9757
8RF	0.9869	0.9741	0.9572	0.6786	0.8697	0.9904
9RF	0.8742	0.9739	0.9738	0.3089	0.5711	0.9551
10RF	0.9560	0.9925	0.9835	0.4801	0.7448	0.9841
11RF	0.9964	0.9819	0.9204	0.8286	1.0307	0.9902
12RF	0.9526	0.9231	0.8384	0.7999	1.8067	0.9347
13RF	0.8598	0.9542	0.9204	0.8609	1.4070	0.9281
14RF	0.9711	0.9602	0.8754	0.9562	1.2995	0.9674
15RF	0.9912	0.9951	0.9406	0.8916	1.0350	0.9981
16RF	0.7672	0.8606	0.9190	0.8469	1.0512	0.8311
17RF	0.9866	0.9777	0.8738	0.7208	1.6809	0.9850
18RF	0.6538	0.9544	0.8573	0.8516	1.3960	0.8584
19RF	0.8376	0.9745	0.9036	0.9009	1.4309	0.9498

Similarly, earlier studies have reported the development of garlic-derived enteric coated sustained release tablets formulated using polymers such as HPMC, carbopol, ethyl cellulose, and xanthum gum through a non-aqueous wet granulation method. These tablets achieved 85.66% drug release over 12 h and followed diffusion controlled kinetic models **(Ojaswi and Ravindra, 2010)**. In another study, an oral controlled release matrix tablet of lamivudine was developed using varying concentration of guar-gum as the release retarding polymer. The formulated tablets were evaluated for physicochemical properties and *in vitro* dissolution, and the formulation containing 15% guar gum which sustained drug release for 12 h. The diffusion and erosion-controlled drug kinetics, improved the therapeutic efficacy over conventional formulations **(Jain *et al.*, 2011)**.

More recently, the herbal FTs have been formulated to remain buoyant in the stomach for an extended period of time, thereby improving bioavailability and achieving targeted drug delivery. One such formulation, composed of amla, ginger, fenugreek, isabgol husk, cellulose, calcium carbonate, talc and magnesium stearate, was successfully compressed into tablets. These herbal FTs exhibited a release profile ranging from 94.5% to 99% in 0.1 N HCl within 60 min **(Ramanamma *et al.*, 2025)**.

This novel ciprofloxacin floating tablet was developed using biocompatible excipients to achieve sustained drug release. The optimised formulation (18RF) exhibited a sustained release profile, delivering 99% of the drug over 120 h. ***To the best of our knowledge, this specific combination of excipients and its extended release behaviour has not been previously reported, and it has been published under an Indian patent***. In contrast, the FTs incorporating fresh garlic juice remained buoyant for only 3 h. This reduced floating duration may be attributed to increased porosity and the reactive nature of garlic constituents in the gastric fluid, resulting in early disintegration. Therefore, a well-designed wet granulated garlic-encapsulating formulation is required to achieve stable, and sustained release profile under simulated conditions.

4.3 Microspheres

Following the evaluation of floating tablets, the study extended to investigate the microsphere-based drug formulations for enhanced or sustained drug release. In this study, we utilised fresh garlic juice, for their enhanced and sustained pharmaceutical applications. The microsphere formulations were prepared using emulsion solvent evaporation method, which was characterised by evaluating the encapsulation efficiency, surface morphology and *in vitro* drug release study.

4.3.1 Microsphere Preparation and Encapsulation Efficiency

The standardisation of microspheres was performed by varying the presence of emulsifiers (PVP or PVA), and the presence or absence of PEG. The formulations were evaluated based on the shape, size and uniformity of microspheres using FESEM imaging **(Figure 19)**. The formulation MS1 were composed of PCL, HPMC, PEG and 1% PVP as emulsifier, resulted in microspheres with a spherical morphology and an average size of 2.2 µm. The presence of PEG act as stabilizer, enhancing improved emulsion formation and spherical particle size distribution. Furthermore, the polymers used- PCL, HPMC, PEG and PVP are biocompatible and applicable for encapsulating therapeutic drugs by acting as a drug carrier **(Dash *et al.*, 2012; Buske *et al.*, 2012; Filipović-Grčić *et al.*, 2003; Kemala *et al.*, 2012)**.

Similarly, the MS2 formulated without PEG, with 1% PVP as emulsifier, produced spherical microspheres with an average size of 2.1 µm. In addition, the formulations MS1a and MS2a, prepared with and without PEG, and 1% PVA as emulsifier, resulting in microspheres with spherical and irregular shapes with average size of 2.9 µm and 6.3 µm, respectively. The increased irregularity and large sized MS2a can be due to lack of PEG, which leads to less emulsification efficiency. Based on the shape, size and stable emulsion formation, the formulation MS1 was selected for nano-drug encapsulation and further sustained drug release studies. Therefore, from the blank microspheres, the presence of PEG helps in improving the formation of microspheres, while PVP effectively stabilised the emulsion and ensured uniform particle formation. **Table 15** represents the average size and morphology of blank microspheres (MS1, MS1a, MS2, MS2a).

Table 15. Average Size and Morphology of Blank Microspheres

Sample code	FESEM	
	Shape	Average size (µm)
MS1	Spherical	2.23
MS1a	Spherical with other shapes	2.90
MS2	Spherical	2.12
MS2a	Spherical with other shapes	6.31

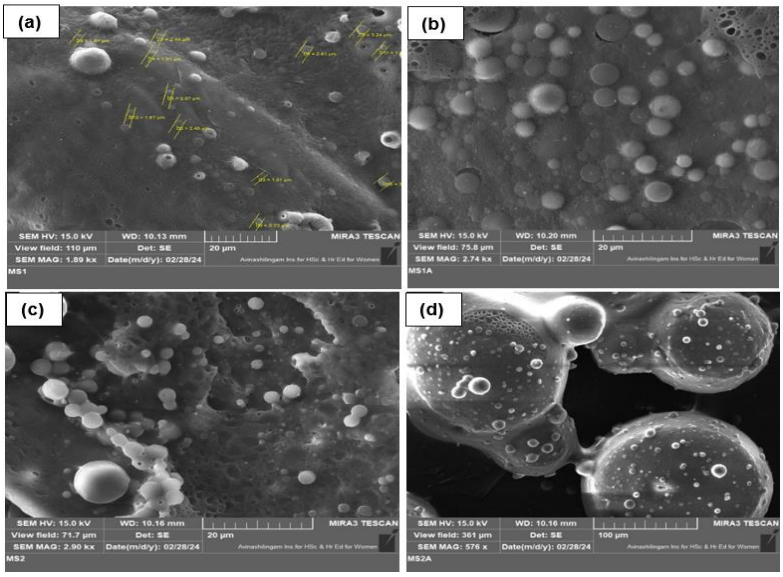

Figure 19. FESEM image of Blank microspheres (a) MS1; (b) MS1a; (c) MS2; (d) MS2a

The selected formulation was prepared using garlic juice loaded microspheres (MS1G) and metformin loaded microspheres as standard (MMS1), for evaluating the sustained drug release behaviour. The garlic juices were incorporated into polymeric microspheres using the optimised formulation (MS1) and standard metformin-based microspheres, to evaluate the potential in sustained DDS. The percentage encapsulation efficiency of the garlic metabolite loaded microspheres (MS1G) and the drug loaded microspheres (MMS1) was determined to quantify the amount of active ingredient entrapped within the microspheres relative to the initial amount used in the formulation. The encapsulation efficiency of metformin in the control formulation (MMS1) was found to be 90%, indicating effective drug entrapment within the polymer matrix. In contrast, the garlic juice loaded formulation (MS1G) exhibited a slightly lower encapsulation efficiency of 80.5%, which may be attributed to the presence of hydrophilic and reactive metabolites which interfere with the polymer-drug interactions during microsphere formation.

There are similar reports on polymer-based drug-controlled system prepared with encapsulation of lipophilic drugs (simvastatin and carvacrol) into the PEG-PLGA microspheres *via* emulsion solvent evaporation method. High encapsulation efficiency and reduced particle size of drug loaded polymeric microspheres was achieved **(Fu *et al.*, 2025)**. The chitosan loaded hydroxyapatite-based gelatin microspheres were formulated with improved entrapment efficiency of cisplatin from 58% to 99% **(Wu *et al.*, 2025)**.

4.3.2 Characterisation of Microspheres

4.3.2.1 FESEM and EDS of Microspheres

Figure 20 represents the FESEM image of drug loaded microspheres (MMS1) with a spherical morphology with rough and irregular surfaces, indicating the effective stabilisation and emulsification using PEG and PVP. FESEM monograph of MMS1 revealed an average diameter of 4.99 µm. Compared to the blank microsphere (MS1) formulation, the increase in the average particle size indicates the successful drug encapsulation along with slight swelling of polymer, which may be due to the hydrophilic drug entrapment, increased hydration of HPMC and PEG matrix results in larger microspheres than blank MS1. For the garlic loaded sample MS1G **(Figure 21a and 21b)**, showed a heterogenous distribution of spherical particles with an average size of 10.46 µm. At higher magnification, the particles were found to be smaller fine granules embedded within microsphere matrix, which are from the phytocomponents of fresh garlic juice incorporated during emulsion formation process. Thus, the FESEM analysis confirmed that the average size of the formulated microspheres was MMS1 (4.99 µm), and MS1G (10.46 µm), with distinct morphological variations depending on the encapsulated material.

Similar studies related to the morphology of polymeric metformin loaded microspheres were spherical with smooth and uneven surface was observed for the 75% drug loaded microspheres **(Kotha *et al.,* 2023)**. The surface of eudragit loaded microspheres were found to have excess particles on the surface possess faster drug release within few hours of complete dissolution. The eudragit NPs loaded spherical smooth particles contributes to the high release retarding capability of drug **(Hasan *et al.,* 2013)**.

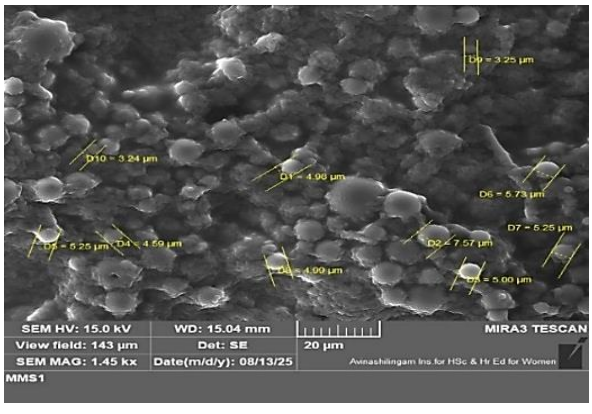

Figure 20. FESEM image of MMS1 microspheres

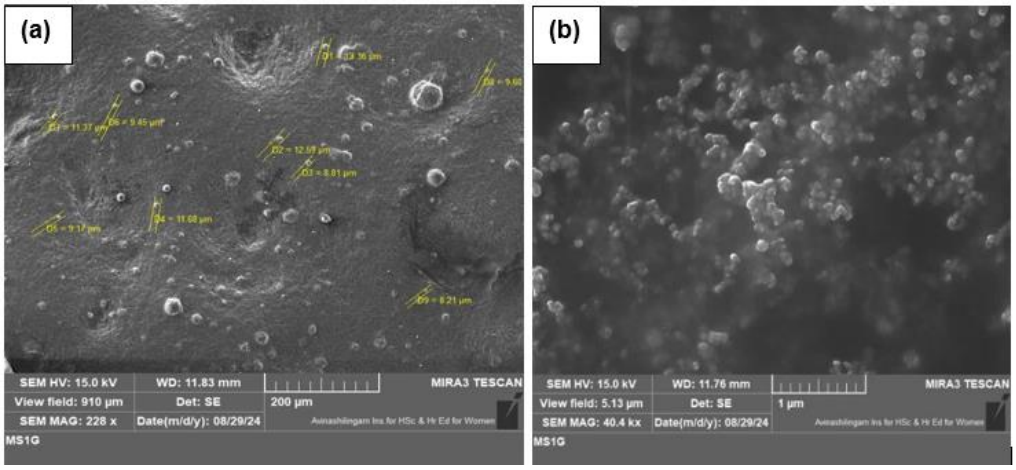

Figure 21. FESEM image of MS1G microspheres (a) MS1G at 200 µm; (b) MS1G at 1 µm

The elemental distribution of MMS1 microspheres confirms C, N, and O **(Figure 22a)**. Whereas for MS1G, the garlic loaded microspheres exhibits the presence of C, N, O, S and K as shown in **Figure 22b** Therefore, the presence of elements such as S and K, further confirmed the incorporation of garlic juice loaded in the microsphere formulation.

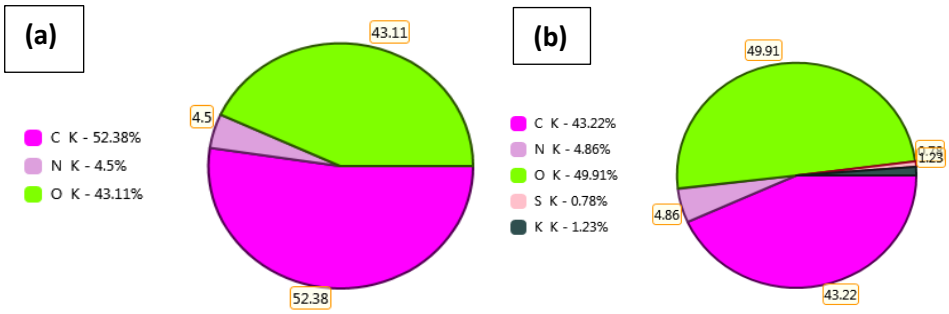

Figure 22. EDS pie-chart of MMS1 (a); and MS1G (b)

4.3.2.2 FTIR and XRD Analysis of Microspheres

FTIR spectra of standard metformin **(Figure 23)** showed the characteristic peak at 3363.86 cm^{-1}, which corresponds to N–H stretching of primary and secondary amines, 1627.92 cm^{-1} corresponds to C=N stretching, and 1550.77 cm^{-1} (N–H bending), represents the presence of biguanide functional group. The peaks at 1056.99 cm^{-1} and 933.55 cm^{-1} attributed to C–N stretching and N-H out of plane bending. The other peak at 655.80 cm^{-1}, 594.08 cm^{-1}, 540.07 cm^{-1}, 478.35 cm^{-1}, and 455.20 cm^{-1} corresponds to N-C-N skeletal bending vibrations, N-H wagging and other out of plane deformation within the biguanide ring. These spectral results confirm the structural formation of metformin as are in par with the data reported by **Sheela *et al.*,2010**.

The blank microspheres (MS1) prepared using biocompatible polymers like PCL, HPMC, PEG, and PVP showed the characteristic peak at 1728.22 cm^{-1} (C=O stretching of ester), 1651.07 cm^{-1} (C=O stretching of amide (PVP)), 1458.18 cm^{-1} and 1350.17 cm^{-1} (CH_2 bending and C-N stretching), 1288.45 cm^{-1}, and 1095.57 cm^{-1} represents C-N stretching and C-O-C asymmetric stretching from polymer excipients **(Figure 24)**.

Similar peaks were observed in MMS1 the peak at 1651.07 cm^{-1} corresponds to C=O stretching of pyrrolidone ring of PVP and 1288.45 cm^{-1} (C-N stretching of metformin), which confirmed the incorporation of metformin within the polymer matrix, without the appearance of crystalline drug peaks. The peak at 2977.79 cm^{-1} correspond to C-H asymmetric stretching, 2877.79 cm^{-1} correspond to symmetric stretching of aliphatic -CH_2 group, confirming the presence of PEG and PCL polymers. The peak at 1095.57 cm^{-1} (C-O-C vibrations) and other peaks at 948.98 cm^{-1}, 655.80 cm^{-1} and 462.92 cm^{-1} correspond to N-H out of plane bending, N-H wagging and skeletal deformations in the biguanide structure. Therefore, these results depict the metformin encapsulation without chemical alteration and polymer matrix retains its functional integrity **(Figure 25)**.

In the MS1G formulation loaded with fresh garlic juice, presented the FTIR spectrum exhibited the distinct peaks at 2978.09 cm^{-1}, and 2885.51 cm^{-1} which attributed to aliphatic C-H stretching vibrations, peak at 1643.35 cm^{-1} correspond to C=C stretching of unsaturated Allicin or C=O stretching from polymer matrix (PVP or PCL). The peaks at 1458.18 cm^{-1} (CH_2 bending) and 1381.03 cm^{-1} attributed to C-N stretching. Minor peaks at 1288.45 cm^{-1}, and 1249.87 cm^{-1} are assigned to C-N and C-O stretching vibrations. The broad peak at 1064.71 cm^{-1} corresponds to S=O; and peak at 941.26 cm^{-1}, 833.25 cm^{-1} and 671.23 cm^{-1} attributed to C-S and S-S vibrations, respectively confirming the presence of sulphur constituents in the microsphere formulation **(Figure 26).**

XRD pattern of pure metformin HCl, blank microspheres (MS1), metformin loaded microspheres (MMS1) and garlic loaded microspheres (MS1G) are presented in **Figure 27**. The diffraction pattern of metformin HCl (**Figure 27a)** exhibited sharp and intense peaks, confirming its highly crystalline nature, with an average crystallite size of 58.62 nm. The blank microspheres (MS1, **Figure 27b**) revealed a broad diffraction peak, with significantly reduced peak intensity, centred at 2θ values of 19.4˚, 21.50˚, and 24.05˚, which indicates the semi-crystalline or amorphous nature of polymer containing PCL, PEG, HPMC and PVP. The calculated average crystallite size of MS1 microspheres was 28.031 nm. The metformin

encapsulated microspheres (MMS1, **Figure 27c**) showed an average crystallite size of 17.52 nm. Similarly, the garlic fresh juice extract loaded microspheres (MS1G, **Figure 27d**) also showed semi-crystalline and amorphous pattern, with the average crystallite size of 12.98 nm, indicating the polymer-bioactive compound interaction.

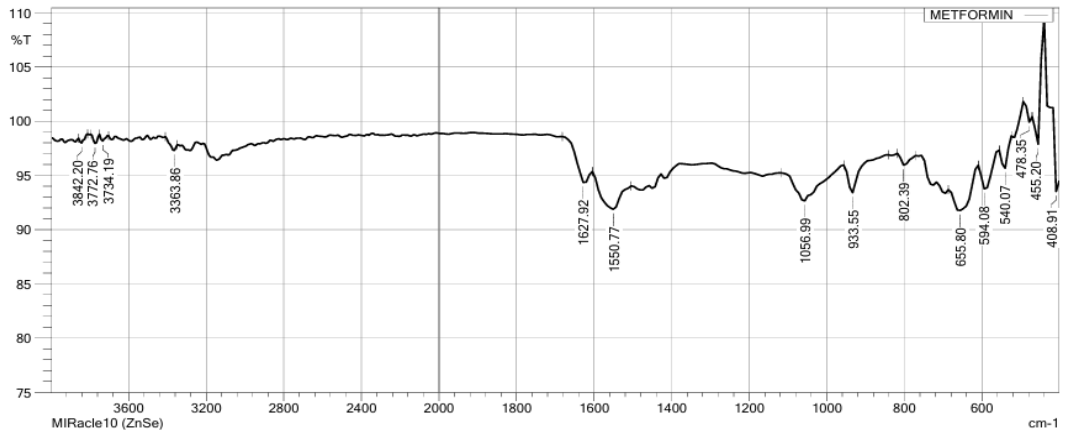

Figure 23. FTIR spectrum of pure drug metformin HCl

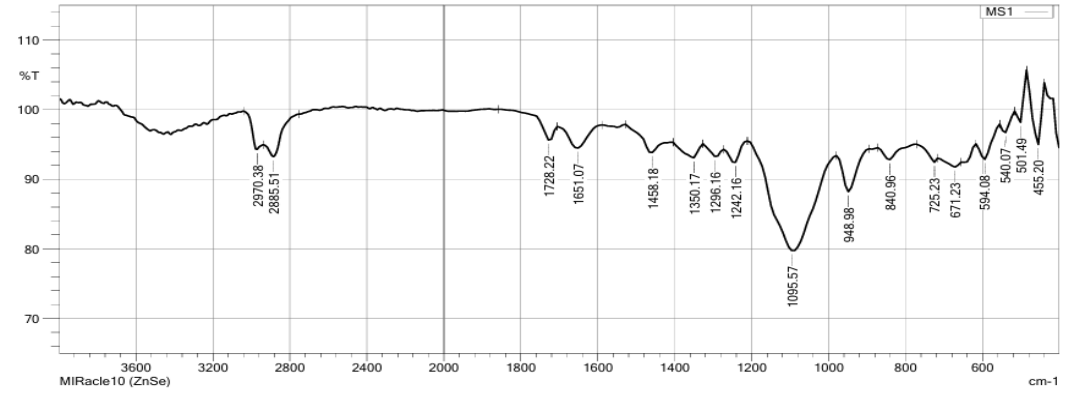

Figure 24. FTIR spectrum of bank microsphere (MS1)

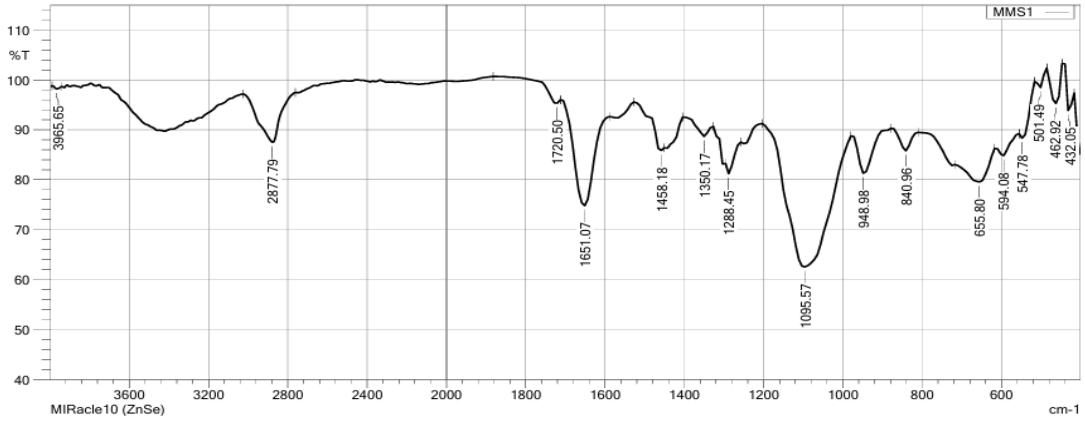

Figure 25. FTIR spectrum of drug loaded microsphere (MMS1)

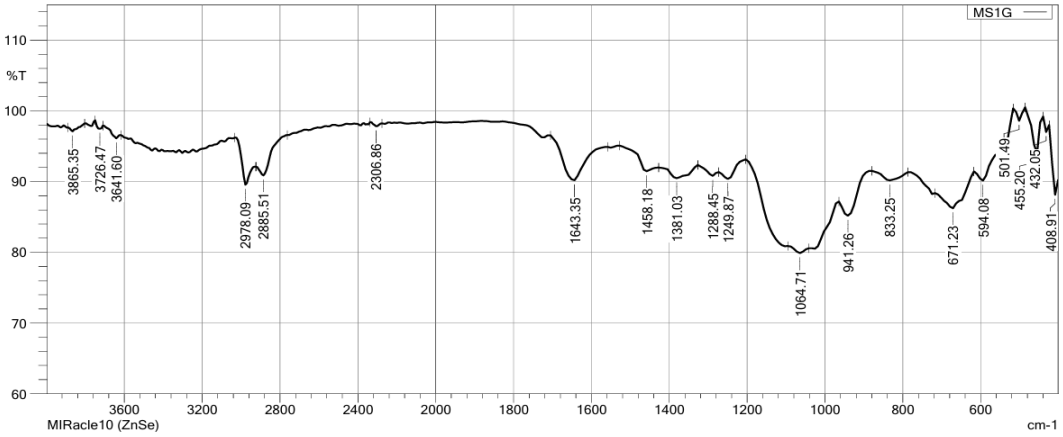

Figure 26. FTIR spectrum of garlic fresh juice loaded microsphere (MS1G)

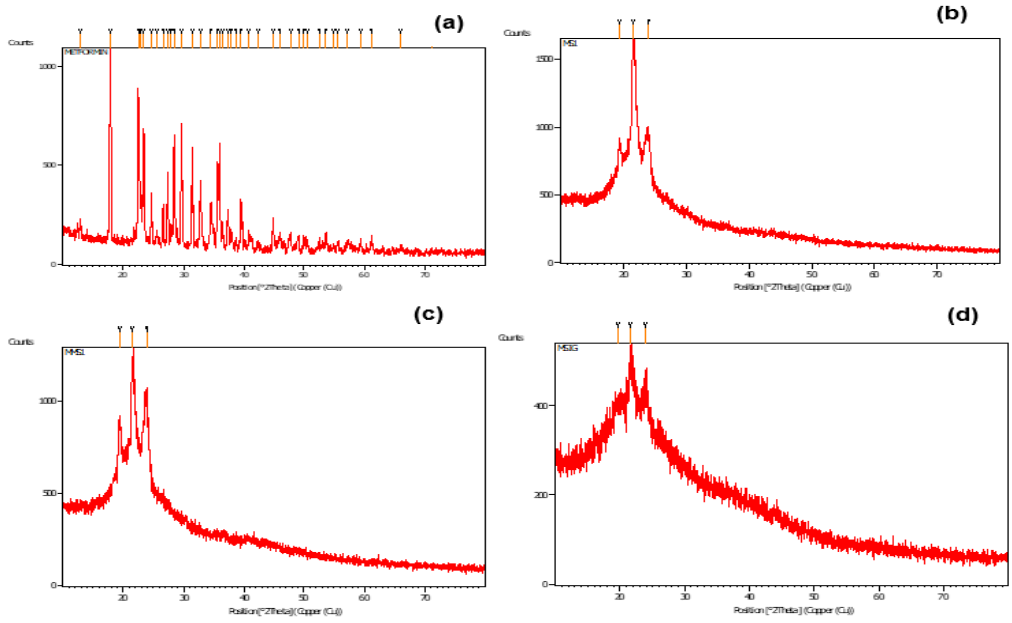

Figure 27. XRD patterns of (a) pure metformin HCl; (b) blank microspheres (MS1); (c) Metformin encapsulated microspheres (MMS1); (d) Garlic encapsulated microspheres (MS1G)

From the characterisation results, it was observed that the FTIR pattern confirmed that there are no significant chemical alterations between the drug and the excipients. Further, FESEM image revealed the spherical morphology with the average size of formulated microspheres such as MMS1 (4.99 µm), and MS1G (10.46 µm), respectively. The XRD pattern revealed the highly crystalline nature of metformin to semi-crystalline or amorphous nature of other microsphere formulations, with notable decrease in crystallite size. The broad diffraction pattern and reduced peak intensity represents the improved molecular dispersion of drug with the polymer drug carrier matrix **(Sakkal *et al.*, 2024)**. From the overall characterisation of

formulated microspheres, which indicates the stable drug formation in DDS providing the sustained or enhanced drug release for pharmaceutical applications.

4.3.3 Antibacterial Activity of Garlic loaded Microspheres

The antibacterial activity of blank microspheres (MS1), garlic encapsulated microspheres (MS1G), and heated crushed garlic (GH) was evaluated against *S. aureus*, *B. subtilis*, *K. pneumoniae*, and *E. coli* **(Figure 28)**. The ZOI values of each sample are presented in **Table 16**. Blank microspheres and heated crushed garlic (GH) showed no inhibitory activity against any of the tested strains, confirming the absence of antibacterial properties in the polymer matrix as well in heated crushed garlic. The loss of antibacterial property upon heat treatment, which are consistent with the thermal instability and rapid degradation of Allicin. The sample MS1G exhibited notable antibacterial activity, with the inhibition zone of 11 mm to 16 mm on bacterial strain. The maximum inhibition was observed against *K. pneumoniae* (16 mm), followed by S. *aureus*, *B. subtilis* and *E. coli*. From the results, the garlic encapsulated microspheres results in preventing the instability of Allicin and exhibiting highest inhibition against bacterial strains. The standard ciprofloxacin exhibits the highest ZOI across all strains, with the values ranging from 12 mm to 15 mm.

From the results, the garlic loaded nanoencapsulated microspheres significantly enhanced the physicochemical stability and bioavailability of Allicin, resulting in improved antibacterial efficacy and therapeutic performance.

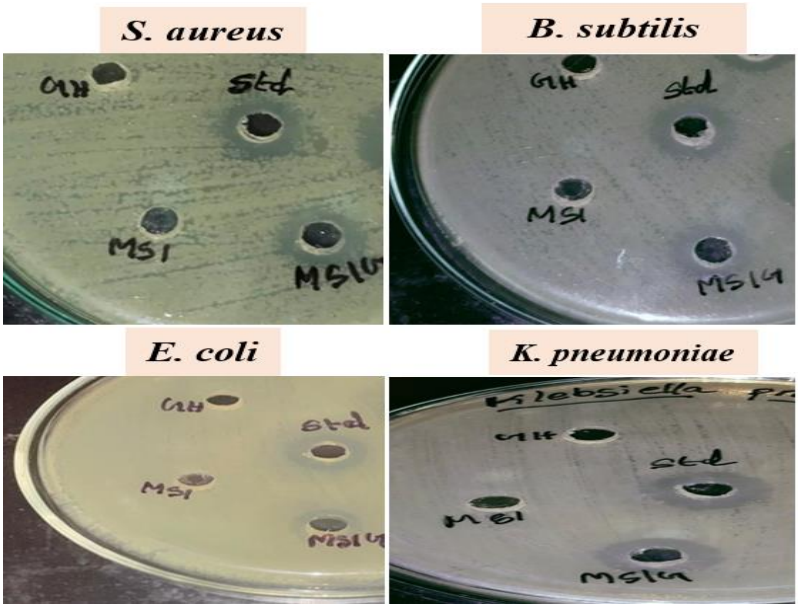

Figure 28. Antibacterial activity of blank, GH and MS1G against *S. aureus*, *B. subtilis*, *K. pneumoniae*, and *E. coli*

Table 16. ZOI of blank, GH and MS1G against *S. aureus*, *B. subtilis*, *K. pneumoniae*, and *E. coli*

Sample code	Zone of inhibition (mm)			
	S. aureus	***B. subtilis***	***K. pneumoniae***	***E. coli***
Std	12	14	15	12
GH	-	-	-	-
MS1	-	-	-	-
MS1G	**11**	**12**	**16**	**13**

(-) indicates no zone of inhibition

4.3.4 *In vitro* Dissolution and Drug Release Kinetics of Microspheres

The calibration curve for standard metformin HCl (0.1 mg/mL) in 0.05 M PBS at pH 6.8 was prepared with different concentrations (1-15 µg/mL), and were measured at λ_{max} 231 nm. The results showed an increase in absorbance with increasing concentration, exhibited good linear regression coefficient (R^2) of 0.990 (**Figure 29a)**. Similarly, calibration curve for fresh garlic juice (0.25 mg/mL) was prepared at different concentration between 3 to 20 µg/mL, measured at λ_{max} 251 nm. The absorbance increased as with concentration, exhibiting R^2 of 0.995 **(Figure 29b)**. The standard curves were used to analyse the drug content and entrapment efficiency of metformin and garlic loaded microsphere formulations.

In vitro release of the microsphere formulations MMS1 (metformin loaded) and MS1G (garlic-loaded) were studied in 0.05 M PBS for 120 h. The cumulative percentage of drug released at pre-determined intervals are shown in **Figure 30**. Both formulations exhibited a biphasic release pattern, which was exhibited by initial lag phase followed by a sustained release phase.

The drug release rate from PCL-HPMC-PEG based matrix microspheres for metformin and garlic were found to have initial lag phase followed by sustained release pattern. This effect may be due to an increase in the hydration and swelling of polymer blend forming diffusion barrier and restricts the immediate release rate. The release rate between 1 to 9 h, increased gradually reaching 51.31% (MMS1) and 62.7% (MS1G), representing the diffusion-controlled phase to polymer-erosion mediated release. At 9 to 120 h, the sustained drug release rate of 96.45% (MMS1) and 96.44% (MS1G) at 120 h, was observed. The drug release mechanism was evaluated and their corresponding values are given in **Table 17**. The kinetic model revealed that both formulations exhibited first-order release mechanism, which indicates that highest R^2 values (0.9717 for MMS1 and 0.9469 for MS1G), confirming the rate of drug release was concentration

dependent. The Higuchi model exhibited the R^2 value of 0.86-0.93, represents diffusion mechanism. The Korsmeyer -Peppas model indicates non-Fickian (anomalous) diffusion behaviour (R^2= 0.64-0.71), indicating polymer relaxation and diffusion in release kinetics. Therefore, the release of metformin and garlic bioactive from the microspheres could be described as diffusion controlled and concentration dependent process. Thus, controlled release model ensures the prolonged therapeutic availability and reducing frequent dosing and enhancing patient compliance.

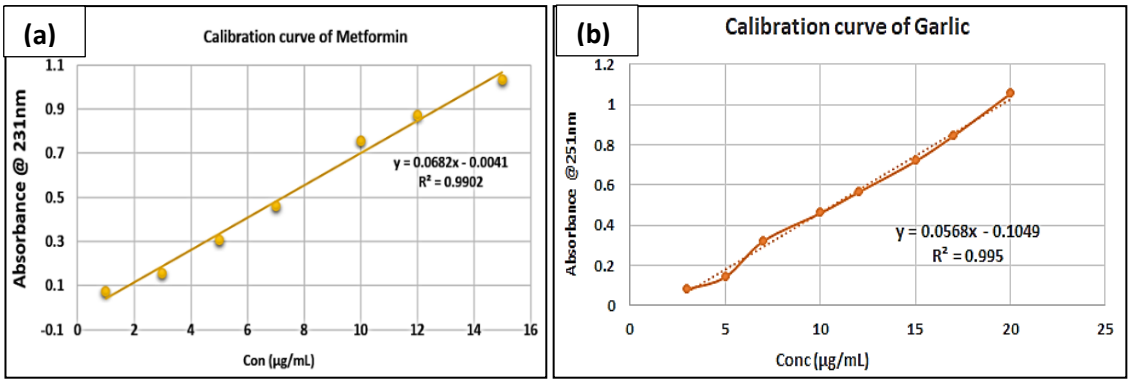

Figure 29. Calibration cure of standard metformin HCl (a); and garlic (b)

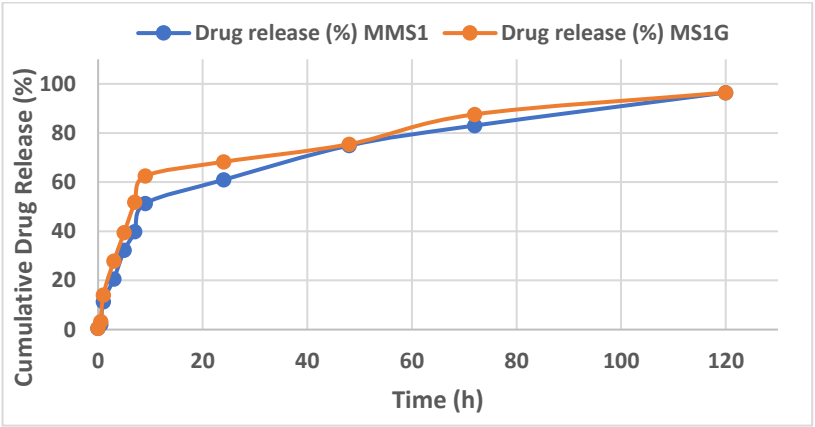

Figure 30. Graph Represents the Drug Release (%) of MMS1 and MS1G by varying time (h)

Table 17. Drug Release Kinetics Model Fitting of the Formulated Microspheres

Sample code	MODEL NAME (R^2)			
	Zero order	First order	Higuchi	Koresmeyer-Peppas
MMS1	0.7521	0.9717	0.9273	0.7128
MS1G	0.6546	0.9469	0.8568	0.6458

The results are consistent with those reported by Earle *et al*. 2018, the sustained release of metformin (97.02%) over 12 h, which was best fit with zero order model, indicating a concentration independent release, while Higuchi model suggested diffusion-controlled mechanism **(Earle *et al.*, 2018)**. Another study on the metformin loaded microspheres

formulated with sodium alginate and khaya gum using the ionic gelation method showed 62% - 80% drug release, following Koresmeyer-Peppas model **(Ozoude *et al.*, 2020)**. Metformin microspheres prepared using ethyl cellulose exhibited a controlled release pattern which followed both first order and Higuchi model kinetics **(Choudhury and Kar, 2009)**. Similarly, metformin microspheres prepared by spray drying with HPMC polymers possesses sustained drug release for up to 6 h, following the Korsmeyer-Peppas model with non-Fickian diffusion **(Moorthy *et al.*, 2024)**.

From the results, it can be generalised that prepared microsphere formulations are suitable for sustained drug release applications. Both formulations (MMS1 and MS1G) showed the highest cumulative drug release over 120 h, reaching 96%. This indicates that nano encapsulated bioactive/metformin microspheres are effective in achieving extended release over time. Therefore, Allicin based formulations could also be developed using the nano encapsulated microspheres to achieve a stable and sustained release of bioactive compounds.

Phase -III Sustainable Synthesis and Characterisation of Metallic Nanoparticles

4.4 Extraction and Phytochemical Screening of Selected Plants

Phytomedicines derived from plant extracts are easily available, effective, less expensive and safe, with rare side effects. About 80% of individuals in developed countries prefer using traditional medicines derived from plant sources **(WHO, 1993)**. However, proper investigation and scientific validation are required to better understand their properties, efficacy and safety. The extraction process for selected plants, including *Amphilophium paniculatum* (AP) [65 g leaves], *Tristellateia australasiae* (TA) [35 g leaves], *Haematocarpus validus* (BF) [20 g fruits] and *Phoenix dactylifera* (DS) [22 g seeds], was carried out using the reflux method for 6 h, with both nonpolar and polar solvents. The corresponding sample codes for the extracts, as outlined in section 3.8.1, along with the percentage extractive yields, are provided in **Table 18**.

Table 18. Extractive Yield Obtained from AP, TA, BF and DS by Reflux Method

Extracts	Yield (g)	Extractive yield (%)	Extracts	Yield (g)	Extractive yield (%)
APH	0.80	1.23	TAC	0.56	1.62
APC	1.20	1.84	TAEA	23.5	67.14
APEA	0.70	1.07	TAM	0.19	0.57
APM	2.30	3.53	TAE	0.31	0.90
APE	4.40	6.77	BFE	0.60	3.00
TAH	0.30	0.87	DSE	2.58	11.71

The results in **Table 18** clearly shows that the ethanolic extracts of AP yielded the maximum extraction compared to AP extracts with other solvents. Therefore, the yield obtained from the various extracts represents a large quantity of polar compounds present in the plant material, which are effectively extracted during the sequential extraction process. The polarity dependent extraction increases both the yield as well as the antioxidant properties **(Nawaz *et al.*, 2020)**.

Similarly, the TA extracts showed the highest yield from TAEA, followed by TAH, TAC, TAE, and TAM extracts. During the extraction of TAC residues with ethyl acetate under reflux conditions for 1.5 h, the solution formed large to medium-sized bubbles, resulting to foam formation. As a result, the reaction was stopped, and the mixture was cooled. The collected plant residue was then further extracted by adding ethyl acetate (1.5 L) and boiling in a water bath for 5 h. After the appearance of a yellow-coloured solution, the solvent was replaced at hourly intervals to minimise foaming. The collected TAEA filtrate (750 mL) was then distilled to obtain the extract.

Foaming during TAEA extraction may be due to the plant material containing natural products such as proteins, carbohydrates, polysaccharides, saponins, lipids, and volatile organic compounds, which are amphiphilic. These reduce the surface tension between the solvent and air, leads to foam formation **(Wu and Ju, 1998; Tiso *et al.*, 2024)**. The TA extracts clearly shows that the ethyl acetate extract possesses the highest yield, as the bioactive components in TA are more soluble in ethyl acetate, followed by chloroform and ethanol extract, indicating that bioactive metabolites namely alkaloids, terpenoids, flavonoids, tannins, quinones, and carbohydrates are more effectively extracted by these solvents. Since most of the bioactive compounds are eluted from the crude powder (AP and TA) during the sequential extraction process, aqueous extraction was not performed.

In addition, the ethanol extracts of BF and DS yielded 3% and 11.7%, respectively, indicating the maximum soluble portion of bioactive compounds such as flavonoids, alkaloids, anthocyanins, anthraquinones, and tannins are in polar solvent. Sequential extraction was not performed due to the limited availability of these samples. From the comparative extractive values of AP, TA, BF and DS, it is evident that more polar based bioactive compounds predominate in AP, BF, and DS, while TA contains both polar and non-polar compounds, as evidenced in **Table 18**.

Phytochemical screening of plant extracts is essential to identify the fundamental information about the nature of bioactive constituents such as primary and secondary metabolites

present in a particular plant extract. The phytochemical screening results for AP, TA, BF and DS extracts obtained from different solvent-based extractions are provided in **Table 19**.

The qualitative phytochemical analysis confirmed the presence of secondary metabolites such as alkaloids, flavonoids, terpenoids, anthraquinone, carbohydrates, tannin, coumarin, and volatile oils in the leaf, fruit, and seed extracts. These findings are supported with earlier reports by **Samy *et al.* (2015, 2021)** who identified lignans, triterpenoids, flavonoids, phenylethanoids, and glycosides in the 95% ethanolic extract of AP leaves. Similarly, Mo (1996) documented Hexitol, Dulcitol, Friedelin, Lupeol, Sitosterol, Beta amyrin, Beta sitosterol and Isorhamnetin in TA leaf and stem. **Momin *et al.*, 2018** identified alkaloids, reducing sugar, non-reducing sugar, polyphenol, tannin, flavonoid, and anthocyanins in methanolic extract of blood fruit**.** Furthermore, **Adeosun *et al.*, 2015** confirmed the presence of alkaloids, flavonoids, anthraquinones, saponins, tannins and terpenoids in ethanolic extracts of dates palm seeds. The phytochemical results indicated that the maximum secondary metabolites are present in the selected plants when extracted with increasing polarity (ethanol) of the solvent. These secondary metabolites in APE, TAE, BFE and DSE extracts may stabilise the formation of metallic NPs through the binding of carbonyl or amine groups to the surface of NPs, thus preventing the agglomeration.

Table 19. Phytochemical Screening of AP, TA, BF and DS Extracts

Secondary Metabolites	*Amphilophium paniculatum* (leaf)					*Tristellateia australasiae* (leaf)					BFE *(Fruit)*	DSE *(Seed)*
	APH	APC	APEA	APM	APE	TAH	TAC	TAEA	TAM	TAE		
Alkaloids	+	+	+	+	+	+	+	+	+	+	+	+
Flavonoids	+	+	+	+	+	-	-	-	-	+	+	+
Terpenoids	+	+	+	-	-	+	+	-	+	+	-	-
Anthraquinone	-	+	+	+	+	+	+	+	+	-	+	+
Anthocyanin	-	-	-	-	-	-	-	-	+	+	+	+
Quinones	+	+	+	+	+	+	+	-	+	+	-	-
Carbohydrates	+	+	+	+	+	+	+	+	+	+	+	-
Tannin	+	+	+	-	-	+	+	-	-	-	+	+
Saponin	-	-	-	+	+	-	-	-	-	-	+	+
Polyphenol	+	+	+	-	+	-	-	-	-	-	+	+
Glycosides	+	+	+	-	+	-	-	-	-	-	+	-
Lignin	+	+	+	-	-	-	-	-	-	-	-	-
Coumarin	+	+	+	-	-	+	+	-	+	+	-	-
Volatile oil	+	+	+	-	-	+	+	+	-	-	+	+

(+) detected and (-) not detected the secondary metabolites

There are no reports available with the specific solvent-based extracts for the synthesis of metallic NPs using APE, TAE, BFE and DSE extracts. Therefore, the active secondary

metabolites in these extracts are considered as bioreductants/capping agents/stabilising agents which is being utilised for the rapid formation of metallic NPs, such as GNPs and SNPs.

4.4.1 Sustainable Synthesis of Metallic Nanoparticles

In this research work, metallic NPs such as gold and silver nanoparticles were synthesised using

- ❖ AP leaves (APE) – ethanol extract in aqueous dispersion
- ❖ TA leaves (TAE) – ethanol extract in aqueous dispersion
- ❖ BF fruits (BFE) – ethanol extract in aqueous dispersion
- ❖ DS seeds (DSE)– 75% ethanol extract in aqueous dispersion

To optimise the study, the varying concentration of plant extracts and method adopted for synthesis of NPs were varied. Relevant results obtained from each synthesis process and conditions are detailed with supporting information.

4.4.1.1 Sustainable Synthesis of Gold Nanoparticles at Room Temperature

The sustainable synthesis of gold nanoparticles (GNPs) was carried out using all four selected plant extracts (APE, TAE, BFE and DSE) in aqueous medium, utilising two different synthesis methods: Room temperature (RT) and Solar light irradiation (SL). Both methods are considered to be more economical, energy efficient and time-saving. The GNPs were preliminarily screened using both methods, and based on the rapid formation time of GNPs, that particular method was selected for the synthesis of silver nanoparticles (SNPs). In the preliminary screening, the concentration of auric chloride in aqueous solution was kept constant due to cost concerns.

Room temperature (RT) is considered a simple, economic, convenient and accessible method for the synthesis of GNPs. The results of GNPs synthesised from four selected plant extracts using room temperature method are presented in **Table 20**. The sample code assigned for the synthesised GNPs by RT method were represented as APEGRT, TAEGRT, BFEGRT and DSEGRT.

The visible colour changes from pale green (leaf extracts) or pale orange (fruit and seed extracts) to purple was observed, as shown in **Figure 31.** The time required for APEGRT NPs formation decreases from 240 min to 30 min as the concentration of extract increased by maintaining a constant auric chloride ratio (1:1 to 5:1). Similarly, the time of formation of TAEGRT NPs decreased from 45 min to 7 min with an increase in extract concentration. A similar trend was observed for BFEGRT and DSEGRT, with the time of formation decreasing

from 120 min to 45 min, and from 5 min to 1 min, respectively, as the plant extract concentration increased. These reduced formation time may be due the presence of higher concentration of secondary metabolites (discussed in section 4.4) present in the selected plant extracts, which quickly undergoes rapid reduction of Au^{3+} ions to metallic gold (Au^0). These biomolecules not only reduce the metal ions, but also stabilise the NPs by preventing aggregation.

From the overall results of GNPs, synthesised using the RT method, shows the lesser time of formation at 5:1 extract to auric chloride ratio; APEGRT formed in 30 min, TAEGRT in 7 min, BFEGRT in 45 min, and DSEGRT in 1 min, with a distinct purple colour.

By comparing the four different plant extracts, APEGRT and BFEGRT NPs requires longer formation time (more than 45 min), whereas TAEGRT and DSEGRT NPs showed rapid formation time of 7 min and 1 min, respectively. These variations in formation time may be due to the nature of stabilising agents or extract concentrations, which impacts the rapid or longer time in NPs formation. Also, the external activation may be required to accelerate the reduction of Au^{3+} to Au^0 for shorter time of formation. Therefore, the specific chemical and biological characteristics of each plant material also contributes to variations in shape, size and colour of synthesised NPs.

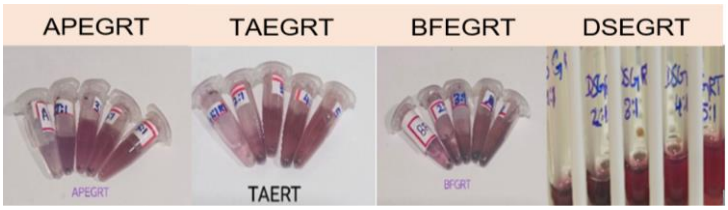

Figure 31. Synthesised GNPs using four plant extracts at room temperature

Table 20. Comparison of GNPs formation time using four different plant extracts at Room Temperature

Sample code	Varying plant extract: Constant Auric chloride	By room Temperature (RT)	
		Time of formation (min)	Colour of GNPs
APEGRT	1:1	240	**Purple**
	2:1	138	
	3:1	55	
	4:1	45	
	5:1	**30**	

Sample code	Varying plant extract: Constant Auric chloride	By room Temperature (RT)	
		Time of formation (min)	Colour of GNPs
TAEGRT	1:1	45	Purple
	2:1	20	
	3:1	20	
	4:1	10	
	5:1	**7**	
BFEGRT	1:1	120	Purple
	2:1	90	
	3:1	60	
	4:1	60	
	5:1	**45**	
DSEGRT	1:1	5	Purple
	2:1	4	
	3:1	3	
	4:1	3	
	5:1	**1**	

Samples which require less time for GNPs formation

The previous reports on the synthesis of GNPs at normal (RT) was found to be less than two minutes using the reducing agents such as ascorbic acid and sodium citrate, with polyvinyl pyrrolidone as a stabilising agent, which possess different size and shaped NPs **(Poklepovich-Caride *et al.*, 2022)**. Similarly, aqueous extracts from *Acorus calamus, Alternanthera sessilis, Portulaa oleracea and Sterculia foetida* were reacts with auric chloride at RT, forming ruby red, violet, purple, and pink coloured NPs with spherical and anisotropic shapes **(Peng *et al.*, 2024; Firdhouse and Lalitha, 2020)**. In addition, aqueous extracts of date palm leaves, seeds, and fruits were used to synthesise metallic NPs with various shapes, as reported by **Ghani and Hussain, 2021**.

4.4.1.2 Sustainable Synthesis of Gold Nanoparticles by Solar Light Irradiation

The solar or sunlight irradiation (SL) method is safe, eco-friendly, energy saving, cost effective, and sustainable approach for synthesising metallic NPs. SL irradiation helps in rapid formation of NPs, ensuring more stable particle generation **(Wei *et al.*, 2012)**. The results of the

synthesised GNPs from four selected plant extracts using SL irradiation method are presented in **Table 21**. The visual colour changes from pale green (leaf extract) or pale orange (fruits and seed extracts) to purple was observed, as shown in **Figure 32**. The sample code assigned for the synthesised GNPs by solar light irradiation was represented as APEG, TAEG, BFEG, and DSEG.

The time required for APEG NPs formation decreased from 3 min to 48 s as the concentration of extract increased while maintaining a constant auric chloride ratio (1:1 to 5:1). Similar trends were observed for other GNP formations: the formation time for TAEG NPs decreased from 10 min to 5 min, BFEG NPs from 10 min to 4 min, and DSEG NPs from 1 min to 30 s. The results indicate that increasing the concentration of plant extract, while keeping auric chloride constant, reduces the time of formation of NPs. This might be due to the synergistic action of secondary metabolites present in the selected plant extracts.

The optimisation studies reveal that higher concentrations of extract solutions decreases the time required for GNPs formation. Hence, solar light irradiation enhances the rapid formation of violet coloured GNPs due to the photoreduction of Au^{3+} to Au^{0} ions in the presence of bioactive molecules **(Zhao *et al.,* 2019)**.

The observed colour of NPs is due to the phenomena called localized surface plasmon resonance (LSPR). LSPR occurs when conduction electrons on the surface of NPs resonate with specific wavelengths of light, ensured by the size and shape of nanomaterials. The purple or violet appearance of NPs is typically due to SPR absorption, which shifts to longer wavelength, red shift. When red light is absorbed and blue light is reflected, the colour of solution turns purple or blue **(Hung *et al.,* 2010)**.

Similar studies have reported solar light assisted green synthesis of GNPs with cubic shaped purple NPs using *Equisetum diffusum* leaf extract **(Khan *et al.,* 2024)**; while reddish brown GNPs were formed using hydrogel from *Cydonia oblonga* seeds **(Batool *et al.,* 2022)**. Thus, natural sunlight acting as a driving force for NPs formation, making the process eco-friendly and economical.

The results indicated that the time required for the formation of GNPs significantly reduced with solar light irradiation compared to the room temperature method.

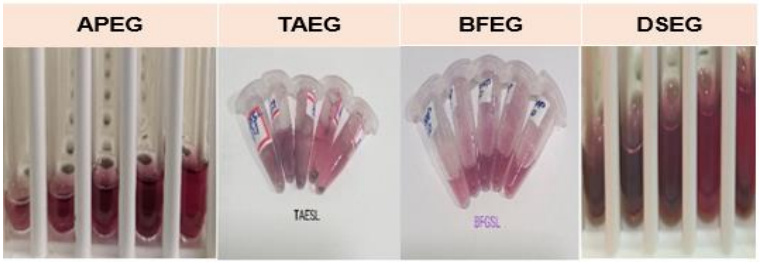

Figure 32. Synthesised GNPs using four plant extracts by solar light irradiation

Table 21. Comparison of GNPs formation time using four plant extracts by Solar light irradiation

Sample code	Varying plant extract: Constant Auric chloride	by Solar light irradiation (SL)	
		Time of formation (min)	Colour of GNPs
APEG	1:1	3	Purple
	2:1	2	
	3:1	1	
	4:1	1	
	5:1	0.8	
TAEG	1:1	10	Purple
	2:1	10	
	3:1	7	
	4:1	7	
	5:1	5	
BFEG	1:1	10	Purple
	2:1	7	
	3:1	5	
	4:1	5	
	5:1	4	
DSEG	1:1	1	Purple
	2:1	1	
	3:1	1	
	4:1	1	
	5:1	0.5	

Samples which require less time for GNPs formation

4.4.1.3 Comparison of Time of Formation of Gold Nanoparticles by Different Synthesis Method

A comparison study was made between two different methods for the synthesis of GNPs *viz.* room temperature and solar light irradiation. From the above discussed section (4.4.1.1 and 4.4.1.2), reveals that GNPs formation using four different plant extracts (APE, TAE, BFE and DSE) shows shorter time in formation of GNPs produced with higher concentration of plant extracts and constant volume of gold chloride. Therefore, comparative study was made between two methods with respect to higher concentration of selected plant extract interacts with constant volume of gold chloride (5:1) and time of formation (min) were represented in **Table 22.**

Table 22. Comparison of GNPs formation time using different synthesis methods for four selected plant extracts

Sample code	Varying plant extract: Constant Auric chloride	Time of formation (min)
APEGRT	5:1	30
APEG	5:1	0.8
TAEGRT	5:1	7
TAEG	5:1	5
BFEGRT	5:1	45
BFEG	5:1	4
DSEGRT	5:1	1
DSEG	5:1	0.5

Samples which require less time for GNPs formation

The lesser time of formation of GNPs (30 s to 5 min) were noted under solar light irradiation method, when compared to room temperature method (1 min to 45 min), respectively. In this method, exposure to sunlight accelerates the electron transfer process, which promotes the reduction of gold chloride to GNPs through the bioactive molecules present in the extract.

Compared with the room temperature method, GNP formation is faster under solar light irradiation. Overall, external stimulation is required to attain rapid formation of stable GNPs.

4.4.1.4 Probable mechanism of Gold nanoparticles Formation

The sustainable synthesis of GNPs can take place through the reduction of gold metal ions with the help of plant extracts containing bioactive constituents **(Pradeep *et al.*, 2021)**. The process of GNP formation, involves the reduction of gold metal ions (Au^{3+}) which stabilises or

reduces to metallic gold (Au^0) with the aid of phytochemical compounds present in the plant extract. The following steps involved are (i) Initiation phase via., the reduction of Au^{3+} to Au^0 ions, (ii) Nucleation and growth phase: after reduction, atomic nuclei tend to cluster with each other to form NPs formation (iii) Stabilisation phase. After attaining the maximum size, the NPs attract the capping/ reducing agents on to their surface and stabilise NPs electrostatically **(Elia *et al.*, 2014)**. The most common reducing agents present in the bioactive compounds has the functional group moieties such as enol (C=C-OH), carboxyl (COOH), hydroxyl (-OH), thiol (-SH) and amine ($-NH_2$) groups, which facilitates the reduction of gold ions (Au^{3+}) to metallic gold (Au^0). The morphology and size of NPs impact the electrostatic interactions between metallic gold and bioactive compounds from plant source *via.* redox reactions **(Timoszyk *et al.*, 2022)**. The proposed mechanism for GNPs formation is represented in **Figure 33.**

The underlying mechanism involves the reduction of Au^{3+} to Au^0 through bioactive compounds present in the plant extract. However, the exact mechanism involved in the reduction of Au^{3+} and stabilisation of NPs are to be explored due to their complex nature of bioactive constituents. Therefore, the exact identification, qualitative and quantitative analysis of bioactive compounds are the key objectives for the synthesis of metallic NPs. The hydroxyl and carboxyl groups in phenols and flavonoids facilitate NPs formation due to their high nucleophilicity and strong interaction with metal ions.

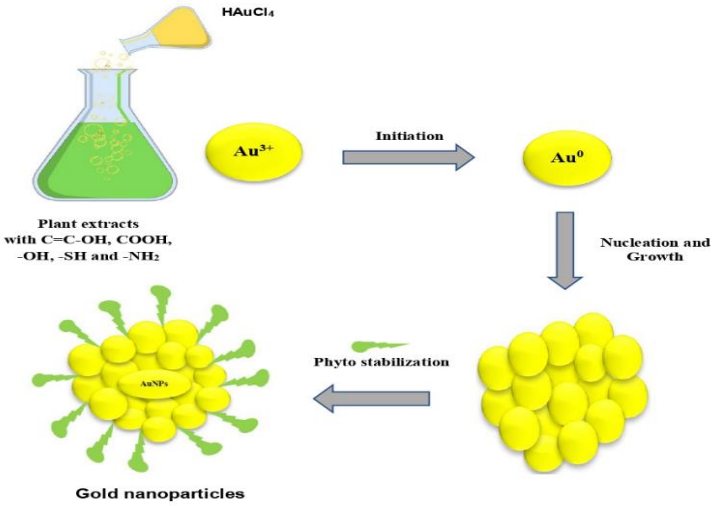

Figure 33. Pictorial representation of mechanism for gold nanoparticle formation

Previous reports on the biosynthesis of GNPs from various plant sources such as *Salix alba* **(Islam *et al.*, 2019),** *Acorus calmus* **(Firdhouse *et al.*, 2024)**, *Alternanthera sessilis*, *Portulaca oleracea* and *Sterculia foetida* **(Firdhouse and Lalitha, 2020)**, coriander leaf **(Narayanan and Sakthivel, 2008)**, *Camellia sinensis* **(Boruah *et al.*, 2012)**, *Nigella arvensis*

(Chahardoli *et al.*, 2018), *Curcumae kwangsiensis* leaf extract **(Chen *et al.*, 2021)** effectively reduced Au^{3+} to Au^{0} ions with vibrant GNPs formation. As demonstrated from previous studies, green synthesis of GNPs offers advantageous over chemical methods due to its safety, cost effective, simple process, easy availability of source material, biocompatibility, energy efficient and suitable for large scale production **(Santhosh *et al,* 2022)**. All these factors led to prefer an eco-friendly synthesis-based approach than conventional chemical methods.

4.4.2 Sustainable Synthesis of Silver Nanoparticles by Solar Light Irradiation

As discussed in section 4.4.1.3, two synthesis methods were adopted for GNP formation: room temperature method and solar light irradiation method. Among these, the solar light irradiation method demonstrated quicker reduction of Au^{3+} to Au^{0} and shorter time in GNP formation, which was monitored by observing the colour change in the reaction mixture. Hence, the solar light irradiation method was also chosen for silver nanoparticles (SNPs) synthesis.

The solar/ sunlight irradiation (SL) method is considered to be accessible energy source, used as inducive catalyst for the stable SNP formation in a shorter time. The main advantages of solar light irradiation method include being non-toxic, eco-friendly, cost effective, safe, energy efficient, and sustainable process **(Wei *et al.*, 2012)**. The results of SNPs synthesised from four selected plant extracts (APE, TAE, BFE and DSE) by solar light irradiation method are presented in **Table 23.** A visual colour changes from pale green (leaf extract) or pale orange (fruits and seed extracts) to brown was observed, as shown in **Figure 34**. The sample code assigned for the synthesised SNPs by solar light irradiation method was represented as APES, TAES, BFES, and DSES NPs.

The results showed that the time required for SNPs formation increased with higher extract concentration by maintaining a constant silver nitrate ratio (1:1 to 5:1). For APES, formation time increased from 40 s to 2 min; for TAES, from 1- 5 min; for BFES, from 4 - 10 min; and for DSES, from 2 - 5 min. From the results, it is evident that an equal ratio of sample to silver nitrate resulted in lesser time for SNPs formation in all four extracts. This may be attribted to the synergistic action of secondary metabolites as discussed in section 4.4. These metabolites facilitate the reduction of sliver ions (Ag^{+}) to metallic silver (Ag^{0}) under SL irradiation. Solar light acts as a photocatalyst, promoting rapid electron transfer in the reaction mixture and hence enabling quicker SNP formation. The successful formation of SNPs was further confirmed by spectroscopic analysis.

Similar studies on various plant materials, including the seeds of *Alpinia katsumadai*, *Thymbra spicata*, and flowers of *Abelmoschus esculentus* are reported to effectively reduce silver ions (Ag^{+}) to metallic silver (Ag^{0}), resulting in SNPs formation with potent antibacterial, antiproliferative, antifungal and cytotoxic activities **(He *et al.*, 2017; Erci *et al.*, 2018; Devanesan *et al.*, 2021)**. Also, *Salvadora persica* aqueous root extract has also been utilised for the formation of SNP for various biomedical and environmental applications **(Arshad *et al.*, 2022)**.

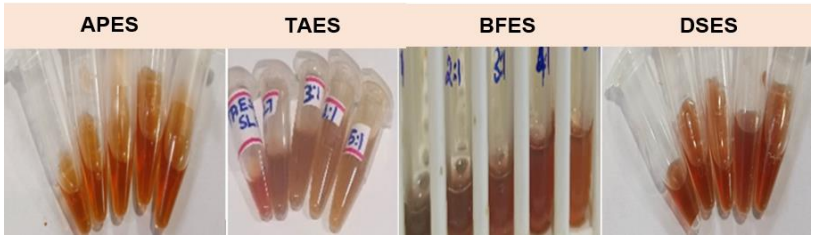

Figure 34. Synthesised SNPs using four plant extracts using solar light irradiation

Table 23. Comparison of SNPs formation time using four plant extracts using Solar light irradiation

Sample code	Varying plant extract: Constant Silver nitrate	By Solar light irradiation (SL)	
		Time of formation (min)	Colour of SNPs
APES	1:1	0.67	Brown
	2:1	0.67	
	3:1	1	
	4:1	2	
	5:1	2	
TAES	1:1	1	Brown
	2:1	2	
	3:1	2	
	4:1	3	
	5:1	5	
BFES	1:1	4	Brown
	2:1	4	
	3:1	6	
	4:1	8	
	5:1	10	

Sample code	Varying plant extract: Constant Silver nitrate	By Solar light irradiation (SL)	
		Time of formation (min)	Colour of SNPs
DSES	1:1	2	Brown
	2:1	3	
	3:1	4	
	4:1	4	
	5:1	5	

Samples which require less time for SNPs formation

4.4.2.1 Probable mechanism of formation of Silver nanoparticles

The rapid reduction of metal ions is attributed to sunlight induced photoactivation, which accelerates electron transfer faster and converts Ag^{+} to Ag^{0} ions. Upon exposure to solar light, the silver nitrate-extract mixture undergoes three step mechanism in the SNPs formation: nucleation, successive growth of particles, and phyto-stabilisation.

In the first step, the solution containing silver metal ion (Ag^{+}) is reduced by a reducing agent, resulting in production of nucleation center (atoms). Once these atoms are formed, they catalyse the reduction of remaining metal ions which homogeneously distributed throughout the bulk solution. Hence, these atoms mingle together (atomic coalescence) to form metal clusters. This phase is referred as nucleation and successive growth phase. The potent bioreductants containing functional groups (-OH, -C=O, -COOH) plays a crucial role which precisely control and stabilising the SNPs formation **(Haibullah *et al.*,2022** and **Mallick *et al.*,2004)**. The probable mechanism for the SNPs formation is represented in **Figure 35**.

In the present study, the selected four plant extracts of APE, TAE, BFE and DSE are shown to contain various phytoconstituents (as listed in table 19 of phytoconstituents), which exhibits synergistic action in the redox mechanism by reducing metal ions from Ag^{+} to Ag^{0}. The bioactive compounds especially flavonoids and polyphenols, oxidizes from their enolic to quinoid formation under photoactivation. During this oxidation process, the removal of two electrons ($-2H^{+}$) from two hydroxyl groups in flavonoids, followed by the reduction of silver ions ($2Ag^{+}$), leading to the formation of SNPs ($2Ag^{0}$). Followed by the nucleation and growth of Ag^{o}, the assembly and stabilisation of SNPs forming large clusters. The phytochemical constituents bind to or embedded in the surface of the NPs and stabilising them are shown in **Figure 35**. Therefore, the bioactive constituents in the plant extracts serve as reducing and stabilising agents in SNPs formation, which helps in reducing the toxicity, agglomeration of NPs and improving their potential pharmaceutical applications **(Rizwana *et al.*, 2022)**.

To date, there is a notable absence of studies on synthesising gold and silver NPs using the ethanolic leaf extracts of A. paniculatum, T. australasiae, and H. validus (fruits) as well as the 75% ethanolic extract of P. dactylifera (seeds). The potent phytochemical constituents present in the extract proved their reduction properties in the synthesis of GNPs and SNPs for biological applications.

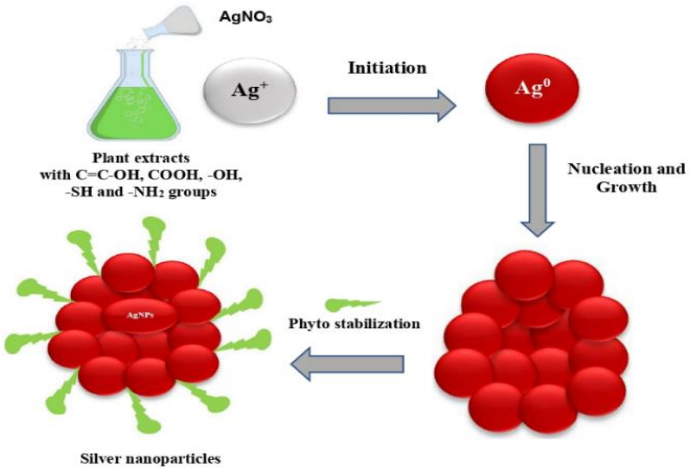

Figure 35. Pictorial representation of mechanism for silver nanoparticles formation

4.4.3 Analytical Characterisation of Synthesised Metallic Nanoparticles

The synthesised metallic NPs, such as GNPs and SNPs, were characterised using UV-visible spectrophotometer, FTIR, XRD, zeta potential, FESEM and EDS analysis. All samples were completely dispersed prior to further analysis. Proper dispersion of the NPs ensures homogeneity, greater surface area, and provides accurate and reliable results.

4.4.3.1 UV- Visible Spectral Characterisation of Synthesised Gold Nanoparticles

UV BioSpec nano spectrophotometer is a commonly used tool provides fast and efficient analysis for characterising NPs. Metallic NPs possess unique optical properties due to SPR, where the oscillation or conduction of electrons on surface of NPs occurs in response to an incident light, results in a distinct absorption spectrum. The strong absorbance band related to the SPR of GNPs is observed between 500 to 580 nm in the visible region **(Mishra *et al.*, 2012)**. The SPR spectrum provides valuable information about the kinetic behaviour, size, and shape of the NPs. A lower wavelength of SPR band represents smaller particle size with an increase in surface-volume ratio, also the intense extinction absorption band represents the uniformity of the synthesised NPs **(Haiss *et al.*, 2007)**.

The UV-visible spectra of synthesised GNPs are presented in **Figure 36, 37, 38, and 39**. The biosynthesised GNPs show absorption bands at 528 nm (APEG), 536 nm (TAEG), 532 nm (BFEG), and 544 nm (DSEG), indicating excellent SPR characteristics within the range of 528 nm to 544 nm, confirming the successful formation of GNPs. The purple colour of synthesised GNPs was observed upon the addition of gold chloride to the selected plant extracts which indicates the reduction of Au^{3+} to Au^{0} ions. Higher optical density (OD) values of the GNPs indicated a higher concentration of synthesised NPs.

GNPs have outstanding application in various fields owing to their distinctive characteristics, which makes them appropriate for therapeutic, diagnostic tools, biosensor, targeted therapy, photothermal, antimicrobial agents, and coating materials **(Hammami *et al.*, 2021)**. Recent studies on the eco-friendly sustainable synthesis of GNPs using aqueous fruit extracts of *Aegle marmelos*, *Eugenia jambolana*, soursop and the microalgae of *Synechococcus moorigangae* reported pink and wine/ruby red colours due to SPR, with absorption bands at 519 nm, 523 nm, 526 nm and 552 nm, respectively **(Vijayakumar, 2019; Rosyidah *et al.*, 2024)**.

The results from the literature of GNPs correlate with the findings of the present study, confirming the synthesised NPs to be GNPs

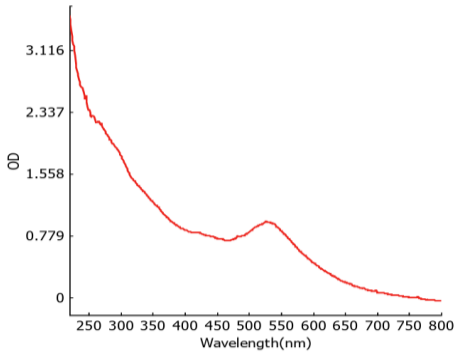

Figure 36. UV-Visible spectrum of APEG

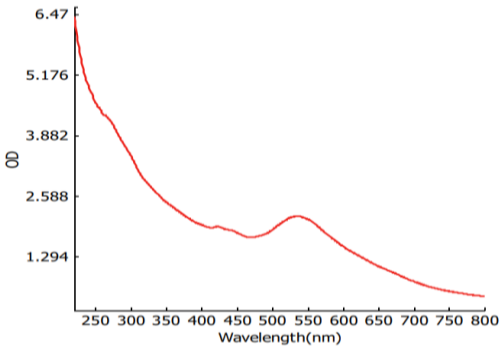

Figure 37. UV-Visible spectrum of TAEG

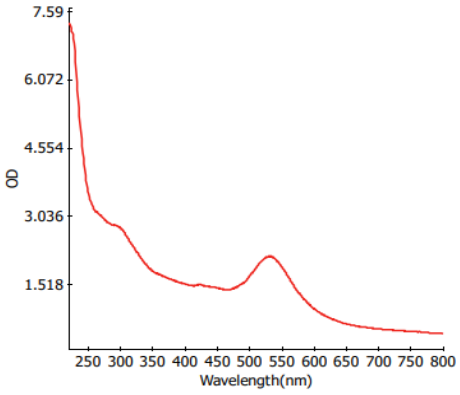

Figure 38. UV-Visible spectrum of BFEG

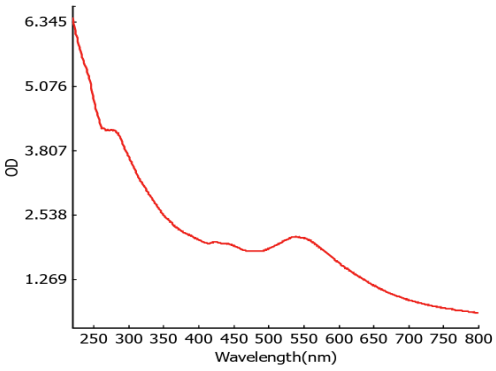

Figure 39. UV-Visible spectrum of DSEG

4.4.3.2 UV- Visible Spectral Characterisation of Synthesised Silver Nanoparticles

UV BioSpec nano spectrophotometer was used to monitor the SNPs formation over wavelength range of 220 to 800 nm. The SPR of SNPs extends in the range from 350 to 490 nm, depending on the shape, size and distribution of the particles **(Ider *et al.*, 2016)**. The UV-visible spectra of the synthesised SNPs are presented in **Figures 40, 41, 42, and 43.** The biosynthesised SNPs possess absorption bands at 444 nm (APES), 428 nm (TAES), 429 nm (BFES), and 445 nm (DSES), confirming SPR in the range from 420 nm to 450 nm for the successful formation of SNPs. The colour transition from orange to brown in the synthesised SNPs, observed after addition of silver nitrate to the selected plant extracts, indicating the reduction of Ag^{+} to Ag^{0} ions. In addition, the absorbance bands between 230 to 280 nm correspond to the chromophore groups present in the plant extracts. Therefore, these observations suggesting the phytochemical constituents in the selected plant extract effectively reducing the metal ions, confirming the formation of SNPs.

As the extinction absorption spectra of NPs becomes more complex, an increase in particle size is observed **(Mekshun *et al.*, 2020)**. The extinction spectra of SNPs with a single distinct peak corresponds to spherical shaped particles, whereas, two plasmon peaks corresponding to long wavelength (longitudinal) and short wavelength (transverse) in the extinction spectra from 400 to 800 nm, representing disk, dumbbell and triangular-shaped particles **(Kondorskiy *et al.*, 2018; Lam *et al.*, 2019)**.

SNPs have emerged as fascinating and attractive nanomaterials due to their unique physicochemical properties, size, and shape. More efficient shape-controlled SNPs can be synthesised using different methods. Biological microorganisms or secondary metabolites present in plant extracts such as phenols, flavonoids, terpenoids, alkaloids and anthocyanins, widely reduce the silver salts from Ag^{+} to Ag^{0}. SNPs are recognised for their broad-spectrum antimicrobial activity, antibiotic resistance, anticancer, and anthelmintic applications. Multifunctional properties of SNPs, enable them for various biological applications, including would healing, drug delivery, detection platforms, photonics, biological labelling, biosensing and medical device coatings **(Xu *et al.*, 2020)**. Recent reports on the green synthesis of SNPs from plant extracts, such as *Cannabis sativa* (root), *Bougainvillea glabra* (flower), *Nigella sativa* (seed), reports SPR bands at 408 nm, 436 nm, 420 nm in the visible spectrum, respectively **(Suman *et al.*, 2022; Oves *et al.*, 2023; Daoudi *et al.*, 2024)**.

From the literature findings, SNPs formation correlates with the results of the present study confirming that the synthesised NPs to be SNPs.

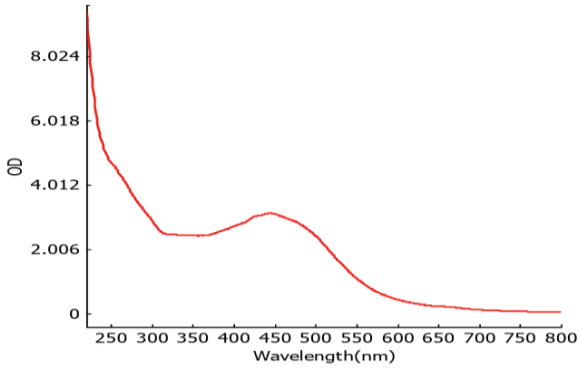

Figure 40. UV-Visible spectrum of APES

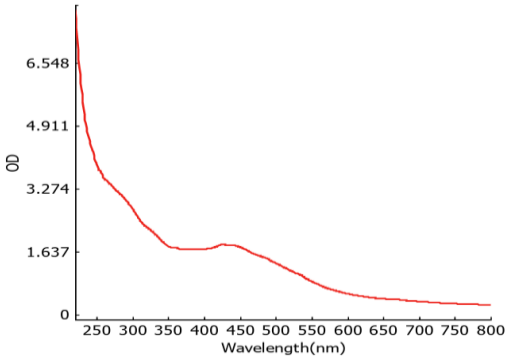

Figure 41. UV-Visible spectrum of TAES

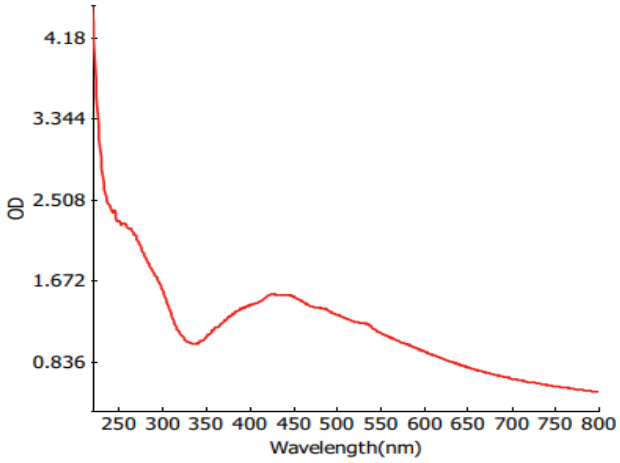

Figure 42. UV-Visible spectrum of BFES

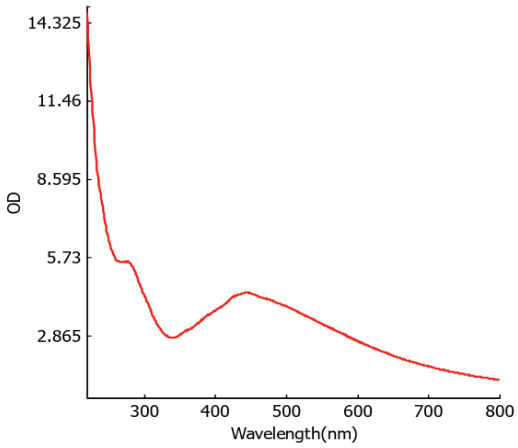

Figure 43. UV-Visible spectrum of DSES

UV-visible spectra of the biosynthesised GNPs and SNPs revealed that the SPR of the samples falls within their respective regions, confirming the formation of GNPs and SNPs.

4.4.3.3 FTIR Spectral Characterisation of Synthesised Metallic Nanoparticles

4.4.3.3.1 FTIR Spectral Characterisation of Synthesised Gold Nanoparticles

FTIR analysis was recorded to characterise the functional groups present in the samples. FTIR spectra of the selected plant extract and their synthesised GNPs are shown in **Figure 44, 45, 46, and 47.**

The plant extracts contain functional groups which serve as reducing and capping agents during GNP synthesis. In the FTIR spectrum of *A. paniculatum* ethanol extract (APE), a broad band at 3348.42 cm^{-1} corresponds to -OH stretching vibrations, the weak peak at 2924.09 cm^{-1} is

attributed to C-H stretching, the intense peak at 1620.21 cm^{-1} represents C=C stretching of conjugated alkenes, 1388.75 cm^{-1} represents C-H bending of aldehyde, the intense peak at 1049.28 cm^{-1} corresponds to carbonyl (C-O) carbohydrate chain, and strong band at 671.23 cm^{-1} corresponds to -CH bending (out of plane) vibration.

The FTIR spectra of APEG showed the broad peaks at 3356.4 cm^{-1} (-OH), 678.94 cm^{-1} (CH out of plane bending vibrations), and a medium peak at 1635.64 cm^{-1} corresponds to C=C stretching of conjugated alkenes. Also, the weak peak at 2978.09 cm^{-1} (C-H stretching of alkene), 1388.75 cm^{-1} (C-H bending aldehyde), were observed, along with weak peaks at 1257.59 cm^{-1} and 1149.57 cm^{-1} corresponding to C-N stretching of amine, the peak at 1080.14 cm^{-1} attributed to C-O aromatic stretching. The C-metal peak appeared in the region from 500 to 400 cm^{-1} confirms the formation of GNPs.

The reduction in FTIR peak intensity of APEG NPs within the fingerprint region (1000-1500 cm^{-1}) indicates involvement of phytochemicals from extract during NPs formation. The phytochemicals present in APE extract as mentioned in Table 19, which serve as capping/stabilising agents during the GNPs synthesis. Their bioactive molecules containing functional groups interacts with the NPs surface, resulting in effective stabilisation of formed GNPs. FTIR spectra of APE and APEG NPs are represented in **Figure 44.**

Similarly, *T. australasiae* ethanol extract (TAE) shows the characteristic strong peak at 3286.70 cm^{-1} corresponds to -OH group, and medium peak at 2924.09 cm^{-1} corresponds to C-H stretching, 1720.50 cm^{-1} (C=O stretching of carboxylic acid), 1211.30 cm^{-1} (C-N stretching of amine), 1041.56 cm^{-1} (carbonyl (C-O) carbohydrate chain), and 671.79 cm^{-1} (CH out of plane bending vibrations). In addition, the FTIR spectra of BFE shows the broad peak at 3356.14 cm^{-1} (-OH group), 2924.09 cm^{-1}(C-H stretching), 1720.50 cm^{-1} (C=O stretching of carboxylic acid), 1381.03 cm^{-1} (C-H bending aldehyde), 1041.56 cm^{-1} (carbonyl (C-O) of carbohydrate chain, and 663.51 cm^{-1} (CH out of plane bending vibrations). The results obtained from FTIR of BF fruits were corresponds to the literature reported by **Blessymole *et al.*, 2018**. Also, FTIR spectra of DSE shows the characteristic peaks at 2924.09 cm^{-1} and 2854.65 cm^{-1} corresponds to phenolic O-H stretching, 1743.65 cm^{-1} (C=O stretching of esters), 1604.7 cm^{-1} (C=C stretching of conjugated alkene), 1442.75 cm^{-1} (O-H bending of carboxylic acid), 1221.16 cm^{-1}, 1157.29 cm^{-1}, 1103.28 cm^{-1}, and 1049.28 cm^{-1} corresponds to C-N stretching of amine, and the peak at 725.23 cm^{-1} corresponds to C=C bending of alkene, respectively.

The prominent functional groups of DSE shows phenolic OH, amide NH, carbonyl and C-OH stretching modes are responsible for the presence of secondary metabolites such as phenols, flavonoids, proteins, carbohydrates, and terpenoids **(Ghani and Hussain, 2021)**.

The FTIR spectra of the synthesised GNPs, namely: TAEG, BFEG and DSEG showed similar characteristic peak at 3325.28 cm^{-1}, 1635.64 cm^{-1}, 1257.59 cm^{-1}, and 678.94 cm^{-1} corresponds to -OH, C=C stretching of alkenes, C-O stretching of aromatic ester, and CH out of plane bending vibrations. The peak appeared at 420 to 486 cm^{-1} represents the C-metal group, confirming the NPs formation. The FTIR spectra of TAE and TAEG, BSE and BSEG, and DSE and DSEG are given in **Figure 45, 46, and 47.**

FTIR analysis of the selected plant extracts and the synthesised GNPs, revealed that the functional groups present in the extracts helps in the reduction of Au^{3+} to Au^{0}, enables the GNPs formation.

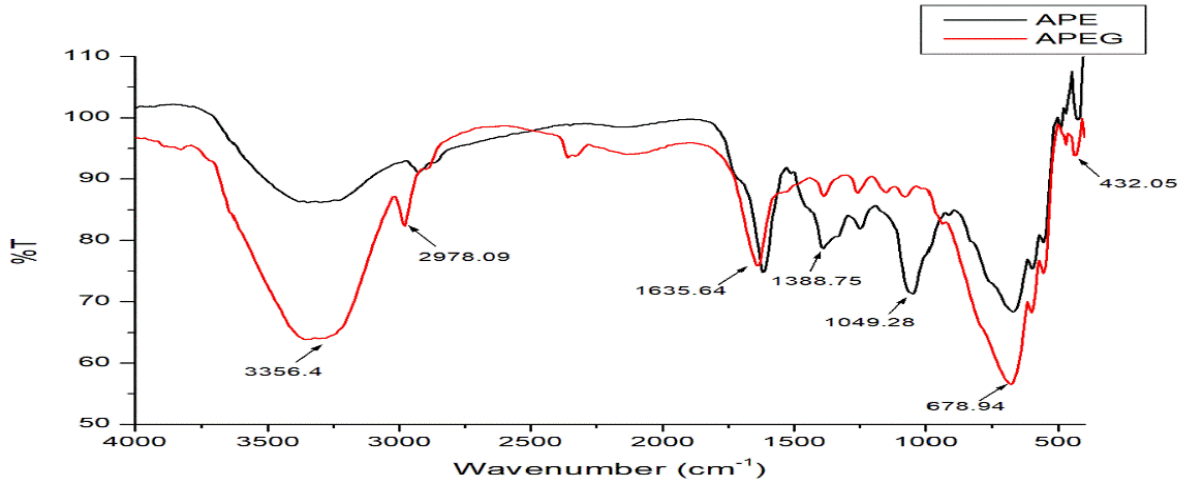

Figure 44. FTIR Spectra of APE extract and APEG NPs

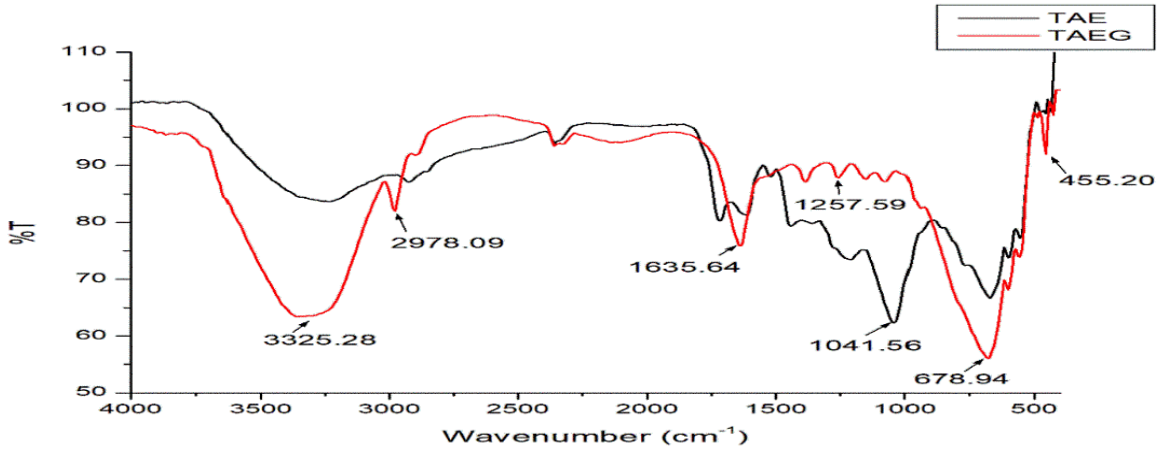

Figure 45. FTIR Spectra of TAE extract and TAEG NPs

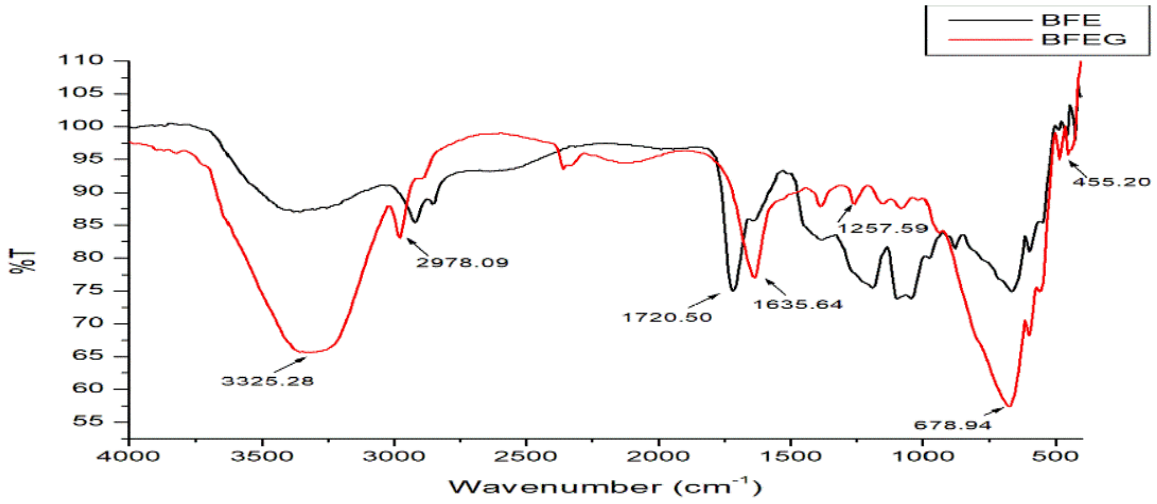

Figure 46. FTIR Spectra of BFE extract and BFEG NPs

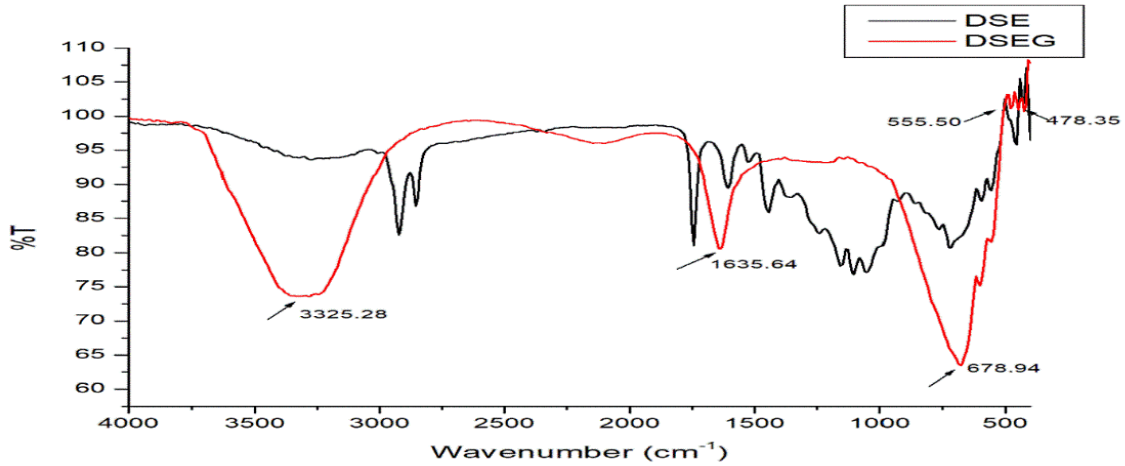

Figure 47. FTIR Spectra of DSE extract and DSEG NPs

4.4.3.4 FTIR Spectral Characterisation of Synthesised Silver Nanoparticles

FTIR spectra of synthesised APE, TAE, BFE and DSE aided SNPs such as APES, TAES, BFES and DSES showed the upward peak in the region from 410 to 480 cm^{-1} which corresponds to C-metal peak representing the formation of SNPs in all samples. The FTIR spectra of APES, TAES, BSES and DSES are given in **Figure 48, 49, 50, and 51.**

The FTIR spectrum of all the synthesised SNPs showed the similar major prominent peaks at 3340.7 cm^{-1} (-OH group), 2978.09 cm^{-1} (C-H stretching), 1635.64 cm^{-1} (C=C stretching of conjugated alkenes), and 678.94 cm^{-1} (CH out of plane bending vibrations). The minor peaks at 2978.09 cm^{-1}, 1388.75 cm^{-1}, 1257.59 cm^{-1}, 1149.57 cm^{-1}, and 1080.14 cm^{-1} corresponding to

C-H stretching of alkane, C-H bending of aldehyde, C-N stretching of amine, and C-O aromatic stretching, which attributed to the functional groups present in plant extracts helps in the biosynthesis of SNPs. The results obtained for the SNPs synthesis agreed with the previous literature **(Aramwit *et al.*, 2014; Prabu and Johnson, 2015; Albeladi *et al.*, 2020)**.

FTIR peak intensity of APES, TAES and BFES was decreased in the fingerprint region (1000 to 1500 cm^{-1}) is due to the involvement of phytochemical constituents present in the extract, which helps in reducing the metal ions from Ag^{+} to Ag^{0}. Hence, the phytochemicals such as flavonoids, carbohydrates, glycosides, terpenoids, quinones, saponins, and alkaloids present in the extract act as capping/stabilising agents which reduces silver nitrate to form SNPs. The bioactive molecules contain various functional groups, which binds to the surface of the NPs, and stabilises SNP formation.

According to **Devaraj *et al.*, 2013**, the synthesised SNPs from ethanol extract of cannonball leaves showed the promising characteristic peak at 3432 cm^{-1} (OH stretching), 2777 cm^{-1} (C-H aldehydic stretching), 1637 cm^{-1} (C=C) ,1121 cm^{-1} (-C=O) and 685.86 cm^{-1} (CH out of plane bending). The green synthesised SNPs were prepared from the aqueous seeds of *Tectona grandis.* FTIR peak of seed power revealed the characteristic peaks at 1745 cm^{-1} (C=O stretching of carboxylic acid/ester), 1643 cm^{-1} (N-C=O amide), and 1038 cm^{-1} (C-N amine bond). The peak shift in synthesised SNPs demonstrates the participation of functional groups in the formation of SNPs **(Rautela *et al.*, 2019)**.

From the results, the identified peaks in the FTIR spectra of synthesised SNPs using the aqueous -ethanolic extracts of A. paniculatum, T. australasiae, H. validus and P. dactylifera shows potentiality of functional groups as stabilising agents which are responsible for the formation of SNPs

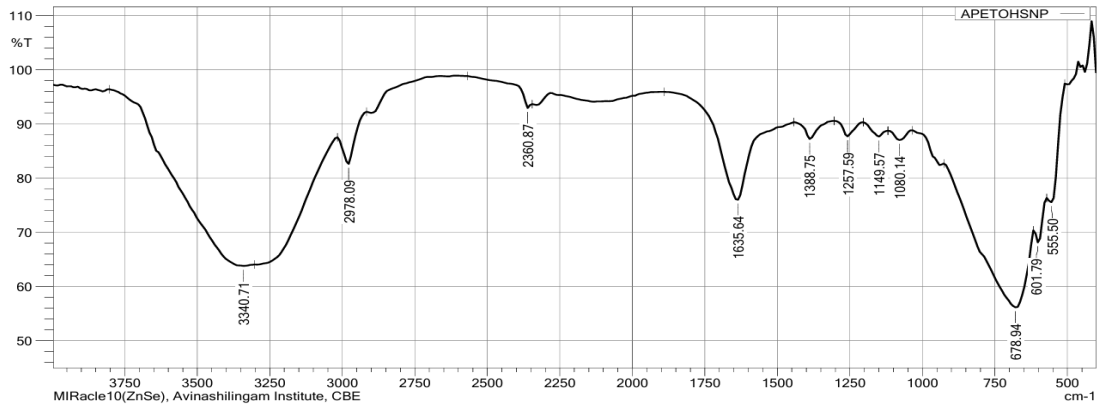

Figure 48. FTIR spectrum of APES NPs

Figure 49. FTIR spectrum of TAES NPs

Figure 50. FTIR spectrum of BFES NPs

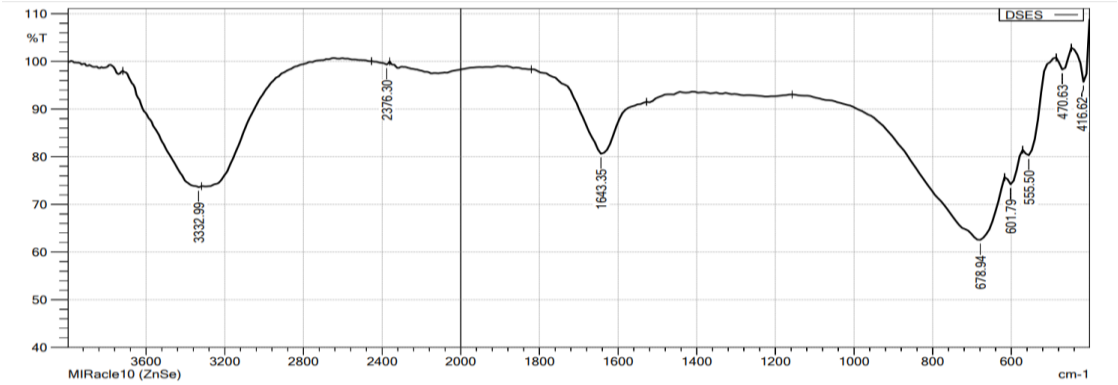

Figure 51. FTIR spectrum of DSES NPs

4.4.3.5 XRD Pattern of Synthesised Metallic Nanoparticles

4.4.3.5.1 XRD Pattern of Synthesised Gold Nanoparticles

XRD is a non-destructive technique which gives detailed information about the physical properties of crystalline materials including, the crystal structure, average grain size, phase identification, phase quantification, crystal orientation, lattice strain, and chemical compositions **(Bunaciu *et al.*, 2015)**. XRD pattern of synthesised GNPs from aqueous ethanolic extracts of *A. paniculatum , T. australaesiae, H. validus and P.dactyleferia* were given in **Figure 52a, 52b,**

53a and 53b. In specific, the XRD pattern shows the diffraction peaks (2θ) at 26.4˚, 39.02˚ (111), 43.04˚ (200), 54.22˚ (220), 70.07˚(220), 74.07˚(311) and 78.37˚(311) for APEG; 28.9˚, 32.86˚(122), 38.73˚(111), 44.90˚(200) and 59.17˚(220) for TAEG; 28.91˚, 38.83˚(111), 44.89˚ (200), and 59.17˚(220) for BFEG; 28.98˚, and 38.95˚ (111) for DSEG, respectively which are similar with the reported literature and the face centered cubic (fcc) structure of standard Au^0 according to JCPDS card no: 04-0784 and JCPDS, USA digital standards **(Gopinath *et al.*, 2017; Rajeshkumar *et al.*, 2013)**.

The appearence of diffraction peak (2θ) at 26.4˚, and 28.9˚ which correponds to the plant extract act as reducing and stabilising agents utilised for NP synthesis **(Khalir *et al* .,2020)**. Therefore, the biosynthesised GNPs are found to be crystalline in nature which are validated by XRD. The average crystallite size of GNPs are found to be APEG (79.87 nm), TAEG (91.38 nm), BFEG (55.08 nm) and DSEG (21.49 nm), respectively which is estimated by Debye-Scherrer equation **(Cullity,1956)**. XRD pattern of GNPs and their peak details are given in **Table 24**.

The results obtained from the XRD patterns of biosynthesised GNPs are found to be crystalline in nature. The size and morphological characteristics of the GNPs can be determined using electron microscopic analysis.

Table 24. XRD Pattern of Synthesised Gold Nanoparticles

Sample code of GNPs	Pos. [°2Th.]	Height [cts]	FWHM Left [°2Th.]	d-spacing [Å]	Rel. Int. [%]	Mean D (nm)
APEG	26.4111	41.36	0.0502	3.37471	100.0	79.57443 =79.57
	39.0284	37.87	0.4015	2.30791	91.58	
	43.0440	7.89	0.8029	2.10146	19.09	
	54.2255	15.99	0.0612	1.69020	38.65	
	70.0766	5.53	0.5353	1.34281	13.37	
	74.0774	13.33	0.0612	1.27881	32.24	
	78.3718	13.33	0.0612	1.27881	32.24	
TAEG	28.9184	2760.41	0.0502	3.08757	100.0	91.37741 =91.38
	32.2582	48.89	0.2007	2.77513	1.77	
	38.7379	46.26	0.9368	2.32455	1.68	
	59.1724	247.49	0.0816	1.56016	8.97	
	59.3254	136.09	0.0816	1.56036	4.93	
BFEG	28.9158	2497.52	0.1171	3.08784	100.00	55.08259 =55.08
	38.8326	116.53	0.4015	2.31910	4.67	
	44.8916	28.43	0.8029	2.01917	1.14	
	59.1708	81.46	0.0612	1.56019	3.26	
	78.5287	14.12	0.8029	1.21810	0.57	
DSEG	28.9803	42.99	0.2676	3.08111	100.00	21.48511 =21.49
	38.9578	32.49	0.8029	2.31194	75.56	

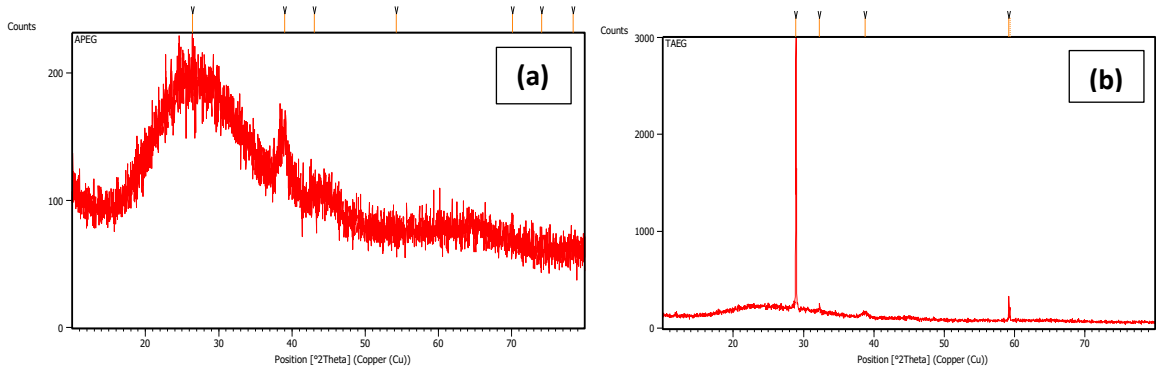

Figure 52. XRD Pattern of Gold nanoparticles (a) APEG; (b) TAEG

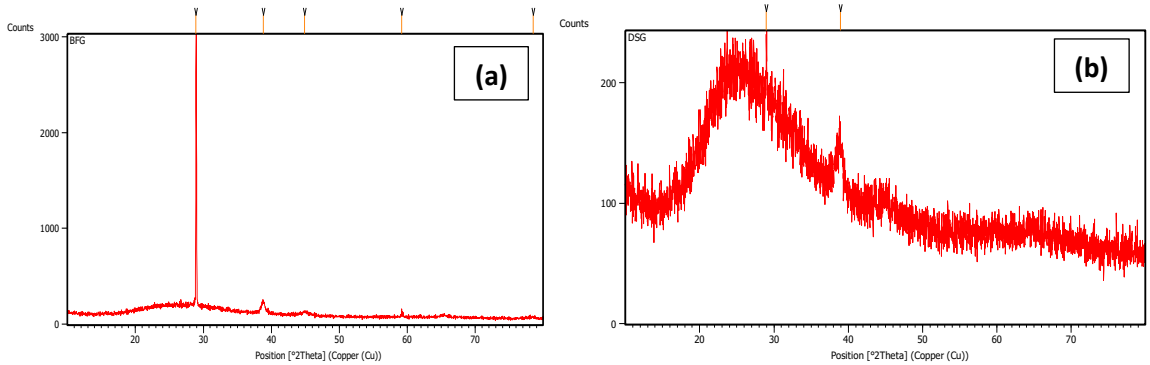

Figure 53. XRD Pattern of Gold nanoparticles (a) BFEG; (b) DSEG

4.4.3.6 XRD Pattern of Synthesised Silver Nanoparticles

The XRD profiles of the synthesised SNPs are presented in **Figure 54a, 54b, 55a and 55b**. The APES sample displayed distinct different peaks at 2θ values of 28.44˚, 32.8˚, 38.7˚, 44.9˚, and 46.9˚. The reflections at 32.8˚, 38.7˚ indicate the formation of nano-crystalline SNPs and are consistent with patterns reported for the plant-mediated SNPs **(Jemal *et al.*, 2017; Ali *et al.*,2023)**. The peaks at 32.8˚, 38.7˚, and 46.9˚ corresponds to the (122), (111), and (200) lattice planes of crystalline silver, respectively matching the standard reference data for silver (JCPDS card No: 04-0783) **(Jemal *et al.*, 2017; Ali *et al.*, 2023)**. The average crystallite size of APES NPs was found to be 44.81 nm **(Figure 54a)**. Similarly, XRD pattern of TAES shows the sharp, intense peak of 32.42˚ corresponds to the (122) plane, confirming the formation of SNPs with the crystallite grain size found to be 35.28 nm **(Figure 54b).**

Further, XRD pattern of BFES shows the diffraction peaks (2θ) at 32.82˚ (122) and 68.03˚ (220), and for DSES shows 2θ at 38.71˚ (111) was correlated with the indexed FCC of crstallographic lattice planes of Ag^0 (JCPDS Card No: *01-087-0719*) which is given in **Figure 55a and 55b (Khalir *et al.*, 2020)**. The average crystallite size of BFES and DSES are found to be 52.41 nm and 13.47 nm. Therefore, the biosynthesised SNPs are found to be crystalline properties which are confirmed by XRD pattern. The average crystallite size of SNPs are found

to be APES (44.81 nm), TAES (35.28 nm), BFES (52.41 nm) and DSES (13.47 nm), respectively which is estimated by Debye-Scherrer equation **(Cullity, 1956)**. XRD pattern of SNPs and their peak details are given in **Table 25**.

The results obtained from the XRD patterns of biosynthesised SNPs are found to be crystalline in nature. The size and morphological characteristics of the SNPs can be determined using electron microscopic analysis.

Table 25. XRD Pattern of Synthesised Silver Nanoparticles

Sample code of SNPs	Pos. [°2Th.]	Height [cts]	FWHM Left [°2Th.]	d-spacing [Å]	Rel. Int. [%]	Mean D (nm)
APES	28.4493	77.32	0.1004	3.13740	60.08	44.80544 =44.81
	32.8682	128.70	0.1673	2.72500	100.00	
	38.7444	34.64	0.4015	2.32418	26.91	
	44.9021	12.05	0.8029	2.01872	9.36	
	46.9021	44.00	0.1673	1.93720	34.19	
TAES	32.4277	156.53	0.2448	2.75872	100.00	35.28468 =35.28
BFES	32.8293	236.24	0.1004	2.72814	100.00	52.40702 =52.41
	68.0307	7.12	0.5353	1.37811	3.01	
DSES	38.7187	35.06	0.6528	2.32373	100.00	13.46693 =13.47

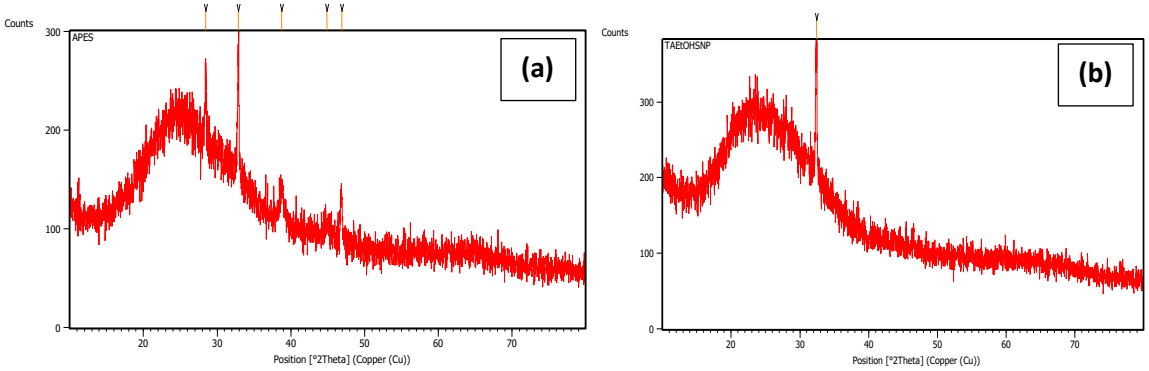

Figure 54. XRD Pattern of Silver nanoparticles (a) APES; (b) TAES

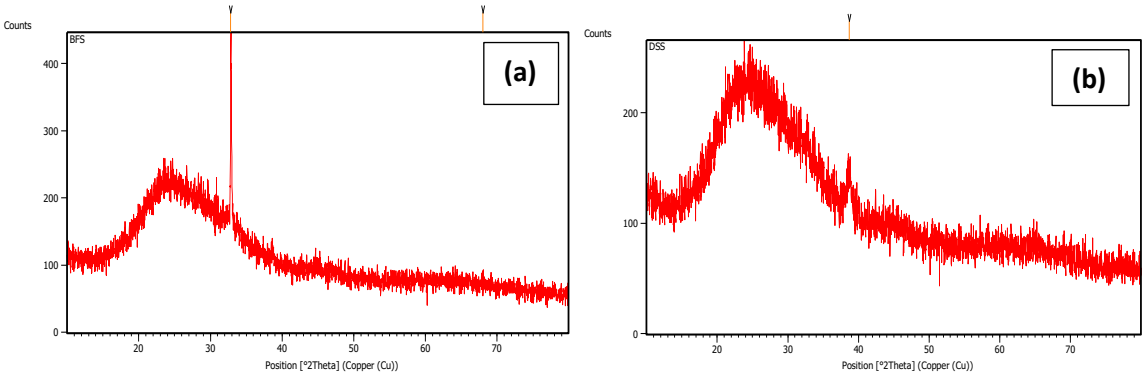

Figure 55. XRD Pattern of Silver nanoparticles (a) BFES; (b) DSES

4.4.3.7 Zeta Potential Measurement of Synthesised Metallic Nanoparticles

The surface charge of the synthesised GNPs and SNPs were measured using zeta potential analysis. Particle suspensions in a solvent with a highly negative or positive surface charge tend to repel each other due to the stern potential layer (the inner layer surrounding the liquid surface). This repulsion prevents particles from adhering to one another, thereby reducing the flocculation or aggregation. Zeta potential values can be significantly modified by various factors, including pH, solvent viscosity, ionic strength, temperature and surface characteristics **(Smith *et al.*, 2017)**. In general, NPs with excellent colloidal stability exhibit zeta potential values between ±30 mV and ±60 mV. Furthermore, zeta potential depends on the dispersant; when the particle density is higher than the dispersing medium, sedimentation likely occurs (**Honary *et al.*, 2013; Müller, 1996; Nemeth *et al.*, 2022)**.

The zeta potential analysis of the synthesised GNPs and SNPs from aqueous ethanolic extracts of *A. paniculatum* (APEG NPs and APES NPs), *T. australaesiae* (TAEG NPs and TAES NPs), *H. validus* (BFEGNPs and BFES NPs) *and P.dactyleferia* (DSEG NPs and DSES NPs) exhibited consistently negative values across all samples **(Table 26)**. Among the GNPs, all the samples possess strong collidal stability and remained within the stable range **(Figure 56a to d)**. For SNPs, APES exhibits highest stability followed by TAES, BFES and DSES **(Figure 57a to d)**. From the analysis, all the synthesised NPs carried negative surface charge potential, suggesting the NPs to be surrounded by negatively charged organic moieties such as carbonyl or hydroxy groups present in the phytoconstituents of the plant extracts, which contributes to electrostatic repulsion and prevent aggregation. The order of colloidal stability from zeta potential measurements was:

APES >TAES > APEG > BFEG > TAEG > BFES > DSEG > DSES

This confirms that SNPs from *A. paniculatum* (APES, -43.3 mV) and *T. australasiae* (TAES, -39.2 mV) were most stable among all synthesised samples, whereas *P. dactylifera* (DSES, -32.0 mV) exhibited least stability. These findings suggested the plant derived phytoconstituents helps in stabilising the NPs through surface functionalization.

Table 26. Zeta Potential Analysis of Synthesised GNPs and SNPs

Sample code of GNPs	Zeta potential (mV)	Sample code of SNPs	Zeta potential (mV)
APEG	-38.4	APES	-43.3
TAEG	-36.1	TAES	-39.2
BFEG	-37.5	BFES	-34.8
DSEG	-34.0	DSES	-32.0

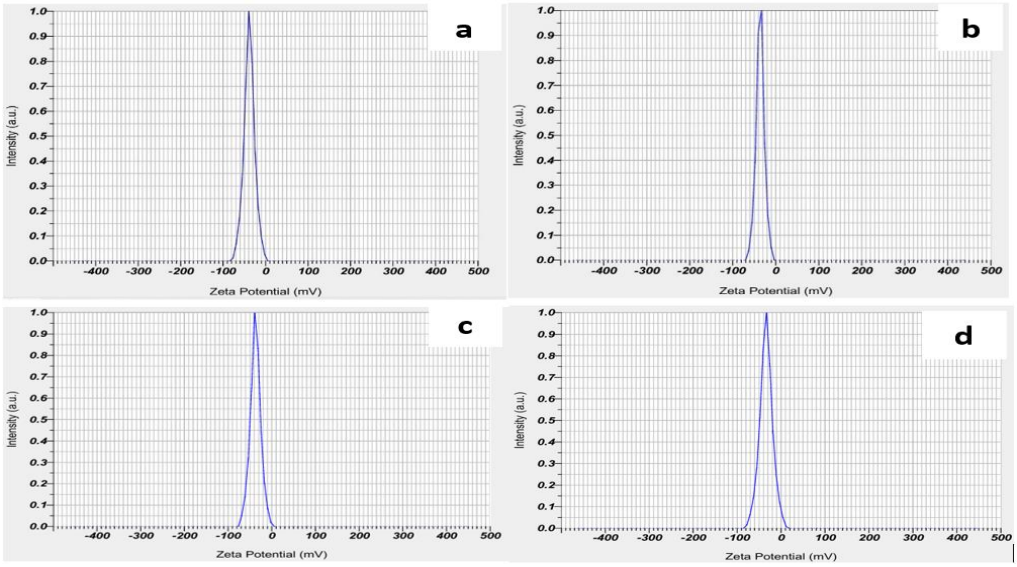

Figure 56. Zeta potential analysis of Gold Nanoparticles (a) APEG NPs; (b) TAEG NPs; (c) BFEG NPs; and (d) DSEG NPs

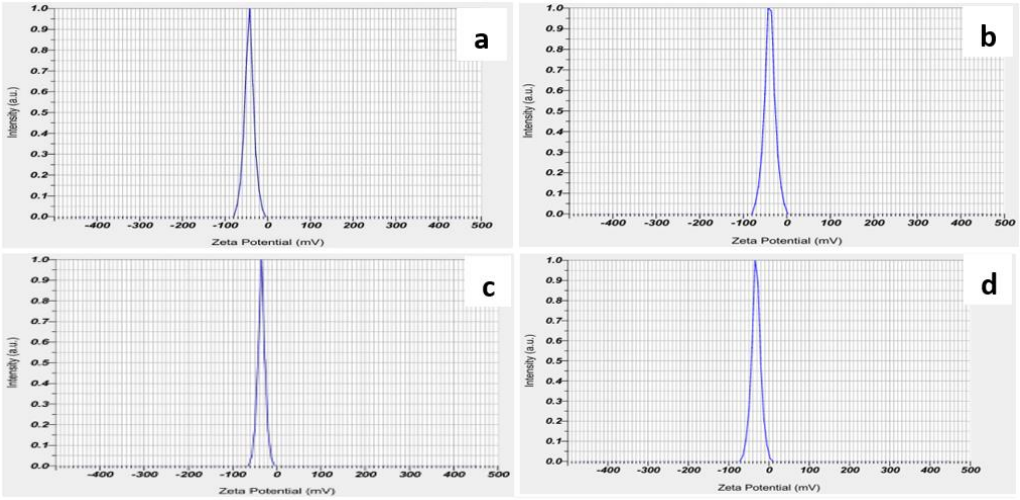

Figure 57. Zeta potential analysis of Silver Nanoparticles (a) APES NPs; (b) TAES NPs (c) BFES NPs; (d) DSES NPs

Moreover, the cellular level uptake of NPs is highly dependent on their size, shape, and their surface charge, which influence both cellular and tissue-level binding process. The adsorption of NPs is influenced by electrostatic interactions between the cell membrane and the NPs (nanocarriers). Studies on polystyrene-based NPs indicate that particles carrying a positive surface charge which tend to interact with proteins that possess relatively low isoelectric points such as albumin. In contrast, proteins with higher isoelectric points such as immunoglobulin G, preferably show a stronger affinity for negatively charged NPs. Therefore, by modifying the surface charge of NPs with negatively charged (-COOH) or positively charged (amine) groups, which allows the selective interaction with particular protein based on their charge properties

(Caldorera-Moore *et al.,* 2010; Honary and Zahir, 2013a). Similar study reported a zeta potential value of -14.8mV for GNPs synthesised from pomegranate leaves, confirming their stability **(Serdar, 2024)**.

Zeta potential analysis revealed that both GNPs and SNPs were more stable, and exhibited negatively charged surfaces that surrounded and stabilised the NPs.

4.4.3.8 FESEM Imaging and EDS Analysis of Synthesised Metallic Nanoparticles

4.4.3.8.1 FESEM Imaging and EDS analysis of Synthesised Gold Nanoparticles

FESEM and EDS analysis were employed to determine the surface morphology, topology, size, and elemental distribution or mapping of NPs. FESEM and EDS images of synthesised GNPs from aqueous ethanolic extracts of *A. paniculatum* (APEG) , *T. australaesiae* (TAEG), *H. validus* (BFEG) *and P.dactyleferia* (DSEG) are presented in **Figure 58a, 58b; 59a, 59b; 60a, 60b; and 61a, 61b**. The FESEM and EDS spectra of APEG show a scattered spherical shape with an averge size of 13.39 nm, and the elemental mapping revealed the presence of Au, C, O, Mg, Na, Al, Si, Ca and K **(Figure 58 a and 58b)**. The samples TAEG and BFEG displayed densely packed spherical morphologies of NPs with average particle size of 12.88 nm and 20.11nm, respectively, with the presence of elements such as Au, C and O, as shown in **Figure 59a and 59b; and Figure 60a and 60b**. Similarly, DSEG showed a spherical form of NPs with an average particle size of 15.38 nm. The elemental mapping revealed the presence of Au, C and O **(Figure 61a and 61b)**. All the synthesised GNPs were recorded at an electric potential of 15kV, with a working distance ranging from 9.09 nm to 10 mm.

From the over all results, the plant extract aided synthesised GNPs were found to have an average particle size range of 12 nm to 20 nm. The elemental distribution of the synthesised GNPs depicts the presence of Au, further confirming the formation of GNPs. The presence of other elements such as O, C, Mg, Na, K, and Ca is attributed to the plant materials (precursors) utilised as reducing agents, which are embedded on the surface of the GNPs for stabilisation. The presence of element Si, may be due to the glass plate used for sample coating. Also, the element Al present in sample APEG is considered an impurity. Earlier reports on GNP synthesis using pomagranate leaf extract showed an average particle size of 23.51nm, exhibiting mutiple shapes such as triangular, spherical and hexagonal **(Serdar, 2024)**. Also, GNP synthesised from leaf extract of *Nothapodytes foetida* showed 14.97 nm with spherial shape **(Susanna *et al,* 2023)**.

FESEM morphology and EDS mapping of synthesised GNPs using four bioreductants revealed spherical shapes with a particle size ranging from 12 nm to 20 nm, and the presence of element Au confirming the formation of GNPs.

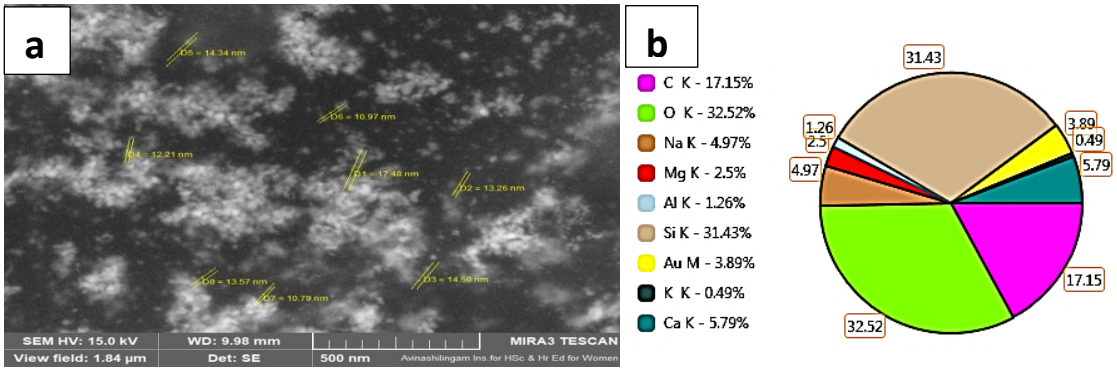

Figure 58. FESEM morphology of Synthesised APEG (a); EDS mapping of APEG (b)

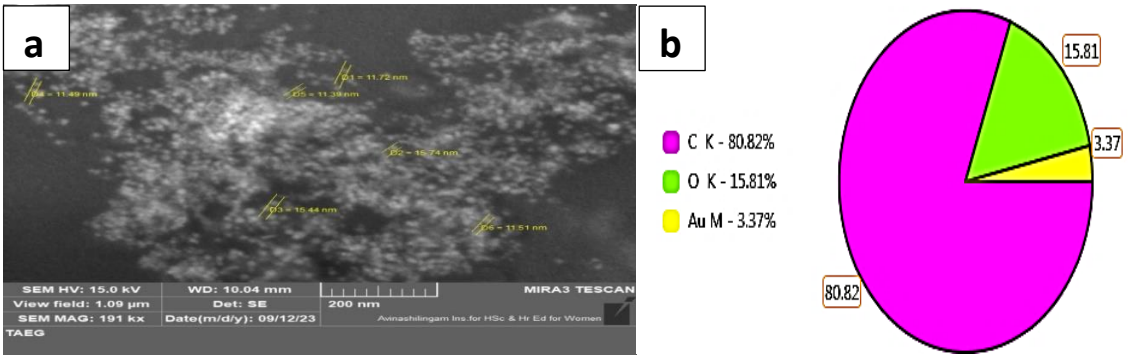

Figure 59. FESEM morphology of Synthesised TAEG (a); EDS mapping of TAEG (b)

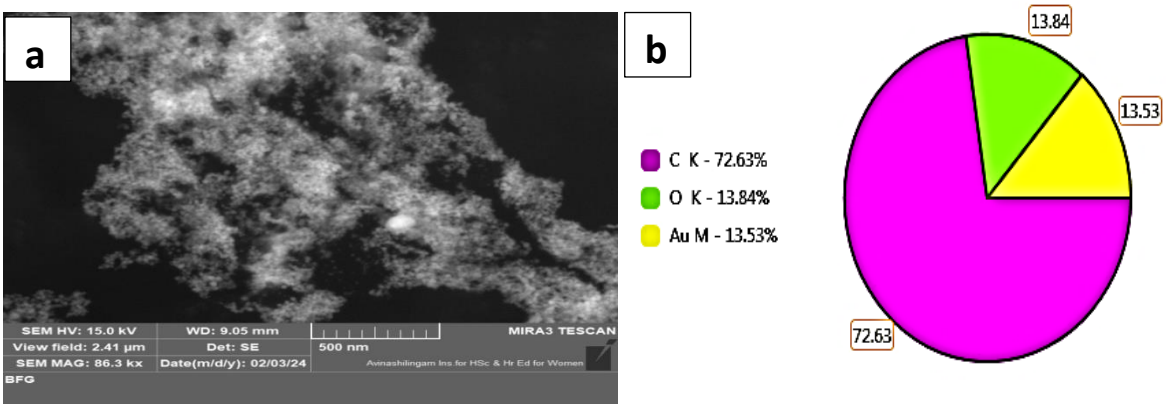

Figure 60. FESEM morphology of Synthesised BFEG (a); EDS mapping of BFEG (b)

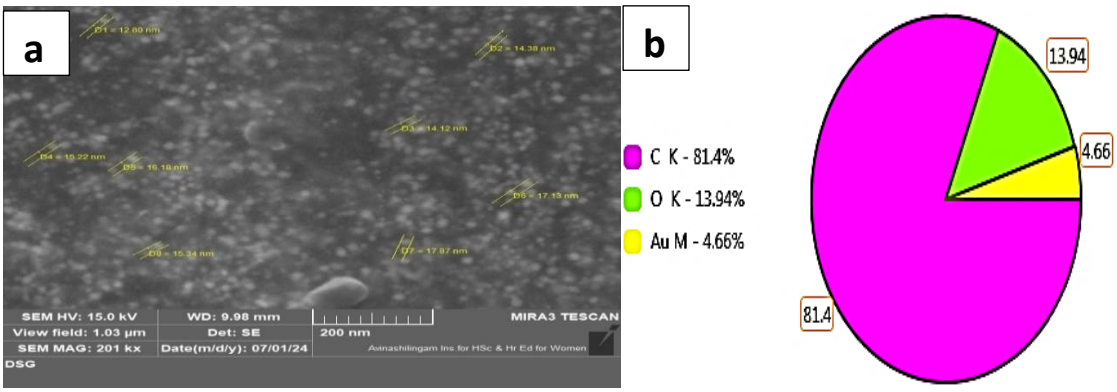

Figure 61. FESEM morphology of Synthesised DSEG (a); EDS mapping of DSEG (b)

4.4.3.8.2 FESEM Imaging and EDS Analysis of Synthesised Silver Nanoparticles

The surface features and elemental composition of the synthesised SNPs were determined using FESEM Imaging and EDS. The sample (APES NPs) displayed particles with an anisotropic, and the mean particle was measured as 26.6 nm under imaging conditions of 15 kV and a working distance of 6.93 mm (**Figure 62a)**. The EDS spectrum showed the elements of O, Ca, Si, Ag, Na, Mg, and Al, which are from the plant extracts and contributes to reducing/stabilising the NPs. The presence of silver in the elemental map confirmed the successful formation of APES NPs, as represented in **Figure 62b**. The spherical morphology of TAES NPs displayed a mean particle size of 32.8 nm **(Figure 63a)**. The elemental distribution of the synthesised TAES NPs cconfirmed the presence of C, O, Ag, and Si, with silver confirming the SNPs formation **(Figure 63b)**. Similarly, the BFES NPs and DSES NPs displayed spherical NPs with mean sizes of 31.44 nm and 27.57 nm, respectively, along with the elements of Ag, C and O, as shown in **Figure 64a and 64b; and Figure 65a and 65b**.

Based on the overall findings, the plant extract aided synthesised SNPs were found to have an particle size ranging from 26 nm to 33 nm. The elemental distribution of the synthesised SNPs depicts the presence of Ag, further confirming the formation of SNPs. The additional elements such as O, Na, Mg, C and Ca orginated from the plant extracts used during synthesis, as these phytochemicals embedded on the SNPs surface and undergoes stabilisation. The high proportion of Si is attributed to the glass substrate used during sample coatings, while the presence of Al in APES NPs is attributed to trace impurities.

The previous reports on SNP synthesis using herbal extract of *Salvinia molesta* showed an average particle size of 12.46 nm, exhibiting roughly spherical shaped SNPs **(Verma *et al.*, 2015)**. Also, the ealier reports on SNP synthesised from *Gossypium hirsutum* leaf extract showed average particle size of 13 to 15nm with spherical morphology **(Kanipandian and Thirumurugan, 2014)**. The aqueous extracts of date palm seed and date palm leaf aided SNPs showed spherical and poly diverse morphology with an average particle diameter frrom 14 to 26 nm **(Rajalakshmi *et al.*, 2023)**. The biosynthesised SNPs from *Fioria vitifolia* leaves showed an average size of 5 to 15 nm with spherical shape possess stronger antibacterial and cytotoxicity against HeLa cancer cell lines **(Imath *et al.*, 2024)**.

FESEM morphology and EDS mapping of synthesised SNPs using four bioreductants revealed anisotropic and spherical shapes with an average particle size from 26 nm to 33 nm, and the presence of element Ag confirming the formation of SNPs.

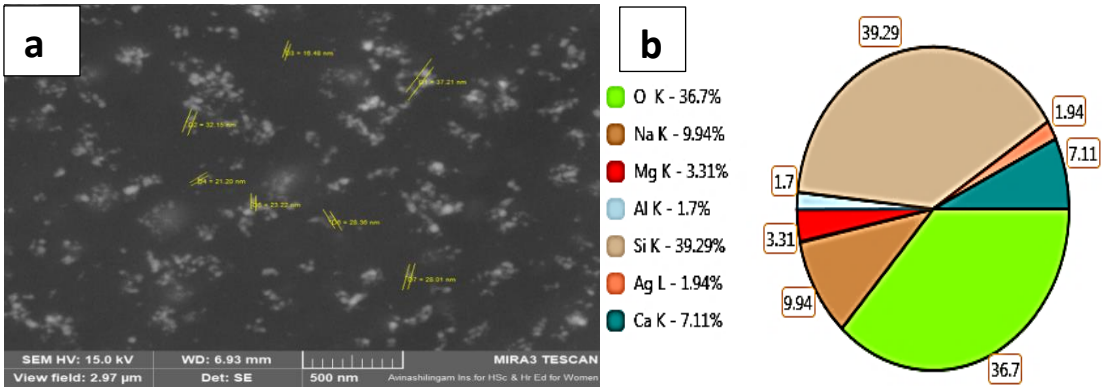

Figure 62. FESEM morphology of Synthesised APES NPs (a); EDS mapping of APES NPs (b)

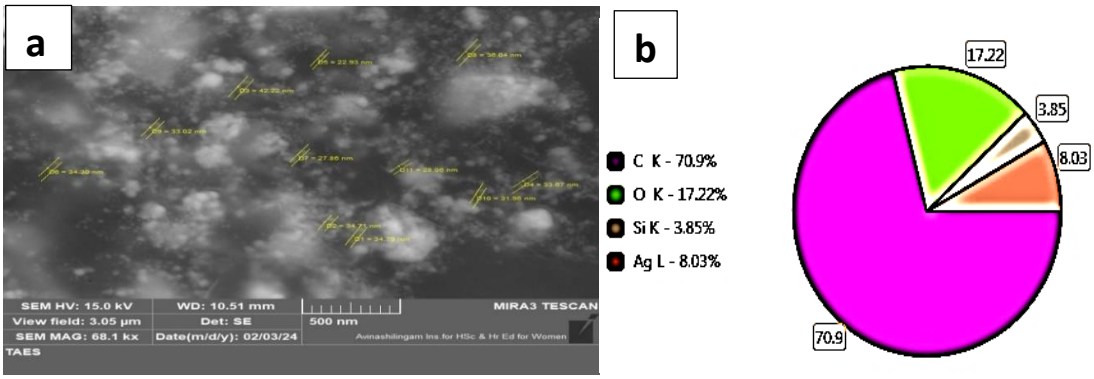

Figure 63. FESEM morphology of Synthesised TAES NPs (a); EDS mapping of TAES NPs (b)

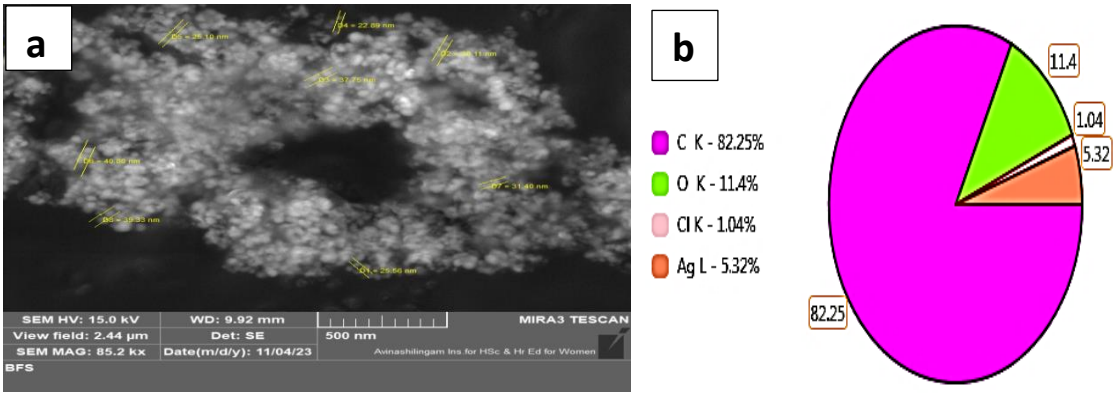

Figure 64. FESEM morphology of Synthesised BFES NPs (a); EDS mapping of BFES NPs (b)

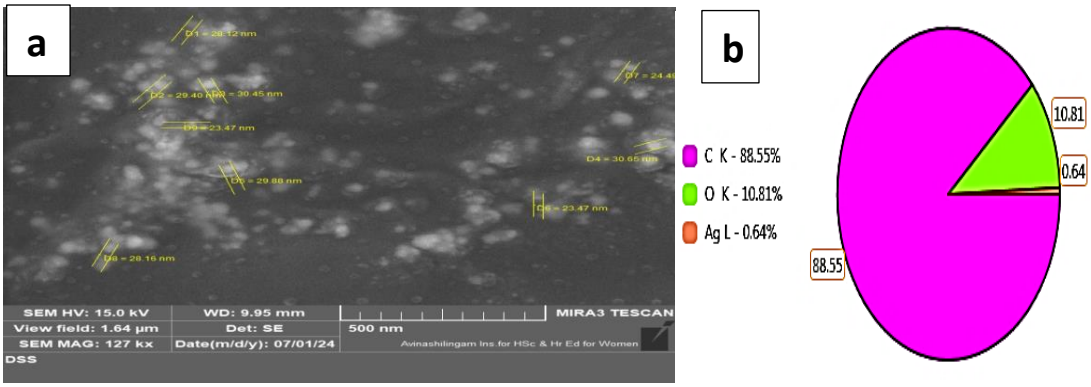

Figure 65. FESEM morphology of Synthesised DSES NPs (a); EDS mapping of DSES NPs (b)

Phase-IV *In silico* Screening of Bioactive Compounds Present in Selected Plants

4.5 *In silico* Screening of Bioactive Compounds Present in Selected Plants

In silico studies are essential for predicting the therapeutic potential of drug-like bioactive lead compounds and enabling their use in drug discovery and development prior to *in vivo* studies. Screening millions of compounds for particular disease conditions through *in vivo* or *in vitro* is impractical due to chemical waste, time consuming and sacrificing animal models. Therefore, *in silico* screening provides a viable alternative for evaluating the physicochemical and ADMET properties of compounds. Molecular docking further helps researchers narrow down potential lead compounds, ultimately leading to the identification of lead compounds for further wet lab validation. In the present study, bioactive compounds from the selected plants namely *Amphilophium paniculatum* (AP), *Tristellateia australasiae* (TA), *Haematocarpus validus* (BF), *Phoenix dactylifera* (DS), and organo-sulphur compounds from garlic (OSC) were evaluated to identify potential inhibitors to the management of *Diabetes mellitus*.

4.5.1 Physicochemical and ADME Properties of Bioactive Compounds

The physicochemical and ADME characteristics of the chosen bioactive compounds derived from AP, TA, BF, DS and OSC are presented in **Table 27 and 28**, which helps in identifying and optimising lead compounds in early drug discovery. According to Lipinski's rule of five, (i) molecular weight (<500 Da), (ii) hydrogen bond donor (HBD $\leq$5), (iii) hydrogen bond acceptor (HBA$\leq$10), and (iv) log p $\leq$5 and other physicochemical properties such as the bioavailability of drugs, number of rotatable bonds (<12), polar surface area (PSA <140 $A^{\circ 2}$), hydrophilic-lipophilic balance (HLB within 0-20), and molar refractivity (40-130), further helps in evaluating the passive intestinal absorption, cellular permeability, and systemic bioavailability **(Lipinski, 2021; Turner *et al.*,2004)**.

Evaluation of the physicochemical and ADME properties of the twenty-two compounds identified from *Amphilophium paniculatum* (AP) is discussed below. The molecular weight of the compounds varied from 178.14 Da (Aesculetin) to 754.69 Da (Glucopyranoside), while log P values ranged from -1.91 and 9.18, possesses diverse values in lipophilicity. Only eight of the twenty-two compounds (36%) obeys Lipinski rule of five, indicating that the remaining compounds may cause challenges to oral bioavailability. Also, HBD and HBA exceeds the limits ($\leq$5 and $\leq$10, respectively) in many of glycosylated flavonoids and triterpenoid-based compounds, and exhibited high polar surface areas. Only two ligands such as ligand 15 (Glucopyranoside) and ligand 16 (Kaempferol glycoside) exhibited acceptable molar refractivity, while other ligands remained within the acceptable range.

The ADME analysis revealed the pharmacokinetic profiles of AP ligands. Compounds such as Apigenin (ligand 17), Chrysin (ligand 18), and Acacetin (ligand 19) exhibited high gastrointestinal absorption (GI), moderate bioavailability score (0.55), and were not identified as P-glycoprotein (P-gp). In addition, glycosides namely Diacetylmartynoside (ligand 8), Cynaroside (ligand 9), and Kaempferol glycoside (ligand 16), exhibited poor GI absorption and P-gp substrates, correlated with their high PSA and HBA/HBD values. The potential blood brain barrier (BBB) permeability was predicted for the compounds such as Epiloliolide (ligand 4), Chrysin (ligand 18), Linoleic acid (ligand 20) and Acacetin (ligand 19). Notably, the flavonoids (Apigenin and Chrysin) were predicted to inhibit cytochrome P450 enzymes (CYP1A2, CYP2D6 and CYP3A4), indicating drug-drug interaction risk. The bioavailability score of Ursolic acid and Linoleic acid exhibited high values of 0.85, with limitations of low solubility and high log P values.

Similarly, the physicochemical and ADME properties of eight selected bioactive compounds from *Tristellateia australasiae* (TA) were analysed to assess their potential drug molecules. The molecular weight of eight compounds ranged from 182.17 Da (Hexitol) to 428.73 Da (Epifriedelinol), falls within the acceptable range for oral drugs. However, several compounds such as Friedelin (ligand 25), Epifriedelinol (ligand 26), Lupeol (ligand 28) and Beta amyrin (ligand 27), indicates exceeding log P values. In addition, the ligands namely Hexitol and Galactitol exhibited higher HBD values (6), violating Lipinski's rule. The triterpenes such as Epifriedelinol and Beta amyrin also showed high molar refractivity values (~130), suggesting to large molecular volume and lower polarizability. Out of eight ligands, Isorhamnetin and Flavonol obeys the Lipinski's rule of five, representing the drug-likeliness. ADME properties of both compounds exhibited high GI absorption, no P-gp substrate and moderate bioavailability scores (0.55), supporting oral delivery.

Most of sugar molecules such as Hexitol, Galactitol, as well as triterpenoids such as Friedelin and Lupeol, exhibited low GI absorption and lack of BBB permeability, considering physicochemical limitations. Flavonol exhibited potential to cross BBB, and inhibiting the multiple cytochrome P450 enzymes, indicating drug-drug interactions risk. All eight compounds showed a moderate bioavailability score (0.55), suggested for oral suitability under optimised formulation conditions.

The physicochemical properties of twenty-three bioactive compounds from *Haematocarpus validus* (BF), were evaluated to assess their drug-likeliness and pharmacokinetic profiles. The molecular weight of BF ligands ranged from 116.16 Da (2- ethyl butyric acid) to 610.52 Da (Rutin). According to Lipinski's rule of five, only twelve out of twenty-three i.e. 52%

compounds follows four criteria. Some of the compounds (Eicosane, bis (2-ethyl hexyl) phthalate, Trimethylsilyl esters and Myristic acid) exhibited high HBD, HBA and PSA values, which restrict membrane permeability. In contrast, the smaller molecules such as Furanone, Catechin, 2-coumaric acid and 2-ethyl butyric acid follows Lipinski's parameter and showed PSA values of <90 $Å^2$, resulting as promising lead compounds for further investigations. HLB values for most of ligands were within the optimal drug-like range (0 to 20), except Rutin, which showed a high PSA (265.52 $Å^2$) and HLB (22.20), indicating poor permeability and oral bioavailability. Similarly, the molar refractivity values of all ligands are within limits of 40 to 130, except ligand 46 (3,5 dehydro-6-methoxy pivalate), due to differences in molecular size or polarizability.

ADME analysis revealed that only 30% of ligands exhibited a high bioavailability score of 0.85, including Myristic acid (ligand 31), Palmitic acid (ligand 32), 2-monostearin (ligand 42), and Catechin (ligand 51), found to be oral drug-like molecules. Seventeen of the twenty-three ligands showed high gastrointestinal absorption, which are correlated with their moderate molecular weight and log P values. Eicosane (ligand 33) and bis (2-ethyl hexyl) phthalate (ligand 37) resulted in high log P >8, possess good absorption due to non-polar and hydrophobic nature. The ligand 31, 32 and 51 possess BBB permeability indicating potential central nervous system (CNS) activity, whereas the large polar compounds such as Rutin (ligand 53), Epigallocatechin (ligand 49) and Gallic acid (ligand 50) were predicted to have no BBB permeability and low GI absorption rate, due to their high PSA and hydrogen bonding capacity. Cytochrome P450 inhibition was limited for most BF compounds, except Myristic acid (ligand 31), Palmitic acid (ligand 32) and Quinic acid (ligand 34) showed inhibition of CYP1A2 or CYP2C9.

From these results, BF ligands possesses low risk towards drug-drug interactions. P-gp substrates exhibits reduced intra cellular accumulation for smaller molecule-based ligands of 35 and 52. Based on these findings, small to medium molecular weight compounds with moderate lipophilicity such as Catechin, 2-ethyl butyric acid (ligand 41) and 2-coumaric acid (ligand 52) exhibited good pharmacokinetics and oral bioavailability. High lipophilic or larger molecules such as Rutin and Epigallocatechin may require formulations to overcome their poor GI adsorption and limited bioavailability.

The physicochemical and ADME analysis of fifteen bioactive ligands from *Phoenix dactylifera* (DS), exhibited good pharmacokinetics profiles which are relevant to drug development. Results presented in **Table 27 and 28** revealed that most DS ligands possess molecular weights below 500 Da and falls within acceptable hydrogen bonding based on

Lipinski's rule. However, a few compounds such as Chlorogenic acid (ligand 58) and 3-O-caffeoyl shikimic acid (ligand 57) violated hydrogen bonding characteristics and exhibited higher PSA values. In addition, sterols such as Lupeol, Ergosterol, and Beta Sitosterol, exhibited high log P values, indicating excess lipophilicity and reduced aqueous solubility.

ADME properties of DS ligands revealed high GI absorption and were non-substrates of P-glycoprotein, representing oral drug delivery. The compounds such as Nicotinic acid (ligand 54), Palmitoleic acid (ligand 66), and L-serine (ligand 65) revealed both high GI absorption and predicted BBB for CNS activity. Also, the polar compounds such as Chlorogenic acid (ligand 58) and L-cysteine (ligand 62) showed lower GI absorption, likely due to their high PSA and polarity.

Cytochrome P450 enzyme interaction of Apigenin (ligand 17), Quercetin (ligand 60) and Diosmetin (ligand 56) resulted as CYP inhibitors, indicating moderate to high risk of drug-drug interactions. Most DS ligands exhibited a bioavailability score of 0.55 or higher, while Nicotinic acid (ligand 54) and Palmitoleic acid (ligand 66) resulted in higher score of 0.85, exhibiting strong oral availability. Overall, the DS bioactive compounds exhibited good oral drug like profiles and required preclinical evaluation.

Among the compounds identified from AP, TA, BF and DS, ligand 62 (L-cysteine from *Phoenix dactylifera* (DS) seeds) having a unique functional thiol (-SH) group, which are distinguished from other compounds. The thiol groups contribute to potent antioxidant and redox regulatory activities, and play an essential role in the biosynthesis of glutathione, cells primary defence against oxidative stress. Therefore, oxidative stress is considered as central pathological mechanism in *Diabetes mellitus*, resulting insulin sensitivity and β-cell function. Therefore, by restoration of redox homeostasis, L-cysteine (ligand 62) has significant therapeutic potential to overcome the oxidative damage associated with diabetes **(Jain *et al.*, 2009; Achari and Jain, 2017)**.

The physicochemical properties and ADME of L-cysteine from date palm seeds exhibits better drug likeness with low molar refractivity value, suggesting less lipophilicity and orally bioavailable at moderate levels (0.55), which could be used as a safe co-drug formulation in drug delivery. Hence, we focused on organosulphur based compounds (OSC) such as Allicin, Alliin, and Diallyl sulphides, exhibited cytoprotective effects, anti-inflammatory effects through sulphur moieties **(Lee *et al.*,2012)**.

About thirty-four OSC and modified OSC compounds were analysed for their physicochemical and ADME properties. The molecular weight ranged from 62.14 to 310.5 Da,

log P (-2.36 to 3.92), and PSA (0 to 177.24 Å^2), falls within the Lipinski rule representing desirable oral drug likeliness. Some of the compounds exceeds the rule of five, the compounds namely L-cystine (ligand 70), 2-amino-4-(3,4-diaminophenyl) sulphonyl benzene -1,2- diamine (ligand 86) and standard metformin hydrochloride (ligand 103) which exceeds the PSA and hydrogen bond.

Similarly, the compounds such as Allicin, Diallyl sulphide and Dimethyl sulphide complied with Lipinski's rule, suggesting good bioavailability and passive diffusion. ADME evaluation further revealed that the majority of OSCs exhibited high GI absorption, indicating strong potential for oral bioavailability. The compounds such as L-cystine (ligand 70), and standard metformin hydrochloride (ligand 103) exhibited poor predicted GI absorption. The ligand 104, 80 and 72, exhibited high log P values and good bioavailability scores (3.03, 2.97 and 2.70). Cytochrome P450 enzyme interactions, which are essential for liver's drug metabolism and drug-drug interactions **(Han *et al.*, 2019; Mishra and Dahima, 2019)**, revealed that most bioactive OSCs did not inhibit CYP1A2 and CYP2C19. However, ligand 80, 96, 104 and 72 were predicted to inhibit CYP2C9, CYP3A4, or CYP2D6. Overall, four out of thirty-three screened OSC compounds could be metabolised in the liver.

Drug elimination is influenced by factors such as molecular weight and solubility, and the evaluated molecules satisfied Lipinski's rule for oral drug-likeness, and absorption properties.

Therefore, OSCs such as Allicin, Allyl methyl disulphide and Diallyl trisulphide emerged as promising lead compounds due to their physicochemical properties, and high GI absorption. In contrast, the compounds with high PSA, excessive hydrogen bonding or low bioavailability scores may require formulation-based optimisation to improve pharmacokinetics.

Table 27. Physicochemical Properties of Selected Ligands of AP, TA, BF, DS and OSC

	Ligand	Name of compound	MW (g/mol)	Log P	HBD	HBA	HLB	PSA ($A^{\circ 2}$)	Molar Refractivity
AP bioactive compounds	1.	Ursolic acid	456.70	6.58	2	3	1.69	57.53	133.70
	2.	Aesculetin	178.14	1.18	2	3	10.00	66.76	45.51
	3.	Caffeic acid	180.16	1.53	3	4	9.54	77.76	47.02
	4.	(+)-Epiloliolide	196.24	1.11	1	2	6.99	46.53	52.56
	5.	4,5-dihydroblumenol A	226.31	1.39	2	3	5.82	57.53	64.18
	6.	Daucosterol	576.85	6.09	4	6	4.27	99.38	162.18
	7.	Luteolin	286.24	2.40	4	6	11.06	107.22	74.89
	8.	Diacetylmartynoside	736.71	1.99	5	14	19.76	235.43	175.67
	9.	Cynaroside	448.38	0.14	7	11	16.83	186.37	107.04
	10.	Linarin	592.55	-0.14	7	14	19.04	214.06	140.41
	11.	Isomartynoside	652.64	1.11	7	14	19.69	223.29	157.37
	12.	Ursane	412.73	9.03	0	0	0.60	0	129.62
	13.	Oleanane	412.73	9.04	0	0	0.60	0	129.54
	14.	Cycloartane	412.73	9.18	0	0	0.60	0	129.67
	15.	Glucopyranoside	754.69	-1.91	10	19	24.23	293.21	172.82
	16.	Kaempferol 3-O-β-D glucopyranosyl -7-O-α-L-rhamnopyranoside	594.52	-1.06	9	15	20.66	245.29	137.90
	17.	Apigenin	270.24	2.71	3	5	9.36	86.99	72.91
	18.	Chrysin	254.24	3.01	2	4	7.62	66.76	70.93
	19.	Acacetin	284.26	2.85	2	5	9.56	75.99	77.40
	20.	Linoleic acid	280.45	6.42	1	2	1.90	37.30	88.52
	21.	Acetoside	624.59	0.82	9	14	19.96	245.29	148.40
	22.	(+)-Lyoniresinol-3-alpha-O-betaD-Glucopyranoside	582.59	-0.31	7	13	19.00	196.99	143.21
	23.	Hexitol	182.17	-3.73	6	6	15.52	121.38	38.40
	24.	Isorhamnetin	316.26	2.30	4	7	12.86	116.45	81.34

	Ligand	Name of compound	MW (g/mol)	Log P	HBD	HBA	HLB	PSA ($A^{\circ 2}$)	Molar Refractivity
TA bioactive compounds	25.	Friedelin	426.72	8.12	0	1	1.13	17.07	130.21
	26.	Epifriedelinol	428.73	7.73	1	1	0.92	20.23	131.13
	27.	Beta amyrin	426.72	7.40	1	1	0.92	20..23	131.91
	28.	Lupeol	426.72	7.45	1	1	0.92	20.23	130.91
	29.	Galactitol	414.71	-3.73	6	6	15.52	121.38	38.40
	30.	Flavonol	238.24	2.72	1	3	5.84	46.53	68.94
BF bioactive compounds	31.	Myristic acid	228.37	5.37	1	2	3.33	37.30	67.88
	32.	Palmitic acid	256.42	6.26	1	2	2.59	37.30	77.08
	33.	Eicosane	282.55	9.36	0	0	0.60	0	93.82
	34.	Quinic acid	192.17	-2.70	5	6	14.16	118.22	39.71
	35.	Decane	318.64	5.86	0	2	8.64	18.46	83.40
	36.	Trimethylsilyl (9E)-9-Octadecenoate	354.64	7.63	0	1	3.44	26.30	103.81
	37.	bis (2-ethylhexyl) phthalate	390.56	8.03	0	2	3.18	52.60	114.41
	38.	2-Bromotetradecane	277.28	6.76	0	0	0.87	0	74.00
	39.	3-Ethyl-3-methyl heptane	142.28	4.61	0	0	1.35	0	47.63
	40.	Isohexyl neopentyl ester	288.38	3.05	0	3	8.96	61.83	75.89
	41.	2-Ethyl butyric acid	116.16	1.91	1	2	7.14	37.30	31.05
	42.	2-Monostearin	358.56	5.97	2	3	4.82	66.76	103.31
	43.	2-Palmitoyl glycerol	330.50	5.08	2	3	5.53	66.76	94.11
	44.	Furanone	126.15	1.22	0	1	7.01	26.30	33.78
	45.	Acetyl valeryl	128.17	1.99	0	2	6.27	34.14	35.37
	46.	3,5-Dehydro-6-methoxy pivalate	498.78	8.28	0	2	2.01	35.53	147.79
	47.	Deca-6,9-diene-2,8-dione	166.22	2.35	0	2	4.62	34.14	50.18

	Ligand	Name of compound	MW (g/mol)	Log P	HBD	HBA	HLB	PSA (A°2)	Molar Refractivity
	48.	1H-indole-3-ethanamine	160.22	1.49	2	1	11.34	41.81	50.37
	49.	Epigallocatechin	306.27	1.49	6	7	13.56	130.61	75.98
	50.	Gallic acid	170.12	0.72	4	5	12.54	97.99	39.26
	51.	Catechin	290.27	1.80	5	6	11.87	110.38	74.00
	52.	2-coumaric acid	164.16	1.83	2	3	7.63	57.53	45.04
	53.	Rutin	610.52	-0.87	10	16	22.20	265.52	140.15
DS bioactive compounds	54.	Nicotinic acid	123.11	0.41	1	3	10.13	50.19	31.16
	55.	3-benzoyl pyridine	183.21	2.21	0	2	4.61	29.96	54.48
	56.	Diosmetin	300.26	2.55	3	6	11.22	96.22	79.38
	57.	3-O-caffeoylshikimic acid	336.29	0.79	5	7	12.63	144.52	82.49
	58.	Chlorogenic acid	354.31	-0.27	6	8	14.25	164.75	83.23
	59.	Apigenin	270.24	2.71	3	5	9.36	86.99	72.91
	60.	Quercetin	302.24	2.16	5	7	12.74	127.45	76.86
	61.	Ergosterol	396.65	6.63	1	1	0.94	20.23	127.13
	62.	L-cysteine	121.16	-0.53	3	3	19.31	63.32	28.22
	63.	Lupeol	426.72	7.45	1	1	0.92	20.23	130.91
	64.	L-rhamnose	164.16	-2.52	4	5	13.21	97.99	35.80
	65.	L-serine	105.09	-1.63	3	4	19.17	83.55	22.04
	66.	Palmitoleic acid	254.41	5.89	1	2	2.60	37.30	78.20
	67.	Beta sitosterol	414.71	7.84	1	1	0.93	20.23	129.77
	68.	Stigmasta-4,22-dien-3-one	410.67	8.05	0	1	1.15	17.07	129.83
	69.	Methyl sulphonyl methane	94.14	-0.40	2	3	10.64	42.52	20.05
	70.	L-cystine	240.30	-1.30	4	6	27.56	177.24	54.87

	Ligand	Name of compound	MW (g/mol)	Log P	HBD	HBA	HLB	PSA ($A^{\circ 2}$)	Molar Refractivity
OSC compounds	71.	4-(Cyclopentyl Sulphonyl) aniline	225.31	1.42	2	3	5.37	68.54	60.75
	72.	N-[(3,3-dimethyl piperidin-2-yl)methyl]-4-ethyl sulphonyl aniline	310.50	2.18	2	4	11.45	66.58	88.33
	73.	4-amino-N-(4-aminophenyl) benzene sulphonamide	263.32	1.04	3	4	8.02	106.59	72.29
	74.	Allicin	162.30	2.02	0	1	11.78	61.58	44.93
	75.	Alliin	177.22	-1.49	2	4	17.31	99.60	43.72
	76.	Allyl cysteine	161.22	0.11	2	2	17.12	91.12	42.16
	77.	Allyl disulphide	146.30	2.69	0	0	9.66	50.60	45.42
	78.	Diallyl sulphide	114.21	2.37	0	0	8.05	25.30	37.32
	79.	Diallyl trisulphide	178.30	3.31	0	0	3.31	75.90	51.17
	80.	Diallyl tetra sulphide	210.40	3.92	0	0	12.12	101.20	56.93
	81.	Allyl methyl sulphinate	120.17	0.87	0	1	12.91	45.51	29.27
	82.	S-propyl cysteine sulphoxide	211.3	0.20	2	3	22.30	127.40	49.63
	83.	Dipropyl disulphide	150.30	2.83	0	0	9.53	50.60	45.64
	84.	Dimethyl sulphide	62.14	1.10	0	0	12.98	25.30	18.89
	85.	S-Methyl 2-Propene-1-Sulphinothioate	136.20	1.32	0	1	13.24	61.58	35.80
	86.	2-amino-4-(3,4-diaminophenyl) sulphonylbenzene-1,2-diamine	278.33	-0.26	4	6	8.25	146.60	78.39
	87.	2-(3-aminophenyl) sulphonyl aniline	248.30	1.71	2	4	6.57	94.56	68.99
	88.	Allyl methyl disulphide	120.20	1.99	0	0	11.39	50.60	36.28
	89.	Modified Structure of 88 IUPAC: 2-{[(pyridine-3-yl sulphanyl) methyl] sulphanyl} ethan-1-imine	198.30	1.27	1	2	12.14	87.34	66.55
	90.	Modified Structure of 88 IUPAC: [(2-	122.20	0.11	2	2	19.40	100.47	42.16

	Ligand	Name of compound	MW (g/mol)	Log P	HBD	HBA	HLB	PSA ($A^{\circ 2}$)	Molar Refractivity
		iminoethyl) disulphanyl] amine							
	91.	S-methyl cysteine sulphoxide	151.19	-2.36	2	4	19.10	99.60	34.59
	92.	Methyl allyl trisulphide	152.30	2.60	0	0	12.55	75.90	42.04
	93.	Dipropyl sulphide	118.24	2.51	0	0	7.91	25.30	37.54
	94.	3-Vinyl-4H-1,2-dithiin	144.30	2.39	0	0	9.62	50.60	43.57
	95.	2-Vinyl-4H-1,3-dithiin	144.30	2.38	0	0	10.68	50.60	43.22
	96.	E-ajoene	234.40	1.67	0	1	10.05	86.88	69.00
	97.	Methyl Allyl thiosulphinate	152.20	0.74	0	1	12.98	45.51	29.35
	98.	Gamma-L-Glutamyl-[(S)-Allyl]-L-Cysteine	289.33	0.07	3	5	17.77	134.79	73.73
	99.	Modified structure of 98 IUPAC:(2R) -2-(methylamino) -3-(prop-2-en-1-yl sulphanyl) propanoic acid	175.25	0.84	2	3	18.08	74.63	46.86
	100.	3-({2-[(2-iminoethyl) sulphanyl] ethyl} amino) phenol	210.30	0.99	3	3	10.54	81.41	73.14
	101.	Thiacremonone	160.19	-0.11	2	3	12.59	82.83	41.18
	102.	4-hydroxy-5-methyl-2H-thiophen-3-one	130.16	-0.40	2	3	12.17	62.60	34.97
	103.	Metformin hydrochloride	129.16	-1.30	4	6	23.48	88.99	56.64
	104.	Curcumin	368.40	4.85	2	6	8.16	93.06	103.81
	105.	Captopril	217.28	0.51	2	3	12.14	96.41	54.63

Table 28. ADME Properties of Selected Ligands of AP, TA, BF, DS and OSC

Ligand	Log kp (cm/s)	BBB permeation	GI absorption	CYP1A2 Inhibitor	CYP2C19 Inhibitor	CYP2C9 Inhibitor	CYP2D6 Inhibitor	CYP3A4 Inhibitor	P-gp substrate	Bioavailability Score
1	-3.87	No	Low	No	No	No	No	No	No	0.85
2	-6.52	No	High	Yes	No	No	No	No	No	0.55

Ligand	Log kp (cm/s)	BBB permeation	GI absorption	CYP1A2 Inhibitor	CYP2C19 Inhibitor	CYP2C9 Inhibitor	CYP2D6 Inhibitor	CYP3A4 Inhibitor	P-gp substrate	Bioavailability Score
3	-6.58	No	High	No	No	No	No	No	No	0.56
4	-6.79	Yes	High	No	No	No	No	No	No	0.55
5	-7.07	Yes	High	No	No	No	No	No	No	0.55
6	-4.32	No	Low	No	No	No	No	No	No	0.55
7	-6.25	No	High	Yes	No	No	Yes	Yes	No	0.55
8	-9.87	No	Low	No	No	No	No	No	Yes	0.17
9	-8.00	No	Low	No	No	No	No	No	Yes	0.17
10	-9.56	No	Low	No	No	No	No	No	Yes	0.17
11	-10.17	No	Low	No	No	No	No	No	Yes	0.17
12	-0.67	No	Low	No	No	No	No	No	No	0.55
13	-0.57	No	Low	No	No	No	No	No	No	0.55
14	-0.47	No	Low	No	No	No	No	No	No	0.55
15	-11.68	No	Low	No	No	No	No	No	Yes	0.17
16	-10.35	No	Low	No	No	No	No	No	Yes	0.17
17	-5.80	No	High	Yes	No	No	Yes	Yes	No	0.55
18	-5.35	Yes	High	Yes	No	No	Yes	Yes	No	0.55
19	-5.66	No	High	Yes	No	Yes	Yes	Yes	No	0.55
20	-3.05	Yes	High	Yes	No	Yes	No	No	No	0.85
21	-10.46	No	Low	No	No	No	No	No	Yes	0.17
22	-9.57	No	Low	No	No	No	No	No	Yes	0.17
23	-9.61	No	Low	No	No	No	No	No	No	0.55
24	-6.90	No	High	Yes	No	No	Yes	Yes	No	0.55
25	-1.94	No	Low	No	No	No	No	No	No	0.55
26	-1.76	No	Low	No	No	No	No	No	No	0.55
27	-2.41	No	Low	No	No	No	No	No	No	0.55
28	-1.90	No	Low	No	No	No	No	No	No	0.55
29	-2.20	No	Low	No	No	No	No	No	No	0.55

Ligand	Log kp (cm/s)	BBB permeation	GI absorption	CYP1A2 Inhibitor	CYP2C19 Inhibitor	CYP2C9 Inhibitor	CYP2D6 Inhibitor	CYP3A4 Inhibitor	P-gp substrate	Bioavailability Score
30	-5.34	Yes	High	Yes	Yes	No	Yes	Yes	No	0.55
31	-3.35	Yes	High	Yes	No	No	No	No	No	0.85
32	-2.77	Yes	High	Yes	No	Yes	No	No	No	0.85
33	-0.60	No	Low	Yes	No	No	No	No	No	0.55
34	-9.15	No	Low	No	No	No	No	No	Yes	0.56
35	-3.80	No	High	No	No	No	Yes	No	Yes	0.55
36	-2.06	No	Low	Yes	No	No	No	No	No	0.55
37	-3.39	No	High	No	No	Yes	No	Yes	Yes	0.55
38	-2.60	No	Low	No	No	Yes	No	No	No	0.55
39	-3.48	Yes	Low	No	No	No	No	No	No	0.55
40	-5.44	Yes	High	No	No	No	No	No	No	0.55
41	-5.82	Yes	High	No	No	No	No	No	No	0.85
42	-3.36	No	High	No	No	No	No	No	No	0.55
43	-3.96	Yes	High	No	No	No	Yes	No	No	0.55
44	-6.32	Yes	High	No	No	No	No	No	No	0.55
45	-6.40	Yes	High	No	No	No	No	No	No	0.55
46	-2.64	No	Low	No	No	No	No	No	No	0.55
47	-6.41	Yes	High	No	No	No	No	No	No	0.55
48	-6.78	Yes	High	Yes	No	No	No	No	No	0.55
49	-8.17	No	High	No	No	No	No	No	No	0.55
50	-6.84	No	High	No	No	No	No	Yes	No	0.56
51	-7.82	No	High	No	No	No	No	No	Yes	0.55
52	-5.86	Yes	High	No	No	No	No	No	No	0.85
53	-10.26	No	Low	No	No	No	No	No	Yes	0.17
54	-6.80	Yes	High	No	No	No	No	No	No	0.85
55	-6.08	Yes	High	Yes	No	No	No	No	No	0.55
56	-5.93	No	High	Yes	No	Yes	Yes	Yes	No	0.55

Ligand	Log kp (cm/s)	BBB permeation	GI absorption	CYP1A2 Inhibitor	CYP2C19 Inhibitor	CYP2C9 Inhibitor	CYP2D6 Inhibitor	CYP3A4 Inhibitor	P-gp substrate	Bioavailability Score
57	-8.76	No	Low	No	No	No	No	No	No	0.56
58	-5.80	No	Low	No	No	No	No	No	No	0.11
59	-3.44	No	High	Yes	No	No	Yes	Yes	No	0. 55
60	-8.81	No	High	Yes	No	No	Yes	Yes	No	0.55
61	-1.90	No	Low	No	No	Yes	No	No	No	0.55
62	-8.79	No	High	No	No	No	No	No	No	0.55
63	-9.12	No	Low	No	No	No	No	No	No	0.55
64	-3.18	No	High	No	No	No	No	No	Yes	0.55
65	-2.20	No	High	No	No	No	No	No	No	0.55
66	-2.76	Yes	High	Yes	No	Yes	No	No	No	0.85
67	-0.72	No	Low	No	No	No	No	No	No	0.55
68	-7.82	No	Low	No	No	Yes	No	No	No	0.55
69	-7.16	Yes	High	No	No	No	No	No	No	0.55
70	-11.37	No	Low	No	No	No	No	No	No	0.55
71	-6.43	Yes	High	No	No	No	No	No	No	0.55
72	-6.19	Yes	High	No	No	No	Yes	No	No	0.55
73	-8.89	No	Low	No	No	No	No	No	No	0.55
74	-6.36	Yes	High	No	No	No	No	No	No	0.55
75	-9.89	No	High	No	No	No	No	No	No	0.55
76	-8.65	No	High	No	No	No	No	No	No	0.55
77	-5.63	Yes	High	No	No	No	No	No	No	0.55
78	-5.46	Yes	High	No	No	No	No	No	No	0.55
79	-5.51	Yes	High	No	No	No	No	No	No	0.55
80	-5.40	No	High	No	No	Yes	No	No	No	0.55
81	-6.73	Yes	High	No	No	No	No	No	No	0.55
82	-7.72	No	High	No	No	No	No	No	No	0.55
83	-5.30	Yes	High	No	No	No	No	No	No	0.55

Ligand	Log kp (cm/s)	BBB permeation	GI absorption	CYP1A2 Inhibitor	CYP2C19 Inhibitor	CYP2C9 Inhibitor	CYP2D6 Inhibitor	CYP3A4 Inhibitor	P-gp substrate	Bioavailability Score
84	-6.05	Yes	High	No	No	No	No	No	No	0.55
85	-6.66	Yes	High	No	No	No	No	No	No	0.55
86	-8.00	No	Low	No	No	No	No	No	No	0.55
87	-9.08	No	High	No	No	No	No	No	No	0.55
88	-5.93	Yes	High	No	No	No	No	No	No	0.55
89	-8.12	No	High	No	No	No	No	No	No	0.55
90	-7.20	No	High	No	No	No	No	No	No	0.55
91	-10.25	No	High	No	No	No	No	No	No	0.55
92	-5.82	Yes	High	No	No	No	No	No	No	0.55
93	-5.13	Yes	High	No	No	No	No	No	No	0.56
94	-5.72	Yes	High	No	No	No	No	No	No	0.55
95	-5.55	Yes	High	No	No	No	No	No	No	0.55
96	-6.52	No	High	No	No	Yes	No	No	No	0.55
97	-6.54	Yes	High	No	No	No	No	No	No	0.55
98	-10.08	No	Low	No	No	No	No	No	No	0.55
99	-8.48	No	High	No	No	No	No	No	No	0.55
100	-6.29	No	High	No	No	No	No	No	No	0.55
101	-6.95	No	High	No	No	No	No	No	No	0.55
102	-6.51	Yes	High	No	No	No	No	No	No	0.55
103	-7.64	No	High	No	No	No	No	No	No	0.11
104	-6.28	No	High	No	No	Yes	No	Yes	No	0.55
105	-7.38	No	High	No	No	No	No	No	No	0.55

4.5.2 *In silico* Toxicity Prediction of Bioactive Compounds

In the early stage of drug development, the toxicological evaluation and safety profiling of bioactive compounds are essential to minimise drug failure and ensure patient safety. In this study, *in silico* toxicity assessments of selected bioactive compounds from AP, TA, BF, DS, and OSCs were performed using two established computational tools: OSIRIS toxicity property explorer and Toxtree. These software helps to assess the drug-likeliness, solubility (log S), mutagenicity, tumorigenicity, reproductive effect, irritant, skin sensitisation, genotoxic, carcinogenicity, and Crammer's rules of toxicity, thereby reducing time, cost and wet lab studies **(Sai *et al.*, 2017)**.

One of the primary physicochemical parameters analysed was drug solubility (log S), which enhances the oral bioavailability, and the compound must undergo dissolution in GI fluids before being absorbed into systemic circulation. The compounds with log S values greater than -6, are considered to possess acceptable solubility for drug development **(Han *et al.*, 2019; Bergstrom, 2005)**. In addition, the drug score defines the various parameters such as drug-likeliness, log P, molecular weight, and toxicity alerts, provides overall potential of the compound. A drug score above zero suggested favourable drug-like characteristics, whereas values near or below zero implies the limited potential of drug likeliness.

The toxicity prediction included are mutagenicity, tumorigenicity, reproductive toxicity and irritancy effects. The risk levels associated as no risk (1.0), medium risk (0.8), and high risk (0.6). The compounds with values less than 1.0 were considered potentially hazardous and may require structural optimisation before further screening. Similarly, Toxtree applies Cramer's classification as class I (low toxic), class II (intermediate toxic) and class III (high toxic) represents the toxicity risk of particular compounds. **Table 29 and 30** represents the toxicity predictions of the selected ligands from AP, TA, BF, DS, and OSC using OSIRIS and Toxtree software.

The bioactive ligands from AP exhibited moderate to high toxicity, with toxicity values at or below 1.0. Several ligands (1,6, 12 to 14) possess low solubility (log S < -2), indicating lower bioavailability. In addition, the drug-likeliness and drug scores of many ligands were negative or near zero in OSIRIS, particularly ligands 6, 12, 13 and 14, having higher molecular weight or log P values. The other ligands such as ligand 7, 11 and 17 possess good drug scores (>0.5), lower log S (< -6), and acceptable drug likeliness indicating the drug like molecules. The toxicity risk of AP ligands ranged from moderate to high safety, with most ligands possess toxicity value of 1.0, indicating no predicted effects. However, ligands 2, 5, 16 and 17 possess

medium risk values (0.6 to 0.8) related to reproductive and irritant effects. Among the AP ligand, ligand 17 (Apigenin) exhibited good drug score (0.472), moderate solubility (-2.85) and no major toxicity alerts, resulted in promising lead compound. In comparison, Toxtree analysis revealed that 75% of the AP ligands were found to have skin sensitisation and no genotoxic or carcinogenicity risks were identified. Overall, ligands 17, and 7 exhibited drug like properties and safety profiles, making them suitable for drug development. The other AP ligands may require structural optimisation to reduce skin sensitisation and improve solubility for oral bioavailability.

The TA ligands exhibited log S values ranging from -6.91(ligand 24) to 0.546 (ligand 23 and 29). The ligand with log S values greater than -6.0 represents good solubility with better oral absorption. The ligands 23, 25, 29 and 30 falls within the acceptable range. Similarly, ligand 30 (drug score 0.761) and ligand 29 (drug score 0.715), exhibited high drug likeliness values. Meanwhile, the other ligands 26 to 28 exhibited lower drug score (<0.15) suggesting poor pharmacokinetic profiles. Toxicity risk assessment using OSIRIS revealed no high-risk alerts for any TA ligand. Most ligands were predicted to be non-toxic for mutagenicity, tumorigenicity, reproductive effects, and irritancy. Only ligand 23, 24 and 25 exhibited medium risk (0.6) values with reproductive and irritant effects. Toxtree predictions further confirmed the moderate safety profile of ligands 23, 24, and 25 under high toxicological risk (class III), with skin sensitisation and genotoxicity alerts. The other ligands 26, 27 and 28, exhibited lower class with no toxicity risk, whereas ligand 23, 29 and 30 were exhibited low or intermediate toxicity classes. Overall, ligand 29 and 30, with high drug score, good solubility and minimal toxicity alerts, were considered as drug-like compounds.

Similarly, most BF ligands showed negative drug likeliness and low drug scores (< 0.2), along with poor solubility (log S < -3.5), particularly ligand 31 to 38, indicating lower dissolution potential in the GI tract. However, ligands 34, 41 and 51 to 53 exhibited higher drug scores ($\geq$ 0.5) and drug likeliness properties. Toxicity risk assessment showed the BF ligands had no predicted mutagenic, tumorigenic, reproductive, or irritancy effects, with toxicity values of 1.0 in OSIRIS. Notably, ligand 34 and 51 exhibited excellent drug like profiles. In contrast, ligands 35, 36 and 37 showed medium to high toxicity risk (0.6 to 0.8), which related to reproductive or irritant effects and low drug score (< 0.2). Toxtree analysis classified ligand 31 to 33 and 39 to 43 under low toxicological Cramer's class (Class I). Meanwhile, ligands 34 to 36 and 44 to 47 under Cramer class (III), but these ligands did not exhibit genotoxic or carcinogenicity effects. Overall, BF ligands exhibited moderate *in silico* toxicity, and further structural optimisation and improve their safety profiles.

The DS ligands displayed a safety profile in both OSIRIS and Toxtree. Most DS ligands exhibited good drug likeliness and solubility, indicating potent GI absorption. Ligand 54, 55, 56, 58, 61, and 62 exhibited drug scores above 0.48, indicating strong drug-likeliness. Toxicity evaluation showed values of 1.0 for these ligands, indicating no risk effects. The few ligands (57, 59, and 60) exhibited medium risk scores (0.6 to 0.8) to reproductive toxicity or irritancy. The Toxtree classifications supported these findings, with ligands (54, 61, 62, 63, 64 and 66) comes under low to intermediate Cramer's class, indicating lower toxicity. Most DS ligands exhibited no skin sensitisation or genotoxicity, except ligand 68. Therefore, DS ligands were predicted to possess strong safety profiles.

The OSC compounds revealed good solubility values (-3.1 to 0.3), suitable for oral bioavailability. The ligands 99 to 102 exhibited moderate to high drug scores (> 0.63), with positive or near- neutral drug likeness values. Toxicity predictions for most OSC ligands scored 1.0, indicating no risks of mutagenicity, tumorigenicity, reproductive toxicity or irritancy. A few ligands (73, 86 and 87) exhibited moderate toxicity risk (0.6 to 0.8), for reproductive and irritant effects. Noteworthy, ligands 100, 101 and 102 exhibited excellent drug score (>0.8), with no toxicity alerts. Toxtree predictions further confirmed that ligands 99, 100, 101 and 102 have drug like safety profiles, with no genotoxic or carcinogenic. In comparison, with standard metformin hydrochloride (ligand 103), indicates excellent drug-likeliness (drug score 0.875).

In silico toxicity analysis of bioactive compounds from AP, TA, BF, DS and OSC revealed distinct safety profiles. Among these, the DS and OSC ligands exhibited lowest toxicity, minimal risk and strong drug-likeliness, resulting in safe drug development.

Table 29. Toxicity Predictions of Selected Ligands of AP, TA, BF, DS and OSC using OSIRIS

Ligand	log S	Drug likeness	Drug score	Toxicity			
				Mutagenic	Tumorigenic	Reproductive	Irritant
1	-6.111	-3.658	0.170	1	1	1	1
2	-1.643	-5.852	0.292	1	0.6	1	1
3	-1.407	1.621	0.190	1	1	1	1
4	-1.920	-4.216	0.485	1	1	1	1
5	-2.191	-1.930	0.316	1	1	1	0.6
6	-6.369	-8.300	0.122	1	1	1	1
7	-2.559	1.895	0.84	1	1	1	1
8	-3.733	1.854	0.433	1	1	1	1
9	-2.446	-1.790	0.453	1	1	1	1
10	-3.263	0.563	0.471	1	1	1	1
11	-2.913	1.965	0.502	1	1	1	1
12	-7.298	-8.599	0.123	1	1	1	1
13	-7.315	-6.619	0.123	1	1	1	1

Ligand	log S	Drug likeness	Drug score	Toxicity			
				Mutagenic	Tumorigenic	Reproductive	Irritant
14	-7.409	-5.199	0.121	1	1	1	1
15	0.251	-3.776	0.504	1	1	1	1
16	-2.88	-1.353	0.212	0.6	1	1	1
17	-2.855	1.208	0.472	0.6	1	1	1
18	-3.151	0.972	0.748	1	1	1	1
19	-3.169	-1.465	0.511	1	1	1	1
20	-4.322	-25.561	0.238	1	1	1	1
21	-2.285	0.971	0.490	1	1	1	1
22	-2.343	-5.690	0.307	1	1	1	1
23	0.546	-0.199	0.257	0.6	0.6	1	1
24	-2.804	1.166	0.470	0.6	1	1	1
25	-2.804	1.166	0.468	0.6	1	1	1
26	-6.916	-2.824	0.136	1	1	1	1
27	-6.652	-2.485	0.145	1	1	1	1
28	-6.802	-22.172	0.129	1	1	1	1
29	0.546	-0.199	0.715	1	1	1	1
30	-3.675	1.616	0.761	1	1	1	1
31	-3.698	-25.215	0.115	0.6	1	1	0.6
32	-4.239	-25.215	0.092	1.0	0.6	1	0.6
33	-5.843	-20.397	0.159	1	1	1	1
34	-0.137	0.510	0.479	0.6	1	1	1
35	-2.710	-62.428	0.152	1	1	1	0.6
36	-4.786	-85.493	0.110	1	1	1	0.6
37	-5.517	-12.966	0.029	0.6	0.6	0.6	0.8
38	-4.692	-31.650	0.078	0.6	0.6	1	1
39	-2.940	-5.300	0.183	1	0.6	1	0.8
40	-2.287	-14.225	0.443	1	1	1	1
41	-1.429	0.357	0.770	1	1	1	1
42	-4.571	-27.756	0.179	1	1	0.8	1
43	-4.030	-27.756	0.227	1	0.6	0.8	1
44	-1.197	-2.783	0.520	1	1	1	1
45	-1.638	-11.157	0.232	1	1	0.6	0.8
46	-6.903	-1.062	0.141	1	1	1	1
47	-2.158	-15.377	0.108	0.6	0.8	0.8	0.6
48	-2.212	1.073	0.498	0.6	1	1	1
49	-1.467	-1.097	0.815	1	1	1	1
50	-0.740	0.122	0.269	0.6	1	1	1
51	-1.763	1.921	0.871	1	1	1	1
52	-1.703	0.507	0.782	1	1	1	1
53	-2.398	3.305	0.573	1	1	1	1
54	-0.833	0.370	0.782	1	1	1	1
55	-2.921	1.072	0.799	1	1	1	1
56	-2.873	2.073	0.830	1	1	1	1
57	-1.681	0.271	0.350	1	1	1	0.6
58	-1.496	0.172	0.702	1	1	1	1
59	-2.855	1.208	0.472	0.6	1	1	1
60	-2.49	1.595	0.299	0.6	0.6	1	1
61	-5.907	-1.175	0.196	1	1	1	1

Ligand	log S	Drug likeness	Drug score	Toxicity			
				Mutagenic	Tumorigenic	Reproductive	Irritant
62	-1.063	-11.18	0.492	1	1	1	1
63	-6.802	-22.172	0.129	1	1	1	1
64	-0.175	-3.318	0.306	1	1	1	1
65	-3.917	-10.073	0.496	1	1	1	1
66	-4.010	-26.101	0.275	1	1	1	1
67	-6.669	-4.475	0.134	1	1	1	1
68	-6.492	1.391	0.148	1	1	0.6	1
69	-0.570	-0.990	0.630	1	1	1	1
70	-1.132	-6.762	0.484	1	1	1	1
71	-3.162	-0.597	0.612	1	1	1	1
72	-3.480	1.221	0.752	1	1	1	1
73	-3.100	1.506	0.189	0.6	0.8	0.6	0.8
74	-1.220	-6.126	0.481	1	1	1	1
75	-0.138	-10.743	0.493	1	1	1	1
76	-1.695	-5.658	0.490	1	1	1	1
77	-2.706	-4.703	0.451	1	1	1	1
78	-2.009	-3.928	0.288	0.6	1	1	1
79	-3.304	-4.703	0.445	1	1	1	1
80	-3.903	-4.703	0.426	1	1	1	1
81	-1.439	-5.783	0.293	1	1	0.6	1
82	-0.199	-8.163	0.492	1	1	1	1
83	-2.828	-2.342	0.472	1	1	1	1
84	-1.126	-1.971	0.330	1	1	1	0.6
85	-0.779	-5.900	0.489	1	1	1	1
86	-3.455	-6.889	0.126	0.8	0.6	1	0.6
87	-3.303	-8.672	0.267	1	1	1	0.6
88	-2.265	-4.467	0.474	1	1	1	1
89	-1.730	-0.117	0.707	1	1	1	1
90	-1.313	1.423	0.585	1	1	1	1
91	0.302	-7.541	0.495	1	1	1	1
92	-2.863	-4.467	0.467	1	1	1	1
93	-2.131	-1.587	0.544	1	1	1	1
94	-2.724	-2.387	0.487	1	1	1	1
95	-2.881	-3.666	0.473	1	1	1	1
96	-3.460	-3.732	0.459	1	1	1	1
97	-0779	-5.900	0.489	1	1	1	1
98	-1.382	-13.766	0.475	1	1	1	1
99	-1.138	-0.852	0.635	1	1	1	1
100	-1.174	0.592	0.800	1	1	1	1
101	-2.315	2.632	0.920	1	1	1	1
102	-1.592	1.391	0.876	1	1	1	1
103	-0.133	1.205	0.875	1	1	1	1
104	-3.620	0.018	0.395	1	1	1	1
105	-1.714	-0.956	0.610	1	1	1	1

lead compounds with excellent drug safety profiles

Table 30. Toxicity Predictions of Selected Ligands of AP, TA, BF, DS and OSC using Toxtree

Ligand	Crammer's class	Skin sensitization	Genotoxic carcinogenicity	Potential carcinogenicity	Ligand	Crammer's class	Skin sensitization	Genotoxic carcinogenicity	Potential carcinogen
1	Low	no	no	no	54	Intermediate	no	no	no
2	High	yes	yes	no	55	High	no	no	no
3	Low	yes	no	no	56	High	yes	no	no
4	High	yes	no	no	57	Intermediate	yes	no	no
5	High	no	no	no	58	Intermediate	yes	no	no
6	High	no	no	no	59	High	yes	no	no
7	High	yes	no	no	60	High	yes	no	no
8	High	yes	no	no	61	High	no	no	no
9	High	yes	no	no	62	High	no	no	no
10	High	yes	no	no	63	Low	no	no	no
11	High	yes	no	no	64	Low	no	no	no
12	Low	no	no	no	65	High	no	no	no
13	Low	no	no	no	66	Low	no	no	no
14	Low	no	no	no	67	High	no	no	no
15	High	yes	no	no	68	High	yes	yes	no
16	High	yes	no	no	69	High	no	no	no
17	High	yes	no	no	70	Intermediate	no	no	no
18	High	yes	no	no	71	High	no	yes	no
19	High	yes	no	no	72	High	no	no	no
20	Low	no	no	no	73	High	no	yes	no
21	High	yes	no	no	74	High	no	no	no
22	High	yes	no	no	75	High	no	no	no
23	Low	no	yes	no	76	High	no	no	no
24	High	yes	yes	no	77	High	no	no	no
25	High	no	yes	no	78	Intermediate	no	no	no
26	Low	no	yes	no	79	High	no	no	no
27	Low	no	yes	no	80	High	no	no	no
28	Low	no	yes	no	81	High	no	no	no

Ligand	Crammer's class	Skin sensitization	Genotoxic carcinogenicity	Potential carcinogenicity	Ligand	Crammer's class	Skin sensitization	Genotoxic carcinogenicity	Potential carcinogen
29	High	no	yes	no	82	High	no	no	no
30	High	yes	yes	no	83	High	no	no	no
31	Low	no	no	no	84	Low	no	no	no
32	Low	no	no	no	85	High	no	no	no
33	Low	no	no	no	86	High	yes	yes	no
34	High	no	no	no	87	High	no	yes	no
35	High	no	no	no	88	High	no	yes	no
36	High	no	no	no	89	High	yes	yes	no
37	Low	no	yes	no	90	High	no	yes	no
38	High	yes	no	no	91	High	no	yes	no
39	Low	no	no	no	92	High	no	yes	no
40	High	no	no	no	93	Low	no	yes	no
41	Low	no	yes	no	94	High	no	yes	no
42	Low	no	no	no	95	High	no	yes	no
43	Low	no	no	no	96	High	no	yes	no
44	High	yes	no	no	97	High	no	yes	no
45	High	yes	no	no	98	High	yes	yes	no
46	High	yes	no	no	99	High	no	yes	no
47	High	yes	no	no	100	Low	yes	yes	no
48	Low	yes	no	no	101	High	no	no	no
49	Low	no	no	no	102	High	no	no	no
50	Low	no	no	no	103	High	no	yes	no
51	Low	no	no	no	104	High	no	yes	no
52	High	no	no	no	105	High	yes	yes	no
53	High	no	no	no					

4.5.3 Molecular docking Studies

Medicinal plant based bioactive compounds offers therapeutic role in the management of Type 2 diabetes by modifying the metabolic pathways, delaying the progression of diabetic complications, and restoring glycemic balance **(Howes and Simmonds, 2005)**. Prabhakar and Doble proposed the mechanisms of antidiabetic action for plant extracts, have an ability to stimulate insulin secretion **(Prabhakar and Doble, 2011)**. Target of interest associated with serine protease dipeptidyl peptidase (DPP-IV), which cleaves N-terminal dipeptides from DPP-IV substrates such as GLP-1 (Glucagon like peptide -1) and GIP (glucose-dependent insulinotropic polypeptide), containing proline or alanine based secondary residues **(Havale and Pal, 2009**). Therefore, these peptide cleavage results in inactivation or reduces the insulin stimulation **(Mentlein *et al.*,1993; Holst, 2007; Drucker, 2007)**.

In this study, the selected ligands from *Amphilophium paniculatum* (AP), *Tristellateia australasiae* (TA), *Haematocarpus validus* (BF), *Phoenix dactylifera* (DS) and organo sulphur compounds from garlic (OSC) were evaluated using molecular docking against the target DPP-IV (PDB ID: 2RIP), using Hex software and further validated using commercially available Maestro Schrodinger software. Molecular docking helps to predict the binding affinity of each ligand to the active site of DPP-IV, thereby knowing the potential lead compounds with high binding efficiency with the standard drug metformin. The ligands showing the higher negative binding energy or docking score considered to exhibit stronger interactions as DPP-IV inhibitors for further drug development against Type 2 diabetes.

Initially, the molecular docking of ligands from AP, TA, BF, DS and OSC was performed using Hex software to evaluate their binding affinity against DPP-IV enzyme. The binding energy scores of 103 ligands against DPP-IV target was performed using Hex software are summarized in **Table 31.**

Table 31. Molecular Docking Interaction of Selected Ligands from AP, TA, BF, DS and OSC using HEX

Ligand	E Total value (kcal/mol)	Ligand	E Total value (kcal/mol)	Ligand	E Total value (kcal/mol)
1	-218.52	36	-180.58	71	-161.29
2	-152.77	37	-233.77	72	-212.24
3	-186.91	38	-168.61	73	-190.39
4	-138.68	39	-149.34	74	-146.64
5	-167.52	40	-207.88	75	-144.07
6	-289.19	41	-121.53	76	-141.91
7	-232.61	42	-209.05	77	-138.90
8	-291.81	43	-215.51	78	-116.10
9	-252.54	44	-145.04	79	-132.57

Ligand	E Total value (kcal/mol)	Ligand	E Total value (kcal/mol)	Ligand	E Total value (kcal/mol)
10	-275.61	45	-147.93	80	-160.09
11	-309.23	46	-244.09	81	-120.49
12	-204.72	47	-225.92	82	-158.93
13	-207.82	48	-153.56	83	-138.90
14	-194.69	49	-228.28	84	-86.67
15	-360.24	50	-126.49	85	-146.27
16	-259.39	51	-213.96	86	-181.77
17	-200.94	52	-159.39	87	182.44
18	-202.15	53	-332.87	88	-111.41
19	-223.30	54	-147.01	89	-160.52
20	-180.48	55	-78.73	90	-117.98
21	-268.71	56	-103.38	91	-149.57
22	-311.04	57	-142.00	92	-132.39
23	-147.08	58	-213.67	93	-116.10
24	-212.29	59	-200.94	94	-135.21
25	-222.77	60	-116.76	95	-136.56
26	-210.48	61	-218.04	96	-178.62
27	-203.01	62	-119.35	97	-121.51
28	-206.93	63	-207.13	98	-201.78
29	-147.08	64	-110.07	99	-138.90
30	-199.29	65	-117.47	100	-159.26
31	-169.24	66	-196.33	101	-132.31
32	-177.04	67	-231.94	102	-125.72
33	-166.16	68	-204.25	103	-158.33
34	-129.33	69	-101.81		
35	-219.79	70	-210.12		

Molecular docking results obtained for the AP ligands (ligand 1 to 22), ligand 15 exhibited the strongest binding energy score of -360.24 kcal/mol**,** followed by ligand 11 (-309.23 kcal/mol), and ligand 22 (-311.04 kcal/mol), which indicates high potential for DPP-IV inhibition. For TA (ligands 23 to 30), ligand 30 possess more negative binding energy score of -199.29 kcal/mol, against DPP-IV. In BF (ligand 31 to 53), the ligand 53 showed excellent binding energy of -332.87 kcal/mol, suggesting the strong inhibitory interaction with the target enzyme. In addition, the DS (ligands 54 to 68), ligand 58 (-213.67 kcal/mol) and ligand 61 (-218.04 kcal/mol), exhibited moderate to strong binding energy potential. For OSC compounds (ligand 69 to 102), most of the ligands exhibited higher negative energy score, compared with standard metformin (-158.33 kcal/mol). Notably, the ligand 72 (-212.24 kcal/mol), ligand 70 (-210.12 kcal/mol) and ligand 92 (-201.78 kcal/mol) exhibited strong interactions with the target enzyme.

To further validate the docking results obtained from initial screening of ligands using Hex software, the top performing ligands from each group (AP, TA, BF, DS and OSC) were

subjected to molecular docking using the commercially available Schrodinger software suite. The OPLS molecular mechanics force field helps to evaluate the physical interactions, predicting molecular conformations, geometry, and ligand-protein binding process, including Vander Waals forces and electrostatic interactions within or between molecules. With OPLS external support more reliable molecular docking process, optimises the position and conformation of ligands within the active binding site to determine the structure-based drug discovery **(Roos *et al.*,2019)**.

The molecular docking results from Schrodinger software given in **Table 32**, revealed the docking score of selected ligands from AP, TA, BF, DS and OSC with the DPP-IV target enzyme. The results show that AP ligand 22 exhibited the strongest binding, with a docking score of -6.783 kcal/mol. This was followed by ligand 10 (Linarin), ligand 21 (Acetoside) and ligand 15 (Glucopyranoside), representing the stable interactions within the active site of target protein. Compound 22 belongs to lignan class, a polyphenolic compounds commonly present in various plant sources **(Xu *et al.*, 2008; Suhikh *et al.*, 2023; Wang *et al.*, 2015; Jafari *et al.*, 2022)**. Similarly, Linarin, a major flavonoid has been identified as a promising therapeutic drug for the management of Type 2 diabetes **(Wang *et al.*, 2022)**.

For TA, ligand 30 (flavanol) possess better docking score of -6.488 kcal/mol, with the target enzyme. The Flavonol glycosides from *Cleome droserifolia*, inhibited the DPP-IV enzyme with better IC_{50} compared to standard vildagliptin **(Motaal *et al.*, 2020)**. In BF, ligand 53 (Rutin) possess better docking score of -6.898 kcal/mol, which are reported to be strong potential DPP-IV inhibitor. Similar reports on Rutin and Morin revealed as inhibitors in blocking the enzymes and receptor which contributes to diabetes development **(Kerry *et al.*, 2025)**. Among the DS ligands, ligand 59 (Apigenin), showed the docking score of -5.983 kcal/mol, and especially Rutin which is also present in dates seed possess promising interactions. The literature report on Apigenin and Isorhamnetin based flavonoid which effectively binds to the active site of target and act as potential DPP-IV inhibitor **(Onyeka, 2025; Kalai *et al.*, 2022)**. In organo sulphur based compounds (OSC), the modified structure of ligand 72 (N-[(3,3-dimethyl piperidin-2-yl)methyl]-4-ethyl sulphonyl aniline) possess the docking score of -3.391 kcal/mol. These docking scores obtained from the selected bioactive compounds of AP, TA, BF, DS and OSC were comparable with the metformin's docking score of -5.010 kcal/mol, considered to be potent natural DPP-IV inhibitor with promising therapeutic potential for managing Type 2 diabetes, by offering safer alternative to conventional drugs. **Table 33** represents comparative binding interactions of ligands with DPP-IV.

The molecular docking of selected phytocompounds such as ligand 10, ligand 22, ligand 30, ligand 53, and ligand 72 against DPP-IV target enzyme, exhibited binding interactions, and were compared with metformin (ligand 103). The above ligands were found to have better docking scores, suggested to have strong molecular binding interaction affinity towards to the active site of DPP-IV. In particularly, the ligand 53 (Rutin) stands the most favourable binding score (-6.898 kcal/mol), the multiple hydroxyl groups on the Rutin structure formed numerous hydrogen bonds with amino acid residues such as ARG 356, ARG 358, GLU 205, GLU 206 and SER 209, indicating strong polar and aromatic interactions, which leads to stable binding within the active site of DPP-IV. **Figure 68** represents the molecular docking pose of ligand 53 and its 2D residue interactions with amino acid of DPP-IV enzyme. Similarly, the ligand 22 showed good binding score of -6.783 kcal/mol, due to hydrogen bond interactions with SER 209, GLU 205, ARG 669, ASN 710, and ARG 358, as well as π–π stacking interactions of PHE 357 and TYR 547, which are aligned parallel with the phenyl ring of ligand 22. Docking pose and 2D interaction of ligand 22 with DPP-IV active site are shown in **Figure 67.**

The ligand 10 (Linarin), possess docking score of -6.621 kcal/mol, formed hydrogen bonds with the active residues including GLU 205, ARG 358 and SER 360. The glyosidic chain with hydroxyl groups undergoes additional hydrogen bonding interactions with the active site residues, enhances the binding affinity of ligand-protein interactions **(Figure 66)**. Similarly, TA bioactive compound Flavonol (ligand 30) showed a docking score of -6.488 kcal/mol, the two-hydroxyl group on the Flavonol structure formed hydrogen bonding interactions with GLU 205 and GLU 206. The ligand (59) Apigenin showed slightly lower docking score of -5.983 kcal/mol, with hydrogen bond interactions with amino residues of GLU 205, GLU 206, CYS 551, and TYR 585.

The ligand 72 possess lower binding score of -3.391 kcal/mol, which are due to few polar interactions and hydrophobic stabilisation. The π–π stacking interaction was observed between PHE 357 and aromatic ring of ligand 72, and hydrogen bond interactions were observed, where NH_2^+ group formed bonds with residue GLU 206 and GLU 205, though NH bonding was directed toward GLU 206. From the 2D interactions of ligand 10, 22, 30, 39, 53 and 72 with DPP-IV, exhibited phenylalanine residue (PHE 357) around the active site, favours the ligand stability within the binding pocket and results in better binding affinity. The ligand 22 and 72 aligned with PHE 357, suggesting π–π stacking, while bulky groups in Linarin, Apigenin, Flavonol and Rutin contributes to additional hydrophobic surroundings.

The clinically used antidiabetic drug metformin (ligand 103), showed a moderate docking score of -5.01 kcal/mol, with the formation of hydrogen bond interaction were observed between the three NH_2 interlinkage with GLU 206, GLU205 and TYR 666 amino acid residues **(Figure 69)**. The overall interactions of ligands with DPP-IV, the ligand 53 and ligand 22 exhibited better lead compounds followed by Linarin, Apigenin, and sulphur-based compounds for further anti-diabetic drug development. Further, structure-activity relationship analysis, pharmacokinetic profiling, and structural optimisation are required due to limited bioavailability of natural compounds such as glycosylated flavonoids. Therefore, by enhancing the stability, absorption and therapeutic potential of lead compounds could be more effective and suitable for clinical development as DPP-IV inhibitors in Type 2 diabetes.

From the overall results, the selected bioactive compounds from Amphilophium paniculatum, Tristellateia australasiae, Haematocarpus validus, Phoenix dactylifera, and organo-sulphur compounds were found to be potential DPP-IV inhibitors for managing Type 2 diabetes. *To validate the above findings, further steps includes are the selection, extraction and separation of active compounds, followed by in vitro, in vivo studies, toxicity profiling and anti-diabetic mechanism beyond in silico DPP-IV inhibition are essential to utilise their therapeutic value and safety.*

Table 32. Molecular Docking Interaction of Selected Best Ligands from AP, TA, BF, DS and OSC using Maestro Schrodinger

Ligand	Docking score (kcal/mol)	Ligand	Docking score (kcal/mol)	Ligand	Docking score (kcal/mol)
6	-4.585	25	-3.276	51	-6.396
8	-4.955	26	-3.215	**53**	**-6.898**
9	-5.439	27	-3.663	58	-4.696
10	**-6.621**	28	-2.988	**59**	**-5.983**
11	-5.982	29	-5.148	61	-4.029
15	-5.674	**30**	**-6.488**	66	-2.430
16	-5.090	35	-2.406	67	-3.174
17	-5.983	37	-4.146	68	-4.066
21	-6.160	42	-4.271	72	-3.391
22	**-6.783**	43	-3.614	103	-5.010
23	-4.876	46	-4.836		
24	-6.033	49	-6.271		

Table 33. Represents Comparative Amino Acid Interactions with Selected Ligands and Metformin in DPP-IV active sites, Docking Scores and Molecular type interactions

Ligand	Compound Name	Docking score (kcal/mol)	Interactions
10	Linarin	-6.621	[GLU 205, ARG 358, SER 360] – H-bond
22	(+)-Lyoniresinol-3α-O-β-D-Glucopyranoside	-6.783	[SER 209, GLU 205, GLU 206, ARG 669, ASN 710, ARG 358] – H bond [PHE 357, TYR 547]- π-π stacking
30	Flavonol	-6.488	[GLU 205, GLU 206] – H bond
53	Rutin	-6.898	[GLU 206, GLU 205, SER 209, ARG 356 ARG 358] – H-bond
59	Apigenin	-5.983	[GLU 205, GLU 206, CYS 551, TYR 585] – H bond
72	N-[(3,3-dimethyl piperidin-2-yl)methyl]-4-ethyl sulphonyl aniline	-3.391	[GLU 205, GLU206] – H bond PHE 357 - π-π stacking
103	Metformin	-5.010	[GLU 205, GLU 206, TYR666] – H bond

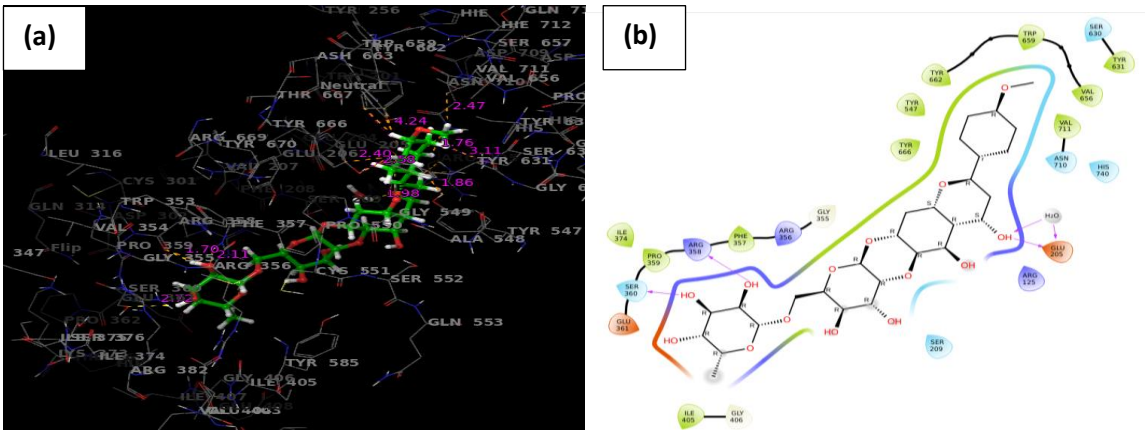

Figure 66. Docking orientation of ligand 10 within the target DPP-IV (2RIP) (a); 2D schematic showing interactions between ligand 10 and amino acid residues of the active site (b)

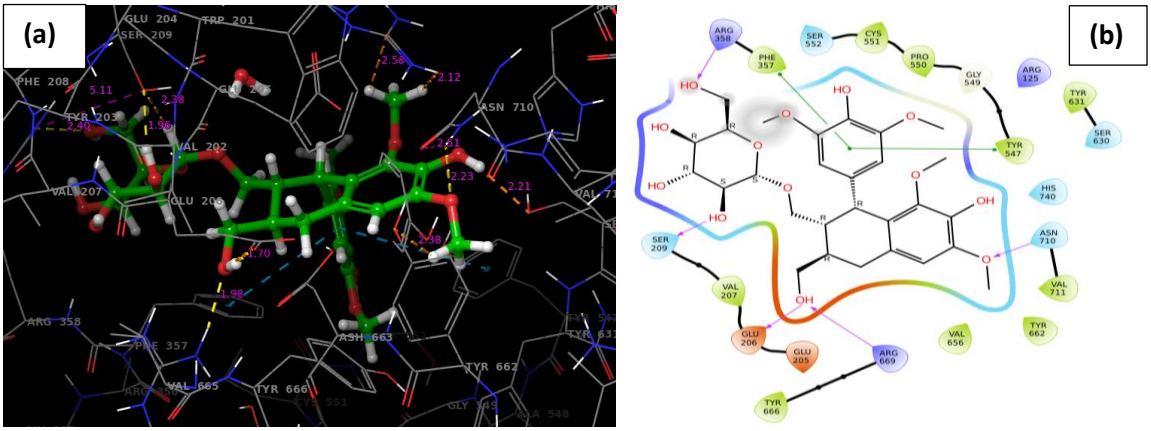

Figure 67. Docking orientation of ligand 22 within the target DPP-IV (2RIP) (a); 2D schematic showing interactions between ligand 22 and amino acid residues of the active site (b)

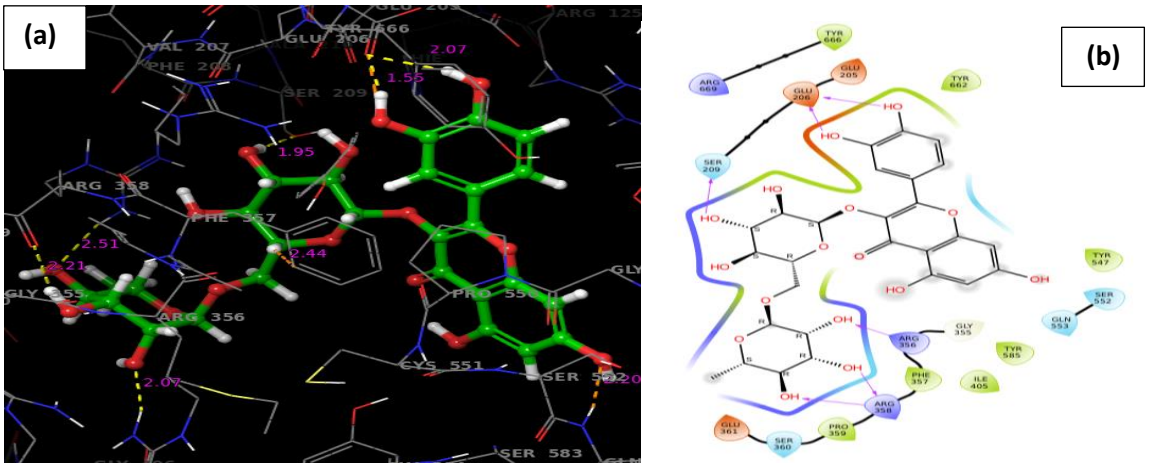

Figure 68. Docking orientation of ligand 53 within the target DPP-IV (2RIP) (a); 2D schematic showing interactions between ligand 53 and amino acid residues of the active site (b)

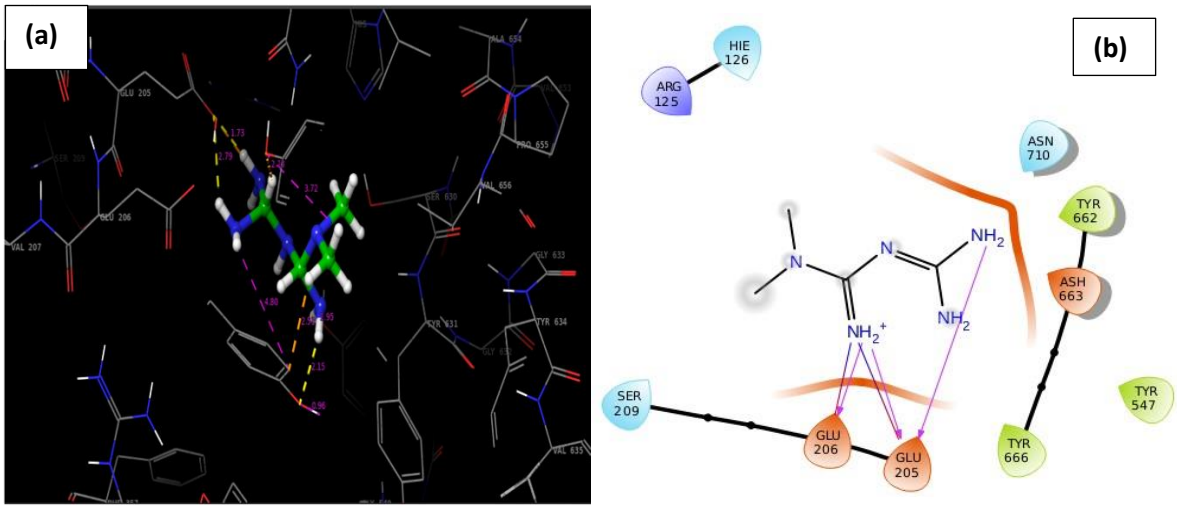

Figure 69. Docking orientation of metformin within the target DPP-IV (2RIP) (a); 2D schematic showing interactions between metformin and amino acid residues of the active site (b)

Phase -V *In vitro* Selected Biomedical Applications of Plant Extracts and Synthesised Metallic Nanoparticles

4.6 *In vitro* Biomedical Applications of Extracts and Synthesised Metallic Nanoparticles

4.6.1 Antioxidant Activity of Plant Extracts and Synthesised Metallic Nanoparticles

Antioxidant assessments are essential for protecting cells from oxidative damage, which is a contributing factor to various chronic diseases. In this study, we investigated the antioxidant potential of four selected plant extracts and their synthesised metallic NPs (GNPs and SNPs) using *in vitro* DPPH assay. DPPH assay is commonly used reliable and rapid method for

assessing the free radical scavenging potential of antioxidant molecules through colorimetric or spectrophotometric method. DPPH in methanolic solution is a stable free radical which exhibits purple colour and reduced to yellow with the presence of antioxidants, which is measured at a wavelength of 517 nm **(Kedare and Singh, 2011)**.

The antioxidant assay was performed for four different plant extracts, GNPs and SNPs, at varying concentrations (5-375 µg/mL). Ascorbic acid (vitamin C) was used as standard at five different concentrations (3-15 µg/mL). The ascorbic acid exhibited the percentage inhibition ranging from 62.3% at 3 µg/mL to 95.9% to 15 µg/mL, as presented in **Figure 70a**. The antioxidant activity for the solvent based extracts of AP, TA, BFE and DSE are shown in **Figure 70b**. The results revealed that all samples were found to be dose-dependent antioxidant effect, with the significant free radical scavenging even at the lowest concentrations.

Among the AP and TA extracts, the ethanolic extracts of APE and TAE showed maximum radical scavenging effects, with 80.3% and 93.4% inhibition at 375 µg/mL, respectively. The methanolic and ethyl acetate extracts of AP and TA exhibited comparatively lower activity. Similarly, BFE and DSE extracts showed higher inhibition with 59.02% at 375 µg/mL for BFE and 94.26% at 75 µg/mL for DSE. These results suggested the polarity of extracts and their secondary metabolites influence on antioxidant potential, with greater scavenging activity for more polar based extracts. The percentage inhibition obtained for the above results confirmed that the ethanolic extracts from four plants were found to be more potent and act as free radical scavengers or hydrogen donors. Hence, the antioxidant-rich ethanolic extracts of APE, TAE, BFE and DSE were utilised to synthesise GNPs and SNPs.

The antioxidant scavenging potential of the synthesised GNPs and SNPs and their results are shown in **Figure 71**. The synthesised GNPs exhibited dose-dependent maximum scavenging potential with 59.02% inhibition for APEG at 75 µg/mL; 54.92% for TAEG at 75 µg/mL; 59.02% for BFEG at 125 µg/mL; 77.87% for DSEG at 125 µg/mL. In comparison, the SNPs exhibited higher activity, with 91.8% inhibition for APES at 125 µg/mL; 81.15% for TAES at 375 µg/mL; 72.95% for BFES at 375 µg/mL; and 87.7% for DSES at 75 µg/mL. **Table 34** exhibits the % scavenging potential and IC_{50} values of plant extracts and their synthesised GNPs and SNPs. The free radical scavenging activity, as indicated by IC_{50} values, the SNPs exhibited highest antioxidant activity, followed by GNPs and plant extract, which attributed to large surface area of SNPs, providing more active sites for interactions with free radicals. The results were comparable to the IC_{50} value of ascorbic acid (9.30 µg/mL), which aligns closely with the values reported in earlier studies **(James *et al.*, 2011)**. Based on the overall results, among the

synthesised GNPs and SNPs, BFEG (10.37 µg/mL), DSEG (28.92 µg/mL), APES (29.14 µg/mL), TAES (128.87 µg/mL), BFES (122.17 µg/mL), and DSES (26.98 µg/mL) exhibited lower IC_{50} values, indicating maximum free radical scavenging activity.

The increased radical scavenging activity may be due to the presence of secondary metabolites (biomolecules) in the plant extracts such as flavonoids, polyphenols, anthraquinones, and alkaloids, which are embedded or bind on the surface of metal NPs and exhibit synergistic action in redox mechanism. Therefore, DPPH radical interacts with biomolecules containing hydroxyl groups of phenols and flavonoids, undergoes reduction mechanism. The hydrogen atom abstraction from phenolic hydroxyl group to the DPPH radical (DPPH•), results in neutralisation of DPPH radical and transforming into a stable structure (DPPH-H). The extent of colour change from purple to pale yellow indicates the antioxidant potential of the molecules **(Gulcin and Alwasel, 2023)**.

Earlier antioxidant studies reported that extract of *Arctium lappa* and their gold and silver NPs, exhibit maximum inhibition potential for SNPs compared to GNPs **(Lafta *et al.*, 2025)**. According to research by Soliman *et al.,* SNPs possess higher antioxidant activity with a lower IC_{50} value of 19.7 µg/mL, compared to GNPs with 194.0 µg/mL **(Soliman *et al.*, 2010)**. In addition, strong DPPH efficacy was reported for SNPs with an IC_{50} of 30.04 µg/mL **(Mohanta *et al.*, 2017)**.

From the antioxidant activity, it was observed that all four ethanolic plant extracts and their GNPs and SNPs were found to have better inhibition potential against free radicals. Among them, SNPs exhibited higher inhibition as compared to GNPs, suggesting that SNPs more effectively enhances the free radical scavenging activity than GNPs. These results suggested that the plant derived NPs acts as effective antioxidant for therapeutic and biomedical applications, by combating the oxidative stress related diseases.

(a)

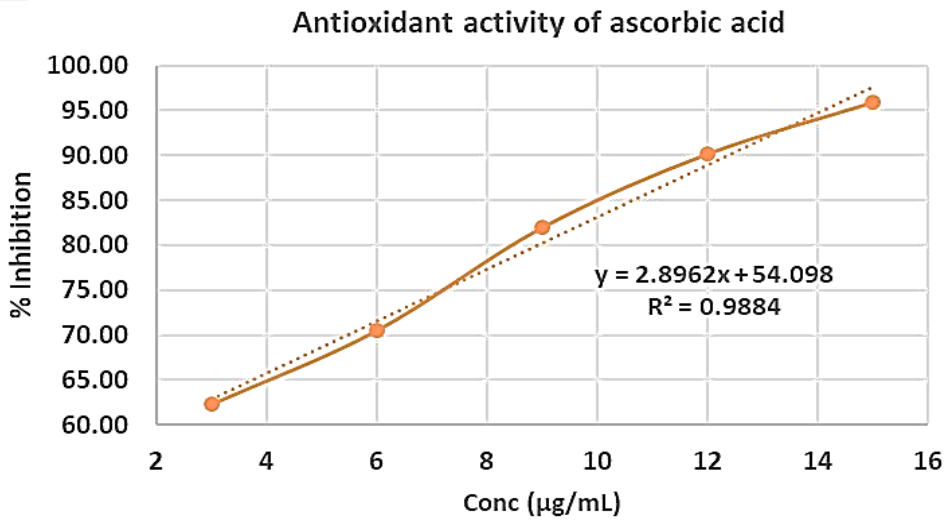

(b)

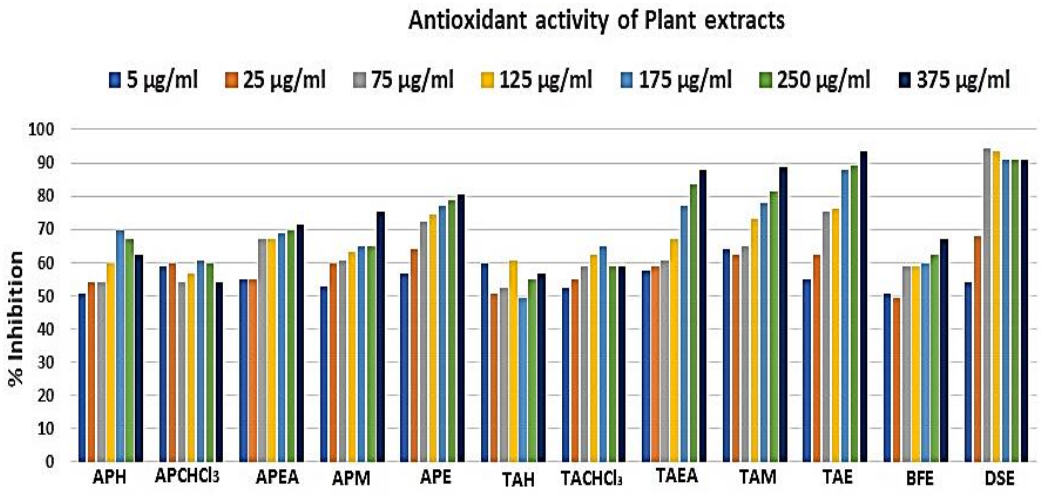

Figure 70. Calibration curve for ascorbic acid at five different concentration (a); Antioxidant free radical scavenging assay of four selected plant extract (b)

Table 34. Antioxidant Free Radical Scavenging Assay of Extracts and Metallic Nanoparticles

Concentration of sample (µg/mL)	Scavenging activity % of plant extract and their synthesised GNPs and SNPs											
	AP (% inhibition)			TA (% inhibition)			BF (% inhibition)			DS (% inhibition)		
	APE	APEG	APES	TAE	TAEG	TAES	BFE	BFEG	BFES	DSE	DSEG	DSES
5	56.56	50.82	56.56	54.92	52.46	52.46	50.82	48.36	50.82	54.1	48.36	52.46
25	63.93	54.1	68.85	62.3	52.46	57.38	49.18	50.82	54.92	68.03	59.02	60.66
75	72.13	59.02	81.15	75.1	54.92	62.3	59.02	50.82	57.38	94.26	68.85	87.7
125	74.59	57.38	91.8	76.23	54.92	63.93	59.02	59.02	60.66	93.44	77.87	85.25
175	77.05	50.82	89.34	87.7	54.1	74.59	59.84	56.56	67.21	90.98	77.87	81.15
250	78.69	49.18	86.89	89.34	52.46	78.69	62.3	52.46	67.21	90.98	70.49	68.03
375	80.33	48.36	79.51	93.44	44.26	81.15	67.21	50.82	72.95	90.98	69.67	63.93
IC_{50} (µg/mL)	39.86	188.06	29.14	73.08	264.8	128.87	63.88	10.37	122.17	26.41	28.92	26.98

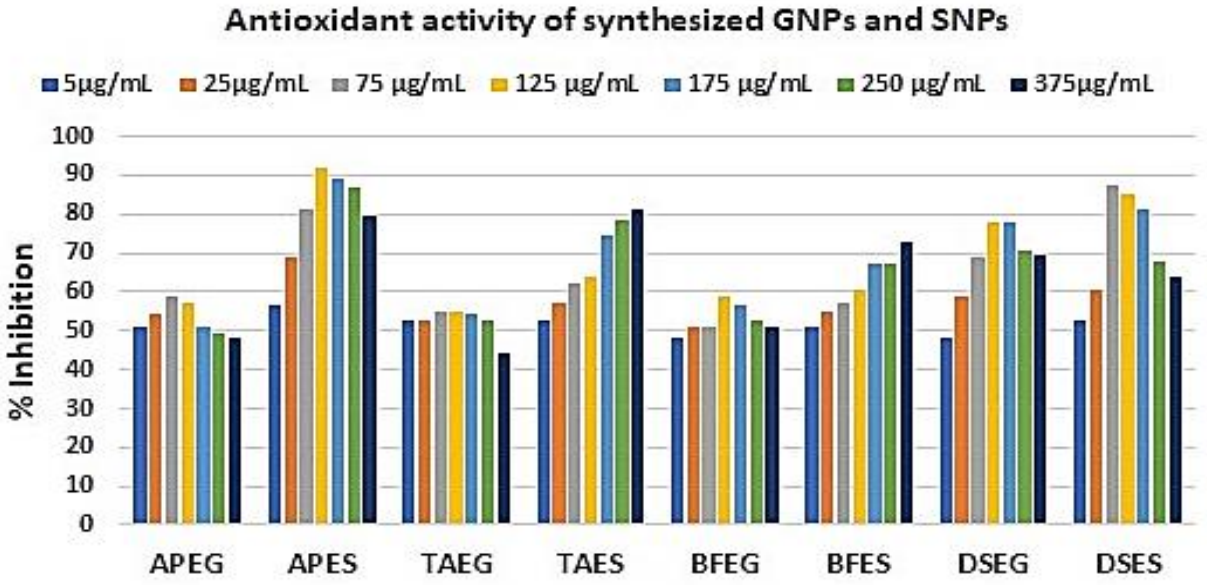

Figure 71. Antioxidant free radical scavenging assay of four selected ethanolic extracts and synthesised GNPs and SNPs

4.6.2 Antibacterial Activity of Extracts and Biosynthesised Metallic Nanoparticles

An in-depth investigation on the literature reports and traditional knowledge on the use of AP, TA, and BF has been outlined in chapter 2. There is research gap on the antibacterial activity of the GNPs and SNPs synthesised from AP, TA and BF extracts, and hence the study intended to test the antibacterial properties. The commercially available drug ciprofloxacin, a broad-spectrum antibiotic which was used as standard for comparing the prepared samples against microbial strains.

The choice of bacterial strains utilised in this study includes *S. aureus*, and *B. cereus* which represent gram-positive bacteria, while *K. pneumoniae, P. aeruginosa* and *E. coli*, represent gram-negative bacteria; was chosen due to their relevance to human infections and microbial resistance concerns. The differences between the gram-positive and gram-negative bacteria include cell wall structure, response to gram staining, outer membrane, and susceptibility to antibiotics. Gram-positive bacteria do not have an outer membrane, and are more susceptible to antibiotics which target the thick peptidoglycan layer (20-80 nm) in the cell wall. In contrast, gram-negative bacteria having a thin peptidoglycan layer (<10 nm), along with addition of outer membrane (lipopolysaccharides) in the cell wall, provides bacterial susceptibility to antibiotics. Therefore, the variations in the bacterial cell membrane structure possess different properties to the cell, and impact to external stresses like heat, UV radiations and antibiotics **(Mai-Prochnow *et al.*, 2016)**.

Table 35. Antibacterial Activity of Extracts and Metallic Nanoparticles

Sample code	Zone of Inhibition (mm)				
	S. aureus	***B. cereus***	***K. pneumoniae***		***E. coli***
Std CIP	22	21	20		22
APE	10	-	-		8
APEG	**15**	12	11		11
BFE	12	9	-		-
BFEG	13	**14**	12		12
BFES	**15**	11	11		12
TAE	13	9	8		9
TAEG	9	**15**	11	***P. aeruginosa***	**15**
TAES	10	12	10		12
Std CIP	13	16	13		15
Clinically isolated bacteria					
APEG	-	*	-		*
APES	**18**	*	**14**		*
Std CIP disk	24	*	16		*

(-) represents no zone of inhibition; (*) represents not performed for the particular strain; Std CIP – standard ciprofloxacin drug; Std CIP disk - commercially available standard disk loaded with 5 µg ciprofloxacin drug against clinically isolated strains.

Table 35 showed the ZOI obtained for the samples against the gram-positive and gram-negative bacteria. From the results, *S. aureus* and *B. cereus* was found to be susceptible to extracts, GNPs and SNPs, except APE ethanol extract possess no zone against *B. cereus*. Similarly, *K. pneumoniae and E. coli* was found to be susceptible to the extracts, GNPs and SNPs, except APE, and BFE extracts possess no zone against *K. pneumoniae.* Also, BFE extract possess no inhibition against *E. coli* **(Figure 72 and 73)**.

In brief, APE ethanol extract (1 mg/mL) exhibited ZOI of 10 mm and 8 mm against *S. aureus* and *E. coli*; and not susceptible to *B. cereus* and *K. pneumoniae*. APE synthesised GNPs were tested against gram-positive and gram-negative bacterial strains. APEG exhibited ZOI of 15 mm for *S. aureus*; 12 mm zone for *B. cereus* and 11 mm zone for *K. pneumonia* and *E. coli*. The results are compared with the extract and APEG NPs, indicate that the APE extract-mediated GNPs have exhibit superior antibacterial activity against both gram-positive and gram-negative bacteria. ZOI obtained for the APE and APEG in comparison with the standard are given in **Figure 72 and 73**. Similarly, we have tested both APEG NPs and APE SNPs against clinically isolated bacterial microorganisms such as *S. aureus* and *K. pneumoniae* by disk diffusion method. The standard ciprofloxacin drug loaded (5 µg) commercial disk was utilised to compare the efficacy of NPs.

From the results, APES NPs exhibited good inhibition of 18 mm for *S. aureus* and 14 mm for *K. pneumoniae*, in comparison with the zone obtained for standard (24 mm for *S. aureus* and 16 mm for *K. pneumoniae*). There is absence of zone for APEG NPs against clinical pathogens. From these results, it was noteworthy that APES NPs were well comparable with the standard against *K. pneumoniae*, rather than *S. aureus*. In general, *K. pneumoniae* is significantly associated with pneumonia and lung infections. Therefore, these NPs were further examined with lung cancer cell lines. The clinically isolated microorganisms such as *K. pneumoniae*, and *S. aureus* were tested with standard drug and APES NPs are given in **Figure 76**, *via* disc diffusion method. Therefore, the findings suggest that APES NPs may serve as effective antibacterial agents, with the potential to control drug-resistant bacterial strains. Similar studies have also reported enhanced antimicrobial activity of SNPs against various bacterial pathogens **(Akter *et al.*, 2020; Hovhannisyan *et al.*, 2022)**.

The agar-well diffusion method was performed for evaluating the antibacterial potential of following samples namely TAE, and BFE extracts at 1 mg/mL concentration and their synthesised metallic NPs such as TAEG, TAES, BFEG and BFES. TAE against gram-positive (*S. aureus and B. cereus*) and gram-negative (*K. pneumoniae* and *E. coli*) bacteria are given in

Figure 74. The results of TAE extracts exhibit antibacterial properties with 13 mm zone against *S. aureus*; 9 mm against *B. cereus*; 8 mm against *K. pneumoniae* and 9 mm for *E. coli*, respectively. In comparison with the standard, TAE extract is more effective against *S. aureus* bacteria compared to other microbes. Therefore, the synthesised TAE mediated NPs such as TAEG, and TAES along with standard ciprofloxacin were tested against gram-positive (*S. aureus and B. cereus*) and gram-negative (*P. aeruginosa* and *E. coli*) bacteria which are illustrated in **Figure 75**.

P. aeruginosa is also commonly acquired infections associated with chronic lung (pneumonia), blood and urinary tract infection **(Sathe *et al.*, 2023)**. ZOI of TAEG was measured as 9 mm for *S. aureus*; 15 mm for *B. cereus*; 11 mm for *K. pneumoniae* and 15 mm for *E. coli*. Similarly, for TAES NPs showed a good ZOI at 10 mm for *S. aureus* and *K. pneumoniae*; 12 mm for *B. cereus* and *E. coli*. The comparative results of TAEG and TAES NPs with respect to the standard drug, TAES NPs is effective against *S. aureus,* which is related to skin related infections and therefore we utilised TAES NPs in textile applications which are explored in Phase VI. In addition, TAE mediated GNPs (TAEG) exhibited maximum ZOI in comparison with standard against *B. cereus, P. aeruginosa* and *E. coli* represented in **Table 35**.

Antibacterial activity of BFE extract, BFEG and BFES NPs were tested against bacterial strains such as *S. aureus*, *B. cereus*, *K. pneumoniae* and *E. coli* given in **Figure 72 and 73**. Among them, BFE extract shows a specific inhibition against *S. aureus* (12 mm) *and B. cereus* (9 mm), while no inhibition was observed for BFE extract against gram-negative bacteria. This may be due to the presence of thick outer layer containing lipopolysaccharides, which is difficult for the extract to penetrate into the outer membrane and to reach inner membrane, resulting in absence of inhibitory effect **(Yamamura *et al.*, 2021)**.

Similarly, for the BFE extract mediated synthesised metallic NPs such as BFEG and BFES NPs exhibits significant antibacterial activity against both gram-positive and gram-negative bacterial strains. ZOI obtained for BFEG and BFES NPs are as follows: ZOI measured at 13 mm for BFEG and 15 mm for BFES against *S. aureus*; for *B. cereus* inhibitory effect with BFEG exhibited 14 mm zone and 11 mm for BFES; 12 mm and 11 mm for BFEG and BFES NPs against *K. pneumoniae.* Finally, both NPs were susceptible against *E. coli* with ZOI of 12 mm, respectively. Based on the comparative analysis of BFE extract and their synthesised NPs, BFES NPs is found to be more effective against *S. aureus, K. pneumoniae* and *E. coli*. While, BFEG NPs exhibits better susceptible activity against both gram-positive and gram-negative

bacterial strains. Owing to the unique properties of GNPs and SNPs, which effectively combat the bacteria by enhancing the release of ROS, disrupting the bacterial cell membrane which leads to cell death, and interfering with inhibiting bacterial enzymes possessing better antimicrobial activity **(Ali *et al.*, 2024)**.

From the overall comparative analysis of antibacterial activity of plant extracts and their synthesised GNPs and SNPs from the ethanolic leaf extract of *Amphilophium paniculatum*, *Tristellateia australasiae*, and *Haematocarpus validus* fruits. The synthesised GNPs and SNPs from three extracts were able to combat the selected microbial species. More specifically, TAEG NPs exhibits 69.2%; APEG NPs exhibit 68% and BFEG NPs possess 59%, inhibition against *S. aureus*. For *B. cereus*, the more potent inhibitory effect was recognised as 93.7% for TAEG, 66.6% for BFEG and 57.1% inhibition for APEG NPs. In addition, highest inhibitory effect was 84.6% for TAEG sample against *P. aeruginosa*, followed by 60% and 55% inhibition for BFEG and APEG NPs against *K. pneumoniae*. Also, the TAEG NPs is found to be an excellent inhibitor and acts as effective drug against *E. coli*, as compared with standard ciprofloxacin. Therefore, based on the observed results of synthesised GNPs: TAEG NPs is significantly effective against both gram-positive and gram-negative bacterial strains.

Similarly, among SNPs, TAES exhibits 77% inhibition; APES possess 75% inhibition; followed by 68% inhibition for BFES against *S. aureus*. In addition, highest inhibitory effect was 87.5% for APES NPs against clinically isolated *K. pneumoniae*, followed by 76% inhibitory effect for TAES NPs against *P. aeruginosa* and 54.5% for BFES NPs against *K. pneumoniae.* Also, TAES NPs was found to be more potent against *B. cereus* (75%) and *E. coli* (80%), compared to the standard drug. Therefore, based on the observed results of synthesised SNPs: APES NPs is significantly effective against *K. pneumoniae*; TAES NPs was found to be more effective against *S. aureus, B. cereus* and *E. coli.*

An effective antibacterial activity of synthesised GNPs and SNPs achieved may be attributed to the synergistic effect of secondary metabolites present in the plant extracts of APE, TAE and BFE. Traditional values of plant extracts containing phytochemicals exhibiting various medicinal properties, which boost the activity more effectively with the plant extract mediated metallic NPs against infectious diseases. The shape and size of NPs influences the antimicrobial properties. In general, smaller sized NPs attributed with large-surface-volume which enhances the active interaction with the bacterial cells and penetrate into the cell membrane causing cellular disruption, resulted in effectiveness of NPs against specific bacterial

strains **(Raza *et al.*, 2016; Hameed *et al.*, 2020)**. There are few reported studies on date palm seed extract and mediated GNPs against microbial strains **(Zahid *et al.*, 2022; Mostafa *et al.*, 2022)**. We reported the aqueous extract of date palm seed aided SNPs encapsulated with drug ampicillin to eradicate the microbial strains and to improve bioavailability. Drug-conjugated with SNPs exhibited improved efficiency against *E. coli*, *S. aureus*, *Aspergillus flavus* and *Aspergillus niger* **(Rajalakshmi *et al.*, 2023)**. Similarly, *Phoenix dactylifera* seeds-based SNPs and their antibacterial activities were reported by **Abdel-Alim *et al.*, 2023**.

Figure 72. Antibacterial activity of APE, APEG, BFE, BFEG, BFES and standard ciprofloxacin against *S. aureus* and *B. cereus*

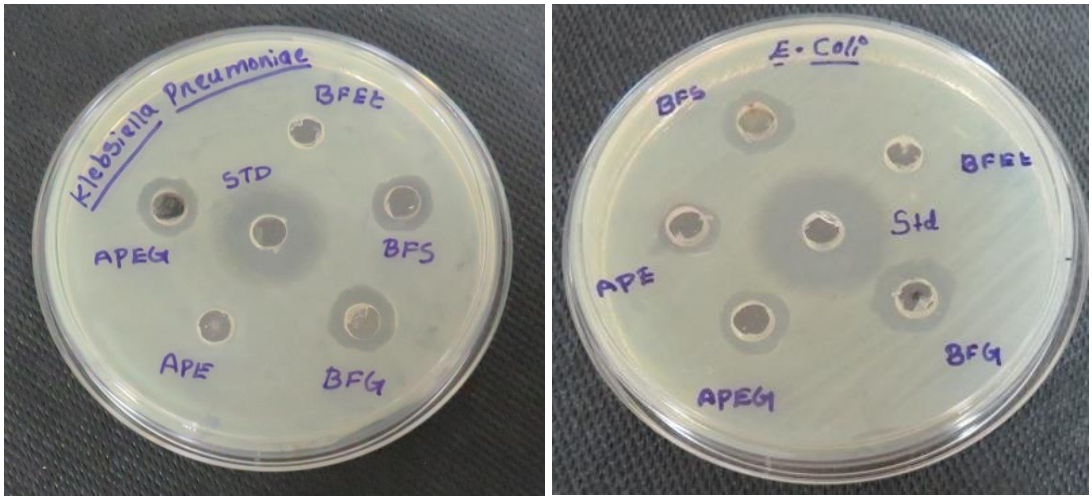

Figure 73. Antibacterial activity of APE, APEG, BFE, BFEG, BFES and standard ciprofloxacin against *K. pneumoniae* and *E. coli*

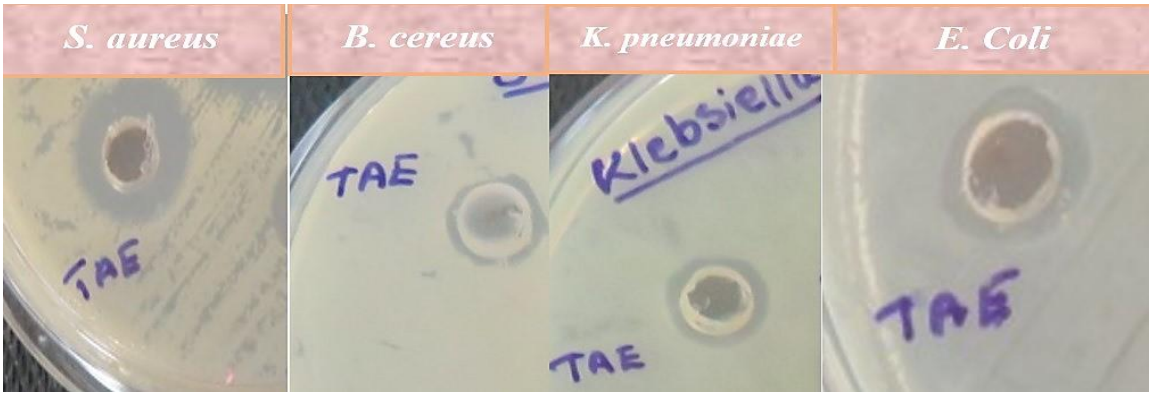

Figure 74. Antibacterial activity of TAE extract against *S. aureus, B. cereus, K. pneumoniae* and *E. coli*

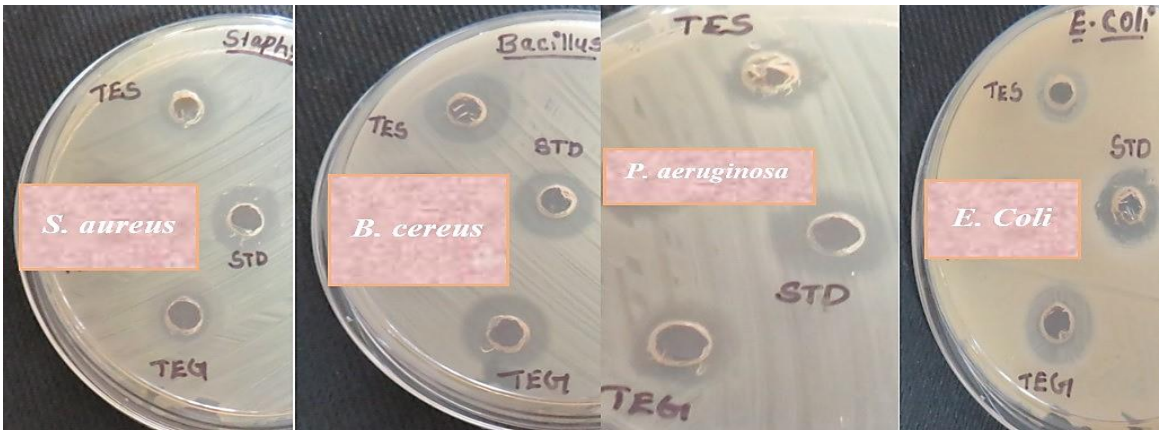

Figure 75. Antibacterial activity of TAEG, TAES and standard ciprofloxacin against *S. aureus, B. cereus, P. aeruginosa* and *E. coli*

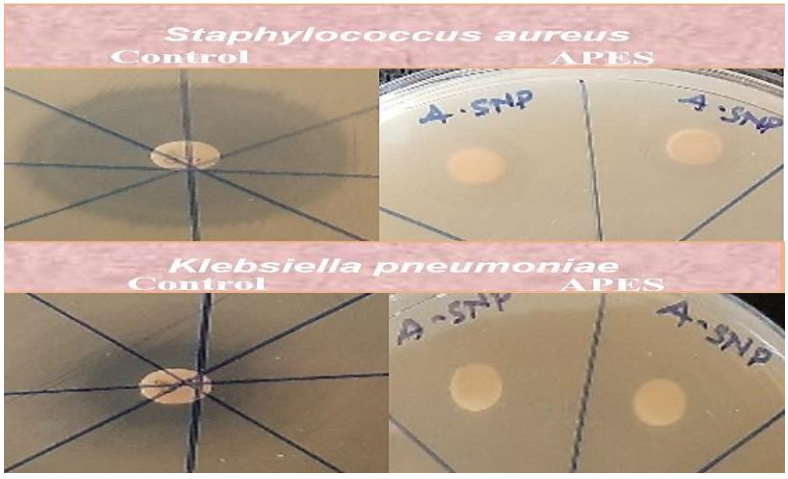

Figure 76. Antimicrobial activity of standard ciprofloxacin (5 µg) and APES against clinical isolates of *S. aureus* and *K. pneumoniae*

Metallic NPs employ their antibacterial effects through the combination of surface-level and intracellular mechanisms. Initially, the metal ions interact with bacterial membrane, and facilities their penetration through the membrane layers. Therefore, this interaction causes membrane integrity, leading to structural destabilisation and leakage at cellular level. In addition to membrane disruption, the NPs and their ionised species could diffuse into the cytoplasm, where they bind to biomolecules such as nucleic acid, enzymes and sulphur or phosphorous based proteins. These interactions facilitate the conformational alteration, inhibit the metabolic pathways and leads to cellular dysfunction to the apoptosis pathway **(Bruna *et al.*, 2021)**.

From the antibacterial study, our findings depict that TAEG and TAES NPs are more effective against gram-positive and gram-negative bacteria. Also, clinical isolates of K. pneumoniae show more susceptible towards APES NPs which are related to chronic lung infections. Hence, APES and other GNPs and SNPs were further screened for anti lung cancer effects. This is the first report on the antibacterial activity of ethanolic leaf extracts of AP, TA and BF fruits against microbial strains.

4.6.3 Anticancer Activity of Biosynthesised Metallic Nanoparticles Against A^{549} Cells

From the antibacterial studies, we observed that the plant extracts (APE, TAE and BFE) and plant extract mediated synthesis of GNPs (TAEG, and BFEG) and SNPs (APES, TAES and BFES) showed good inhibition against *K. pneumoniae* and *P. aeruginosa* which are the strains related to cause chronic lung infections. In this study, anti lung cancer potential was tested for the following NPs against (A^{549}) cell line. The results were compared to standard etoposide.

Amphilophium paniculatum leaf extract reported to have medicinal properties such as antihyperglycemic, antipyretic, antioxidant, and analgesic activities **(Bazana e*t al.*, 2020; and Nasser *et al.*, 2013b)**. Similarly, for *Tristellateia australasiae* (Leaf), and *Haematocarpus validus* (fruits), there are absence of report on the NPs synthesis and potential exploration of antioxidant, antibacterial, anticancer and anti diabetes. So, we made an-attempt to study the potential biological applications of the synthesised metallic NPs (GNPs and SNPs) against lung cancer cell line.

The results obtained from **Table 36 and Figure 77**, exhibits that the cell viability percentage was found to be concentration dependent. As the concentration of sample increases from 25 µg to 200 µg, the cell viability of A^{549} was observed from higher to lower percentage. In particular, the cell viability of APE extract was found to have 89.1% at 20 µg to 51.9% at 200 µg; whereas for the APE extract aided synthesised APES NPs possess excellent cell viability

from 50.69% at 20 µg to 22.48% at 200 µg, respectively. Increased concentration of APES NPs, decreases the growth of cancer cells. The cytotoxicity of TAE, TAE extract aided TAEG and TAES NPs on A^{549} cell line were compared with each other, which implies that TAES NPs were found to have excellent cell viability of 35% at 200 µg, as compared with TAEG NPs (51%) and TAE extract (53%). Similarly, for the BFE extract aided BFEG and BFES NPs exhibited the cell viability of 50.28% and 41.84% at 200 µg, respectively. However, the standard drug possesses significant decrease in cell viability of 13.86% at 50 µg in A^{549} cell lung cancer.

Table 36. Cell viability (%) of Plant Extracts and their Synthesised Nanoparticles at Different Concentrations Against A^{549} cell line

Concentration (µg)	Cell viability (%)						
	APE	APES	TAE	TAEG	TAES	BFEG	BFES
25	89.12	50.69	81.97	80.98	78.28	80.49	79.44
50	88.52	45.68	78.45	77.73	73.48	76.52	73.37
75	87.75	41.76	74.31	72.82	62.29	72.60	68.69
100	85.12	40.80	70.07	68.91	57.28	68.30	62.84
125	75.50	38.34	66.15	64.44	51.27	63.45	57.72
150	75.64	38.19	61.41	60.64	46.25	58.38	51.87
175	52.57	34.55	57.88	56.17	41.01	54.41	46.80
200	51.93	22.48	53.36	51.76	35.06	50.28	41.84

Therefore, from the comparative results of selected samples (APE, APES, TAE, TAEG, TAES, BFEG and BFES), SNPs and GNPs demonstrates to be effective anti-lung cancer activity as evidenced by lower cell viability with effective cell death occurred at 200 µg. IC_{50} values of APE, APES, TAE, TAEG, TAES, BFEG and BFES were found to be 224, 26.34, 222.37, 135.30, 211.96, 200.85 and 160.51 µg/mL, respectively. Interestingly, APES NPs showed strongest anti lung cancer effects as evidenced from half minimal inhibitory concentration and also correlated by revealing better inhibition against clinical isolates of *K. pneumoniae*. Better anti lung cancer effects of the selected NPs are given as APES > TAEG > BFES > BFEG >TAES. From the comparative results of synthesised GNPs and SNPs, APES NPs resulted to have 62% potential as related to standard drug against A^{549} cells, followed by TAES NPs (40%); BFES NPs (33%); BFEG NPs (28%) and TAEG NPs (28%). This is the first reported work on the leaves of *Amphilophium paniculatum, Tristellateia australasiae,* and fruits of *Haematocarpus validus* ethanolic extract aided NPs for its anti-lung cancer effects.

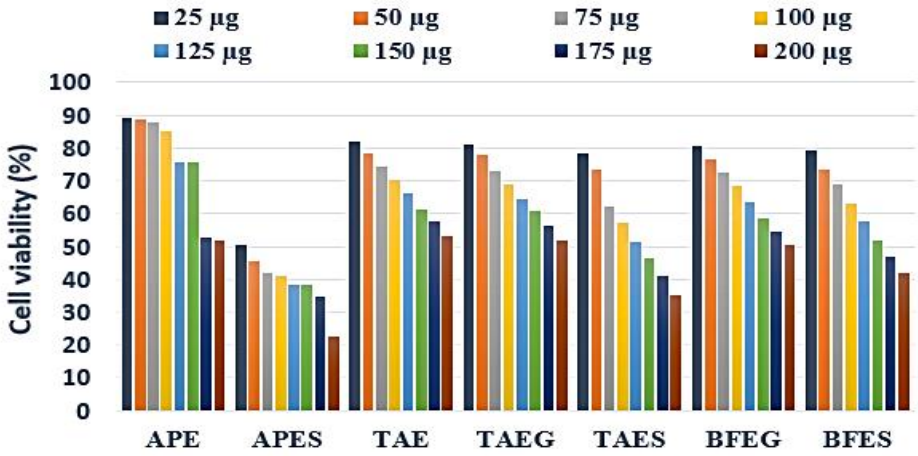

Figure 77. Graphical representation of percentage cell viability of plant extracts and their synthesised nanoparticles at different concentrations against A^{549} cell line

The morphological changes observed in standard drug (etoposide) compared to control (A^{549} cells) are shown in **Figure 78a**. Significant lower cell density, gradual detachment of cells, shrinkage of cell membrane was observed in etoposide treated cells compared to control. In control, these changes were not observed and they are elongated spindle shaped with closely packed polygonal cells **(Figure 78b)**. The morphological surface of A^{549} cell line treated with APES, TAEG and BFES NPs are given in **Figure 79, 80 and 81**. The maximum cell death occurred at 200 µg which indicated through cell disruption, shrinkages and loss of cells were observed in the samples treated against lung cancer cell line (A^{549}). The morphological surface of APES NPs treated towards lung cancer A^{549} cell line exhibits major rounded cells, cell shrinkage, and blebbing in certain cells. At high concentration (200 µg), reduced cell density with weakly attached or scattered cell distribution which further indicates the reduced cell proliferation, cell detachment and high cell death were observed. Hence based on IC_{50} value of APES NPs high cytotoxicity with strong apoptosis were confirmed **(Figure 79d)**.

Similarly, TAEG NPs treated lung cancer cells exhibits moderate-low reduction in cell density with rounded cells. Therefore, moderate-high cytotoxicity level was observed. In addition, BFES NPs treated cells possess moderate reduction in cell density with visible spindle like cells **(Figure 80d)**. Hence, BFES NPs found to have moderate antiproliferative effect compared to APES and TAES NPs. From the morphological surface of spindle like structure in healthy control cells represented in black arrow, for treated cell lines possess cell rounding (yellow arrow); cell blebbing (green arrow); and cell debris (blue arrow) **(Figure 81d)**.

The selected samples of APES, TAEG and BFES NPs showed high to moderate cytotoxic effect towards lung cancer cells, which may be due to synergistic effect of potential

secondary metabolites (mentioned in section 4.1) in APE, TAE and BFE extracts involved in enhancing the anticancer activity.

There are reports on green synthesis of SNPs from the aqueous seeds of *Phoenix dactylifera* exhibited concentration dependant cytotoxicity towards A^{549} cell line with IC_{50} of 9 µg/mL. The loss of mitochondrial membrane, cell cycle arrest and apoptotic cells were noted in the SNPs induced lung cancer cells **(Farshori *et al.*,2022)**. The biological fate and toxicity of GNPs are highly dependent on size, surface and dosage. Studies revealed that the primarily accumulation of GNPs in the spleen, liver, and kidneys, followed by gradual clearance through renal and hepatobiliary pathway **(Naz *et al.*, 2016; Bailly *et al.*, 2019)**. Smaller sized GNPs have fast clearance rate and a lower retention time in the body compared to larger particles. *In vitro* and *in vivo* studies revealed the efficiency of surface modifications like PEGylation, improve biocompatibility and reduces oxidative stress and inflammation **(Takeuchi *et al.*, 2017; Aljohani *et al.*, 2022)**. Experiments have proven the well tolerance of GNPs at a dose upto 5mg/kg in animal models, and cytotoxicity studies exhibited minimal toxicity at a concentration of less than 50 µg/mL. Thus, proper dose regulation and stabilisation of NPs in the body is necessary to minimize bioaccumulation and provide safe biomedical utilisation.

Antilung cancer potential of the seed extract of *Phoenix dactylifera* containing oleic acid and other secondary metabolites possess IC_{50} of 909 µg/mL in A^{549} cell line **(Al-Sheddi, 2019)**. Similarly, GNPs from seeds of *Phoenix dactylifera* possess IC_{50} of 19.1 µg/mL in MCF-7 cells **(Chamkouri *et al.*, 2023)**. Owing to the availability of reported studies on anticancer effect of dates palm seed extract and aided metallic NPs, we considered the importance of date palm seed aided NPs for potential anti lung cancer effect.

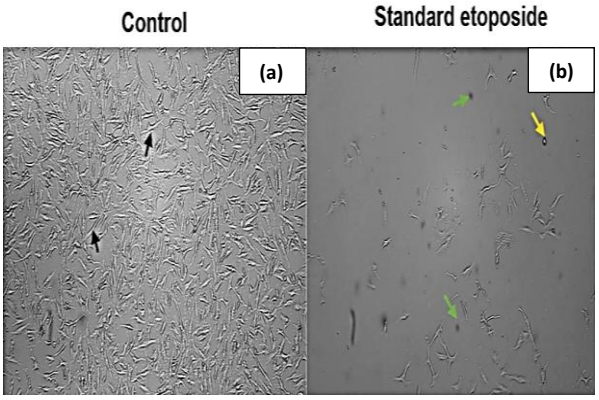

Figure 78. Morphological surface of (a) control (A^{549} human lung cancer); and (b) cell treated with standard etoposide (50 µg)

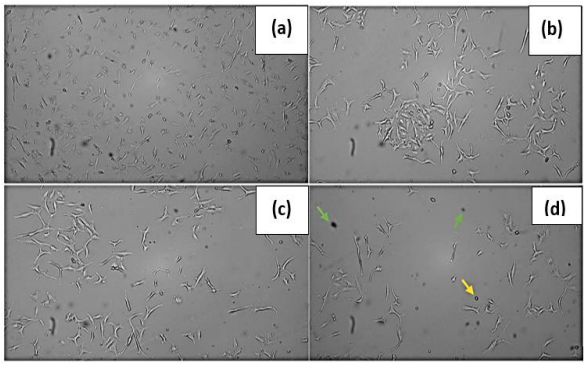

Figure 79. Morphological surface of A^{549} cell line treated with APES NPs after 24h (a) 25 µg/mL; (b) 100 µg/mL; (c) 150 µg/mL; (d) 200 µg/mL

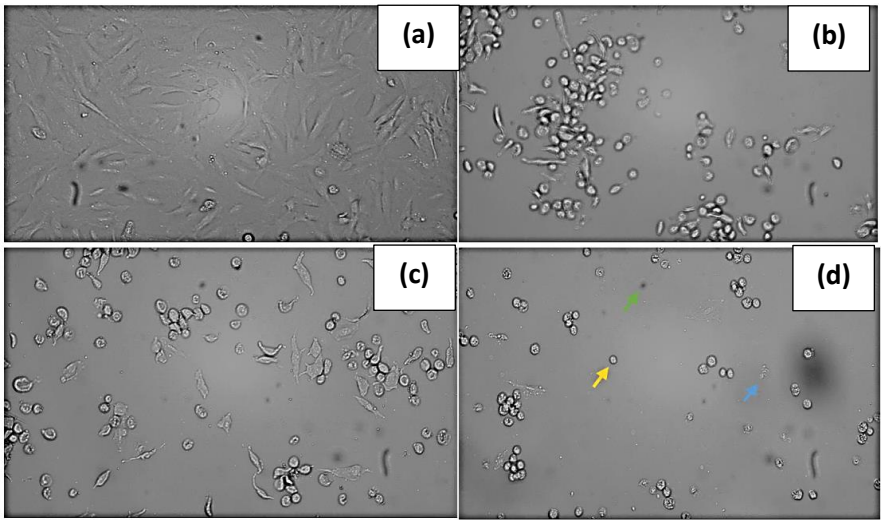

Figure 80. Morphological surface of A^{549} cell line treated with TAEG NPs after 24 h (a) 25 µg/mL; (b) 100 µg/mL; (c) 150 µg/mL; (d) 200 µg/mL

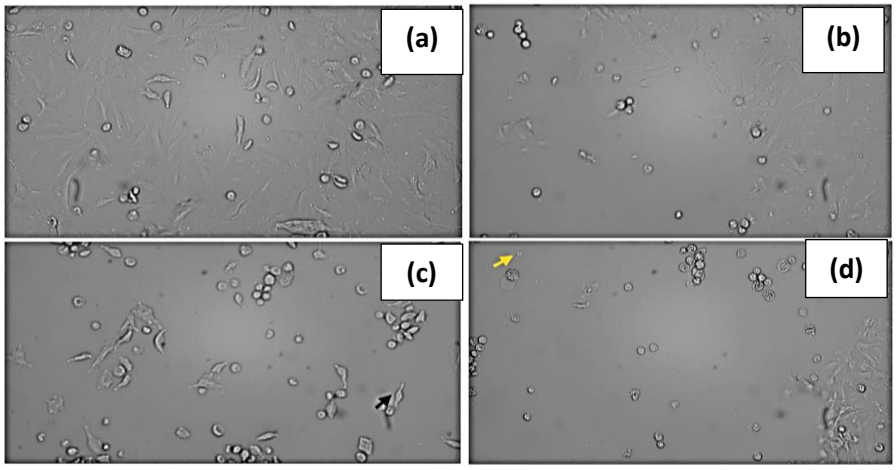

Figure 81. Morphological surface of A^{549} cell line treated with BFES NPs after 24h (a) 25 µg/mL; (b) 100 µg/mL; (c) 150 µg/mL; (d) 200 µg/mL

The results of the study were related with the previous literature reports on the synthesised GNPs and SNPs from *Pleuropterus multiflorus* against A^{549} lung cancer cells exhibited inhibitory potential at 25 µg/mL **(Castro-Aceituno *et al.*, 2017)**. Similarly, SNPs prepared from *Derris trifloiata* and *Juniperus chinensis* aqueous extract reported to possess antilung cancer activity, upon exposure to effective concentration at 86 µg/mL and 3.12 µg/mL **(Cyril *et al.*,2013; Noorbazargan *et al.*, 2021)**. Recent report on *Syzygium malaccense* based SNPs found to possess significant reduction in the cell viability, at 30 µg/mL with IC_{50} value of 7.6 µg/mL against A^{549} cell line **(Bhavi *et al.*, 2025)**.

This is the first report on exploring the antilung cancer activity on the selected plant based GNPs and SNPs. From the over all results, our findings depict that Amphilophium paniculatum ethanol leaf extract mediated SNPs were found to have reduced cell viability (35%) at 200 µg compared with standard etopsoide (13.8%) against A^{549} human lung cancer cells. These results suggested that the plant mediated SNPs exhibit promising potential for the development of drugs for lung cancer treatment.

4.6.4 Antidiabetic α-amylase Inhibitory Potential of Extracts and Synthesised Metallic Nanoparticles

Diabetes is widely recognised to be leading causes of death in worldwide and the prevalence of diabetes may rise to 853 million by 2050 **(Schwarz, 2025)**. Oxidative stress has also been reported to participate in the progression of metabolic disorder especially in Type 2 diabetes. In diabetic conditions, the homeostasis of carbohydrate and lipid metabolism gets altered due to insulin defects in production or resistance. In particular, the post prandial hyperglycaemic conditions, blood glucose level remains high after meal consumption. This condition is considered to be most important to manage diabetes and diabetes related secondary complications such as diabetic- retinopathy, neuropathy, cardiovascular diseases etc.

The enzymes α-amylase and α-glucosidase, helps to digest carbohydrates and increases blood glucose in diabetes affected patient **(Poovitha and Parani, 2016)**. Therefore, inhibiting these enzymes could reduce the risk of complications in diabetes. Several enzymatic inhibitors are available in market for managing Type 2 diabetes, such as acarbose, miglitol, and biguanides like metformin etc., which interferes carbohydrate metabolism and helps to control blood glucose levels. However, these medications cause gastro intestinal side effects, making them less suitable for long-term use **(Kaur *et al.*, 2021)**.

Most of the polyherbal formulations-based extracts and bioactive compounds were found to be effective in regulating diabetes and its complications **(Petchi *et al.*, 2014)**. In this study, we evaluated the *in vitro* antidiabetic potential of selected plant extracts and their synthesised GNPs and SNPs by assessing their α-amylase inhibitory activity using *Aspergillus oryzae* as enzyme source. Attempts to perform *in vivo* studies were not conducted due to the high cost of procedures and requirement of model animals and blood samples, which further increases the expenses.

The α-amylase inhibitory effects of selected aqueous ethanolic extracts from *A. paniculatum, T. australasiae*, *H. validus* and *P. dactylifera* showed good inhibitory activity as given in **Table 37**. From the results, APE extract exhibited the highest percentage of inhibition

at 79.12% (100 µg/mL), followed by BFE (78.73% at 100 µg/mL), and DSE extract (75.27 % at 300 µg/mL). The TAE extract showed lower inhibitory activity of 45.10% at 750 µg/mL. The bioactive compounds present in these extracts (as mentioned in section 4.1) exhibited enzyme inhibitory effects. Literature reports suggested that the phytoconstituents contributes to restore insulin protection by supporting pancreatic β cells **(Sukhikh *et al.*, 2023)**.

The antidiabetic potential of the selected plant-based extracts, GNPs and SNPs were compared with commercially available drugs such as acarbose and metformin. Acarbose showed α-amylase inhibition ranging from 39% to 68%, and metformin from 43% to 69% across concentrations of 100 -750 µg/mL. The α-amylase inhibition was performed for GNPs (APEG, TAEG, BFEG, DSEG) and SNPs (APES, TAES, BFES, DSES) from the selected plant extracts. The absorbance at 540 nm was observed for each concentration from 100, 200, 300, 500, and 750 µg/mL, as shown in **Table 37 and Figure 82**. In comparison, the synthesised GNPs such as APEG, TAEG, BFEG, and DSEG showed inhibition values of 60.93%, 66.17%, 66.27%, and 81.31% respectively, at 100 µg/mL. Among them, DSEG NPs showed the maximum inhibitory activity among GNPs, followed by BFEG, TAEG and APEG NPs. Also, the synthesised GNPs were found to be dose dependant, with decreased inhibition at higher concentrations.

Similarly, for SNPs (APES, TAES, BFES, and DSES), showed inhibition values of 80.51% at 100 µg/mL, 89.71% at 500 µg/mL, 90.31% at 100 µg/mL, and 57.76% at 100 µg/mL, respectively. Among them, BFES NPs exhibited the highest inhibition efficiency, followed by TAES, APES, and DSES NPs.

There are no reports exist on the anti-diabetic evaluation of GNPs and SNPs synthesised using ethanolic extracts of *H. validus* (fruits), *T. australasiae* (leaf), *A. paniculatum* (leaf), and 75% aqueous ethanolic extract of date palm (seeds). Literature indicated that *A. paniculatum* (Bignoniaceae family) possesses antihyperglycemic effects **(Nassar *et al.*, 2013b)**, while *T. australasiae* belonging to *Malpighiaceae* family reported to have antidiabetic, and promising therapeutic potential **(Abbas *et al.*, 2022)**. The major bioactive compounds such as conjugated Linoleic acid and Quinic acid present in methanolic extract of *H. validus* fruit and leaf are suggested to be beneficial in managing diseases such as obesity, cancer, arthritis and diabetes **(Alex *et al.*, 2022)**. In addition, dates seed consumption has been reported to improve glycemic index, reducing lipid profile, oxidative stress and inflammations in Type 2 diabetes patients **(Mohamadizadeh *et al.*, 2024)**.

This is the first report on the α-amylase inhibitory potential of GNPs and SNPs synthesised from selected plant extracts. Our recent work also highlighted the multi-therapeutic potential of *A. paniculatum* based SNPs for antidiabetic, anticancer, antioxidant and antimicrobial activities **(Rajalakshmi *et al.*, 2025)**.

From the comparative analysis of GNPs (APEG, TAEG, BFEG, DSEG) and SNPs (APES, TAES, BFES, DSES), the potential α-amylase inhibition was determined as shown in **Figure 83**. Results, indicated that APE based SNPs exhibited highest percentage of α-amylase inhibition (80.51%), compared to APEG NPs (60.93%) at 100 µg/mL. Similarly, TAE based SNPs exhibited maximum inhibition efficiency (89.71% at 500 µg/mL), compared to TAEG (58.46%). BFE extract aided SNPs exhibited the highest inhibition (90.31%), compared to BFEG NPs (66.27%) at 100 µg/mL. In addition, DSE extract aided GNPs showed highest percentage inhibition of 81.31%, compared to DSES NPs (57.76%) at 100 µg/mL. Therefore, the SNPs exhibited enhanced α-amylase inhibition across all synthesised NPs, except DSES NPs. Among the GNPs, dates seed aided GNPs showed excellent antidiabetic activity as compared to others.

The therapeutic effects of SNPs could be attributed to higher α-amylase inhibition due to their promising high surface reactivity, enhanced microbial resistance, scavenge ROS and synergistic effects of phytochemical compounds in plant extracts. Therefore, these interactions possibly make SNPs as enhanced α-amylase inhibition, by reducing the postprandial glucose levels **(Latha *et al.*, 2021; Virk, 2018)**.

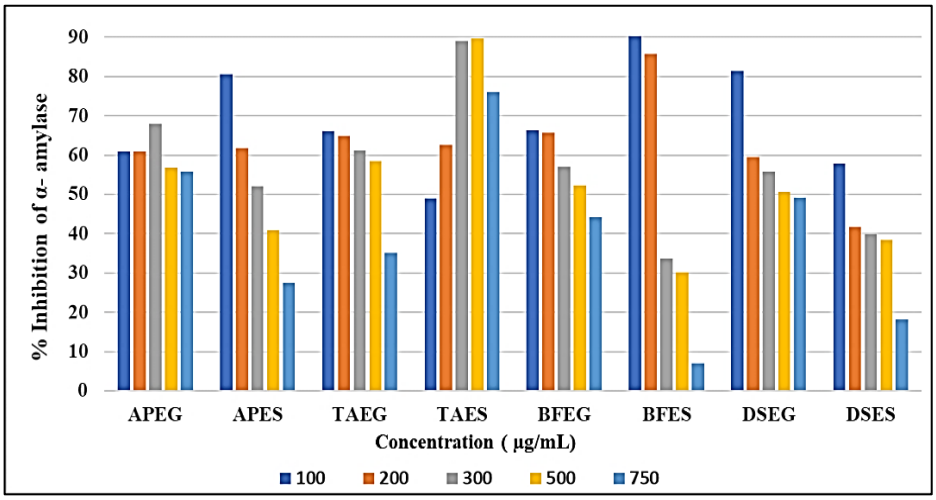

Figure 82. Antidiabetic α-amylase inhibitory potential of synthesised GNPs and SNPs from selected plant extracts

Table 37. Antidiabetic α-amylase inhibitory potential of Selected Plant Extracts, GNPs, SNPs and Standard Drug

Sample code	% α-amylase inhibition	Sample code	% α-amylase inhibition	Sample code	% α-amylase inhibition
APE 100	**79.12**	APEG 100	60.93	APES 100	**80.51**
APE 200	78.14	APEG 200	61.03	APES 200	61.81
APE 300	65.68	APEG 300	**68.05**	APES 300	52.03
APE 500	63.99	APEG 500	56.88	APES 500	40.85
APE 750	59.44	APEG 750	55.79	APES 750	27.49
TAE 100	-31.35	TAEG 100	**66.17**	TAES 100	48.96
TAE 200	-26.51	TAEG 200	64.88	TAES 200	62.51
TAE 300	-25.02	TAEG 300	61.23	TAES 300	89.11
TAE 500	-14.44	TAEG 500	58.46	TAES 500	**89.71**
TAE 750	**45.10**	TAEG 750	35.01	TAES 750	76.06
BFE 100	**78.73**	BFEG 100	**66.27**	BFES 100	**90.31**
BFE 200	77.74	BFEG 200	65.67	BFES 200	85.76
BFE 300	73.49	BFEG 300	56.97	BFES 300	33.72
BFE 500	70.42	BFEG 500	52.32	BFES 500	30.17
BFE 750	63.20	BFEG 750	44.11	BFES 750	6.92
DSE 100	46.78	DSEG 100	**81.31**	DSES 100	**57.76**
DSE 200	57.76	DSEG 200	59.45	DSES 200	41.74
DSE 300	**75.27**	DSEG 300	55.78	DSES 300	39.96
DSE 500	55.89	DSEG 500	50.54	DSES 500	38.47
DSE 750	48.47	DSEG 750	49.16	DSES 750	18.10
Positive control (standard)					
Acarbose 50	39.07	Metformin 50	43.12		
Acarbose 100	45.23	Metformin 100	51.63		
Acarbose 200	58.55	Metformin 200	63.52		
Acarbose 300	**66.75**	Metformin 300	**67.19**		
Acarbose 500	**75.96**	Metformin 500	**76.23**		
Acarbose 750	68.15	Metformin 750	69.22		

Similar reports on the antidiabetic activity of monodispersed GNPs synthesised from aqueous seed extract of date palm exhibited appreciable potential in preventing liver damage and further reducing damages to pancreas and renal tissues, compared to alloxan induced control group **(Zahid *et al.,* 2022)**. Gymnemic acid mediated GNPs exhibited potential antidiabetic activity on streptozotocin induced rats by lowering blood glucose levels and promoted the restoration of pancreatic β cells, compared to the control group **(Seetharaman *et al.,* 2023)**. Eco-friendly synthesised SNPs from the hydroethanolic extract of *Myristica fragrans* (seed) showed significant α-amylase inhibition, comparable to standard acarbose **(Perumalsamy *et al.,* 2022)**. Recently, green synthesised SNPs from ethanolic root extract of *Asparagus officinalis* were reported to exhibit α -amylase inhibition ranging from 18% to 88%, comparable to metformin (23% to 94%) at concentrations of 5 to 35 µg/mL. Also, *in vivo* studies on alloxan induced mice, exhibited that the SNPs tends to lower the blood glucose and

supported restoration of pancreatic and liver cells. The major bioactive compounds, namely Quercetin and β-sitosterol are considered promising anti-diabetic compounds **(Sher *et al.*, 2025)**.

This is the first report on exploring the antidibetic α-amylase inhibitory activity of selected plant based GNPs and SNPs. Based on our findingss, SNPs exhibited highest inhibition at concentration of 100 µg/mL, compared to GNPs. These results suggested that plant synthesised SNPs and GNPs possess α-amylase inhibitory activity and could promote in devlopment of novel therapeutic agents to manage Type 2 diabetes.

4.6.5 *In vivo* Toxicity Evaluation of Extracts and Synthesised Metallic Nanoparticles

4.6.5.1 Allium cepa Toxicity Bioassay of Synthesised Metallic Nanoparticles

Nanotechnology has gained significant applications in various fields such as pharmaceutical, environment, drug delivery, and biosensors, due to their enhanced progress in technological innovations. The exclusive properties of NPs differ from the bulk, which have the ability to enter the cell barrier and interact with intracellular structures, which leads to cellular toxicity or genotoxicity **(Rajeshwari *et al.*, 2016)**. Therefore, NPs toxicity evaluation is essential to confirm their safety use in medicinal applications.

One such widely recognised toxicity evaluation–*Allium cepa* (onion) root tip toxicity bioassay is considered as *in vivo* model, which was first developed by Levan, 1938. It is widely recognised to assess the cytogenic potential of various samples such as extracts, NPs, heavy metals, drugs, pesticides, fungicides, and food products **(Mohammed *et al.*, 2014)**. In this study, we have determined the toxic effects of plant extract aided synthesised GNPs and SNPs (1 mg/mL), based on the chromosomal aberrations and physical cell division of mitosis phases in meristematic cells of the apical roots of onion at different concentrations (25, 75 and 150 µg/mL) exposed to 4 h. Potassium dichromate (PD) at a concentration of 1 mg/mL was used as the positive control, while double-distilled H_2O was served as the blank. Treatment groups, total number of cell count, and different mitotic phases (prophase, metaphase, anaphase, and telophase) were observed to determine the percentage mitotic index. **Table 38** provides the phase indices and mitotic index, which are measured after meristematic root tip cells of *A. cepa*, exposed to blank, control, extracts and NPs.

Mitotic index for the blank (H_2O solvent) root tip cells was 65.8 %; and no chromosomal aberrations were observed, indicating actively dividing cells in the mitotic phase **(Figure 83)**. In contrast, the calculated mitotic index values of positive control (Potassium dichromate-PD) after treated with various concentrations of 25 µg/mL (41.4%), 75 µg/mL

(33.6%) and 150 µg/mL (4.87%), respectively. For plant extracts of APE, TAE, BFE and DSE exhibited the mitotic indices (49.7%, 59.5%, 53.0% and 55.1%) after treatment with 75 µg/mL **(Figure 85)**. Similarly, the mitotic indices of plant extract aided GNPs such as APEG, TAEG, BFEG and DSEG NPs after exposure of meristematic root tips of *A. cepa* at various concentrations of 25 µg/mL (62.4%, 46.8%, 60.0% and 80.97%), 75 µg/mL (50.7%, 42.4%, 44.3% and 57.56%) and 150 µg/mL (26.8%, 20.4%, 33.1% and 29.2%), respectively. In addition, the plant extract aided synthesised SNPs such as APES, TAES, BFES and DSES NPs after exposure of meristematic root tips of *A. cepa* at different concentration of 25 µg/mL (74.6%, 82.9%, 65.3% and 63.4%); 75 µg/mL (55.1%, 54.1%, 33.1% and 38.0%), and 150 µg/mL (27.6%, 40.48%, 20.4% and 10.7%), respectively.

From the mitotic indices of GNPs and SNPs, a concentration dependent decrease in mitotic index percentage was observed in the treated groups, after exposure to 25, 75 and 150 µg/mL. Similar results were observed for positive control, the mitotic index percentage was found to be 41.4% at 25 µg/mL as shown in **Figure 84**. At higher concentration, increased chromosomal aberrations were noted under optical microscope.

Therefore, in comparison with the control cells, the synthesised NPs were dose dependant with increasing concentration of NPs, decrease in mitotic indices were noticed. The higher concentration of NPs, damages the DNA in root tip cells. At low and medium concentrations of NPs, subsequent stages of cell divisions were observed, at lesser in high concentration treated roots. Further, after exposed to higher concentration of NPs, the cells were not allowed to undergo dividing stage, rather got arrested at interphase. Hence, number of cells in interphase is directly proportional to concentration of samples.

The variety of cytological changes were remarked in the treated meristematic cells in onion root tip, chromosomal aberrations such as chromosomal bridge, break, loss, laggard phase, clumped, sticky anaphase and disturbed metaphase were monitored upon interaction of meristematic root tip with different concentration of samples **(Debnath *et al.*, 2018)**.

When root tips of onion exposed to 25 µg/mL and 75 µg/mL doses of GNPs and SNPs, very less aberrations with prophase, metaphase, anaphase and telophase were observed given in **Figure 86 and 87**. Whereas, at high dose (150 µg/mL) of GNPs and SNPs in treated root tips exhibited aberrations such as slightly disturbed anaphase and telophase due to shifting of poles by depolymerisation of spindle fibres.

From the comparison of mitotic indices between GNPs and SNPs of *A. cepa* root tip, resulted that the mean of SNPs is higher than GNPs at 25, 75 and 150 µg/mL. Therefore, we concluded that synthesised SNPs possesses higher mitotic cell division at lower and medium concentrations than GNPs.

Similar studies, highlights the decreased mitotic indices with dose dependant relationship of SNPs **(Kumari *et al.*, 2009)**. As evidenced from the work by Debnath *et al.*, exposure to GNPs and SNPs showed negative effects in the *A. cepa* root tip toxicity test. Decreased mitotic index were noted for treated GNPs (41%) compared to SNPs (53%) **(Debnath *et al.*, 2018)**. In another study, the cytotoxicity of magnesium oxide NPs and microparticles indicated dose dependant manner with increased chromosomal aberrations by decreased mitotic index percentage **(Mangalampalli *et al.*, 2017)**. Recent study by Stalin *et al.*, synthesised GNPs from leaf extract of *Lilium wallichianum*, exhibits dose dependant effect with 73% mitotic index cell divisions at 50 µg/mL, which suggested the enhanced cell development **(Stalin *et al.*, 2025)**.

This is the first report on exploring the toxicity evaluation of plant extracts (APE, TAE, BFE and DSE), and their synthesised GNPs and SNPs through A. cepa root tip toxicity bio assay. From the A. cepa root tip bioassay, our findings depict that all the samples were found to be dose dependent. It can be generalised that the selective dose dependant GNPs and SNPs, possesses enhanced cell divisions, which can be further validated using in vitro and in vivo models of human cells and animal models to conclude the NPs toxicity.

Table 38. Mitotic Index and Distribution of Meristematic Cell Divisions in Root Tip of *A. cepa* Treated with Blank, Control, Plant Extracts, GNPs and SNPs at Different Concentrations

Sample code	No of counted cells	No of dividing cells	Prophase	Metaphase	Anaphase	Telophase	Mitotic index (%)
Blank (H_2O)	205	135	103	10	14	8	**65.8**
Control (PD- 25 µg/mL)	205	85	71	7	0	7	**41.4**
Control (PD- 75 µg/mL)	205	69	68	1	0	0	33.6
Control (PD- 150 µg/mL)	205	10	0	0	0	0	4.87
APE (75 µg/mL)	205	102	73	18	5	6	49.7
TAE (75 µg/mL)	205	122	98	6	8	10	**59.5**

BFE (75 µg/mL)	205	109	102	5	2	0	53.0
DSE (75 µg/mL)	205	113	97	6	4	6	55.1
APEG (25 µg/mL)	205	128	105	8	5	10	**62.4**
APEG (75 µg/mL)	205	104	89	4	1	10	50.7
APEG (150 µg/mL)	205	55	48	4	1	10	26.8
TAEG (25 µg/mL)	205	96	82	10	3	1	**46.8**
TAEG (75 µg/mL)	205	87	70	10	5	2	42.4
TAEG (150 µg/mL)	205	42	37	3	1	1	20.4
BFEG (25 µg/mL)	205	123	107	8	1	7	**60.0**
BFEG (75 µg/mL)	205	91	77	4	4	6	44.3
BFEG (150 µg/mL)	205	68	61	3	4	0	33.1
DSEG (25 µg/mL)	205	166	143	13	1	9	**80.9**
DSEG (75 µg/mL)	205	118	100	12	5	1	57.5
DSEG (150 µg/mL)	205	60	60	0	0	0	29.2
APES (25 µg/mL)	205	153	128	19	3	3	**74.6**
APES (75 µg/mL)	205	113	94	3	6	10	55.1
APES (150 µg/mL)	205	57	51	0	2	4	27.8
TAES (25 µg/mL)	205	170	141	22	3	4	**82.9**
TAES (75 µg/mL)	205	111	98	8	2	3	54.1
TAES (150 µg/mL)	205	83	73	7	0	3	40.5
BFES (25 µg/mL)	205	134	115	12	4	3	**65.3**
BFES (75 µg/mL)	205	68	65	1	1	1	33.1
BFES (150 µg/mL)	205	42	42	0	0	0	20.4
DSES (25 µg/mL)	205	130	117	7	4	2	**63.4**
DSES (75 µg/mL)	205	78	63	5	2	8	38.0
DSES (150 µg/mL)	205	22	22	0	0	0	10.7

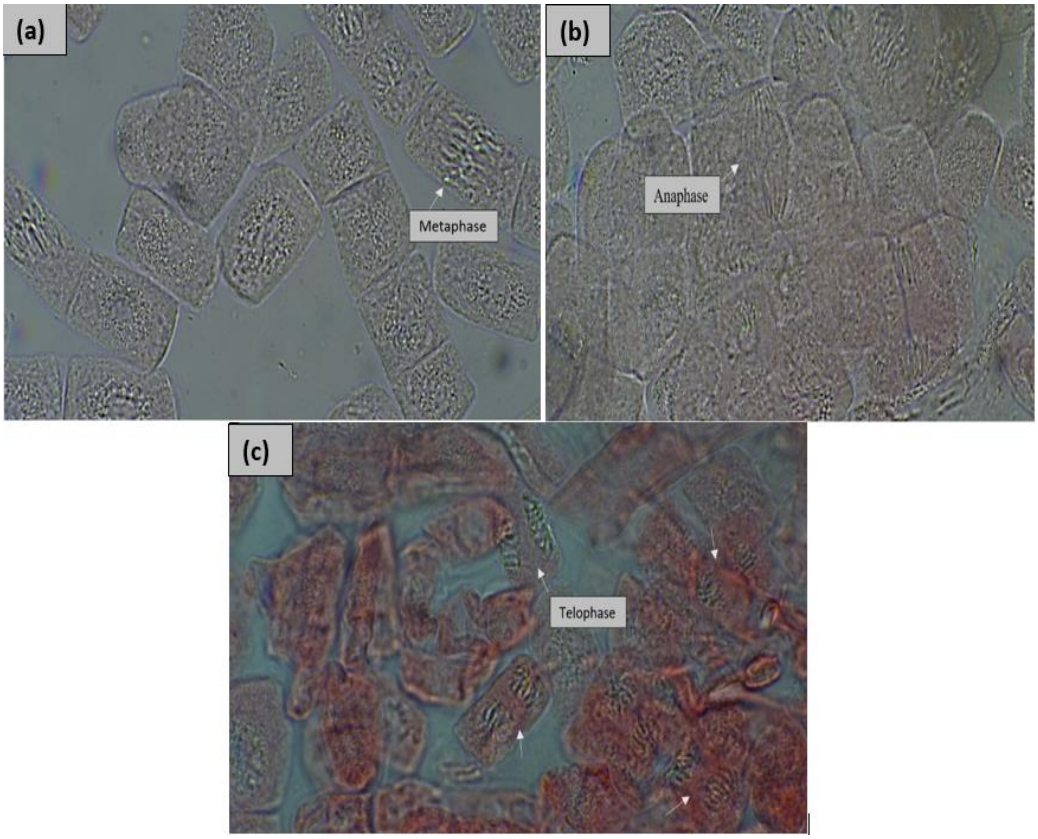

Figure 83. Photomicrograph of blank (H_2O) in root tip cells of *A. cepa*
(a) Metaphase; (b) anaphase; (c) telophase

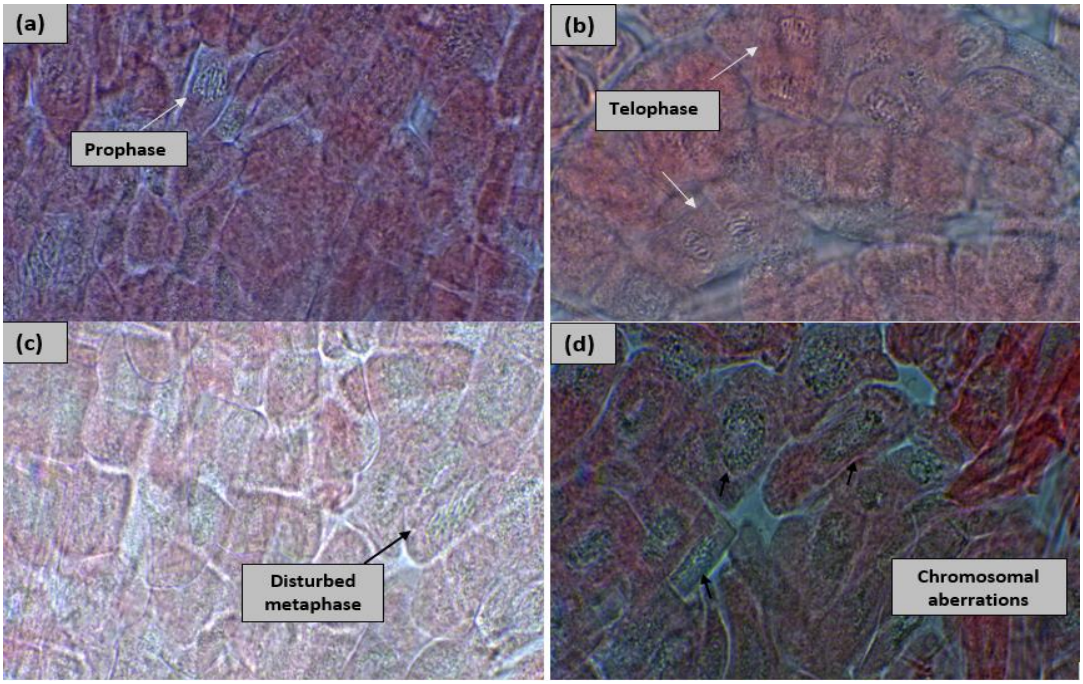

Figure 84. Photomicrograph of positive control (potassium dichromate) exposed in root tip cells of *A. cepa* (a) prophase at 25 µg/mL; (b) Telophase at 25 µg/mL; (c) Disturbed metaphase at 75 µg/mL; (d) chromosomal aberrated at 150 µg/mL

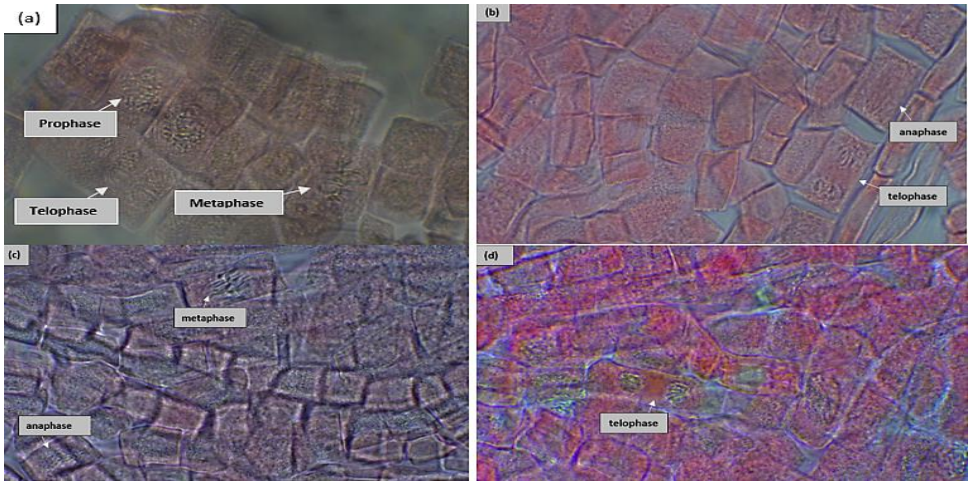

Figure 85. Photomicrograph of plant extracts at 75 µg/mL exposed in root tip cells of *A. cepa* (a) APE; (b)TAE; (c) BFE; (d) DSE

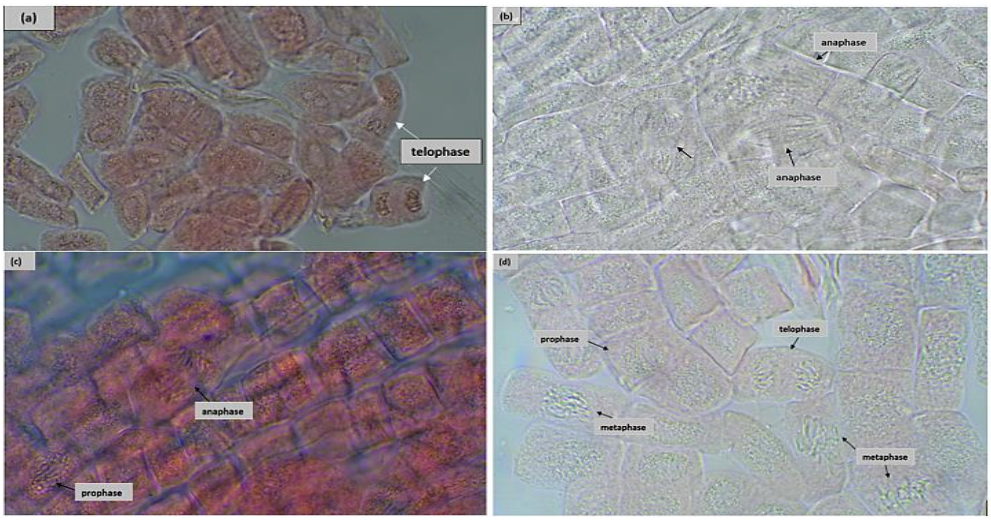

Figure 86. Photomicrograph of GNPs exposed in root tip cells of *A. cepa* (a) APEG; (b) TAEG; (c) BFEG; (d) DSEG NPs

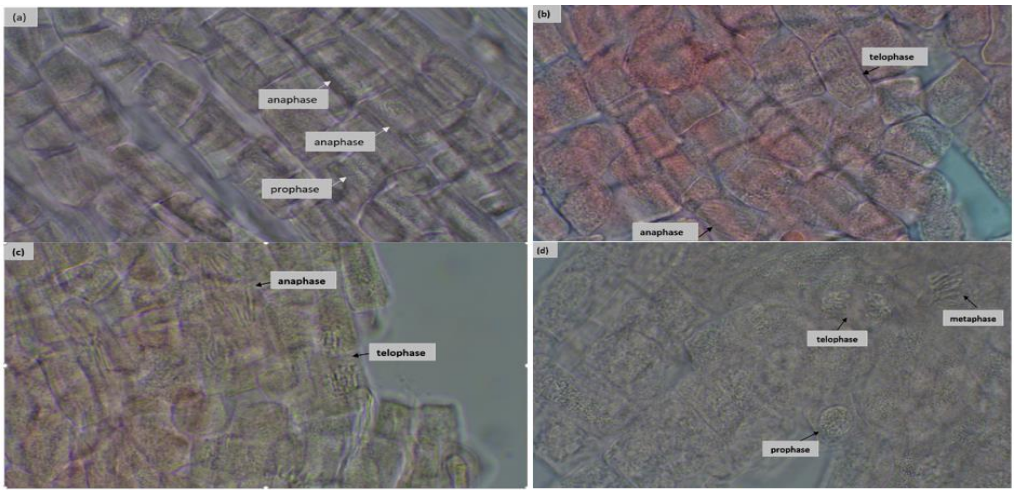

Figure 87. Photomicrograph of SNPs exposed in root tip cells of *A. cepa* (a) APES; (b) TAES; (c) BFES; (d) DSES NPs

4.6.6 Preparation and Encapsulation Efficiency of Nano-drug/ garlic Loaded Microspheres

The metallic NPs such as APES NPs (SNPs synthesised from *Amphilophium paniculatum* extract), and DSEG NPs (GNPs synthesised from *Phoenix dactylifera* extract) were selected for microsphere encapsulation based on their reported α-amylase inhibitory activity and promising *in vitro* biomedical applications. The garlic fresh juice loaded with DSEG NPs (MS1G2) and garlic fresh juice loaded with both APES and DSEG NPs (MS1G2S) were incorporated into polymeric microspheres using the optimised formulation (MS1) to evaluate their potential sustained DDS. The encapsulation efficiency (EE%) of nanodrug and garlic-nano loaded microspheres such as MMS1AS, MMS1DG, MS1G2 and MS1G2S formulations helps to quantify the amount of drug or active ingredient which is entrapped within the microspheres with respect to the initial amount of drug used in formulation by measuring UV BioSpec nano spectrophotometer.

The encapsulation efficiency of metformin in the control formulation MMS1, exhibited encapsulation efficiency of 90.13% indicating effective drug entrapment with the blank polymer matrix. The sample MMS1AS formulation, containing SNPs along with metformin, showed slightly higher encapsulation efficiency (92.05%), due to possible interaction of drug with SNPs, which may enhance the retention or alter the polymer-drug binding interaction. Also, the sample MMS1DG formulation, containing GNPs along with metformin showed the highest encapsulation efficiency (92.10%), suggesting the enhanced stability of polymer matrix and drug retention. It may be due to the better interaction of GNPs with the polymer matrix, by improving the nanodrug entrapment within the microspheres. For the garlic loaded GNPs incorporated microspheres (MS1G2) and gold-silver NPs incorporated microsphere (MS1G2S) formulation showed the encapsulation efficiency of 93.25 % and 93.35 %, respectively. Similar reports on biopolymer (xanthan gum)-based microspheres encapsulated with metformin showed an encapsulation efficiency of 93.11% for sustained release while phytosome-loaded garlic microspheres exhibited encapsulation efficiency of 62.62% **(Yahoum *et al.*, 2023; Nining *et al.*, 2021)**.

4.6.6.1 Characterisation of Nanoencapsulated Microspheres

4.6.6.1.1 FESEM and EDS analysis of Nanodrug/ Garlic-nano Encapsulated Microspheres

FESEM analysis was performed to determine the surface morphology and particle size of the nanodrug encapsulated microspheres (MMS1AS, and MMS1DG) and garlic-nano encapsulated microspheres (MS1G2 and MS1G2S) are shown in **Figure 88, 89**, **and 90**.

The FESEM image of MMS1AS **(Figure 88)** clearly showed spherical microspheres with an average diameter of 3.20 µm. At high magnification (20 µm), the smooth surface of the microspheres with uniform spherical spheres representing stable microsphere formation. Similarly, the MMS1DG formulation, which was encapsulated with both date palm seed aided GNPs and metformin, exhibited spherical morphology with a moderately rough surface (**Figure 89**). The average diameter of MMS1DG ranging from 5.45 to 7.80 µm. The surface morphology revealed that the particle shape and surface were based on the presence of GNPs and partial aggregation of the polymer matrix during the solidification process. Although the morphology exhibited a non-smooth surface, the absence of pores or cracks were observed indicating the stable formation of microspheres. The average size of the nano-drug encapsulated microspheres was 0.18 µm for MMS1AS, and 0.35 µm for MMS1DG, respectively.

The FESEM image of MS1G2 **(Figure 90b)** microspheres formulated using fresh garlic juice combined with GNPs from date palm seed extract, revealed a nearly spherical morphology. The average diameter of MS1G2 is approximately 6.62 µm. For MS1G2S **(Figure 90d)**, representing microspheres synthesised using garlic extract combined with GNPs from date palm seed and SNPs synthesised from *Amphilophium paniculatum* leaf extract, the FESEM image revealed a distinctly spherical particle with a diameter of 6.82 µm. Lower magnification (5 µm) exhibited smooth microsphere formation **(Figure 90c)**. The absence of pores or cracks on the microspheres indicates stable formation.

The EDS spectrum of MMS1AS **(Figure 91a)** revealed C, N, O, Cl, and Ag, indicating the successful incorporation of drug and SNPs within the microspheres. The presence of Ag confirmed the entrapment of SNPs in the MMS1AS formulation. Similarly, the EDS spectrum of MMS1DG **(Figure 91b)** revealed the presence of C, O and Au. The presence of Au peak confirmed the incorporation of GNPs in microsphere formulation.

The EDS spectra of MS1G2 **(Figure 92a)** revealed the presence of C, O, Au, K, P and S, whereas the MS1G2S **(Figure 92b)** exhibited C, O, Mg, Au, Ag, K, P and S. The element C and O represents the polymer utilised for encapsulation matrix, whereas S signifies the presence of sulphur containing bioactive compounds from garlic extract. Au peak in both spectra confirmed the incorporation of GNPs, whereas the presence of Ag in MS1G2S indicated the encapsulation of SNPs. The trace elements such as P, Mg and K which are originated from the garlic extract as natural mineral composition. Therefore, the EDS results confirmed the efficient encapsulation of NPs and bioactive constituents within the microsphere formulations.

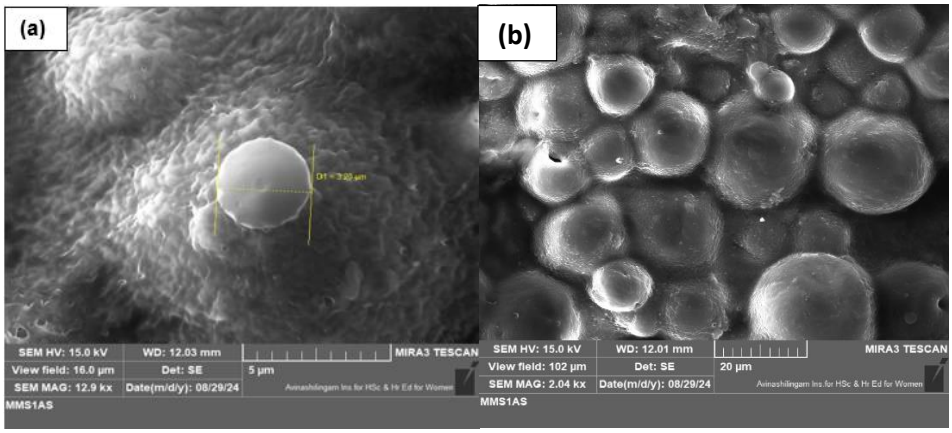

Figure 88. FESEM image of microspheres (a) MMS1AS at 5 µm; (b) MMS1AS at 20 µm

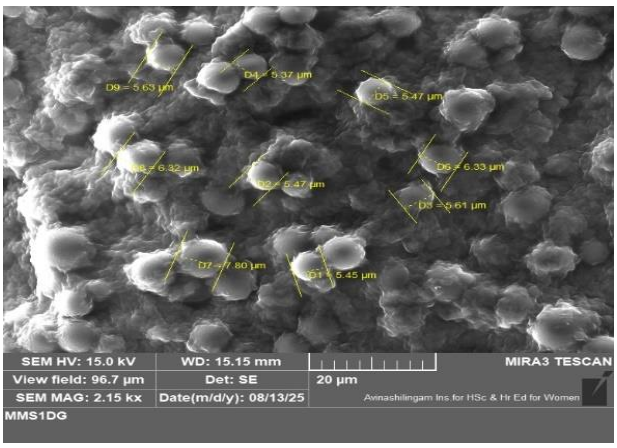

Figure 89. FESEM image of MMS1DG microspheres

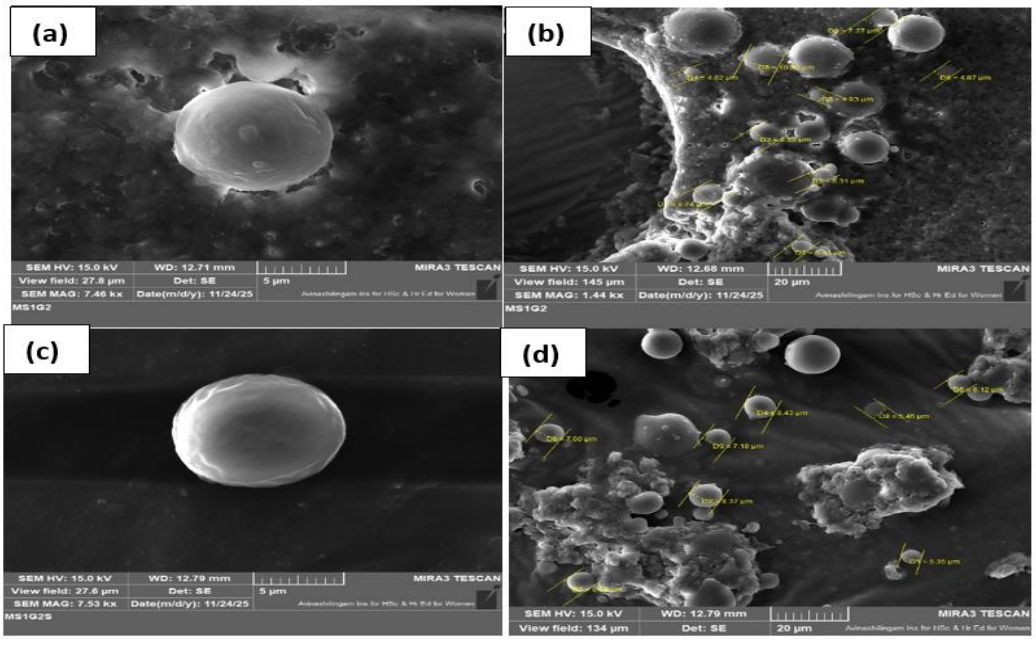

Figure 90. FESEM image of MS1G2 at 5 µm (a); MS1G2 at 20 µm (b); MS1G2S at 5 µm (c); and MS1G2S at 20 µm (d)

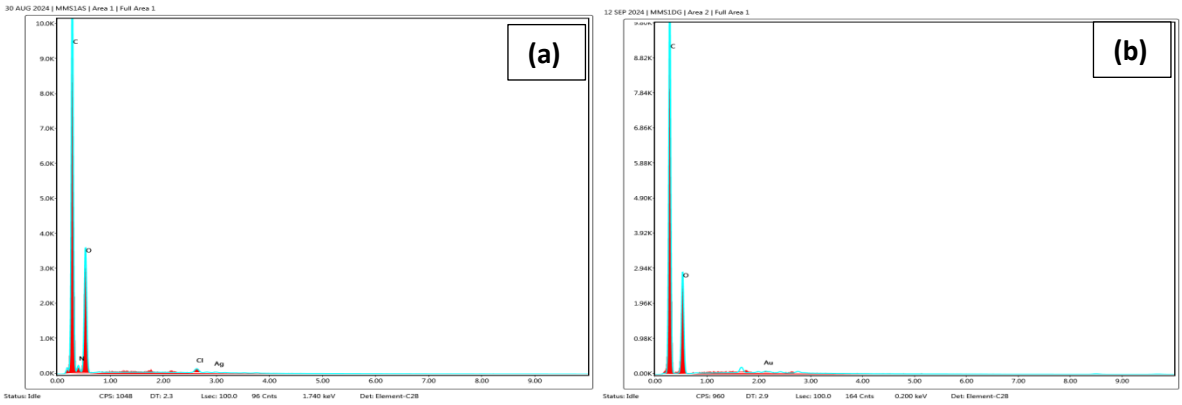

Figure 91. EDS mapping of MMS1AS (a); and MMS1DG (b)

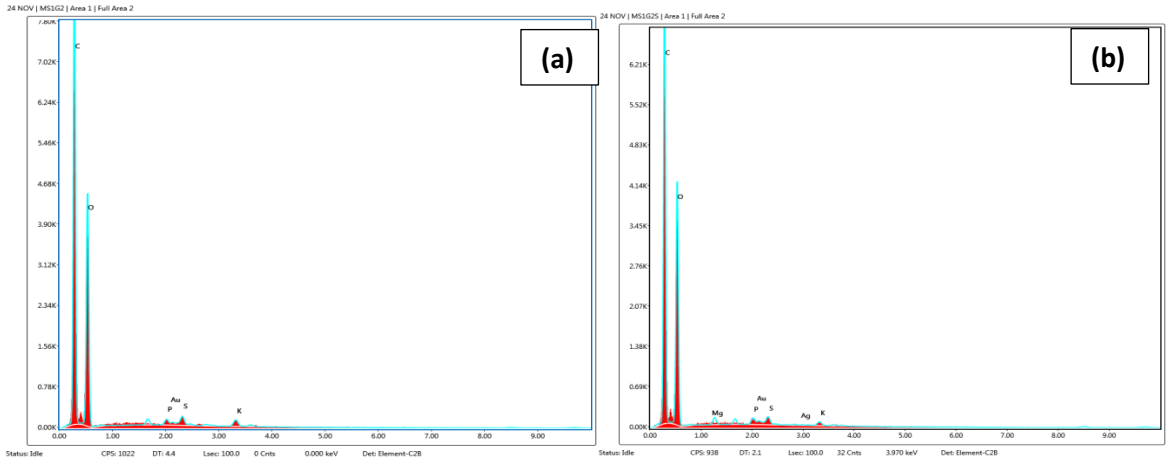

Figure 92. EDS mapping of MS1G2 (a); and MS1G2S (b)

4.6.6.1.2 FTIR and XRD analysis of Nanoencapsulated microspheres

The FTIR spectrum of nano-drug (MMS1AS and MMS1DG) and garlic-nano (MS1G2 and MS1G2S) encapsulated microspheres are given in **Figure 93 to 96.** FTIR spectrum of MMS1AS formulation **(Figure 93)**, exhibited the characteristic peaks at 2877.79 cm^{-1} corresponds to C-H stretching vibrations of aliphatic chain in PEG and PCL, a sharp peak at 1651.07 cm^{-1} attributed to C=N stretching of biguanide group in metformin. The peak at 1458.18 cm^{-1} (CH_2 bending), 1288.45 cm^{-1} corresponds to C-N stretching, and 1087.85 cm^{-1} attributed to C-O-C stretching of the polymer. The peak observed in the finger print region such as 948.98 cm^{-1}, 840.96 cm^{-1}, 663.51 cm^{-1}, 594.08 cm^{-1}, and 547.78 cm^{-1} confirming the presence of metformin. The band at 455.20 cm^{-1} assigned to C-metal group, confirming the presence of SNPs within the microsphere along with the metformin.

Similarly, for MMS1DG formulation **(Figure 94)**, containing DSEG NPs and metformin, exhibited the characteristic peaks at 2870.08 cm^{-1} (C-H stretching vibrations of

aliphatic chains of polymer), distinct peak at 1782.32 cm^{-1} corresponds to C=O stretching vibrations of ester group of phytochemical reductants used in GNPs synthesis. The peaks at 1651.07 cm^{-1}, and 1465.90 cm^{-1} corresponds to C=N stretching and CH_2 bending vibrations of biguanide from metformin. The other peak assigned at 1357.45, cm^{-1}, 1288.45 cm^{-1}, and 1242.16 cm^{-1} corresponds to C-N and C-O stretching, confirms metformin in the formulation. The peak at 1103.28 cm^{-1} represents C-O-C asymmetric stretching from PEG. The minor peaks at 944.98 cm^{-1}, 840.96 cm^{-1}, 732.95 cm^{-1}, 594.08 cm^{-1}, and 547.78 cm^{-1} further confirms the metformin incorporation in the MMS1DG formulation. The band at 501.49 cm^{-1}, and 462.92 cm^{-1} may be assigned to C-metal stretching vibrations, which confirms the GNPs presence within the microspheres. Therefore, these spectral similarities observed between MMS1AS and MMS1DG indicates that metallic NPs (Au and Ag) encapsulation did not affect the polymeric or drug backbone, which ensures the stability and compatibility of microsphere formulation.

The FTIR spectrum of MS1G2 formulation **(Figure 95)** containing fresh garlic extract combined with DSEG NPs, exhibited the characteristic peaks at 3321.848 cm^{-1}, 1635.959 cm^{-1}, 1030.897 cm^{-1}, and 402.323 cm^{-1}. The peak at 3321.848 cm^{-1} (O-H stretching), and 1635.96 cm^{-1} (C=C stretching or C=O vibrations of conjugated carbonyl groups) indicating the presence of bioactive organosulphur compounds. The peak at 1030.897 cm^{-1} (S=O) stretching vibrations confirming the presence of Allicin (organo sulphur constituents) from garlic. The minor peak (402.323 cm^{-1}) attributed to C-metal group which confirmed the encapsulation of GNPs within MS1G2 microspheres. The FTIR spectrum of MS1G2S microspheres **(Figure 96)**, exhibited a similar profile to that of MS1G2 microspheres. However, the band observed at 1031.30 cm^{-1} was slightly shifted in MS1G2S, which is assigned to S=O stretching vibrations. This may be due to possible interactions or incorporation of SNPs within the formulation. Furthermore, the peak at 433.68 cm^{-1} (C–Ag) and 406.29 cm^{-1} (C–Au), confirmed the encapsulation of both NPs within MS1G2S microspheres. Therefore, based on the FTIR spectrum of the nano-drug and garlic-nano encapsulated microspheres, it was observed that drug, bioactive garlic, and metallic NPs were successfully incorporated within the polymeric microspheres, forming stable formulations suitable for drug delivery applications.

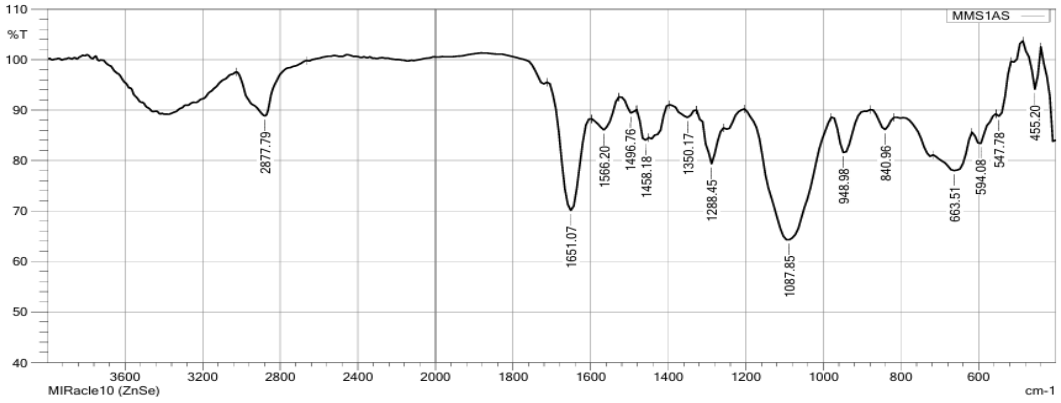

Figure 93. FTIR spectrum of MMS1AS microsphere

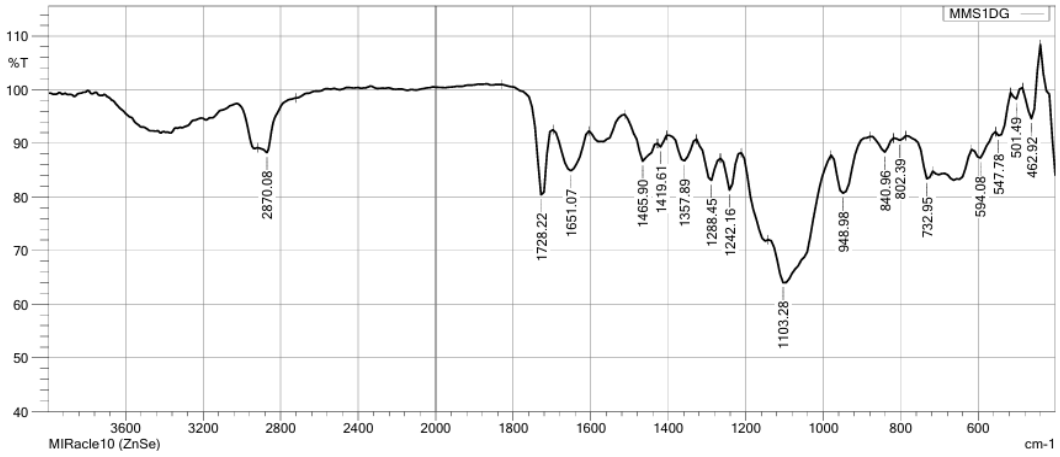

Figure 94. FTIR spectrum of MMS1DG microsphere

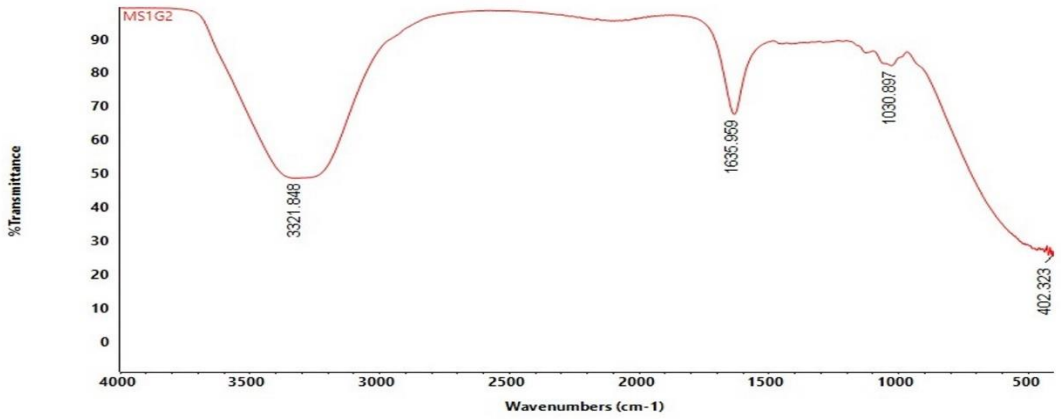

Figure 95. FTIR spectrum of MS1G2 microsphere

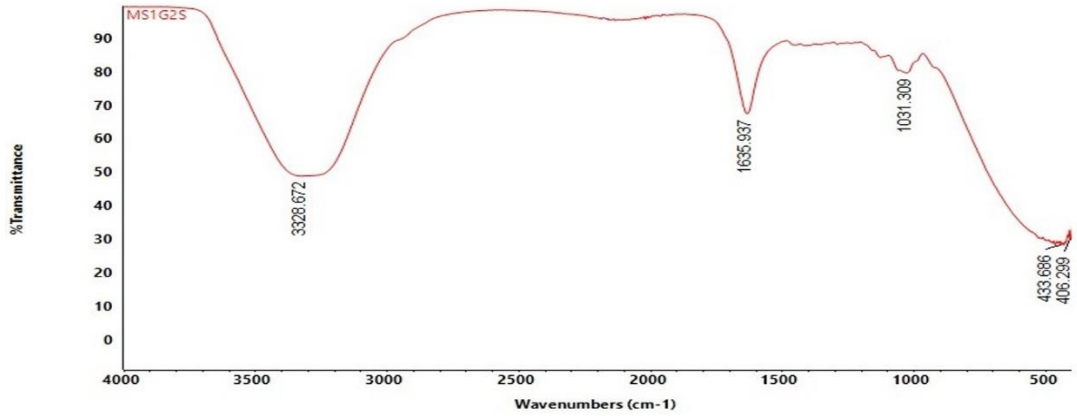

Figure 96. FTIR spectrum of MS1G2S microsphere

The XRD diffraction patterns of nano-drug (MMS1AS and MMS1DG) and garlic-nano loaded microspheres (MS1G2 and MS1G2S) are shown in **Figure 97a to d**. The diffraction pattern of MMS1AS **(Figure 97a),** represents the broad peak between 2θ = 16˚ to 24 ˚, which is the characteristic of semi-crystalline polymeric matrix of PCL, PEG, HPMC and PVP. The absence of peaks corresponding to SNPs and metformin indicates that were well dispersed and encapsulated within the microsphere (MMS1AS), confirming the amorphous pattern with an average crystallite size of 39.4 nm. Similarly, the MMS1DG formulation **(Figure 97b)** exhibits the broad peak at 21.4˚, confirming the amorphous pattern of polymeric materials. The absence of GNPs and metformin intense peak in the formulation, confirms the complete dispersion and encapsulation within the formulation. The average crystallite size was found to be 42.06 nm.

The XRD pattern of MS1G2 microspheres **(Figure 97c)** exhibited the broad pattern at 21˚ to 28˚, corresponds to polymeric materials. The absence of sharp peaks of GNPs and bioactive garlic indicates the uniform distribution within the microsphere formulation. The peak broadness is due to incorporation of GNPs and garlic bioactive constituents within the microsphere. The average crystallite size of MS1G2 was found to be 49.70 nm. Similar pattern was observed for MS1G2S **(Figure 97d)**, representing the broad pattern centred around 2θ = 21˚, corresponds to polymeric materials. The absence of sharp peaks of GNPs, SNPs and bioactive garlic, confirms the well dispersed pattern and encapsulation within the microsphere formulation. The average crystallite size of MS1G2S was found to be 51.77 nm.

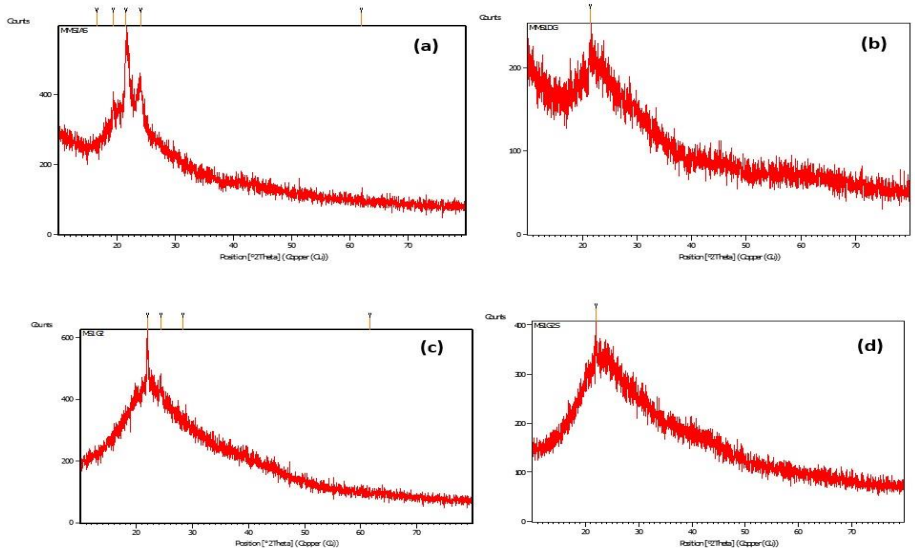

Figure 97. XRD pattern of MMS1AS (a); MMS1DG (b); MS1G2 (c); and MS1G2S (d)

Therefore, the characterisation of the formulated microspheres confirmed the successful incorporation of drug along with SNPs and GNPs, using the emulsion solvent evaporation method. The FTIR analysis resulted no significant chemical alterations between the drug and the polymeric excipients, represents good compatibility. Furthermore, the FESEM image revealed a spherical morphology with average particle size of formulated microspheres such as MMS1AS (0.18 µm), MMS1DG (0.35 µm), MS1G2 (16.39 µm) and MS1G2S (0.17 µm), respectively. The XRD diffraction pattern revealed the highly crystalline nature of metformin to semi-crystalline or amorphous nature of nano-drug and garlic-nano encapsulated microsphere formulations, with notable decrease in crystallite size. The broad diffraction peaks and reduced intensity further suggesting the improved molecular dispersion of the drug, metallic NPs and bioactive garlic constituents within the polymer carrier matrix **(Sakkal *et al*., 2024)**. Overall, the physicochemical characterisation conforms that the formulated microspheres are stable and providing the sustained or enhanced drug release for pharmaceutical drug delivery applications.

4.6.6.2 *In vitro* Antibacterial and Antidiabetic α-amylase Inhibitory Activity

The antibacterial activity of garlic-nano encapsulated microspheres (MS1G2, and MS1G2S) was tested against selected bacterial strains (*S. aureus, B. cereus, K. pneumoniae*, and *E. coli*) by agar well diffusion method. The ciprofloxacin was served as standard. The absence of inhibition zone against tested strains in blank microspheres (MS1), indicates that the polymer excipients have no antibacterial effect. The MS1G microspheres, which contain only fresh garlic extract showed a moderate inhibition zone ranging from 10 to 13 mm. Whereas, MS1G2

formulation, which contain garlic extract along with DSEG NPs, exhibited the slightly improved zone ranges from 11 to 16 mm, particularly against *K. pneumoniae*, indicates that the presence of GNPs enhances the antimicrobial activity. Similarly, the MS1G2S formulation encapsulated with bioactive garlic extract along with DSEG NPs and APES NPs, exhibited the good zone ranging from 17 mm to 19 mm. The better inhibition was observed against *B. subtilis* and *K. pneumoniae*. The enhanced antibacterial activity of MS1G2S is due to the synergistic effect of metallic NPs and the garlic bioactive constituents, which disrupts the bacterial membrane, and alter protein function, thereby providing better antibacterial effects. Therefore, the results suggested that the metallic NPs-enhanced garlic formulations, particularly MS1G2S are considered to be promising broad spectrum antibacterial agents **(as shown in Figure 98 and Table 39)**.

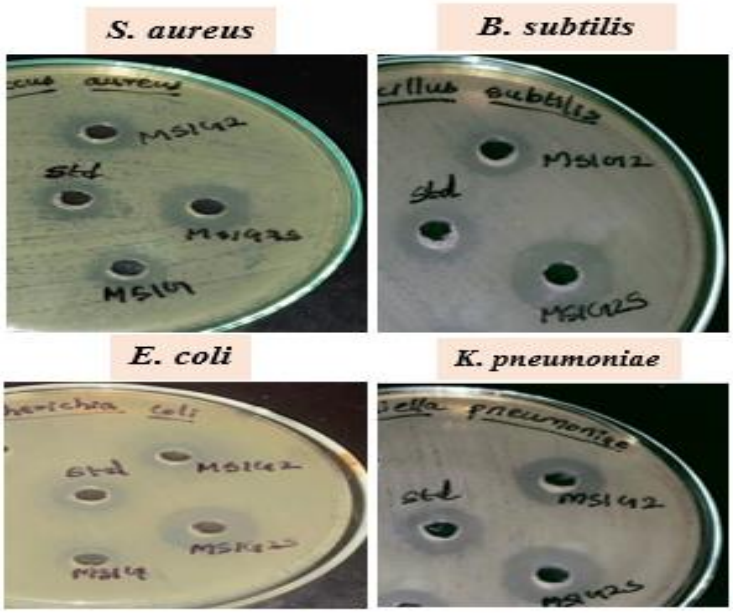

Figure 98. Antibacterial activity of garlic-nano encapsulated microspheres against *S. aureus*, *B. subtilis*, *K. pneumoniae*, and *E. coli*

Table 39. ZOI of blank, GH and MS1G against *S. aureus*, *B. subtilis*, *K. pneumoniae*, and *E. coli*

Sample code	Zone of Inhibition (mm)			
	S. aureus	*B. subtilis*	*K. pneumoniae*	*E. coli*
Std	12	14	15	12
MS1G	11	12	13	10
MS1G2	12	13	16	11
MS1G2S	**17**	**19**	**18**	**17**

The α-amylase inhibitory activity of garlic and garlic-nano encapsulated microsphere formulations (MS1G, MS1G2, and MS1G2S) was evaluated and compared to the standard antidiabetic drug, metformin. The dose-dependent inhibitory effect on α-amylase was observed for all formulations as given in **Figure 99**. The sample MS1G2S exhibited highest inhibitory activity, followed by MS1G2 and MS1G microspheres. At lower concentration of 100 µg/mL, the higher inhibition values were 82.39% (MS1G), 88.922% (MS1G2) and 89.32% (MS1G2S), respectively. The enhanced α-amylase inhibition observed in MS1G2S, could be due to the synergistic effect and interaction between the bioactive garlic derived sulphur compounds, and phyto stabilised gold and silver NPs.

Garlic containing major bioactive compounds, including Diallyl thiosulfinate (Allicin), S-allyl cysteine sulfoxide, S-allyl cysteine, E/Z ajoene, and other sulphur-based compounds. In addition, phenolic compounds such as Pyrogallol, Gallic acid, β-resorcylic acid, Rutin, and Quercetin, helps to reduce oxidative stress, protecting pancreatic cell injury, and effective in treating diabetic complications **(Shang *et al.*, 2019)**. Similarly, the addition of dates seeds aided GNPs, containing flavonoids and polyphenols; and SNPs synthesised from *Amphilophium paniculatum* leaf extract (containing terpenoids, alkaloids and phenolic acids), helps to enhance the bioactivity of the microsphere formulations. As discussed in **section 4.6**, these phyto stabilised metallic NPs possess antioxidant, antibacterial, antidiabetic and anticancer properties.

Moreover, the garlic-nano encapsulated microspheres (MS1G2S) exhibited significant antibacterial and α-amylase inhibition for antidiabetic activity. Therefore, the MS1G2S microsphere formulation exhibits multifunctional bioactive properties which could be recommended for pharmaceutical and therapeutic applications.

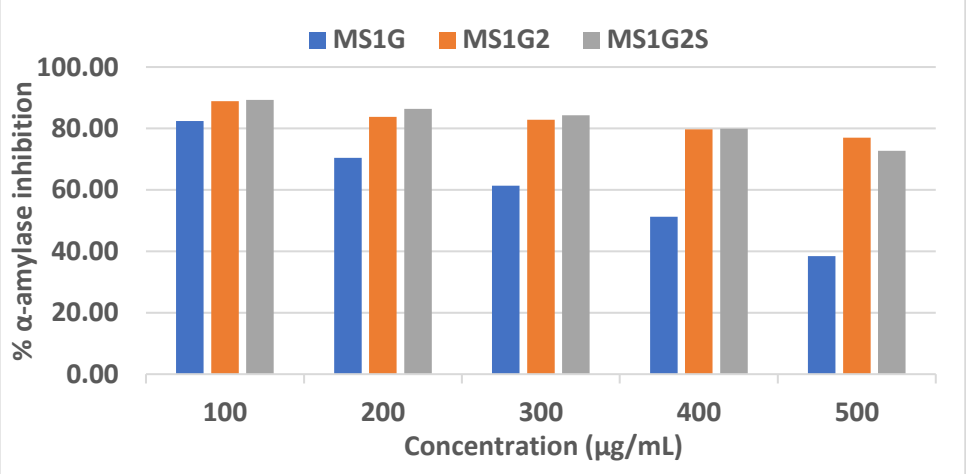

Figure 99. Antidiabetic α-amylase Inhibitory activity of garlic and garlic-nano encapsulated microspheres

4.6.6.3 Thermal Stability Analysis of Bioactive compounds in Garlic/Garlic-nano Encapsulated Microspheres

The thermal stability of garlic and garlic-nano encapsulated microspheres was evaluated using FTIR spectral analysis under three different temperature conditions such as room temperature (MS1G/MS1G2S), moderate heating at 40-50˚C (MS1G40/MS1G2S40), and high heating at 90-100 ˚C (MS1G100/MS1G2S100). The resulting FTIR spectra are shown in **Figure 100 and 101**.

For the garlic encapsulated microspheres (MS1G), the broad band at 3315 cm^{-1} corresponds to O-H stretching vibration of hydroxyl groups, due to residual solvent. The presence of thermally stable sulphur compound Allicin is confirmed by the distinct peak at 1044 cm^{-1} which is associated with sulfoxide (S=O stretching vibrations). The peak at 1636 cm^{-1} is attributed to C=C stretching within the allyl groups of Allicin and other sulphur compounds. The similarity of spectral profiles across all temperature conditions representing no major chemical degradation, which confirms the thermal production of encapsulated garlic bioactive compounds.

Similarly, the FTIR spectrum of garlic-nano encapsulated microspheres (MS1G2S), showed a broad O-H stretching band (3055-3355 cm^{-1}), a peak at 1630 -1635 cm^{-1} corresponding to C=C stretching within allyl group of Allicin, and a band at 1044 -1085 cm^{-1} represents S=O stretching vibrations, confirming the stable sulfoxide group of Allicin. In addition, the peaks at 405 - 437 cm^{-1} are assigned to C-metallic stretching vibrations confirmed the presence of stable encapsulation of GNPs and SNPs within the microsphere formulation. From the overall results, there is no significant peak shift or disappearance of the band at different temperature conditions, revealed the thermal stability of both formulations.

Therefore, the garlic fresh juice encapsulated microspheres effectively provided sufficient thermal protection for Allicin and their bioactive compounds, thereby enhancing the overall thermal stability of the garlic extract, resulting as more suitable carrier for thermally sensitive bioactive compounds.

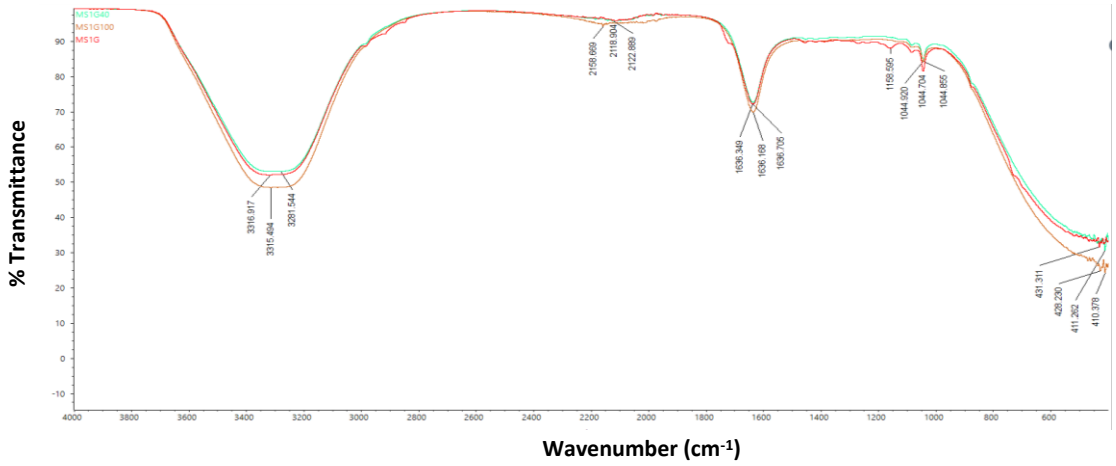

Figure 100. FTIR spectrum comparing the thermal stability of garlic fresh juice encapsulated microspheres (MS1G) at three different temperature conditions

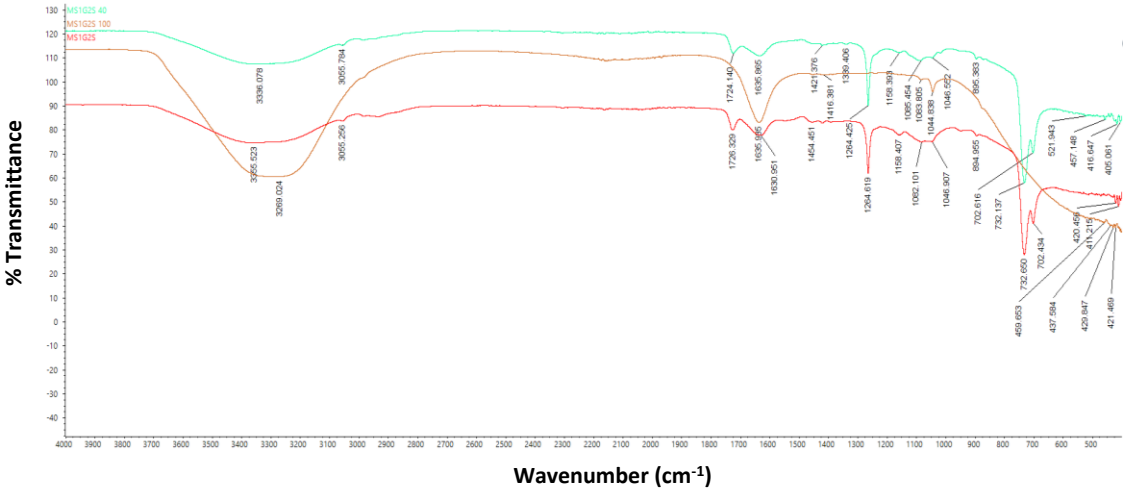

Figure 101. FTIR spectrum comparing the thermal stability of garlic-nano encapsulated microspheres (MS1G2S) at three different temperature conditions

4.6.6.4 *In vitro* Dissolution and Drug Release Kinetics of Nanoencapsulated Microspheres

The cumulative *in vitro* drug release of the nanodrug/ garlic-nano encapsulated microsphere formulations (MMS1AS, MMS1DG, MS1G2 and MS1G2S) over 120 h, and the cumulative percentage of drug release was determined, as shown in **Table 40 and Figure 102.**

All the formulations exhibited biphasic release pattern, comprises of initial lag phase, followed by sustained release pattern. The gradual trend of drug release pattern was observed in the initial phase (0 to 5 h), with a range of 2.21 to 4.02% at 0.5 h and 10.01 to 14.11% at 1 h, among all formulations maximum range of 26.89 to 36.48% at 5 h. In this first phase, where the hydration and swelling of polymer matrix occurs, therefore the slower diffusion of drug and bioactive components takes place. In particular, the PCL-PEG-HPMC polymer blend forms a

diffusion barrier which limits the burst or immediate release of drug and garlic metabolites. Therefore, the slower diffusion pattern suggested the drug-polymer interactions and effective encapsulation, which prevents the burst release attaining controlled drug delivery.

In the second phase (5 to 120 h), the drug release from all formulations possess stable diffusion erosion and sustained release profile. The prolonged exposure to dissolution medium the hydrophilic polymers (HPMC, PEG) tend to hydrate and undergo chain relaxation **(Siepmann and Peppas, 2001)**, whereas the semi-crystalline PCL softens and erodes **(Dash and Konkimalla, 2012)**. The near-linear release profile beyond 24 h to 120 h, and cumulative drug release values of 95 to 97% at 120 h, which revealed non-burst and diffusion-controlled release profile. Therefore, the biphasic release pattern confirms the nanodrug and garlic-nano loaded microsphere formulations as effective sustained release delivery system, by minimising the dosing frequency. Similar biphasic and diffusion-controlled sustained release patterns have been reported in poly (lactide-co-glycolide) based bicalutamide microspheres exhibited sustained release over 40 days **(Su *et al.*, 2022)** and in poly ethylene oxide/poly lactide composite nanofibers, possess a biphasic drug release profile for local cancer treatment **(Kuang *et al.*, 2018)**.

The release kinetics of all formulations were evaluated using zero order, first order, Higuchi and Korsmeyer-Peppas models **(Table 41).** The model fitting revealed that MMS1AS formulation exhibited the best fit with the Higuchi model (R^2= 0.9312), showing the diffusion-controlled mechanism. All the formulations such as MMS1DG (R^2= 0.9746), MS1G2 (R^2= 0.9704), and MS1G2S (R^2= 0.9839) showed good fitting with first-order model indicating the concentration dependent diffusion mechanism, wherein the rate of release is proportional to the amount of drug which is remained in the matrix. The low R^2 values of zero-order model indicates that release of drug did not occur at a constant rate. Korsmeyer-Peppas model (R^2= 0.56 to 0.68) showed that non-Fickian diffusion model represents that both the polymer relaxation and diffusion influence the release pattern. From the overall results, the release kinetic analysis revealed biphasic, diffusion-erosion controlled, sustained release mechanism, where the polymer matrix synergistically works to regulate the drug release. The hydrophilic polymer (HPMC and PEG) has water absorption and swelling properties, whereas PCL leads to mechanical stability and controlled erosion. Therefore, the non-burst, and prolonged release extending was noted up to 120 h, exhibited potential microspheres for sustained drug delivery application.

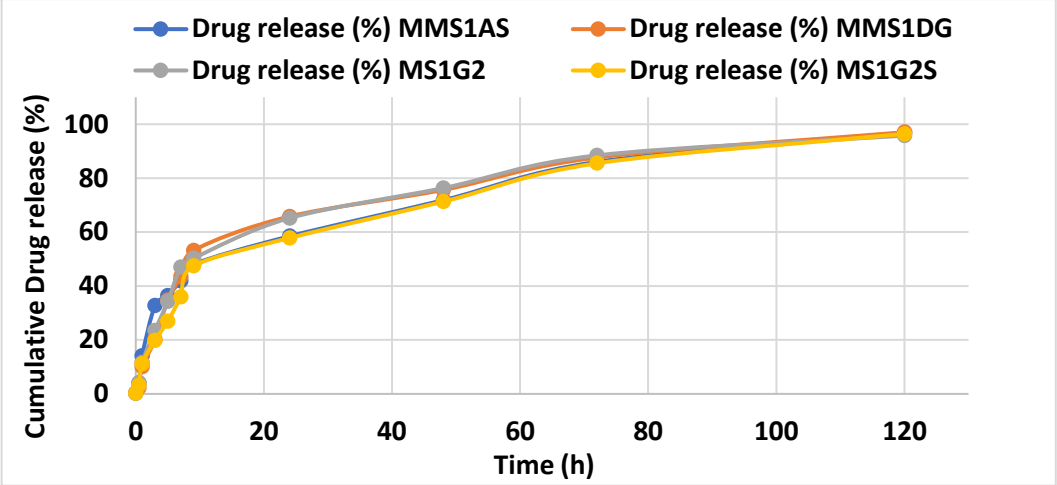

Figure 102. Graph represents the drug release (%) of MMS1AS, MMS1DG, MS1G2 and MS1G2S by varying time (h)

Table 40. Cumulative Drug Release (%) of Nanoencapsulated Microspheres by Varying Time (h)

Time (h)	Drug release (%)			
	MMS1AS	MMS1DG	MS1G2	MS1G2S
0	0.23	0.35	0.24	0.23
0.5	4.02	2.21	3.96	3.19
1	14.11	10.01	11.61	11.16
3	32.73	20.13	23.46	19.80
5	36.48	34.77	34.29	26.89
7	41.94	43.38	46.93	36.00
9	48.04	53.14	50.29	47.42
24	58.45	65.78	65.20	57.81
48	71.82	75.64	76.32	71.29
72	86.03	87.64	88.44	85.52
120	96.80	97.03	95.76	96.43

Table 41. Drug Release Kinetics Model Fitting of the Formulated Microspheres

Sample code	MODEL NAME (R^2)			
	Zero order	First order	Higuchi	Koresmeyer-Peppas
MMS1AS	0.7617	0.2628	0.9312	0.5661
MMS1DG	0.724	0.9746	0.9104	0.6808
MS1G2	0.723	0.9704	0.913	0.6042
MS1G2S	0.7948	0.9839	0.9525	0.6353

Phase -VI Industrial Applications of Metallic Nanoparticles

4.7 Fabrication of Microbial-Resistant and Ultraviolet Rays-Protective Fabrics for Textile Applications

Expanding upon the biological applications of metallic NPs, we have developed performance-oriented silver nanoparticles to improve textile functionality. Additionally, we have utilised top-down approach using ball milling technique to synthesise nanoparticles from bulk materials, thereby improving the performance of nano dye-coated fabrics with enhanced microbial resistance and ultraviolet protection.

4.7.1 Preparation and Characterisation of Ball Milled Red Sandal Powder

The commercially available red sandal powder was subjected to time dependant ball milling for 30 min, 6 h, 12 h, 14 h and 16 h to obtain ball milled red sandal powder (BMRSP). At each interval, the samples were collected and the average crystallite size was calculated from the XRD patterns. The reduction in particle size for ball milled samples as depicted in **Table 42**. The results showed a decrease in particle size with increasing milling duration. Initially, the commercially available unprocessed red sandal powder exhibited the crystallite size of 69 nm. After 30 min of ball milling, the particle size was reduced to be 62.06 nm, and continued to decrease gradually to 43.91, after 16 h of milling. This complete particle size reduction is due to continuous agitation, mechanical impact and attrition during the milling process. The use of large sized balls in ball mill facilities the breakdown of bulk materials into smaller (fine) particles even down to nanoscale. These processes exhibited the effectiveness of the ball milling technique in reducing bulk materials to NPs with prolonged milling time. The powder XRD pattern of BMRSP after 16 h of ball milling is shown in **Figure 103**. The major diffraction peaks at 2θ values of 21.08˚, 26.89˚, 27.24˚, 50.40 ˚, 60.22˚, and 68.54˚, along with several minor peaks was noted. These crystalline peaks are likely associated with the chemical constituents of red sandal wood powder. The peak at 21.08˚ suggesting the presence of crystalline cellulose **(Poletto *et al.*, 2014)**, while remaining crystalline phases may relate to minerals or other inorganic elements naturally present in plant material.

Table 42. Time Dependant Particle Size Reduction of Ball Milled Red Sandal Powder

Time of Ball milling (h)	Sample code	Crystallite size (nm)
0.5	BMRSP 30	62.06
6	BMRSP 6	60.30
12	BMRSP 12	58.06
14	BMRSP 14	56.70
16	**BMRSP**	**43.91**

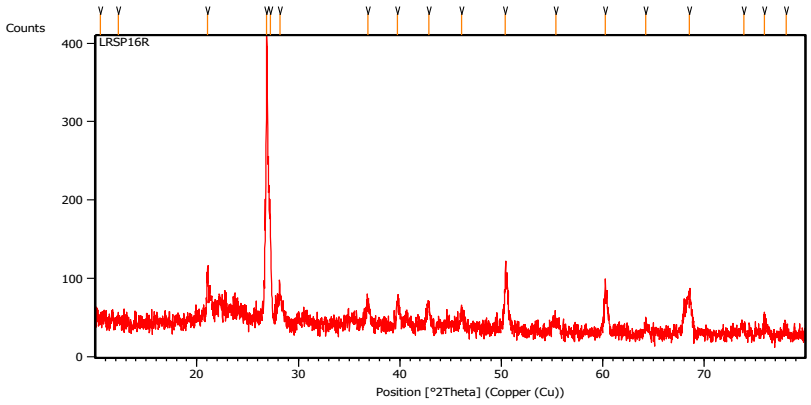

Figure 103. XRD pattern of Ball milled red sandal powder after 16 h milling

To achieve a homogeneous dispersion, both BMRSP (ball milled red sandal powder after 16 h) and RSP (raw red sandalwood powder) samples were dispersed in an aqueous medium and subjected to sonication for 15 min, followed by ultra-homogenisation for 20 min. After homogenisation, the dispersions were left undisturbed to facilitate sedimentation of large particles. The resulting fine supernatant was used for determining the morphology, size and elemental composition. FESEM and EDS spectral analysis of both RSP and BMRSP are shown in **Figure 104a, 104b, and 105a, 105b,** respectively. The FESEM image of RSP sample revealed a polygonal shaped morphology with an average particle size of 0.464 µm. EDS mapping confirmed the presence of C, O, Na, Mg, Si, Mo, K and Ca. The presence of Si was attributed to glass substrate used during sample coating, while the remaining elements are from sample itself.

FESEM image of the BMRSP sample exhibited the formation of clusters with spherical morphology, with a significantly reduced average particle size of 32.93 nm. EDS analysis of BMRSP confirmed the presence of C, O, Na, Mg, Si, K and Ca, while Mo was not detected which may be due to mechanical degradation or surface element redistribution during ball milling and dispersion process.

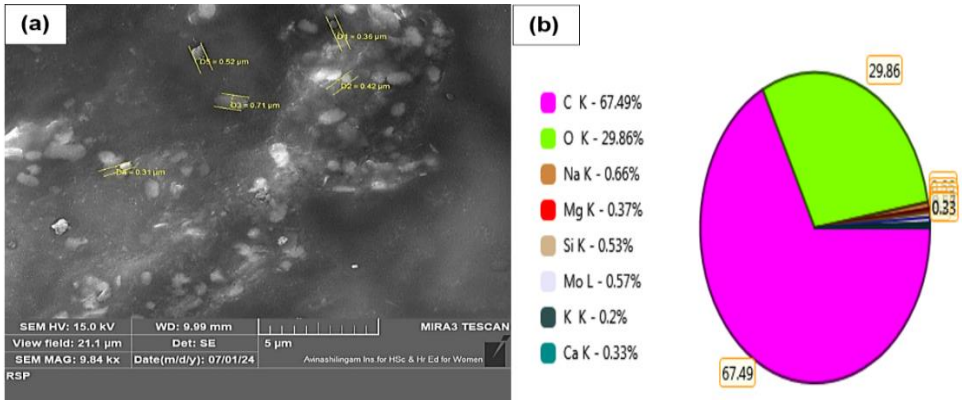

Figure 104. FESEM image of red sandal wood powder (a); EDS pie chart (b)

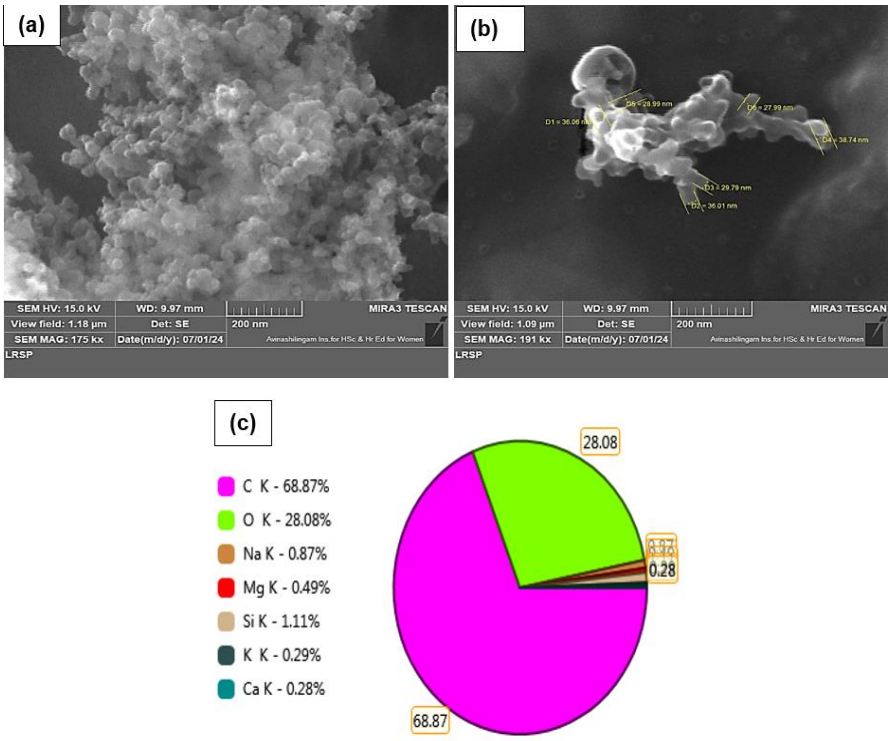

Figure 105. FESEM image of ball milled red sandal wood powder (BMRSP) at 200 nm (a); particle measured at 200 nm (b);EDS pie chart (c)

Similar studies have explored high impact ball milling to prepare nano aluminium oxides, resulting in a uniform dispersion after 20 h of milling. With continuous milling of particle resulted in size reduction and developed spherical morphology **(Han *et al.*, 2016)**. A co-precipitation method was adopted to synthesise nanocomposites (Ca-Fe hydrocalumite layered double hydroxide with a sunscreen agent) and post-synthetic ball milling enhanced its UV-blocking performance, particularly around 320 nm **(Szabados *et al.*, 2024)**. Similarly, ball milled *Moringa oleifera* leaf powder for 8 h reduced the particle size from 3.7 µm to 0.72 µm and decreased the crystallite size from 29.92 nm to 16.27 nm **(Sakr *et al.*, 2023)**. A recent

review highlights the potential use of synthesised ball milled nanomaterials in various applications such as adsorption, battery, electrode, water purification materials, high performance catalysts, supercapacitors, solar cells, agriculture, food industry and cosmetics **(Ali *et al.*, 2025)**.

4.7.2 Surface Pre-Treatment of Cotton Fabrics

4.7.2.1 Effect of Exposure Time in O_3, UV and O_3/UV Treatment on Dyeing Performance of Cotton Fabrics

Cotton fabric (2*2 cm^2) was pre-treated by individually exposed with O_3, and UV treatment at varying time (30 min, 60 min, 90 min, and 120 min). Initially, to optimise the exposure time of cotton fabric in dry O_3/UV treatment, the surface pre-treated cotton fabrics was dyed with alkali extract of ball milled red sandal powder (BMRSP). The difference in weight of fabric before treatment and pre-treated dyed cotton fabric are given in **Table 43.**

Table 43. Percentage weight gain of O_3, UV and combined dry O_3/UV pre-treated BMRSP dyed cotton Fabric at Different Time of Exposure

Exposure time (min)	**Untreated fabric**	**Dry O_3 pre-treated BMRSP alkali dyed cotton fabric**			
		S1CO	**S2CO**	**S3CO**	**S4CO**
	-	30	60	90	120
Weight (mg)					
Before dyeing	37.99	37.99	37.99	37.99	37.99
After Dyeing	51.1	48.2	53.8	56.2	50.3
% Weight gain of fabric	25.65	21.18	29.38	32.40	24.81
Exposure time (min)	**UV pre-treated BMRSP alkali dyed cotton fabric**				
	S1CUV	S2CUV	S3CUV	S4CUV	
	60	120	180	240	
Weight (mg)					
Before dyeing	37.99	37.99	37.99	37.99	
After Dyeing	49.0	50.0	40.0	47.5	
% Weight gain of fabric	22.46	24.02	20.1	20.02	
Exposure time (min)	**Dry O_3/UV pre-treated BMRSP alkali dyed cotton fabric**				
	S1COUV	S2COUV	S3COUV	S4COUV	
Dry O_3 treatment	30	60	90	120	
UV treatment	120	120	120	120	
Weight (mg)					
Before dyeing	37.99	37.99	37.99	37.99	
After dyeing	52.3	53.8	58.8	51.6	
% Weight gain of the fabric	27.36	29.38	35.39	26.37	

From the results, the increased weight of O_3 treated BMRSP dyed samples as compared with untreated dyed fabric. The maximum percentage weight of BMRSP dyed fabric was found to be 32.4% (S3CO) at optimised exposure of O_3 treated for 90 min. Similarly, for the UV pre-treated fabric, the maximum % weight gain of dyed fabric (S2CUV) was found to be 24.02%, at exposure time of 120 min. To maximise the effect of pre-treatment, the combined effect of dry O_3 /UV treatment was performed, by varying the exposure time of ozone (30 to 120 min) and keeping UV treatment as constant at 120 min. The combined effect of dry O_3/UV-treated sample has gained weight after dyeing. The increase in BMRSP dyed fabric weight (S3COUV) was found to be maximum (35.39%) in the sample exposed to dry O_3 for 90 min and UV radiation for 120 min, respectively. The decrease in the weight of the fabric was observed when the duration of the O_3 treatment increased further. The combined dry O_3/UV treatment showed a noticeable improvement in dye uptake compared to individual dry O_3 and UV treatments. The increase in weight of the fabric could be due to the increased uptake of dye (**Table 43**). Hence, the combined dry O_3/ UV treatment (S3COUV) was used for the subsequent study.

Based on the previous results, the large sized cotton fabric was pre-treated with combined dry/wet O_3 (i.e. without water/with water) for 90 min, followed by UV treatment for 120 min. After dyeing the weight gain of the dyed fabric such as COUVS3 and CWOUVS3 was found to be 15.7 g and 16.13 g as given below. From the results, the combination of wet/dry O_3 and UV treatment was considered to be more effective than either treatment alone. The colour strength (K/S) of CWOUVS3 and COUVS3 fabric was found to be 68.297 and 63.059, respectively. The increased colour strength was observed for dry O_3 (without water)/UV treated fabric dyed with BMRSP alkali extract. Therefore, the combined dry and wet O_3 /UV treatment exhibited to increase the overall efficiency of dye uptake.

Sample code	Treatment performed	Weight of fabric Before dyeing (mg)	Weight of fabric Before dyeing (mg)	Weight gain of dyed fabric (mg)	Colour strength (K/S)
CWOUVS3	Wet O_3/UV	60.7113	76.8470	16.135	68.297
COUVS3	Dry O_3/UV	61.8423	77.5492	15.706	63.059

Recent report on O_3 based treatment on cotton fabric at four different stages includes ozonation - during dyeing (45 min), dry ozonation before dyeing (10 min), wet ozonation before dyeing (1 min), and ozonation after dyeing (10 min). Colour strength (K/S) value was higher for ozonation after dyeing compared with conventional dyeing. Increased concentration of O_3 beyond 30%, exhibited decreased colour strength values, due to high amount of nascent oxygen

[O] creates negative impact on fabric dyeing. Therefore, ozone treated dyed fabric achieved higher K/S values, fastness properties and considerable reduction in time and dye sludge **(Anam *et al.*, 2024)**. Similar study on O_3 treatment in fabrics helps to improve the cellulose functionalisation, and decrease its molar mass by removing impurities. Furthermore, O_3 gas combined with UV treatment oxidizes the cellulose surface, and undergo converting aldehyde or hydroxyl groups of fabric to carboxyl or carbonyl functionalities, thereby enhancing the fabric's dye adsorption properties **(Valls *et al.*, 2022)**.

4.7.2.2 Combined dry O_3/UV/Plasma treatment and Plasma-alone treatment

To determine the combined effect of plasma treatment with combined dry O_3/UV treatment, the cotton fabrics of 2*2 cm^2 were surface pre-treated with O_3/UV/plasma treatment and plasma treatment alone for 45 min. One set of pre-weighed fabrics was treated with dry O_3 for 90 min, UV for 120 min, and plasma for 45 min. Another set of pre-weighed fabric was treated only with plasma for 45 min. After each surface treatment, the weight of treated cotton fabrics was noted. All the fabric treatments were done in triplicate (n=3). The whiteness index, brightness index, yellowness index and colour co-ordinate values (L*, a*, b*, c* and H*) were recorded using color lab measurement software. The average weight of cotton fabric before and after treatments are given in **Table 44**.

Table 44. Average Weight and Colour Strength of Cotton Fabric Before and After Surface Treatments

Treatment performed	Weight of fabric (mg)	Whiteness Index	Brightness Index	Yellowness Index	L*	a*	b*	C*	H*	K/S value
Before Surface treated	49.9	20.00	21.71	4.637	47.7	0.93	0.66	1.14	35.3	23.6
After dry O_3 treated	50.4	17.86	20.4	7.62	47.0	1.09	1.32	1.74	48.1	25.5
After dry O_3/UV treated	49.1	18.9	21.20	6.6	46.9	1.00	1.14	1.52	48.6	24.2
After dry O_3/UV/Plasma treated	48.16	18.8	21.25	6.89	28.2	0.79	0.96	1.25	49.9	30.7
After plasma treated	52.3	19.47	21.54	5.41	47.8	0.96	0.83	1.27	40.8	23.7

The results obtained from the surface treated fabrics with combined dry O_3/UV/ plasma and only plasma-treated cotton fabrics shows weight loss of 1.74 mg and 0.6 mg. The initial fabric weight was slightly increased (1 mg) after O_3 treatment due to the oxidizing effect, and a decrease in weight (1 mg) was noted due to exposure to UV radiation for 120 min. Finally, the same cotton fabric was exposed to plasma treatment, and decreased fabric weight was observed. Similarly, plasma alone-treated fabric shows loss of fabric weight due to the formation of more polar groups on the surface of the fabrics and becomes hydrophilic surface, helps in improving the absorption of dye rate. International Commission on Illumination (CIELAB color space) referred to L*, a*, b*, C*, and H* used to assess the colour difference from the known standard. L* represents lightness (L*=100 means perfectly reflecting diffuser), and L*=0 represents perfect black; the values of a*is greater than zero indicate redness and lesser than zero indicates greenness; values of b* greater than zero represents yellowness, and lesser than zero indicates blueness of sample. C* and H* show chroma and hue values, which are determined from the values of a* and b* colour co-ordinates **(Smith, 1997)**.

From both treatments, the whiteness index values decreased due to an increase in the yellowness index when fabrics are applied with O_3, UV radiation and plasma current. There is a slight decrease in brightness index values due to the effect of treatment. Similarly, the colour co-ordinates values lightness (L*) and a* values are decreased after combined (dry O_3/UV/Plasma) treatment and plasma-treated fabrics showed the constant positive values observed for L* and a* co-ordinates. For combined (dry O_3/UV/Plasma treated) fabrics, show L* average value of 28.2 which reduced from 47.7, a* value 0.7 reduced from 0.9, b* value 0.9 increased from 0.6, C* chroma value 1.2 slightly increased from 1.1 and H* hue value 49.9 increased from 35.3, respectively.

On the other hand, plasma alone-treated fabrics show the L*value of 47.8 from 47.7, a* values of 0.9, b* values of 0.8 slightly increased from 0.7, C* values of 1.2 remains constant with untreated fabric and H* values of 40.8 have been increased from 35.9, respectively. Therefore, slight increase or decrease in colour co-ordinates values were noted with respect to untreated fabrics. The positive hue angle (H*) values of combined dry O_3/UV/Plasma and plasma alone-treated fabrics of +14.6 and +4.9 indicates counter clockwise to untreated fabrics' color space values. Therefore, combined dry O_3/UV/Plasma-treated fabrics are more yellow than plasma alone-treated fabrics. The color space (L*C*h*) and (L*a* b*) values determine the plasma-treated process is more preferred over other method.

4.7.2.3 Dyeing of Surface Pre-Treated (Combined dry O_3/UV/Plasma and Plasma alone) Cotton Fabrics

Initially, the cotton fabric (2*2 cm^2) was surface pre-treated with combined dry O_3/UV/Plasma and plasma alone-treated samples, which was dyed with *Tristellateia australasiae* ethyl acetate (TAEA) extract, due to maximum yield of 67.14% with dark brown colour (as mentioned in 4.4). The weight gain and colour strength of pre-treated dyed fabrics is given in **Table 45.** From the results, it was observed that plasma-treated dyed fabric showed weight gain (17.5 mg) with a higher colour strength (115.1) value compared to the combined O_3/UV/Plasma-treated dyed samples. Therefore, for the other composite dye extract, we adopted plasma surface treatment on cotton fabric followed by the dyeing process. All dye-coated fabric samples were done in triplicate and the average mean values are represented in this study. The pre- treated weighed cotton fabrics were plasma treated and dyed using BMRSP alkali extract, TAEA+BMRSP (1:1), TAEA+BMRSP (1:1) + ionic liquid - IL (0.1) % and silver nanocomposite dye (TAEA+BMRSP (1:1) + IL (0.1) % + SNP) solutions. The dyed fabrics showed an increase in weight gain and colour strength values as given in **Table 45**. Similarly, without surface treatment, the conventional method (C5) of dyeing the fabrics was done with TPTBISD nanocomposite dye solution. The increased weight gain (39.2 mg) and colour strength (K/S value =160) of the C5 fabric sample was also observed. From the results, it is well evidenced that the extract dye solutions were well adsorbed into the fabric material treated with plasma alone for 45 min, which increases wettability or adhesion of dyes in fabrics due to the hydrophilic surface plasma treatment in cotton fabrics.

Colour strength (K/S) is defined as numerical value which shows the interaction between fabric matrix and dye molecules, which are determined through Kubelka-Munk equation, which is directly proportional to dye concentration. In general, as dye concentration increases, the presence of dye molecules in dye bath also increases, which results in increased dye uptake to the fiber, leads to higher K/S values. Therefore, the K/S values greater than 100, indicating the high concentration of composite dye formulation leads to dye anchoring and densely packed surface coating **(Jabar *et al.*, 2021)**. The author reported the colour strength percentage of blue pigment dyed cotton fabrics with and without plasma treatment by spectrophotometer. The plasma treated fabrics results in increased etching and oxidation rate with high plasma current (130 to 170 W), which increases the surface area and improved wicking ability of dye on to the fabric. The increased colour yield (K/S) percentage of plasma

untreated pigmented fabric is 100% and plasma treated dyed fabric results greater than 100%, which means increased colour strength yield **(Kan and Man, 2017)**.

Table 45. Weight Gain Observed After Dyeing Cotton Fabric and Colour Strength (K/S) of the Cotton Fabric Dyed with Different Dye Solutions

Sample code	Weight gain observed after dyeing fabric (mg)	Colour strength (K/S) of dyed fabric	Sample code	Weight gain observed after dyeing fabric (mg)	Colour strength (K/S) of dyed fabric
Blank	-	24.6	TPTBD	29.7	104.0
TPTD	17.5	115.1	TPTBID	39.3	111.0
TOUPTD	24.4	108.6	TPTBISD	38.1	161.5
TPBD	20.6	72.7			

Similar studies on plasma assisted pre-treatment-based surface modification of fiber, helped to increase the soy protein dye uptake. The increased colour strength (K/S) values was observed from 1% to 6%, with plasma surface treated dyed fabrics. The plasma surface treatment of fabrics leads to surface etching, and micro-cracks on the fiber, enhances the dye particles to enter the fiber, thereby increases the dye uptake and colour strength **(Li *et al.*, 2023)**. Recently, plasma pre-treated surface improved cotton fabrics coated with silver nanocomposites, improved adhesion is due to high concentration of oxygen-rich functional groups and roughness of fabric surface, enhanced the absorption of silver nanoparticles on cotton fabric. The silver nanocomposite coated fabrics exhibited greater antibacterial activities and retained the activity up to 30 washes **(Sasiporn *et al.*, 2025)**.

4.7.2.4 Characterisation of Dyed Fabrics

4.7.2.4.1 FTIR spectra of blank and dyed cotton fabrics

The FTIR spectra of blank cotton fabric (B), wet O_3/UV pre-treated dyed cotton (CWOUVS3), dry O_3/UV pre-treated dyed cotton (COUVS3), TPTBID and TPTBISD dyed fabric was recorded to evaluate the structural and functional modifications of the fabric coated with samples containing extract, ionic liquid (IL) and silver nanoparticles.

FTIR spectra of blank cotton fabric (B) illustrates the characteristic peaks at 3332.99, 2924.09, 1157.29, 1103.28, 1026.13, 686.66, and 609.51 cm^{-1} **(Figure 106)**. A minor peak appeared at 3332.99 cm^{-1} corresponds to free O-H stretching vibrations from surface moisture or atmospheric interference, which is not associated with intramolecular bonding in cellulose fiber **(Smith, 2011)**. The characteristic minor peak in the region of 2924.09 cm^{-1} attributed to C-H

stretching vibrations of aliphatic methylene groups (-CH_2), which are displayed due to cellulose in natural fiber. The peak at 1157.29 cm^{-1} corresponds to C-O-C asymmetric stretching which indicates the ether linkages between the glucose units in cellulose. In addition, C-O stretching vibrations in secondary and primary alcohols appears between 1200 to 1000 cm^{-1} **(Pavia *et al.*, 2014)**, confirming the characteristic hydroxyl structure of cellulose. The characteristic peak in the finger print region includes 686.66 cm^{-1}, 609.51 cm^{-1}, 540.07 cm^{-1}, 486.06 cm^{-1}, 468.07cm^{-1}, 439.77 cm^{-1}, and 428.91 cm^{-1} are associated with C-H out of plane bending and ring deformation of anhydroglucose units. Therefore, the absence of aromatic or phenolic groups, further confirms the undyed cotton fabric.

The FTIR spectra of cotton fabrics pre-treated with combined dry and wet O_3/UV and dyed with alkali extract of ball milled red sandal wood powder assigned as COUVS3 and CWOUVS3 are presented in **Figure 107 and 108**, respectively. The FTIR spectrum of COUVS3 **(Figure 107)** revealed several distinct peaks which confirms the incorporation of dye-fiber interactions and surface modification of dry O_3/UV treatment. The prominent broad peak at 3332.99 cm^{-1} corresponds to O-H stretching vibration, due to hydrogen bonded hydroxy groups in cellulose fiber and phenolic functional groups of red sandal wood dye. The peak at 1558.48 cm^{-1} corresponds to aromatic stretching of C=C or N-H bending vibrations, which is due to compounds present in the natural dye. The characteristic peak at 1404.18 cm^{-1} attributed to C-H bending or phenolic O-H deformation, which further confirming the presence of aromatic hydroxyl groups. In addition, the strong peak at 1157.29 cm^{-1}, 1103.28 cm^{-1}, and 1026.13 cm^{-1} corresponds to C-O-C asymmetric stretching and C-O stretching of primary and secondary alcohol indicates the possible ether linkage with fiber and dye. Further, the appearance of 848.68 cm^{-1} attributed to aromatic C-H out of plane bending, suggesting the surface treated dye absorption. Additional peaks in the finger print region (671.23 cm^{-1}, 594.78 cm^{-1}, and 493.78 cm^{-1}) indicate aromatic ring deformation and skeletal bending which was altered by O_3 induced oxidation.

Similarly, FTIR spectra of CWOUVS3 **(Figure 108)**, involved wet O_3/UV pre-treatment BMRSP dyed cotton fabric illustrates the characteristic peak at 3286.70 cm^{-1}, slightly broader and shifted as compared to COUVS3, suggesting the enhanced hydrogen bonding interactions due to aqueous pre-treatment of O_3. The peak at 1550.77 cm^{-1}, and 1411.89 $cm^{-1,}$ represents aromatic ring vibrations and C-H or O-H bending, respectively. The peak at 1157.29 cm^{-1}, 1103.28 cm^{-1}, and 1026.13 cm^{-1} corresponds to C-O-C asymmetric stretching and C-O stretching of primary and secondary alcohols, indicates the possible ether linkage with fiber and

dye. The notable peak appeared at 570.93 cm^{-1} which is not present in COUVS3, possibly due to oxidative functionalities or strong bonding interactions between dye molecules and cotton fiber. The other minor peaks of 601.79 cm^{-1}, and 447.49 cm^{-1} attributed to skeletal vibrations or C-X resulting from O_3 induced modifications.

Therefore, both pre-treated methods exhibited chemical bonding with ball milled red sandal wood dye and cotton fiber. However, the wet O_3/UV pre-treated fabric (CWOUVS3) enhanced the hydrogen bonding, appearance of additional oxidation peaks and deeper dye penetration, which are evident from the broader and shifted peaks with presence of additional peaks in fingerprint region.

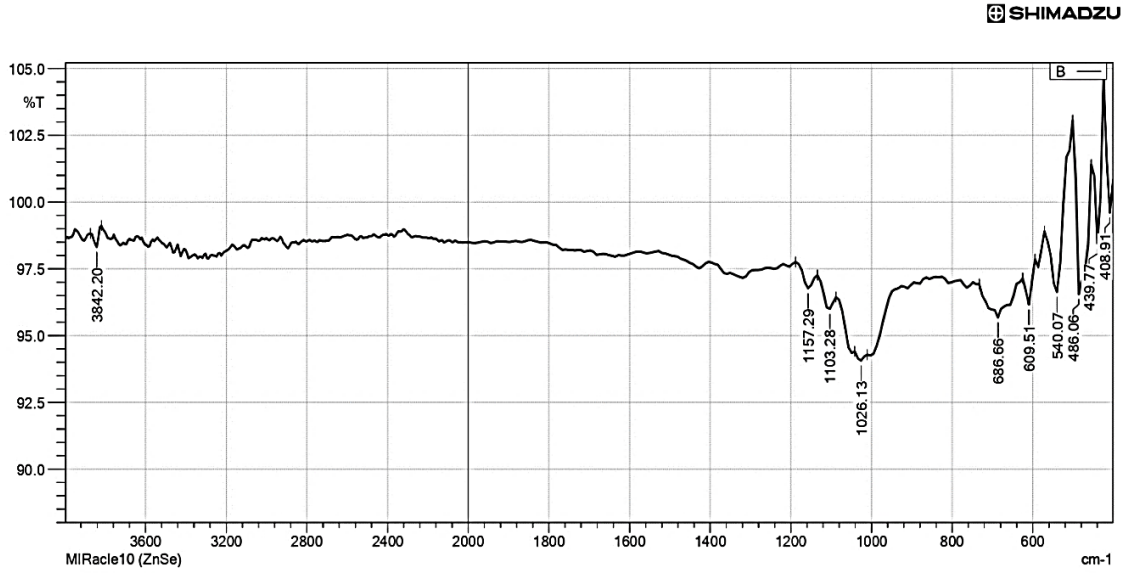

Figure 106. FTIR spectrum of untreated blank cotton fabric (B)

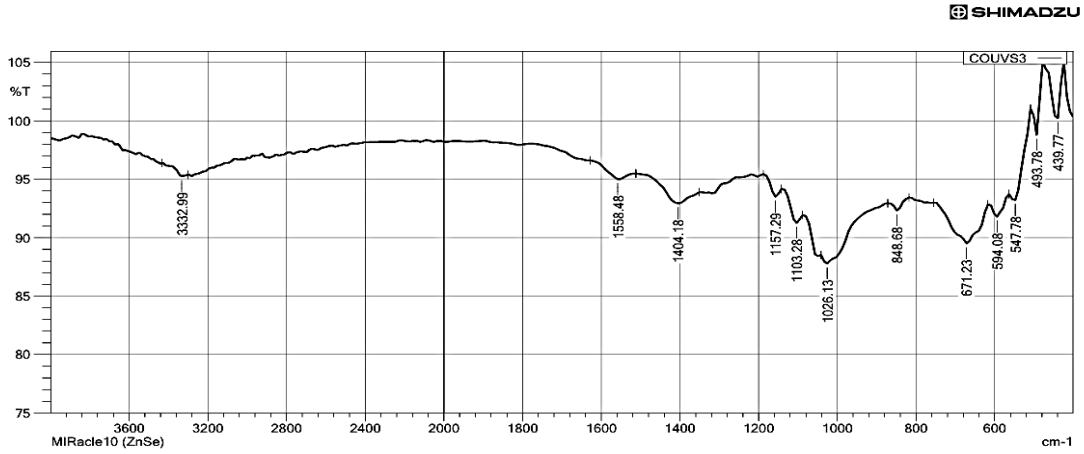

Figure 107. FTIR spectrum of dry O_3/UV pre-treated BMRSP dyed fabric (COUVS3)

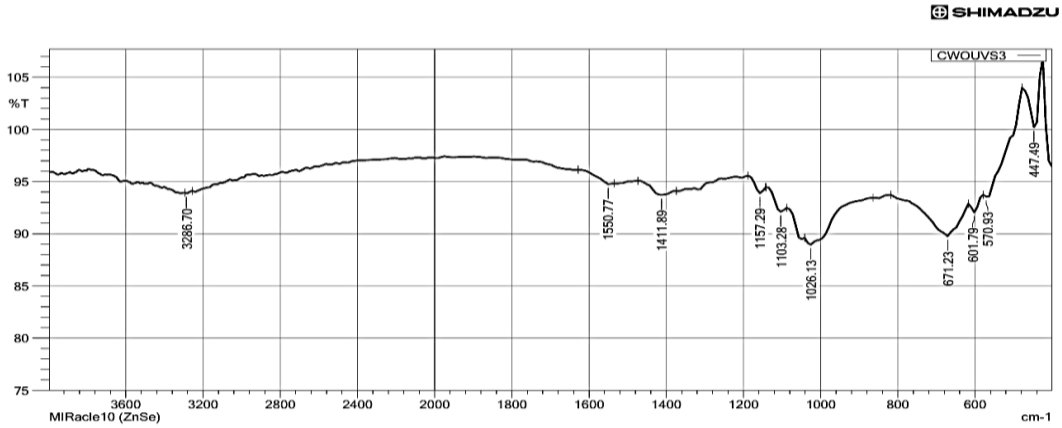

Figure 108. FTIR spectrum of wet O_3/UV pre-treated BMRSP dyed fabric (CWOUVS3)

FTIR spectrum of plasma pre-treated cotton fabrics dyed with composite dye solutions formulated from *Tristellateia australasiae* (TA) ethyl acetate extract, ball milled red sandal powder (BMRSP), ionic liquid (BMIMCl) and optionally, TAE aided silver nanoparticles (TAES NPs) were analysed to investigate the dye-fabric incorporation. The plasma pre-treated fabric dyed without SNPs was assigned as TPTBID, while with the addition of TAES NPs was labelled as TPTBISD.

FTIR spectra of TPTBID **(Figure 109)**, the plasma treated cotton fabric dyed with a composite of *Tristellateia australasiae* extract, BMRSP, and BMIMCl - IL, shows the peaks at 1442.75 cm^{-1} (aromatic C=C stretching and CH_3 bending), and a peak at 1018.47 cm^{-1} corresponds to C–O stretching of phenolic or alcoholic groups from the natural dyes. The appearance of new minor peaks at 848.68 cm^{-1} is attributed to the out of plane bending of aromatic C-H bonds. The other minor peaks at 554.95 cm^{-1}, 486.06 cm^{-1}, and 462.92 cm^{-1} related with IL-related vibrational bands, suggesting the presence of IL on the cotton surface.

Similarly, TPTBISD dyed cotton fabric coated with TAE aided SNPs in addition to natural alkali dye and IL composition as shown in **Figure 110**. The spectrum shows similar peaks related to C-O and aromatic stretching with notable shifts in aromatic region at 1365.60 cm^{-1}, suggesting the interaction of SNPs with phenolic or carbonyl groups. The shifted peaks in finger print region at 848.68 cm^{-1} and 894.97 cm^{-1} corresponds to aromatic C-H bending. The appearance of strong peak at 663.51 cm^{-1} is due to metal-ligand interactions between SNPs and phenolic groups in dye. The medium peak at 555.50 cm^{-1} in both dyed fabrics possess C-Cl (alkyl halide) stretching due to the utilisation of BMIMCl as an ionic liquid in the dye solution. Also, the SNPs-coated dye fabrics possess a C-metallic peak at 470.63 cm^{-1} and 424.34 cm^{-1}, confirmed the SNPs, as coating agent on the surface of treated cotton fabrics.

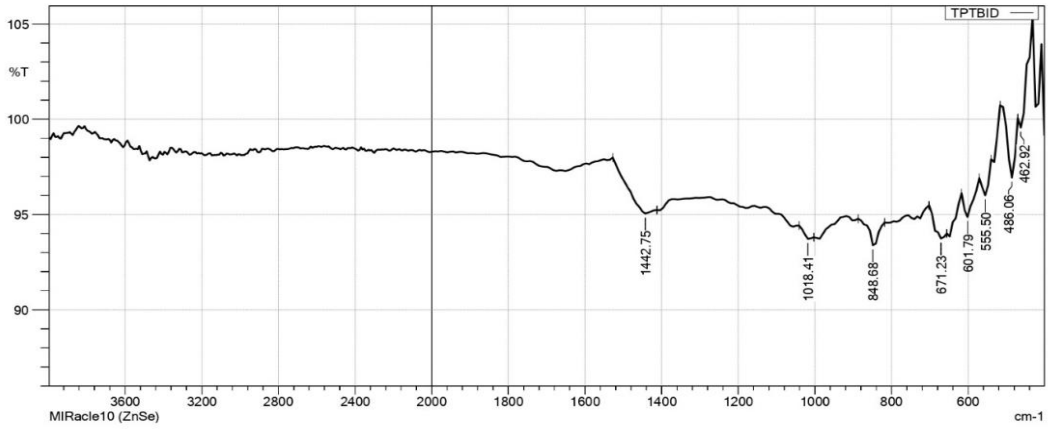

Figure 109. FTIR spectrum of TPTBID dyed fabric

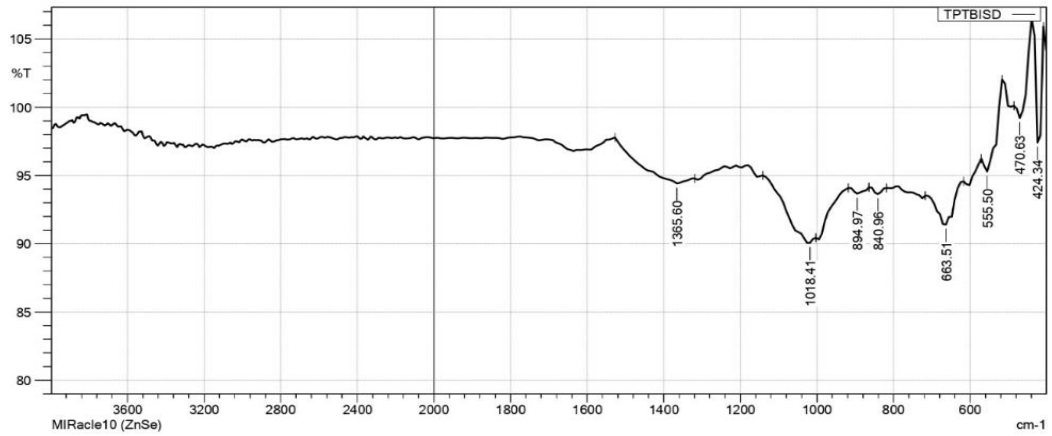

Figure 110. FTIR spectrum of TPTBISD dyed fabric

4.7.2.4.2 XRD pattern of blank and dyed cotton fabrics

Various cotton fabric samples including blank untreated cotton, wet and dry O_3/UV pre-treated dyed cotton (CWOUVS3 and COUVS3), composite dye-coated fabrics treated with O_3/UV/Plasma (TOUPTD), and plasma treated dyed fabrics (TPTBID and TPTBISD) were evaluated using XRD to determine the crystallite nature of samples. **Figure 111a**, represents the XRD pattern of bleached cotton fabric (B) exhibits a diffraction peak at $2\theta \sim 23.1^{\circ}$, corresponds to (200) planes of cellulose, indicates the semi-crystalline structure. This result was on par with the previous report by **Kwak *et al.*, 2015**.

XRD pattern of COUVS3 sample (dry O_3/UV pre-treated cotton fabric dyed with BMRSP alkali dye) exhibited the presence of cellulose crystallinity and additional crystalline peaks which are associated with dye-fiber interactions of the natural dye. The major diffraction peak at 26.93° suggesting the crystalline nature of aromatic compounds or phytoconstituents from BMRSP upon surface binding. This peak is not observed in blank cotton fabric and cellulose associated peaks were appeared at $2\theta = 20.18^{\circ}$, which matches the semi-crystalline

structure of fabric even after dry O_3/UV pre-treatment and dyeing with BMRSP. The other minor additional peaks at 50.43˚, and 60.42˚ supports the incorporation of BMRSP dye components which improved the dye crystallite on the fabric surface. The average crystallite size of COUVS3 was 40.65 ˚as shown in **Figure 111b**. Similarly, for combined wet O_3/UV pre-treated (CWOUVS3) and BMRSP alkaline dyed cotton fabric showed several distinct diffraction peaks indicating the presence of dye-fiber related crystalline formation. The major peak at 2θ = 23.77˚, corresponds to cellulose, represents the semi-crystalline nature of the cotton fabric after it underwent pre-treatment and dyeing. The additional diffraction peaks at 15.47˚, 17.46˚, 20.22˚ and 21.51˚ are also associated with lower angle planes of cellulose, which are rearranged during alkaline dyeing of fabric with BMRSP. The other diffraction peaks at 27.33˚ attributed to crystalline dye components of BMRSP on cotton surface. The crystallite grain size of CWOUVS3 was found to be 21.19 nm as shown in **Figure 111c**.

Therefore, compared to COUVS3, the CWOUS3 exhibited broader and more diverse peaks with lower intensity, which suggested more amorphous but less tightly packed crystalline arrangement. This may be due to wet O_3/UV pre-treatment, attributed to surface hydration and allowing dye-fiber interaction.

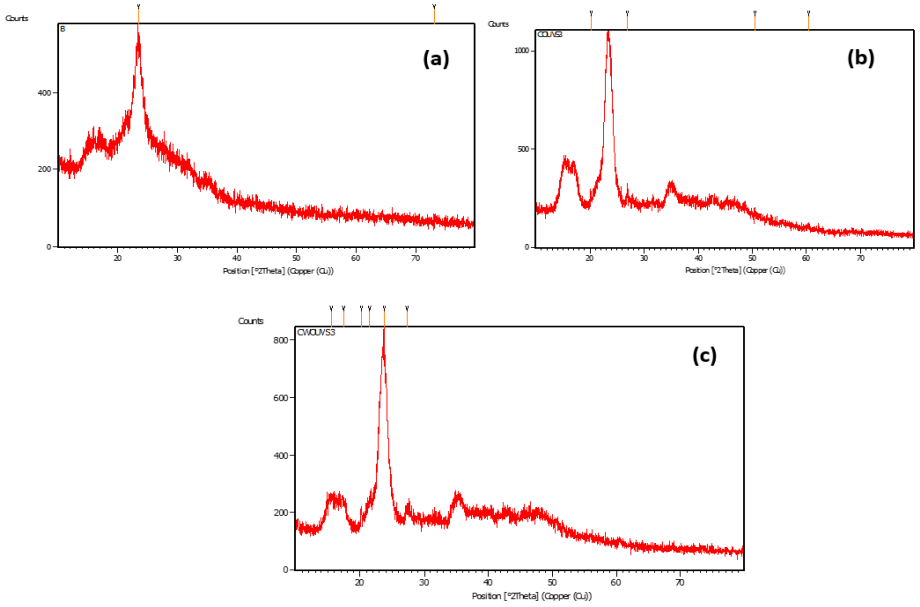

Figure 111. XRD pattern of (a) untreated blank cotton fabric; (b) dry O_3/UV treated dyed cotton fabric (COUVS3); (c) dry O_3/UV treated dyed cotton fabric (CWOUVS3)

The another set of combined O_3/UV/Plasma pre-treated and plasma pre-treated cotton fabrics dyed with composite dye solutions formulated from *Tristellateia australasiae* (TA) ethyl acetate extract, ball milled red sandal powder (BMRSP), ionic liquid (BMIMCl) and optionally,

TAE aided silver nanoparticles (TAES NPs) were analysed to investigate the crystalline nature of dye-fabric incorporation. The combined O_3/UV/Plasma pre-treated cotton fabric dyed with alkaline extract of TAEA, named as TOUPTD. Whereas, the plasma pre-treated fabric dyed with (alkali extract of TAEA + BMRSP + IL) without SNPs was assigned as TPTBID, while with the addition of TAES NPs to the above composite was labelled as TPTBISD.

XRD pattern of combined O_3/UV/Plasma treated (TOUPTD) TAEA alkaline dye coated fabric shows the major intense peaks at 2θ values of 23.1˚, 31.98˚, 45.5˚, 56.5˚, 66.4˚ and 75.42˚. The peak at 23.1˚ matches with blank cotton fabric and another diffraction peaks at 31.98˚, 45.5˚, 56.5˚, 66.4˚ and 75.21˚ which corresponds to the alkaline TAEA dye. The XRD pattern of TOUPTD dyed cotton fabric is shown in **Figure 112a**. Similar diffraction peaks were observed for surface plasma treated fabrics with the same TAEA alkali dye extracts coated fabrics labelled as TPTD, showing the diffraction peaks at 2θ values of 23.1˚, 31.9˚, 45.68˚, 57.7˚, 66.4˚ and 75.6 ˚, respectively **(Figure 112b)**. The surface plasma-treated fabrics coated with BMRSP alkali dye, labelled as TPBD, showed the similar diffraction peaks at 23.4˚, 32.7˚, and 46.4˚ **(Figure 112c)**. Also, the combined alkali dye extract of TAEA and BMRSP coated fabric (TPTBD) showed the respective minor diffraction peaks at 2θ values of 33.6˚, 35.06˚, 39.23˚, 46.46˚ and 58.42˚. The diffraction pattern of the TPTBD coated fabric is presented in **Figure 112d**.

For the sample TPTBID coated surface treated cotton fabrics showed the respective 2θ values of 20.14, 32.6, 33.8, 38.2, 40.5, 45.3 and 57.5˚. The slight shift in peaks towards lesser 2θ values was observed after coating with combined alkali dye solutions in combination with ionic liquid. The mean crystallite size of the TPTBID-coated fabric was determined to be 31.96 nm **(Figure 112e)**.

For SNPs composite containing the combined extract along with ionic liquid (TPTBISD) depicts the different diffraction peaks having 22.77˚, 35.45˚, 38.94˚ and 41.67˚. Whereas the synthesised TAESNP shows the 2θ values at 32.42˚, respectively. The crystallite grain size of TPTBISD coated on the surface of cotton fabrics was 11.84 nm as shown in **Figure 112f**. Therefore, the results of coated dyed fabric clearly depict the dye solutions containing the combined extracts of TAEA and BMRSP, ionic liquid and SNPs are successfully impregnated on the surface of the fabric matrix. The reports on SNPs coated on cotton fabric shows the diffraction peaks (38.4˚, 44.6˚, 64.7˚ and 77.5˚) corresponds to face-centred cubic crystalline structure with 0.49 nm **(Balamurugan *et al.*, 2017; Kwak *et al.*, 2015)**.

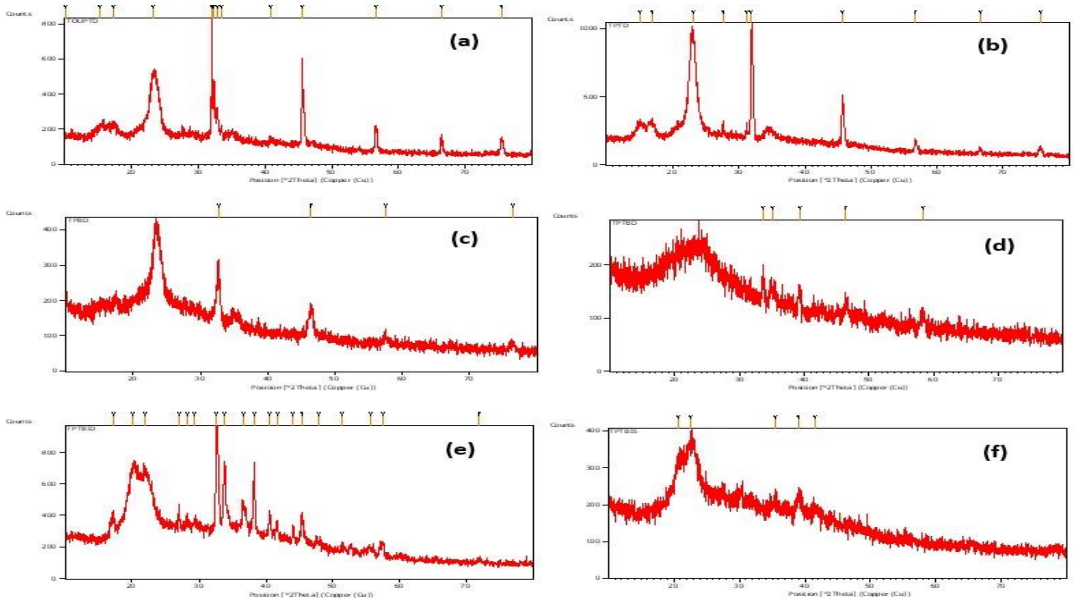

Figure 112. XRD pattern of treated dyed fabric (a) dry O_3/UV/Plasma treated dyed cotton fabric (TOUPTD); (b) Plasma treated TAEA alkali dyed cotton fabric (TPTD); (c) Plasma treated BMRSP alkali dyed cotton fabric (TPBD); (d) Plasma treated composite alkali dye (TAEA and BMRSP) coated cotton fabric (TPTBD); (e) Plasma treated and dyed cotton fabric (TPTBID); (f) Plasma treated and dyed cotton fabric (TPTBISD)

4.7.2.4.3 FESEM and EDS analysis of blank and dyed fabrics

The surface morphology of the blank and dyed cotton fabrics was investigated using FESEM, as shown in **Figure 113 (a to e)**. The image of the blank cotton fabric **(Figure 113a)** revealed clean, smooth, well aligned longitudinal fibrils, and without any visible surface deposits. In contrast, the COUVS3 **(Figure 113e)**, which was pre-treated with dry O_3/UV and dyed with ball milled red sandal powder (BMRSP) showed the surface fibrils were covered with BMRSP dye. The TPTBD fabric sample **(Figure 113b)**, which was treated with plasma and dyed with *Tristellateia australasiae* extract and BMRSP extract, exhibited a dense and uniformly coated dye along the entire fiber surface. The smooth and consistent dye coatings were noted at 2.00 kx magnification, suggesting deeper penetration of dye on the fabrics which are assisted by plasma induced surface roughness. In the TPTBID coated fabric **(Figure 113C)**, exhibited the crystal morphology over the fibrils which are due to incorporation of ionic liquid (BMIMCl) along with the alkali dye extract. In addition, the TPTBISD fabric **(Figure 113d)**, dyed with equal ratio of TAEA and BMRSP alkali extract, ionic liquid and SNPs exhibits an irregular morphology with large crystalline deposition embedded in the fiber. This may be due to the synergistic effect of plasma treatment, composite extracts, ionic liquid and nanoparticle incorporation.

The elemental mapping for the blank and dyed fabrics is shown in **Figures 114a to 114f**. The blank cotton fabric exhibits elements such as O, C and Ca. The conventionally dyed (C5) fabric treatd with the composite dye formulation (TAEA+ BMRSP + ionic liquid + silver nanoparticles) shows the presence of C, O, Ag and Na. The sample COUVS3, which was pre-treated with dry O_3/UV and dyed with BMRSP, display elemental signals for Ca, O, C, Na, and Mg **(Figure 114f).** The TPTBD dyed fabric revealed the presence of Na, C and O, where Na attributed to the alkaline extraction process. Also, the TPTBID dye-coated fabric contains C, O, Na and Cl elements. The element Cl is due to the use of ionic liquid (IL) – 1-butyl 3 methyl imidazolium chloride coated on fabric material. Similarly, the composite dye combining extracts, IL and SNPs (TPTBISD) exhibited the elements such as C, O, Na, Cl, and Ag. Therefore, the presence of Ag in both C5 and TPTBISD coated fabrics confirmed the successful impregnation of SNPs into the fabrics.

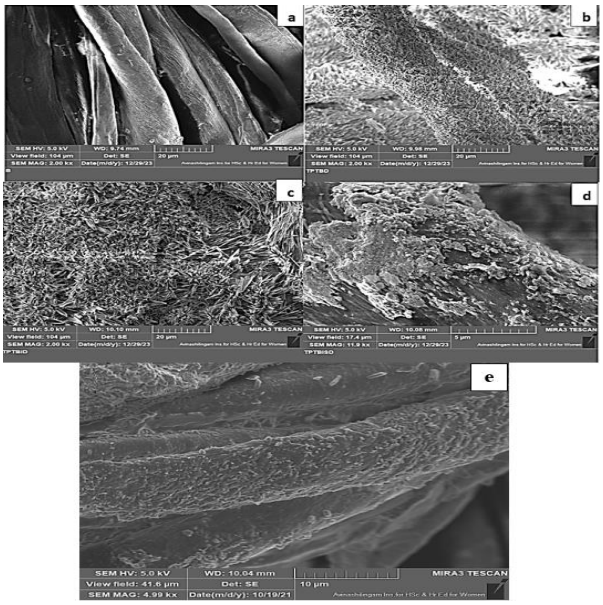

Figure 113. FESEM morphology of blank and dyed cotton fabrics a) Blank cotton fabric; b) TPTBD; c) TPTBID; d) TPTBISD; (e) COUVS3

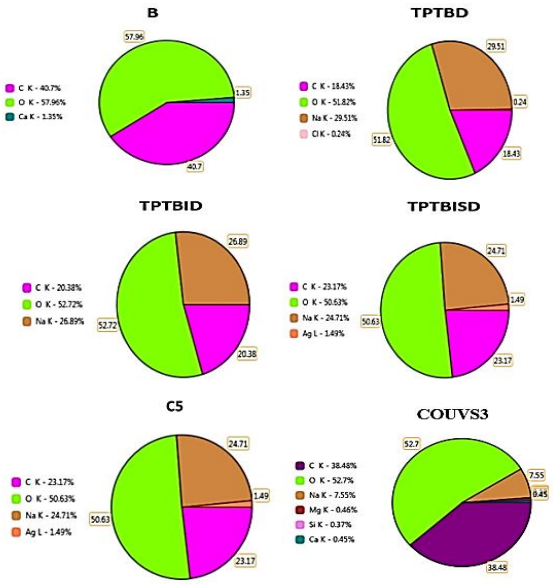

Figure 114. EDS pie chart of blank and dyed cotton fabrics (a) blank; (b) C5; (c) TPTBD; (d) TPTBID; (e) TPTBISD; (f) COUVS3

4.7.2.5.1 Colour on screen and colour fastness of dyed fabrics

The surface-treated (COUVS3, CWOUVS3, TPTD, TPBD, TOUPTD, TPTBD, TPTBID and TPTBISD) dyed fabric samples were evaluated for the coating colour using color on-screen measurement. All dyed fabrics were found to be exhibit dark brown, as shown in **Figure 115**. Several factors assess the colour fastness of dyed fabrics, for retaining the colour and reusability of products throughout wear life. The colour fastness properties of (COUVS3,

CWOUVS3, TPTBID and TPTBISD) dyed fabrics subjected to wet and dry rubbing tests against the original cloth. The stains on the wet/dry rubbing cloth were evaluated using a grey scale, and assigned the ratings. Both samples exhibited dry rubbing colour fastness of 4-5 and wet rubbing colour fastness of 3-4.

Similarly, the sunlight colour fastness of the dyed fabric samples was evaluated by exposing them to sunlight for ten days. After exposure, the colour strength and colour on screen of the dyed fabrics were recorded. On the first day, the colour strength (K/S) values of TPTBID and TPTBISD were 147.95 and 117.80, respectively. After ten days of sunlight exposure, these values slightly decreased to 139.0 and 108.02. The slight decrease in colour strength indicates good retention of dye colour on the fabrics.

Leaching studies of the TPTBID and TPTBISD coated fabrics were carried out by immersing the samples in water, and collecting the dye released solution at different time intervals for UV BioSpec analysis. Within the first 5 to 30 min, the TPTBID coated fabric released the dye more quickly than the SNPs coated-TPTBISD fabric. The TPTBISD sample exhibited minimal dye release up to 30 min and began to leach the dye after this period. These findings suggested that the ability of dyed cotton fabrics to retain or release dye molecules in water depends on the coating composition. Furthermore, the use of stabilisers enhances the adhesive properties of dyes on fabric surfaces **(Aķsit and Onar, 2008).**

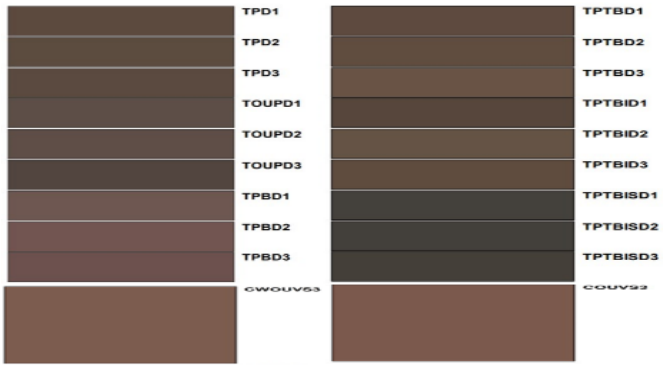

Figure 115. Colour on screen of dyed cotton fabrics

4.7.2.6 Antimicrobial Activity of Dyed Fabrics

4.7.2.6.1 Antibacterial activity of blank and dyed fabrics against *S. aureus*

Antibacterial testing of TPTBD, TPTBID, and TPTBISD fabrics were carriedout against the gram +ve bacterial strain *S. aureus* (**Figure 116)** using the Kirby-Bauer disk diffusion method. The blank cotton fabric was assigned the sample code as B, while ciprofloxacin-coated fabric was used as the standard (std). The zone of inhibition (ZOI) results for all dyed cotton

fabrics are given in **Table 46.** From the results, the standard CIP-coated fabric possesses no bacterial growth beneath the fabric surface, whereas the untreated bleached cotton fabric (B) showed bacterial growth beneath the cotton fabric. Similarly, the surface plasma treated fabrics, the composite of two alkali dye extracts (TPTBD) possesses 21 mm ZOI. The TPTBID coated fabric shows the maximum ZOI (26 mm), indicating better antibacterial activity, while the TPTBISD-coated cotton fabric showed 22 mm ZOI. Therefore, the results suggested that TPTBID possess, maximum inhibition against bacterial strains (*S. aureus*), followed by TPTBISD and TPTBD, respectively. The presence of IL in the composite dye solution enhances the bacterial inhibition, contributing to good antibacterial properties of fabric. In addition, SNPs combined with blended extract and IL exhibited good antibacterial properties, their effectiveness was less when compared to TPTBID-coated fabrics. However, by increasing the thickness on the SNPs coating on fabrics, further improve antibacterial efficacy. Promoting the use of ILs as surface coating agents on fabrics, wool, or polypropylene surfaces promises for creating an antibacterial finished surface, as reported in previous studies **(Kantouch *et al.*, 2013; Sasi *et al.*, 2021)**.

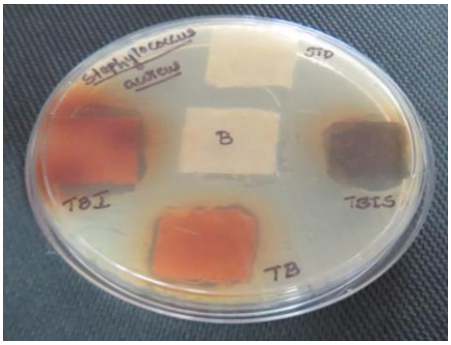

Figure 116. Antibacterial activity of blank and dyed fabrics against *S. aureus*

4.7.2.6.2 Antifungal activity of blank and dyed fabrics against *C. albicans*

The antifungal activity of TPTBD, TPTBID, and TPTBISD fabrics was evaluated against the skin-related fungal species *C. albicans* (**Figure 117)** using the Kirby-Bauer disk diffusion method. Blank cotton fabric (B), while ciprofloxacin-coated fabric served as the standard. The zone of inhibition (ZOI) of the dyed fabrics are given in **Table 46.** From the results, the sample blank and standard CIP-coated cotton fabrics were prone to fungal attacks beneath their surfaces. In contrast, the surface plasma-treated fabrics TPTBD, TPTBID, and TPTBISD showed the ZOI at 27 mm, 24 mm, and 23 mm, respectively. Among these, the composite alkali extract containing TA and BMRSP extract (TPTBD) possess highest efficacy in inhibiting fungal growth on the fabric surface. There are no reports related to TA extract and

its biomedical applications. This is the first report on TA-aided SNPs, as fabric coating agents with antibacterial and antifungal properties **(Ravimoorthy and Pottail, 2025)**.

Tristellateia australasiae , a member of the Malpighiaceae family, is identified for its medicinal properties including antibacterial, antifungal against skin infections, antioxidant and lung infections, etc. **(Michelin *et al.*, 2008; Villanueva-Amador *et al.*, 2020)**. Similarly, *P. santalinus* reported to exhibits antibacterial, antifungal, anti-inflammatory, antimutagenic, dysentery and eye diseases **(Bulle *et al.*, 2016)**. Therefore, the combination of both extracts as a composite coating on fabric surfaces was found to be highly effective against fungal species. The phytoconstituents present in both extracts, such as alkaloids, tannins, flavonoids, glycosides, terpenoids, steroids, carbohydrates, and poly phenolic compounds play an essential role in resisting the invasion of microbial strains on the cotton fabric surfaces. In addition, the prior reports on the susceptibility of linen fabric coated with ionic liquid-dodecyl dimethyl ammonium nitrate possess antifungal resistance **(Foksowicz-Flaczyk and Walentowska, 2013)**. Following TPTBD, the fabrics treated with IL and composite extract dye (TPTBID), and those coated with SNPs (TPTBISD), also shows notable antifungal activity.

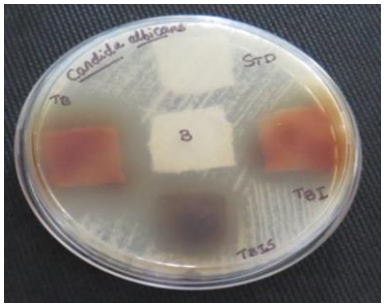

Figure 117. Antifungal activity of blank and dyed fabrics* against *C. albicans

Table 46. Antimicrobial Activity of Blank and Dyed Fabrics against *S. aureus* and *C. albicans*

Sample code	Zone of Inhibition (mm)	
	S. aureus	***C. albicans***
B	0	0
STD	0*	0
TPTBD	21	27
TPTBID	26	24
TPTBISD	22	23

*Indicates no growth of bacteria beneath the surface of fabrics

4.7.2.7 UV-Protective Dyed Fabrics

The UV transmittance spectra of ball milled red sandalwood powder (BMRSP) dyed cotton fabric following different O_3/UV pre-treatments are shown in **Figure 118**. The sample COUVS3 (dry O_3/UV pre-treated) and CWOUVS3 (wet O_3/UV pre-treated) dyed fabrics were evaluated across multiple locations to assess the uniformity and UV blocking performance in the wavelength range from 280 to 460 nm, which covers UV-B (280 to 320 nm) and UV- A (320 to 400 nm). For both samples, the UV transmittance remained below 2.5%, confirms excellent UV protection. However, the sample CWOUVS3 showed lower % transmittance value, particularly in UV-B region. Therefore, the CWOUVS3 dyed fabric offered to be more effective UV shielding, due to denser dye coating with uniform surface as a result of wet O_3/UV pre-treatment, which is due to surface hydration and homogenous deposition of dye on the fabric. In comparison, the sample COUVS3 also exhibited low transmittance across different locations and the dry O_3/UV pre-treated fabric improves dye-fiber interaction, but with less uniformity in surface coating of fabric. Nevertheless, both samples possess minimal difference between the locations, indicating reproducibility and uniform protective performance against UV-A and UV-B.

The UPF value of CWOUVS3 and COUVS3 possess 329 and 256, respectively. The wet O_3/UV pre-treated BMRSP dyed fabric provides superior UV protection, despite lower colour strength (K/S) which are due to stronger absorption and deposition of phytochemical compounds from red sandal wood extract under aqueous O_3 treatment. The presence of UV-absorbing phytocompounds such as tannins, flavonoids and quinones in BMRSP dye extract, are essential in absorbing and scattering UV radiation. Overall findings indicate that both dry/wet ozone/UV pre-treatments and BMRSP dyed cotton fabric, significantly enhanced the UV-protection performance. ***This innovative work has been granted a patent to our research team by government of India for 20 years owing to its novelty (Patent No. 494488) (Appendix vi)***

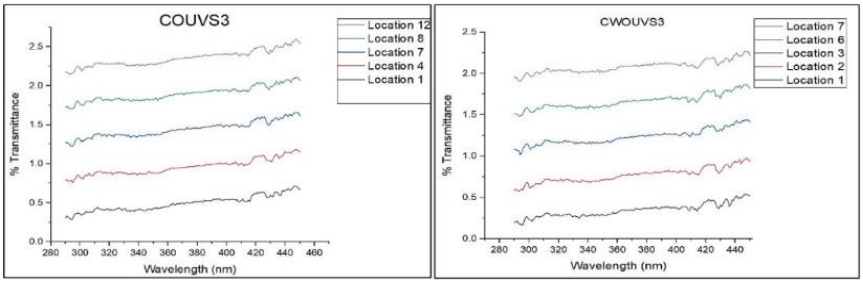

Figure 118. UPF analysis of BMRSP dyed COUVS3 and CWOUVS3 cotton fabric

Similar studies have explored the use of aqueous methanolic extracts of dry and fresh fruits of *Rosa canina* as a natural dye agent. Cotton fabric treated with or without bio-mordant (chitosan), showed excellent UV protection (UPF=50) and antibacterial properties **(Raziye *et al.,* 2023)**. In another study, multifunctional cellulose based fabrics were developed by incorporating zinc oxide NPs and perfluoro octanol into a poly urethane matrix. The coated fabrics exhibits high hydrophobicity with a water angle increasing from 0˚to 135˚ and achieved over 99% bacterial inhibition against *S. aureus* and *E. coli*. Moreover, the coated fabric possesses excellent UV shielding with a UPF value greater than 50 **(Zhang *et al.,* 2025)**. Recent study focused on bamboo derived lignin, synthesised by ethanol pulping to create eco-friendly multifunctional coatings. Ethanolic lignin coated cotton fabrics exhibits enhanced antioxidant and UV blocking properties, including 99.99% UV-A, and 100% UV-B protection with a UPF value of 48.2, and UV transmittance below 3% **(Dong *et al,* 2025)**. In addition, the transparent coating using green synthesised gelatin-based GNPs and combined with TiO_2 NPs, applied by spraying onto machine embroidered fabric. The coated fabric possesses stronger UV shielding and good antibacterial performance **(Alshehri *et al.,* 2025)**.

From the textile applications, ball milled red sandal wood alkali extract was coated onto pre-treated cotton fabrics, resulting in enhanced UV-protective properties. Furthermore, nanocomposite dye coatings incorporated with SNPs showed excellent antimicrobial activity. Therefore, these findings support the potential use of eco-friendly, multifunctional textiles offering simultaneous UV protection and anti-microbial enhancement, which is suitable for advanced textile dyeing industries.

Based on the findings, it can be concluded that sustainably synthesised gold and silver nanoparticles possess significant potential in biomedical, textile, and pharmaceutical applications. According to technology transfer, the knowledge or innovations developed as part of the present research are as follows:

Sustained release Floating tablet for drug release

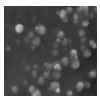

Sustained release microspheres for drug release

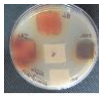

Antimicrobial fabric coated with nanocomposite

UV protective woven fabric